

**Understanding molecular
structure–function relationships
in controlling
nanoscale conductance**

Lynn Groß

Dissertation
with the aim of achieving a doctoral degree
at the Faculty of Mathematics, Informatics and Natural Sciences
Department of Chemistry
of Universität Hamburg

March, 2016

The present work was carried out in the period from April 2013 to March 2016 in the Institute of Inorganic and Applied Chemistry at the Universität Hamburg in the group of Prof. Dr. Carmen Herrmann.

Dissertation accepted on the recommendation of
Prof. Dr. Carmen Herrmann
PD Dr. Christian Klink

Date of admission: 04/01/2013

Date of submission: 03/07/2016

Date of oral defense: 05/13/2016

Approval of dissertation: 05/17/2016

Contents

I. Zusammenfassung	iii
II. Abstract	v
1. Introduction	1
1.1. Experimental architectures in nanoelectronics	2
1.2. Impact of molecular structure on conductance	5
1.3. Switching conductance by external stimuli	6
1.4. Theoretical approaches in molecular electronics: basics	8
1.4.1. Electronic structure calculations: Density functional theory	9
1.4.2. The Landauer picture of electron transport	11
1.4.3. Challenges for DFT-based transport calculations	13
1.5. Scope and outline of this work	14
2. Landauer theory of electron transport through molecular junctions	15
2.1. Derivation of the Landauer ansatz	16
2.2. Analytical transmission function for a single-level system	22
2.3. Analytical transmission function for a two-level system	24
2.4. A first-principles approach and its implementation in ARTAIOS	28
3. Analyzing and predicting force and conductance measurements	31
3.1. Introduction	31
3.2. A mechanically flexible platform-based Zn-porphyrin complex	33
3.2.1. A closer look at the conductance curve	38
3.2.2. Platform contribution to the conductance	41
3.3. Functionalized trioxotriangulenium platforms	42
3.4. Mechanical manipulation of spin states in manganocene	44
3.5. Detecting the dipole moment of carbon monoxide on different surfaces	49
3.6. Conclusion	54
4. Charge transfer and dipole effects in functionalized carbon nanotubes	57
4.1. Introduction	57
4.2. Local dipole moments within the theory of Atoms-In-Molecules	62
4.3. Derivation of a generalized approach to calculate local dipole moments	65
4.4. Implementation in GENLOCDIP	67
4.5. Effects of truncating a CNT on adsorbate-induced property changes	79

4.6. Noncovalent functionalization of carbon nanotubes by diarylethene photoswitches	86
4.7. Conclusion	94
5. Molecular conductance in competition with energy transfer in nanoparticle arrays	97
5.1. Introduction	97
5.1.1. Electron transfer in donor–bridge–acceptor systems and its relation to electron transport in molecular junctions	99
5.1.2. Fluorescence resonance energy transfer	103
5.2. Excitation pathways as a function of transfer rates	105
5.3. Conclusion	107
6. Conclusion and Perspective	109
6.1. Summary	109
6.2. Outlook	111
7. Acknowledgments	113
A. Computational methodology	115
B. Additional data	121
B.1. Local transmissions	121
B.2. Infrared spectra	123
B.3. Additional data on local dipole moments	126
B.4. Additional data on noncovalent functionalization of CNTs	135
C. List of notations	149
D. List of abbreviations	153
E. List of publications originating from this work	157
F. List of Chemicals	159
G. Bibliography	161

I. Zusammenfassung

Eines der grundlegenden Ziele der molekularen Elektronik und verwandter Forschungsfelder ist die Verwendung von maßgeschneiderten Molekülen für die Entwicklung von elektronischen Bauelementen mit neuen Funktionalitäten jenseits von siliziumbasierter Halbleitertechnik. Da sich die Eigenschaften von Molekülen durch den Elektrodenkontakt dramatisch ändern können, ist es wichtig die Verbindung zwischen Molekülstruktur und Funktionalität in solchen elektronischen Bauteilen zu verstehen und zu kontrollieren. Neben der Entwicklung von neuen experimentellen Methoden (Rastertunnelmikroskopie und sogenannte Break Junctions) wurden theoretischen Methoden entwickelt um Ladungstransport durch nanoskalige Systeme zu beschreiben und vorhersagen zu können. Derzeit bestehen wichtige Herausforderungen für die Theorie darin, Antworten auf folgende Fragen zu finden: (1) Was ist ein geeignetes Modellsystem um das jeweilige Experiment zu simulieren? (2) Wie können wir Erkenntnisse auf nanoskopischer Ebene auf die Makrowelt übertragen und so dem komplexen Zusammenspiel von Effekten auf verschiedenen Längen- und Zeitskalen gerecht werden?

In dieser Arbeit wurde der Ladungstransport durch (supra)molekulare Systeme mit Hilfe von theoretischen Methoden untersucht, mit dem Fokus auf mechanisch und photochemisch induzierten Leitfähigkeitsänderungen. Unsere Transportberechnungen basieren auf dem sogenannten Landauer–Imry–Büttiker-Ansatz in Verbindung mit Greensfunktionen und der Kohn-Sham-Dichtefunktionaltheorie (DFT). Ziel ist es, Erklärungen für experimentelle Beobachtungen zu liefern, aber auch interessante Vorschläge für neue Experimente zu machen. Weiterhin zeigen wir, wie die hier gewonnenen Erkenntnisse verwendet werden können, um erste Schritte in Richtung von Multiskalenansätzen zu gehen.

Es wurden Kraft- und Leitfähigkeitsmessungen an plattformgebundenen Molekülen auf einer Gold-Oberfläche durch Kombination von beschränkten Optimierungen mittels statischer DFT und dem Landauer-Ansatz zur Beschreibung kohärenten Tunnelns simuliert. Obwohl die Flexibilität des Moleküls eigentlich ein statistisches Sampling (z.B. durch Molekulardynamik-Simulationen) erfordern würde, stimmen unsere Ergebnisse dank eines qualitativen Scans wichtiger Konformationen gut mit dem Experiment überein. Daher haben wir unseren Ansatz auf weitere interessante Moleküle übertragen. Zum Beispiel haben wir einen Spin-Crossover-Komplex da-

rauffin untersucht, ob ein mechanisch induzierter Spinzustandsübergang in einem Rasterkraftmikroskop realisierbar wäre. Wir mussten jedoch feststellen, dass eine äußerst sorgfältige Beschreibung der nicht-kovalenten Wechselwirkungen des Systems mit der Oberfläche notwendig ist, was oft ein Problem für DFT dargestellt und dass möglicherweise das Molekül von der Spitze nicht in der gewünschten Art verformt wird.

Desweiteren wurden Gate-Effekte von adsorbierten Gas-Molekülen und Photoschaltern auf die elektronischen Eigenschaften und die Leitfähigkeit von Kohlenstoffnanoröhren (englisch carbon nanotubes, CNTs) untersucht. Um den zugrundeliegenden Mechanismus zu ermitteln, haben wir systematisch lokale Eigenschaften nach der Theorie der Atome in Molekülen berechnet und zwei verschiedene DFT-Methodologien verglichen: Ein Plane-Wave-Modell unter periodischen Randbedingungen und einen "abgeschnittenen" Ansatz unter Verwendung einer lokalisierten Einteilchenbasis. Für Adsorbate auf metallischen CNTs hat sich dabei gezeigt, dass die CNT-Länge relativ klein sein kann, ohne dass die Adsorptionsstruktur durch das Abschneiden beeinflusst wird. Halbleitende CNTs tendieren hingegen dazu, sensibler auf eine Längen-Beschränkung zu reagieren. Obwohl einige Ergebnisse bezüglich der Dipolmomente mit den experimentellen Beobachtungen korrelieren, konnten wir keine haltbaren Aussagen zur Übertragbarkeit des Modells auf das Experiment treffen. Durch die Wahl des minimalen Modellsystems haben wir wichtige Effekte (vor allem Grenzflächen-Effekte) vernachlässigt, die einen entscheidenden Einfluss auf die Transporteigenschaften der CNTs haben können. Hier wäre ein Multiskalenansatz hilfreich. Als ersten Schritt in diese Richtung haben wir ein Programm zur Berechnung und Visualisierung von lokalen Dipolmomenten von molekularen Subsystemen entwickelt, welches die Weiterverarbeitung von verschiedenen Elektronenstruktur-Ausgabeformaten ermöglicht. Die so gewonnenen Dipolmomente können in ein grobkörnigeres Modell eingebaut werden, um das Gating-Phänomen in CNT-basierten Transistoren oder auch Lösungsmittelleffekte in der molekularen Elektronik und Spitze-Molekül-Wechselwirkungen in Rasterkraftmikroskopie-Messungen zu verstehen.

Schließlich konnten wir zeigen, dass Elektronentransferraten (welche näherungsweise aus den Leitwerten von Molekülen erhalten werden können) und Ratenkonstanten eines konkurrierenden Prozesses (in diesem Fall Energietransfer) für Donor-Brücke-Akzeptor-Verbindungen in ein einfaches, analytisches Modell eingegeben und daraus Erkenntnisse über die Dynamik von Zustandspopulationen gewonnen werden können.

II. Abstract

The use of tailor-made molecules for the design of nanoscopic devices with advanced functionalities beyond conventional silicon-based counterparts has been the primary goal for molecular electronics and related fields in recent years. Along this path it is crucial to understand and to control the relationship between structure and function in metal–molecule–metal junctions as molecules may change their properties when connected to macroscopic electrodes. Besides the development of novel experimental strategies (e.g., mechanical break junctions and scanning probe microscopy), a variety of theoretical approaches have been presented to describe and predict electron transport in such devices. At present, the challenges for theoretical models include two important questions: (1) what is a proper model system for the given experimental device or the relevant part of it? (2) how can we transfer knowledge from the nanoscopic to the macroscopic level, and thus bridge the wide range of relevant time and length scales?

In this thesis, theoretical investigations of electron transport through (supra)molecular systems focusing on changes in the conductance as a consequence of mechanical and photochemical stimuli are presented. The electron transport calculations are based on the Landauer–Imry–Büttiker approximation combined with a Green’s function approach and Kohn–Sham density functional theory (DFT). The aim is to gain insights into the corresponding experimental measurements, to provide interesting proposals for future experiments and to take first steps towards implementing nanoscopic properties in a coarse-grained multiscale model.

Force and conductance measurements of a platform-mounted molecule on a Au(111) surface by combining constrained optimizations using static DFT and electron transport calculations are simulated. Although the flexibility of the molecule under mechanical stress would suggest that statistical sampling is required (*e. g.*, molecular dynamic simulations), thanks to accounting for the relevant conformations first-principles results show a remarkably good agreement with the experiment. Therefore, the system of interest is extended towards, for instance, a spin-crossover compound to assess whether a mechanically-induced spin transition could be realized using atomic force microscopy. It was found that careful treatment of non-covalent interactions between molecules and surfaces is necessary (which DFT often has problems with) and that, perhaps, the molecule is not deformed by the tip in the

desired manner.

Furthermore, the chemical gating effects of gaseous and photoswitchable molecules interacting with single-walled carbon nanotubes are investigated. To determine the mechanism which affects the nanotube's transport properties, local properties according to the theory of Atoms-In-Molecules are systematically calculated using two different DFT methodologies: a plane-wave periodic boundary model and a truncated approach employing a localized single-particle basis. It was found that for small adsorbates on metallic nanotubes, their length can be fairly small as this does not significantly affect the adsorption structure. Semi-conducting nanotubes on the other hand tend to react more sensitively to truncating the nanotube. Although a change of the adsorbate dipole moment upon photoswitching could be responsible for the observed change in transistor characteristics, it could not be established for certain whether the minimal model system captures the relevant features of the experiment. A multiscale model including the electrode–nanotube interface would be helpful to make reliable predictions of the underlying gating mechanism. As a step towards this goal, a program for calculating and visualizing local dipole moments of molecular subsystems which enables postprocessing of a variety of electronic structure output formats was developed. The dipole moments obtained may be embedded as point dipoles in large-scale approaches to understand the chemical gating phenomena in carbon nanotube transistors but also solvent effects in molecular electronics, and tip–molecule interactions in atomic force microscopy.

Finally, we demonstrated how electron transfer rate constants (*e. g.*, estimated from calculated conductance values) and those of a competing process (in this case energy transfer) that may occur in Donor–Bridge–Acceptor systems can be implemented in a simple analytical model to gain insights into the population dynamics, *e. g.* in colloidal quantum dots relevant for photovoltaic or light-emitting diode applications.

1. Introduction

Facing the need for increased performance of transistors and further miniaturization, the fundamental idea of using molecular components for the fabrication of electronic devices has led to a rapidly growing research field in nanoscience: *Molecular electronics* [1,2]. The first concepts embracing the functionality of molecules for electronics originated in the early 1950s [3–6]. At that time, Kuhn and co-workers were able to measure the electrical conductivity of molecular monolayers [7,8]. The theoretical proposal by Aviram and Ratner in 1974 of a molecular diode acting as a rectifier [9] has since then paved the way for molecular electronics. However, practical attempts of inserting a single molecule in an electronic device have suffered from the limited control of the contact between molecules and macroscopic electrodes [10]. Thus, measuring currents through molecules has benefited enormously (as without doubt many other fields in nanoscience) from the development of scanning probe and break junction techniques, which enabled the manipulation of molecular and supramolecular structures at the nanoscale in the mid-1990s [11–14]. The rectifying behavior of donor–acceptor molecules has now been confirmed experimentally for monolayers [15] and even for single molecules [16], and substantial advances in the design of various applications in nanoelectronics and spintronics have been made, using molecules as building blocks for memory elements, switches, rectifiers, and transistors. Also additional supramolecular and hybrid material device architectures involving the functionalization of carbon-based transistors (*e. g.*, carbon nanotubes filled with bucky balls [17,18]) or arrays of metal nanoparticles in an organic matrix [19] have been introduced lately. In such supramolecular systems, a molecule can affect the electronic properties of the system involved in transport indirectly through covalent and noncovalent interactions.

Theoretical modeling of molecule–metal interfaces has played a significant role in understanding the transport mechanisms and structure–function relationships at the nanometer scale since the beginning of the field. Since the structure of molecular junctions is not precisely known and can be barely controlled in experiments due to structural fluctuations, a comparison with theoretical methods is important to help examine, for instance, whether indeed a single molecule is incorporated in the junction. Quantum mechanical concepts of electron transport [20] (and the closely related electron transfer process [21]) have provided new insights on fundamental questions such as: How do electrons move through single molecules? What

is the impact of structural and electronic changes on electron transport? What mechanisms are responsible? And what are the requirements for well-conducting molecular systems?

In the following, the most common methods of connecting molecules in a electrode–molecule–electrode setup are presented. Furthermore, a brief overview of controlling the conductance through a single molecular junction and challenges that arise for a theoretical description of electron transport through such junctions are given.

1.1. Experimental architectures in nanoelectronics

The development of the scanning tunnelling microscope (STM) [11–13] has contributed substantially to the progress in molecular electronics, since it allows for the fabrication of reproducible atomic-size contacts in a controlled manner (see Refs. [22–24] for a more detailed review). In a STM, a sharp metal tip is brought into contact with a molecule on a conducting surface allowing tunneling current to flow through the molecule. This allows imaging and manipulating a molecule in ultra-high vacuum, air, and various liquids while measuring its electrical properties [25]. Probably the first STM study of a tip–molecule contact has been demonstrated by Joachim and Gimzewski for buckyballs (C_{60}) on a Au(110) surface in 1995 [26]. Later, Tautz *et al.* impressively showed that a STM tip can be used to pick up flat-lying molecules and thus controlling those molecules [27]. The atomic force microscope (AFM) is closely related to the STM, but measures either the short range repulsive or the longer range attractive force between the tip and a (not necessarily conducting) surface [28], instead of the tunneling current. For simultaneous force and conductance measurements of nanoscale junctions, two combinations of STM and AFM have been presented: The conducting AFM (c-AFM) [29] and the combined STM/AFM [30, 31]. The first technique uses a metal-covered tip¹, whereas the latter uses a metal tip attached to the cantilever as illustrated in Fig. 1.1a. Furthermore, several types of two-terminal break junction techniques have been extensively used for the purpose of measuring conductances in single molecular junctions. The basic concept is to control the gap between two electrodes within a range of 1 – 3 nm using a piezoelectric transducer. In a mechanically controllable break junction (MCBJ), a thin metallic wire (*e. g.*, gold) on a flexible substrate is bent or stretched until it breaks, which (ideally) leads to a single molecule trapped between the electrodes (see Fig. 1.1b) [14, 34, 35]. Reed and Tour first employed the MCBJ technique to single molecules by addressing the charge transport through 1,4-benzenedithiol between gold leads [36, 37]. Since conduc-

¹The metal-covered tip of a c-AFM is larger and no longer as sharp as a STM tip [32, 33] which causes a certain amount of uncertainty about the actual number of molecules measured.

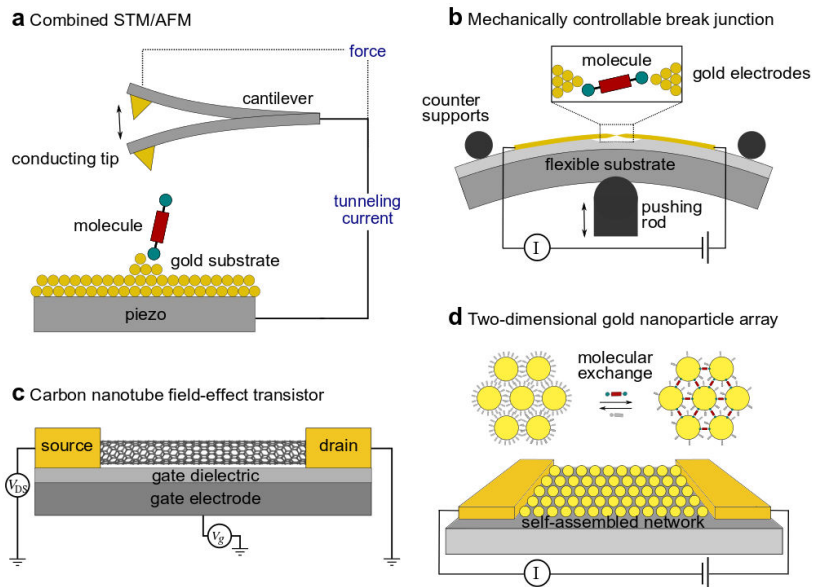


Figure 1.1.: Schematic illustration of different experimental setups for studying molecular conductance. (a) The combined STM/AFM uses a metal tip attached to a cantilever in order to measure forces and conductance simultaneously. (b) In a mechanically controllable break junction (MCBJ), a metal wire on a flexible substrate is strained by bending the substrate which causes the wire to break at a certain point resulting in two electrode contacts. (c) A typical setup of a carbon nanotube field-effect transistor consists of a carbon nanotube as the channel material connecting two electrodes (source and drain). The third metal contact representing the gate electrode is added on the back of a dielectric layer. (d) An electrically contacted two-dimensional gold nanoparticle array. The molecular-exchange reaction enables the bridging of neighboring particles to form a network of junctions.

tance is highly sensitive to variations in the molecular conformation and to the structural details of adsorption to the electrodes, it is almost impossible to identify and reproduce the conductance of a single molecule and hence, a statistical analysis of a large number of measurements is needed [38–42]. Break junction techniques capture structural fluctuations by creating and reforming molecule–metal contacts hundreds of times [43–45]. The histograms of the resulting conductance values are

reproducible and exhibit (in most cases²) a well-defined peak attributed to the most probable conductance of a single-molecule junction [48–50]. Recently, a theoretical model has been proposed to extract additional information from the peak’s line shape about the alignment of the molecular levels relative to the Fermi energy of the electrodes and the molecule–electrode coupling [51,52].

While mechanical break junctions are almost always formed in vacuum, Tao and Xu [53] extended the break-junction method to single molecular junctions in solution using a STM setup. In a STM-based break junction (STM-BJ), vertical molecular junctions are repeatedly formed by moving a STM tip in and out of contact with a molecule on a surface. Compared to MCBJs, STM-BJs are mechanically less stable, but do offer the advantage of being able to monitor the surface before, during, and after junction formation [54].

Compared to two-terminal break junctions, three-terminal devices such as nanotransistors offer extended control of electron transport. While two (source and drain) electrodes pass current into and out of the system, an additional gate electrode can be used to shift the molecular level energies relative to the contact electrodes. A typical three-terminal setup, in which a semi-conducting single-walled carbon nanotube is connected to metal electrodes (usually produced by nanolithography [55]) is shown in Fig. 1.1c. Carbon nanotube field-effect transistors are promising candidates because they offer increased efficiency at small sizes compared to conventional silicon-based ones [56–59].

Moreover, two-dimensional networks of metal nanoparticles have attracted great interest in molecular electronics recently [60–64]. Using *e. g.*, the Langmuir–Blodgett technique [65,66], metal nanoparticles can self-assemble³ into well-defined arrays stabilized by alkanethiols [67,68]. Replacing a part of the thiols by dithiolated molecules (see Fig. 1.1d), a network of hundreds of interlinked molecular junctions can be created in which each nanoparticle acts as a miniaturized contact [69]. Among adjusting the nanoparticle material and size [70], the length and the functionality of incorporated molecules can be used to control the electronic properties of such arrays [19], for instance when bridging the neighboring particles with DNA [71] or molecular switches [72]. Spectroscopic techniques (in particular, infrared and Raman spectroscopy) can be used to identify and confirm the presence of molecules between metal nanoparticles [72,73] as well as between extended electrodes [74]. Metal nanoparticles (NPs) and nanoparticle arrays comprise a nanoscale system in which the NPs may also serve as donor/acceptor. Recently, the idea of using the

²For some molecules with anchoring groups (*e. g.*, thiol) which can bind to various adsorption sites on the electrodes, multiple sets of conductance peaks superimpose resulting in a narrow distribution of the conductance [46,47].

³Self-assembly is a process in which a spontaneous organization of components (*e. g.*, nanoparticles) occurs due to interactions among themselves or with their environment.

knowledge about transport properties of single metal–molecule–metal junctions to estimate the conductance of two-dimensional nanoparticle arrays has been realized by George *et al.* [75]. In a multiscale approach, they used the rate–conductance correlation to describe electronic motion through molecularly linked NPs by a hopping mechanism⁴ (involving temporary charging of NPs) and to overcome the multiple scale transport problem. Such nanoparticle arrays are also interesting for sensor applications, as analyte molecules may affect conductance by changing the conductance of molecular bridges, the dielectric properties of the nanoparticles, or the mechanical properties of the array [77, 78].

Several other methods to create molecular junctions have recently been designed based on *e. g.*, electromigration [79, 80], electrochemistry [81], crossed wires [82], nanopores [83, 84], shadow masking [85], and mercury drop contacts [86]. The interested reader is kindly referred to excellent reviews, see Refs. [87–92].

1.2. Impact of molecular structure on conductance

As stated previously, the conductance through single molecules is sensitive to small changes in the molecular electronic structure, including the molecular conformation, the molecular length, the gap between the highest occupied molecular orbital (HOMO) and the lowest unoccupied molecular orbital (LUMO)⁵, and molecular topology (quantum interference). Therefore, to realize controlled electron transport in molecular junctions by modifying either the alignment of the molecular energy levels relative to the Fermi energy of the electrodes, the molecule–electrodes coupling, or both, it is crucial to understand how these properties are influenced by “molecular design”. For relatively short molecules (< 3 nm) connected by metallic contacts, the conductance through the molecule has been found to decrease exponentially⁶ with increasing length [46, 94–97]. In this case, nonresonant tunneling is assumed to be the dominant transport mechanism. At a certain molecular length (> 4 nm), nearly length-independent (but temperature-dependent) incoherent hopping⁷ transport starts to dominate [98–100]. Furthermore, the choice of anchoring groups has a strong impact on the molecule–electrode electronic coupling as well as on the energies of the molecular orbitals involved in the transport process [101]. According to their electron-withdrawing or electron-donating behavior, changing the anchoring group can increase or decrease the junction conductance

⁴Nitzan has extended the relationship between transfer rate and molecular conduction to thermally activated hopping processes between nearest-neighbor bridge sites [76].

⁵If the HOMO–LUMO gap increases (at constant electronic coupling to the electrodes), the conductance of the system decreases.

⁶A recent combined experimental and theoretical study showed a surprisingly odd length dependence for oligothiophene molecules (although hopping transport could be excluded) [93].

⁷In the hopping regime, electrons can migrate along the molecule by multiple steps.

(similar to adding chemical substituents to the molecular bridge [102]). For example, thiols are known to form strong covalent bonds to gold, but suffer from their large variability in adsorption to gold surfaces and the resulting broadened conductance distributions [103]. Similar difficulties arise for isocyanide [104] and carboxylic acid [105]. Venkataraman *et al.* showed that amine [46, 106, 107] and pyridine [108] anchoring groups provide a well-defined electronic coupling to gold electrodes and an improved molecular junction formation. The same holds true for nitrile groups [109]. The topology-dependence of molecular conductance can be impressively demonstrated by a simple benzene ring, where the zero-bias conductance of the *meta*-connected benzene ring is significantly lower than that of the *para*-connected counterpart [92, 110]. Considering the ring coupled in *meta* position to the electrodes, different possible pathways exist in contrast to the *para*-coupled one, where both pathways have the same length. This effect is attributed to destructive (*meta*) and constructive (*para*) quantum interference [111–114]. Further examples of conformational changes due to structural changes or stereoisomerization will be presented in the following section.

1.3. Switching conductance by external stimuli

A class of functional molecules that have been investigated comprehensively in the past decade with regard to their usage as building blocks for electronic devices are molecular switches [115, 116]. Using switchable molecules as the active channel in a molecular device has the advantage compared with conventional electronics that conductance can be controlled without the need for a gate electrode. A variety of external stimuli can be used to change the structural and electronic properties of a molecule, *e. g.* length, conformation, coordination, dipole moment, spin state, charge state and bonding behavior. One way to induce the switching between a low and a high conductance state is to excite a molecular switch by light of a specific wavelength in order to evoke an isomerization reaction. Typical examples of photochromic switches include diarylethenes [117–122], azobenzenes [123–130], stilbenes [131, 132] and spiropyranes [133–135]. In particular, diarylethene (DAE) derivatives are attractive candidates for switchable devices since they are highly symmetrical and fatigue-resistant [136–139]. These molecules can undergo a reversible transformation⁸ between a π -conjugated (closed) and a doubly cross-conjugated (open) form by illumination with either ultra-violet (closing) or visible light (opening).

Alternatively, conductance switching can be realized by tuning the electronic proper-

⁸Besides using photoexcitation, such a chemical bond rearrangement in DAE derivatives can also be induced by electrochemical oxidation or reduction [140].

ties of the component involved in transport indirectly through chemical gating. For example, irradiation of a chromophore-functionalized carbon nanotube field-effect transistor and concurrent changes in the chromophores' dipole moment can modify the conductance without affecting the atomic structure of the tube. [141, 142].

Another interesting example of a molecular switch is an azobenzene molecule, since a reversible *trans-cis* isomerization can be observed even in the absence of light, induced by an applied electric field [143] or tunneling electrons [144, 145]. More generally, if a bias voltage is applied, the resulting electric field can couple to a dipole moment of a molecule, leading to changes in the molecular conformation [146]. For instance, an electric field can be used to switch between two different non-planar conformations of a Zn(II)-etioporphyrin molecule, depending on the orientation of its dipole moment with respect to a NiAl(110) surface [147]. A prominent example of current-induced switching in molecular junctions is the tautomerization of hydrogen atoms within a naphthalocyanine molecule probed by STM [148]. External gating of the electrochemical potential can be achieved by adding or subtracting charge from the molecular system. Molecular charging can be linked to charge transfer processes in donor-bridge-acceptor systems (or in general, redox reactions) [149], where charge transfer rates can be controlled by *e. g.*, adding small anions [150] or charging a functional group [151]. A charge transfer mechanism can further be used in carbon nanotube field-effect transistors through interaction with molecules acting as donors or acceptors, which also results in a chemical gating effect.

Furthermore, mechanical stretching or compression of a molecular junction can dramatically change the electronic properties of an incorporated molecule [152–154]. Quek *et al.* showed that compression and elongation of bipyridine junctions can mechanically induce conductance switching, which has been attributed to different pyridine–Au binding structures [155]. Recently, Vacek *et al.* demonstrated controlled conductance switching of a helicene molecule by mechanically manipulating the electrode separation [156].

Another interesting class of switchable molecules are spin crossover (SCO) molecules that can undergo a transition between a low-spin and a high-spin state under various external stimuli, such as temperature, light, electric field and current [157–160]. It has been shown that the spin state of a lanthanide ion sandwiched between two organic phthalocyanine units (TbPc₂) can be modified by applying an electric current [161]. Another very recent example is a Fe²⁺ complex in which two of the four terpyridine ligands are functionalized as a push–pull system. Increasing the applied bias voltage of the junction then leads to a distortion of the Fe²⁺ ligand field resulting in a high-spin to low-spin transition [162].

To summarize, several switching mechanisms can play a role depending on the chemical nature of the molecule and its local environment. In this work, we will focus on

mechanically and photochemically induced conductance changes of (supra)molecular systems.

1.4. Theoretical approaches in molecular electronics: basics

Since the experiments described above are challenging and a detailed control over parameters such as the number of molecules studied and their attachment to the contacts is often not possible, it is essential to support the interpretation of those experiments through theoretical simulations. Furthermore, theoretical modeling allows for understanding underlying mechanisms, which in turn allows for the design of new molecules to be studied experimentally.

In the outset of the field of molecular electronics, deducing a mesoscopic understanding of nanoscale conductance from first principles beyond classical descriptions of charge transport like Ohm's law⁹ presented a challenging task for theoreticians. Today, the "standard" recipe for modeling electron transport in nanoscopic devices is a scattering approach [165,166] formulated in terms of Green's functions [20,167–169] to account for the open-boundary situation, which is valid in the coherent tunneling regime.

Another challenge for computational modeling of nanoelectronic devices is posed by the multiple scales – ranging from nano- to micrometres and from femtoseconds to seconds (or even minutes). Since small variations at the nanometer scale can dramatically affect the properties of the macroscopic environment, simulating the device at a coarse-grained level without a proper treatment of the low-scale details will most likely fail in giving an accurate description. On the other hand, calculating all length scales using an all-atom description is unfeasible as well due to the enormous computational cost. Thus, one has to make compromises in attempting to treat both extremes with sufficient accuracy. For this purpose, multiscale methods have been designed to combine computational methods for different scales. The idea is to simulate a small subsystem, and then to incorporate information from the low-scale into a larger-scale model. The density functional theory-based molecular dynamics (DFT-MD) method [170], for example, uses molecular dynamics (MD) simulations to gain insight on possible contact geometries, and first-principles methods to calculate the conductance of individual snapshots. Recently, a multiscale approach dealing with electron tunneling through two-dimensional nanoparticle arrays has been presented by George *et al.* which combines quantum transport with molecular dynamics and kinetic Monte Carlo calculations [75]. To date, various quantum chemical tools are available to describe the active part of a device

⁹Ohm's law fails for electron transport in nanoscale devices due to their quantum nature [36, 163, 164].

by transferring certain properties to a coarse-grained approach *e.g.*, NANOTCAD VIDES [171,172], TIBERCAD [173,174], NEMO5 [175], and gDFTB [176]. However, multiscale approaches are still under development and the exact calculation of the required parameters is often difficult and may depend strongly on the system under study, especially when the properties in the nanoscopic system, as in our case, are manipulated chemically or mechanically.

A combination of the non-equilibrium Green's function (NEGF) formalism with the density functional theory (DFT) is widely used to model single molecular junctions [177]. A basic introduction to DFT¹⁰ and to the main concepts of electron transport through nanoscopic systems within the Landauer approach are provided in the following.

1.4.1. Electronic structure calculations: Density functional theory

In quantum mechanics, a system of N interacting electrons and M nuclei can be described by the time-independent, non-relativistic Schrödinger equation,

$$\hat{H}\Psi_i(\vec{x}_1, \dots, \vec{x}_N, \vec{R}_1, \dots, \vec{R}_M) = E_i\Psi_i(\vec{x}_1, \dots, \vec{x}_N, \vec{R}_1, \dots, \vec{R}_M), \quad (1.1)$$

where \hat{H} is the Hamiltonian, E the energy eigenvalue, and Ψ the wave function of state i . The electron variable \vec{x} is defined as $\vec{x} = (\sigma, \vec{r})$. The vectors \vec{r} and \vec{R} represent the spatial coordinates (x, y, z) of the electrons and the nuclei, respectively. The electron spin coordinate σ has only two discrete states, namely spin up and spin down.

The Born–Oppenheimer approximation (BOA) can be used to simplify the equation [178], since the nuclei are much heavier and, therefore, move much slower than the electrons. This allows the separation of the electronic and nuclear motions. The electronic Hamiltonian \hat{H}_e is then given by¹¹

$$\hat{H}_e = \underbrace{-\frac{1}{2} \sum_{i=1}^N \nabla_i^2}_{\hat{T}} - \underbrace{\sum_{i=1}^N \sum_{A=1}^M \frac{Z_A}{\vec{r}_{iA}}}_{\hat{V}_{Ne}} + \underbrace{\sum_{i=1}^N \sum_{j>i}^N \frac{1}{\vec{r}_{ij}}}_{\hat{V}_{ee}}, \quad (1.2)$$

where \vec{r}_{ij} is the distance between electrons i and j with $\vec{r}_{ij} = |\vec{r}_i - \vec{r}_j|$, \vec{r}_{iA} is the distance between electron i and nucleus A with $\vec{r}_{iA} = |\vec{r}_i - \vec{R}_A|$, and Z_A is the nuclear charge. The first term describes the kinetic energy of the electrons \hat{T} . The other two terms represent the attractive and repulsive potential energy due to the electron–nucleus (\hat{V}_{Ne}) and electron–electron interactions (\hat{V}_{ee}), respectively.

¹⁰In this work, all calculations were carried out within the framework of DFT.

¹¹In atomic units, for which $\hbar = m_e = e = 4\pi\epsilon_0 = 1$.

The nucleus–nucleus interaction is a constant term, which may be added later to the electronic energy to obtain the total energy. This is a prototypical many-body problem, whose solution is difficult due to \hat{V}_{ee} .

The main concept of the DFT [179] is to circumvent the $4N$ -dimensional wave function and instead to calculate the energy as a functional of the ground-state electron density

$$\rho_0(\vec{r}) = N \int \dots \int |\Psi_0(\vec{x}_1, \vec{x}_2, \dots, \vec{x}_N)|^2 ds_1 d\vec{x}_2 \dots \vec{x}_N. \quad (1.3)$$

This is based on the Hohenberg–Kohn theorems [180, 181], which state that the external potential (here due to the nuclei) is uniquely defined by ρ_0 up to an additive constant, and that the energy as a functional of ρ obeys the variational principle,

$$E[\rho(\vec{r})] = \int V_{Ne}(\vec{r})\rho(\vec{r})d\vec{r} + \underbrace{T[\rho(\vec{r})] + E_{ee}[\rho(\vec{r})]}_{F_{HK}[\rho(\vec{r})]} \geq E_0, \quad (1.4)$$

with the potential energy due to the electron–nucleus attraction $V_{Ne}(\vec{r})$ and the ground state energy E_0 . The functional for the kinetic energy $T[\rho(\vec{r})]$ and that for the electron–electron interaction $E_{ee}[\rho(\vec{r})]$ can be combined to the so-called Hohenberg–Kohn functional $F_{HK}[\rho(\vec{r})]$ whose explicit form is unknown. Kohn and Sham suggested to describe the electron density as the density of a reference system of non-interacting fermions, which has the same ground-state density $\rho(\vec{r})$ as the real system [181]. Since the exact wave function of such a system is a single Slater determinant, its kinetic energy can be expressed as a simple-to-evaluate expectation value. Therefore, the following expression for the functional $F_{HK}[\rho(\vec{r})]$ can be introduced,

$$F_{HK}[\rho(\vec{r})] = T_S[\rho(\vec{r})] + J[\rho(\vec{r})] + E_{xc}[\rho(\vec{r})]. \quad (1.5)$$

where $T_S[\rho(\vec{r})]$ is the kinetic energy of the non-interacting fermions and $J[\rho(\vec{r})]$ the classical contribution to the potential energy which includes the nucleus-electron and the classical electron-electron interactions. The exchange–correlation potential $E_{xc}[\rho(\vec{r})]$

(x for exchange, c for correlation) can be defined by rewriting Eq. (1.5) as

$$E_{xc}[\rho(\vec{r})] \equiv (T[\rho(\vec{r})] - T_S[\rho(\vec{r})]) + (E_{ee}[\rho(\vec{r})] - J[\rho(\vec{r})]), \quad (1.6)$$

which includes all exchange and correlation contributions plus a small “correction to the kinetic energy” which describes the difference between the kinetic energy of the interacting and the non-interacting system and is assumed to be small.

Due to the fact that the exact exchange–correlation functional $E_{xc}[\rho(\vec{r})]$ is not known, many approximate functionals have been developed in the last years [182].

The earliest approximation of the exchange–correlation functional is the Dirac–Slater approximation for a homogeneous electron gas known as the local density approximation (LDA) [183]. In general, this approximation provides an unrealistic description of inhomogeneous systems such as atoms and molecules.

The first improvement of the LDA was the generalized gradient approximation (GGA) which includes the first derivative of the density with respect to spatial coordinates. The most commonly used GGAs are the BP86 functional developed by Becke and Perdew [184,185] and the PBE functional designed by Perdew, Burke and Ernzerhof [186,187]. When the second derivative with respect to spatial coordinates is also included, the approximation is known as a meta-GGA functional, *e. g.* TPSS [188]. Another group are the hybrid density functionals, in which the exchange functional is mixed with a part of Hartree–Fock (HF) exchange (“exact exchange”) [189]. Probably the most popular hybrid density functional is B3LYP (20 % HF-exchange) developed by Becke, Lee, Yang and Parr [190,191].

Many “standard” exchange–correlation functionals are unreliable for dispersion interactions, but in such cases empirical corrections such as Grimme’s DFT-D [192] can be employed.

1.4.2. The Landauer picture of electron transport

Owing to the reference system of non-interacting fermions, Kohn–Sham DFT results in an effective single-particle picture. It is therefore well suited for combination with the Landauer approach to electron transport¹². In the Landauer approach, a single molecule or in general a nanoscopic structure (the scattering region) is sandwiched between two metal leads that correspond to macroscopic electrodes (reservoirs). Fig. 1.2 illustrates an (effective) single-particle energy level diagram for a molecular junction. The electrodes are represented by their conductance band continua with the Fermi level denoted by E_F . As is shown, the electron transport through a single molecule depends on the molecular level position, especially the HOMO and the LUMO relative to E_F , and on the level broadening due to the coupling to the electrodes.

The Landauer formalism is based on the following assumptions:

- (1) Transport takes place in a steady-state (*e. g.*, the number of electrons in the scattering region is constant over time).

¹²It should be kept in mind, though, that the single particles under consideration are non-physical noninteracting fermions. As their orbitals usually resemble molecular orbitals in single-determinant wave function theory (Hartree–Fock), they are assumed to be suitable for our purposes (as confirmed by many successful descriptions of electron transport experiments based on DFT).

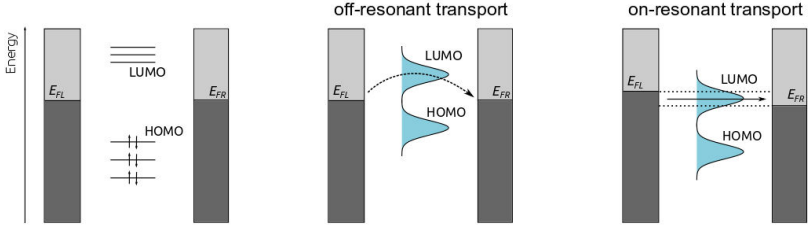


Figure 1.2.: Simplified energy level representation of a molecular junction and transport processes with different electronic coupling strengths between the molecule and the electrodes (the dark gray and light gray areas represent filled and empty single-electron states, respectively). *Left:* In the weak coupling regime, the molecular orbitals are well defined. *Middle:* With stronger coupling to the electrodes, the molecular energy levels become broader and closer to the Fermi energy of the electrodes E_F . Although neither the HOMO nor the LUMO is within the energy window of the Fermi energy, current can flow (off-resonant transport). *Right:* When a bias voltage V resulting in an energy window $eV = E_{FR} - E_{FL}$ (e being the magnitude of electron charge) is applied, either the HOMO or the LUMO of the molecule can enter the energy window of the local Fermi energies (E_{FR}, E_{FL}) allowing current to flow through the molecule (resonant transport).

- (2) Transport is coherent (*i. e.* there are no phase-breaking events as in thermally-activated hopping), which is usually a good assumption for short molecular lengths, low temperatures, and a large difference between the one-particle energy levels of the molecule and the Fermi energies of the electrodes.
- (3) The system is well described within an effective one-particle approach.
- (4) The single-particle basis functions of the junction can be assigned to either the electrodes or the scattering region.
- (5) The contacts connected to electron reservoirs are in thermal equilibrium.

Under these conditions, we obtain the Landauer-Imry-Büttiker expression for the electric current I [165],

$$I(V) = \frac{2e}{h} \int_{E_F - \frac{eV}{2}}^{E_F + \frac{eV}{2}} dE \mathcal{T}(E, V), \quad (1.7)$$

where h is the Planck's constant and \mathcal{T} is the transmission function. The zero-temperature conductance G is determined by the first derivative of the current I with respect to the bias voltage V ,

$$G(V) = \frac{dI(V)}{dV}. \quad (1.8)$$

For low voltages, the zero-bias conductance is given by

$$G = G_0 \mathcal{T}(E_F), \quad (1.9)$$

where G_0 is the conductance quantum, $G_0 = \frac{2e^2}{h} = (12.9 \text{ k}\Omega)^{-1}$. Thus, the system-specific property needed to calculate the conductance of a metal–molecule–metal junction is the energy dependent transmission function [193–195]. Often, \mathcal{T} is calculated for zero bias, which is also a good approximation for low bias voltages. Under a larger applied bias, the electronic structure and thus \mathcal{T} may change considerably (enabling, e.g., rectifying behavior). Large voltages and currents may also affect molecular structures (as exploited in electromigration break junctions). A thorough description of electron transport through molecular junctions will be given in Chapter 2.

1.4.3. Challenges for DFT-based transport calculations

Since they provide reasonable accuracy along with computational efficiency for large systems, DFT-based transport calculations have proven to be quite useful in practice [196]. Nonetheless, we would like to address a few challenging issues one must be aware of when using DFT for transport through nanoscale junctions.

- The explicit form of the exchange–correlation functional is unknown. Thus, in most cases it will be essential (even for an accurate qualitative description) to compare different types of approximate functionals. In particular, functionals which work well for metals are often unsuitable for molecules, and vice versa. This is also reflected in the fact that solid-state electronic-structure codes (which operate under periodic boundary conditions) are often limited to a few functionals such as LDA and PBE in practice (partially due to the need to fit pseudopotentials for all elements involved), while those for molecules have a much broader variety of accessible functionals, but are limited to isolated structures and thus not well suited for describing the semi-infinite nature of the macroscopic electrodes. A general compromise between the two worlds is still lacking.
- Large errors and artefacts in transmission functions may occur due to the inadequacy of Kohn–Sham molecular orbitals to describe the correct position of molecular energy levels involved in transport. This is also a conceptual challenge, as the single particles in KS-DFT are noninteracting fermions rather than electrons.
- DFT is known to give an imperfect description of non-covalently bounded systems making it difficult to predict correct adsorption energies and structures

on surfaces. This problem can, in practice, often be solved with sufficient reliability by various methods that are suitable to describe dispersion interactions [192, 197–204].

- Static DFT approaches that are commonly used in practice do not take into account the statistic results of molecular dynamics of molecules on surfaces. Approaches that take these considerations into account by *e. g.*, combining DFT and molecular dynamic (MD) simulations will be discussed in Section 3.1.

1.5. Scope and outline of this work

The main goal of this work is to understand the mechanisms which lead to changes in the transport properties of nanoscale junctions upon manipulation of molecular or supramolecular systems connected to electrodes. Mechanically and photochemically induced changes to these systems and the capability of DFT combined with the Landauer approach to cope with them (in comparison with the experiment) will be our main focus. Where necessary, new computational tools will be introduced to properly describe the studied phenomena and structures. The thesis is divided into two parts. In Part 1, structurally different molecules on surfaces exposed to mechanical stress in a combined STM/AFM setup are simulated using static DFT. In this context, a detailed description of the Landauer–Imry–Büttiker theory combined with a Green’s function formulation will be given beforehand, and our implementation in the transport code ARTAIOS [205, 206] is presented in detail. Noncovalent functionalization of carbon nanotubes with small molecules and photoactive switches and the resulting chemical gating will be the subject of Part 2. To further clarify the involved mechanisms, we will also present an introduction to local properties, in particular local dipole moments within the atoms in molecules (AIM) theory [207], and a new implementation in the post-processing tool LOCALDIP [208, 209]. In Chapter 4, we will discuss current compared with the rate of electron transfer in Donor–Bridge–Acceptor (DBA) systems. In order to make subsequent predictions on how electron [210] or exciton transfer [211] control population dynamics in DBA systems, a tool which calculates the probability of possible excitation pathways for given transfer rate constants is presented. Finally, we conclude our work in Chapter 6 with a detailed summary of the respective parts, together with future perspectives towards a theoretical description of large molecular systems using multi-scale methods.

2. Landauer theory of electron transport through molecular junctions

In this section we will present a detailed description of coherent transport through metal–molecule–metal junctions (following the derivation in Ref. [212]). Starting with a resonant tunneling model, we will derive an expression for the current by means of Green’s functions. First, let us consider a one-dimensional effective single-

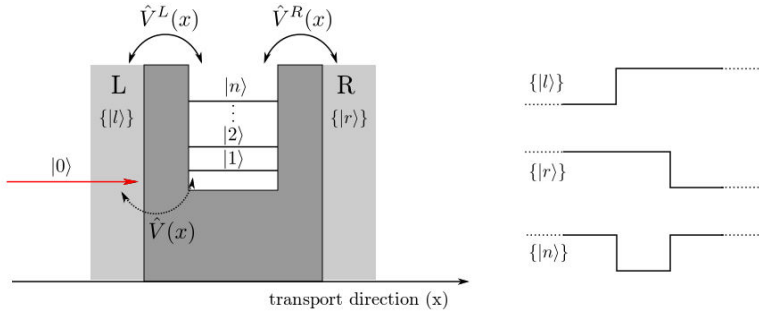


Figure 2.1.: *Left:* Schematic representation of resonant tunneling through a symmetric double barrier. A single particle coming from the left $|0\rangle$ couples to the barrier levels $\{|1\rangle, |2\rangle, \dots, |n\rangle\}$ via \hat{V} , but not to the electrodes. The continua L and R with effective single-particle states $\{|l\rangle\}$ and $\{|r\rangle\}$ couple to the barrier levels via \hat{V}^L and \hat{V}^R , respectively. *Right:* The single-particle states are eigenstates of the respective potentials. Their energy is assumed to be sufficiently low so that they are located within the barrier or to the left or right of it, respectively.

particle system connecting two electron “baths” (continua L and R) that are located on either side of a symmetric double barrier potential as shown in Fig. 2.1. The tunneling process is dominated by quasi-bound states in the region between the two barriers which can couple to the left and the right continua, with a manifold of effective single-particle states $\{|l\rangle\}$ and $\{|r\rangle\}$. A single-particle state representing an incoming electron $|0\rangle$ is considered as the “driving state” carrying the flux through the barrier states $\{|n\rangle\}$. The set of states $\{|l\rangle\}$, $\{|r\rangle\}$ and $\{|n\rangle\}$ are assumed to be

orthonormal,

$$\langle l|l' \rangle = \delta_{l,l'} \quad (2.1)$$

$$\langle r|r' \rangle = \delta_{r,r'} \quad (2.2)$$

$$\langle n|n' \rangle = \delta_{n,n'} \quad (2.3)$$

$$\langle l|n \rangle = \langle r|n \rangle = 0. \quad (2.4)$$

2.1. Derivation of the Landauer ansatz

Together with the steady-state boundary conditions introduced in Section 1.3.2, the system described above is governed by the time-dependent Schrödinger equation (TDSE),

$$i\hbar \frac{\partial}{\partial t} \Psi(t) = \hat{H} \Psi(t). \quad (2.5)$$

where \hbar is the reduced Planck constant and Ψ is the time-dependent wave function of the system¹. This implies that only coherent processes can be described; incoherent transport mechanisms such as thermally activated hopping require a different theoretical approach. Coherent tunneling is usually a good approximation for short bridges, low temperatures and energies far from the Fermi energies of the electrodes. The time-independent Hamiltonian \hat{H} can be written as a sum of matrix elements that correspond either to the isolated subsystem (\hat{H}_0), the coupling to the electrodes ($\hat{V}^{L/R}$) or the coupling to the driving state (\hat{V}),

$$\begin{aligned} \hat{H} = & \sum_{n,n'} H_{n,n'} |n\rangle \langle n'| + \sum_{l,l'} H_{l,l'} |l\rangle \langle l'| + \sum_{r,r'} H_{r,r'} |r\rangle \langle r'| + E_0 |0\rangle \langle 0| \\ & + \sum_{n,l} H_{n,l} |n\rangle \langle l| + \sum_{l,n} H_{l,n} |l\rangle \langle n| + \sum_{n,r} H_{n,r} |n\rangle \langle r| + \sum_{r,n} H_{r,n} |r\rangle \langle n| \\ & + \sum_n H_{n,0} |n\rangle \langle 0| + \sum_n H_{0,n} |0\rangle \langle n|. \end{aligned} \quad (2.6)$$

The formal solution to the TDSE in terms of the single-particle basis is given by

$$\Psi(t) = \sum_n C_n(t) |n\rangle + \sum_l C_l(t) |l\rangle + \sum_r C_r(t) |r\rangle + C_0(t) |0\rangle. \quad (2.7)$$

If we now insert Eq. (2.7) and Eq. (2.6) into the TDSE, many terms will cancel due to the orthonormality of the single-particle states. Multiplying from the left by $\langle n|$ leads to the following equations for determining the coefficients $C_n(t)$,

$$i\hbar \frac{\partial C_n(t)}{\partial t} = \sum_{n'} H_{n,n'} C_{n'}(t) + \sum_l H_{n,l} C_l(t) + \sum_r H_{n,r} C_r(t) + H_{n,0} C_0(t). \quad (2.8)$$

¹The space-dependence of the wave function is not written out explicitly.

In order to get analogous expressions for the coefficients C_k ($k = l, r$), we instead multiply from the left by $\langle k|$,

$$i\hbar \frac{\partial C_k(t)}{\partial t} = H_{k,k} C_k(t) + \sum_n H_{k,n} C_n(t). \quad (2.9)$$

It is advisable to add an imaginary damping factor² $i\frac{\eta}{2} C_k(t)$ to ensure a steady state even when current flows from the molecule into the electrodes and vice versa. Eq. (2.9) is then rewritten as

$$i\hbar \frac{\partial C_k(t)}{\partial t} = H_{k,k} C_k(t) + \sum_n H_{k,n} C_n(t) + i\frac{\eta}{2} C_k(t). \quad (2.10)$$

We now assign the phase factor of the driving state $e^{-i/\hbar E_0 t}$ to all coefficients C_j ($j = n, r, l$) to satisfy the steady-state condition,

$$C_j(t) = c_j e^{-i/\hbar E_0 t}, \quad (2.11)$$

and insert the resulting steady-state solution for C_n into Eq. (2.8),

$$\begin{aligned} i\hbar \frac{\partial}{\partial t} c_n e^{-i/\hbar E_0 t} &= E_0 c_n e^{-i/\hbar E_0 t} \\ &= \sum_{n'} H_{n,n'} c_{n'} e^{-i/\hbar E_0 t} + \sum_l H_{n,l} c_l e^{-i/\hbar E_0 t} \\ &\quad + \sum_r H_{n,r} c_r e^{-i/\hbar E_0 t} + H_{n,0} c_0 e^{-i/\hbar E_0 t}. \end{aligned} \quad (2.12)$$

Dividing Eq. (2.12) by the phase factor on both sides, we obtain

$$E_0 c_n = \sum_{n'} H_{n,n'} c_{n'} + \sum_l H_{n,l} c_l + \sum_r H_{n,r} c_r + H_{n,0} c_0. \quad (2.13)$$

Repeating the steps from Eq. (2.11) using the solution for the continuum K ($K = L, R$), Eq. (2.10) results in an expression for the coefficients c_k ($k = l, r$),

$$\begin{aligned} i\hbar \frac{\partial}{\partial t} c_k e^{-i/\hbar E_0 t} &= E_0 c_k e^{-i/\hbar E_0 t} \\ &= H_{k,k} c_k e^{-i/\hbar E_0 t} + \sum_n H_{k,n} c_n e^{-i/\hbar E_0 t} + i\frac{\eta}{2} c_k e^{-i/\hbar E_0 t} \\ \Leftrightarrow E_0 c_k &= H_{k,k} c_k + \sum_n H_{k,n} c_n + i\frac{\eta}{2} c_k \\ \Leftrightarrow \sum_n H_{k,n} c_n &= \left(E_0 - H_{k,k} - i\frac{\eta}{2} \right) c_k \\ \Leftrightarrow c_k &= \frac{\sum_n H_{k,n} c_n}{E_0 - H_{k,k} - i\frac{\eta}{2}}. \end{aligned} \quad (2.14)$$

² η will be set to zero at the end of the calculation.

These coefficients for the continua, c_l and c_r , can now be substituted into Eq. (2.13), which leads to

$$E_0 c_n = \sum_{n'} H_{n,n'} c_{n'} + H_{n,0} c_0 + \underbrace{\sum_n \sum_l \frac{H_{n,l} H_{l,n'}}{E_0 - H_{l,l} - i\frac{\eta}{2}} c_{n'}}_{\Sigma_{n,n'}^L(E_0)} + \underbrace{\sum_n \sum_r \frac{H_{n,r} H_{r,n'}}{E_0 - H_{r,r} - i\frac{\eta}{2}} c_{n'}}_{\Sigma_{n,n'}^R(E_0)}, \quad (2.15)$$

where $\Sigma_{n,n'}^K$ is the self energy of the barrier states $\{n\}$ due to their interaction with the continuum K . We define an overall self energy as

$$\Sigma_{n,n'}(E_0) = \Sigma_{n,n'}^L(E_0) + \Sigma_{n,n'}^R(E_0). \quad (2.16)$$

Let us now consider the self energy $\Sigma_{n,n'}^K$ in the limit of η approaching zero,

$$\Sigma_{n,n'}^K(E_0) = \lim_{\eta \rightarrow 0} \sum_k \frac{H_{n,k} H_{k,n'}}{E_0 - H_{k,k} - i\frac{\eta}{2}}. \quad (2.17)$$

Assuming that the manifold $\{k\}$ constitutes a continuum of states, the summation over k can be reformulated as an integral

$$\sum_k \rightarrow \int_{-\infty}^{\infty} dE \rho_K(E), \quad (2.18)$$

where ρ_K describes the density of states in the continuum K . When applied to Eq. (2.17), the resulting complex expression can be further simplified using the following general relation

$$\frac{f(x)}{x - x_0 + i\varepsilon} \xrightarrow{\varepsilon \rightarrow 0} \text{PP} \frac{f(x)}{x - x_0} - i\pi \delta(x - x_0) f(x), \quad (2.19)$$

where PP stands for the Cauchy principle part of a finite integral of a function $f(x)$. Therefore, Eq. (2.17) can be rewritten as

$$\Sigma_{n,n'}^K(E) = \underbrace{\text{PP} \int_{-\infty}^{\infty} dE \frac{H_{n,k} H_{k,n'}}{E_0 - H_{k,k}} \rho_K(E)}_{\Lambda_{n,n'}^K(E)} - \underbrace{i\pi [H_{n,k} H_{k,n'} \rho_K(E) \delta(E - H_{k,k})]}_{\frac{\pi}{2} \Gamma_{n,n'}^K(E)}, \quad (2.20)$$

where $\Lambda_{n,n'}^K$ represents the shift and $\Gamma_{n,n'}^K$ the broadening (linewidth) of energy levels due to coupling to electrode K as shown in Fig. 2.2, and where for the sake of generality the self-energy is now evaluated at any energy E rather than at the specific value E_0 .

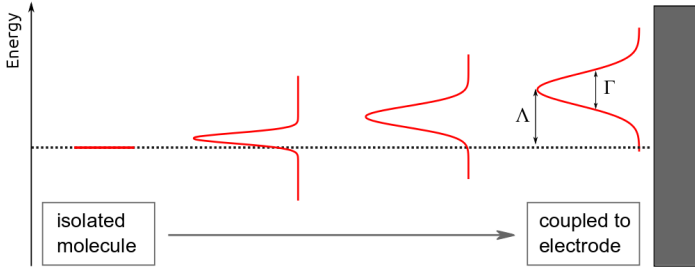


Figure 2.2.: Effect of molecule–electrode coupling on an effective single-particle level (molecular orbital) of the barrier (*e. g.*, a molecular system). The level is broadened and shifted when brought close to an electrode.

Now, we define an element of the Green’s function matrix $G_{n,n'}^\Sigma$ of the barrier (which in practice will often be a molecular subsystem³) in the presence of the electrodes as

$$G_{n,n'}^\Sigma(E) = \left(E - H_{n,n'}^\Sigma\right)^{-1}, \quad \text{with } H_{n,n'}^\Sigma = H_{n,n'} + \Sigma_{n,n'}. \quad (2.21)$$

Inserting Eq. (2.16) into Eq. (2.15) and using the definition of the Green’s function, it follows that

$$\begin{aligned} E_0 c_n &= \sum_{n'} H_{n,n'} c_{n'} + H_{n,0} c_0 + \sum_{n'} \Sigma_{n,n'}(E_0) c_{n'} \\ \Leftrightarrow \sum_{n'} E_0 \delta_{n,n'} c_{n'} &= H_{n,0} c_0 + \sum_{n'} \underbrace{[H_{n,n'} + \Sigma_{n,n'}(E_0)]}_{H_{n,n'}^\Sigma} c_{n'} \end{aligned} \quad (2.22)$$

$$\Leftrightarrow 0 = H_{n,0} c_0 - \sum_{n'} \underbrace{[E_0 \delta_{n,n'} - H_{n,n'}^\Sigma]}_{(G^\Sigma)_{n,n'}^{-1}} c_{n'}, \quad (2.23)$$

or in matrix notation (where $H_{n,0} c_0$ is considered the n th element of a vector ‘ $\mathbf{H}_0 \mathbf{c}_0$ ’),

$$\mathbf{0} = \mathbf{H}_0 \mathbf{c}_0 - (\mathbf{G}^\Sigma)^{-1} \mathbf{c} \Leftrightarrow \mathbf{c} = \mathbf{G}^\Sigma \mathbf{H}_0 \mathbf{c}_0, \quad (2.24)$$

³ As a step towards a quantitatively accurate approach, it would be necessary to include as many electrode atoms into the central (barrier) region as necessary to assure bulk properties at both sides of the barrier–electrode interface. Since such quantitative accuracy would require a massive computational effort (ensuring, *e. g.* proper sampling of all relevant molecular configurations and adsorption positions), and since correctly predicting qualitative behavior is often already very useful for the experiment, we define the central or barrier region as containing the molecule only.

leading to

$$c_n = c_0 \sum_{n'} G_{n,n'}^\Sigma H_{n',0}. \quad (2.25)$$

If we now insert Eq. (2.25) into the last version of Eq. (2.14), we obtain

$$c_k = \frac{\sum_n \sum_{n'} H_{k,n} G_{n,n'}^\Sigma H_{n',0}}{E_0 - H_{k,k} - i\frac{\eta}{2}} c_0. \quad (2.26)$$

Since we are interested in the flux $J_{L \rightarrow R}$, we have to evaluate the transmitted $J_{0 \rightarrow R}$ and reflected $J_{0 \rightarrow L}$ fluxes first. In order to assess how fast the steady state population of levels in the respective continuum disappears into the environment via the decay rate η , let us consider the TDSE for this problem only,

$$\frac{\partial}{\partial t} C_k(t) = \frac{\eta}{2\hbar} c_k e^{\frac{\eta}{2\hbar} t} = \frac{\eta}{2\hbar} C_k(t), \quad (2.27)$$

with

$$\Psi(t) = \sum_k C_k(t) |k\rangle \quad \text{and} \quad C_k(t) = c_k e^{\frac{\eta}{2\hbar} t}. \quad (2.28)$$

The transmitted flux $J_{0 \rightarrow R}$ is then given by

$$\begin{aligned} J_{0 \rightarrow R} &= \frac{\partial}{\partial t} \sum_r |C_r|^2 = \sum_r \left[\left(\frac{\partial C_r^*}{\partial t} \right) C_r + C_r^* \left(\frac{\partial C_r}{\partial t} \right) \right] \\ &= \sum_r \left[\frac{\eta}{2\hbar} |C_r|^2 + \frac{\eta}{2\hbar} |C_r|^2 \right] = \frac{\eta}{\hbar} \sum_r |C_r|^2 \\ &= \frac{\eta}{\hbar} \sum_r |c_r|^2 e^{i/\hbar E_0 t} e^{-i/\hbar E_0 t} \\ &= \frac{\eta}{\hbar} \sum_r |c_r|^2. \end{aligned} \quad (2.29)$$

By replacing k with r in Eq. (2.26) and inserting it into the last version of Eq. (2.29), we get

$$\begin{aligned} J_{0 \rightarrow R} &= \frac{\eta}{\hbar} |c_0|^2 \sum_r \sum_{n_1, n'_1} \sum_{n_2, n'_2} \left(\frac{H_{0, n'_2} G_{n'_2, n_2}^{\Sigma \dagger} H_{n_2, r}}{E_0 - H_{r, r} + i\frac{\eta}{2}} \right) \left(\frac{H_{r, n_1} G_{n_1, n'_1}^\Sigma H_{n'_1, 0}}{E_0 - H_{r, r} - i\frac{\eta}{2}} \right) \\ &= \frac{\eta}{\hbar} |c_0|^2 \sum_r \sum_{n_1, n'_1} \sum_{n_2, n'_2} \left(\frac{H_{0, n'_1} G_{n'_2, n_2}^{\Sigma \dagger} H_{n_2, r} H_{r, n_1} G_{n_1, n'_1}^\Sigma H_{n'_1, 0}}{(E_0 - H_{r, r})^2 + (\frac{\eta}{2})^2} \right) \end{aligned} \quad (2.30)$$

Again, we let η approach zero. Using the definition of the Dirac function⁴, we obtain

$$\begin{aligned} J_{0 \rightarrow R} &\stackrel{\eta \rightarrow 0}{=} \frac{2\pi}{\hbar} |c_0|^2 \sum_r \sum_{n_1, n'_1} \sum_{n_2, n'_2} H_{0, n'_2} G_{n'_2, n_2}^{\Sigma \dagger} H_{n_2, r} H_{r, n_1} G_{n_1, n'_1}^\Sigma H_{n'_1, 0} \\ &\quad \times \delta(E_0 - H_{r, r}). \end{aligned} \quad (2.31)$$

⁴On possible definition of the Dirac function is

$$\delta(x) = \lim_{a \rightarrow 0} \frac{a/\pi}{x^2 + a^2}.$$

In Eq. (2.20), we have defined the matrix elements of the electronic coupling functions as

$$\Gamma_{n_2, n_1}^R = 2\pi \sum_r H_{n_2, r} H_{r, n_1} \delta(E_0 - H_{r, r}) \quad (2.32)$$

$$\Gamma_{n'_1, n'_2}^L = 2\pi \sum_l H_{n'_1, l} H_{l, n'_2} \delta(E_0 - H_{l, l}) \quad (2.33)$$

which allows us to rewrite Eq. (2.31) as follows,

$$J_{0 \rightarrow R} \stackrel{\eta \rightarrow 0}{=} \frac{|c_0|^2}{\hbar} \sum_{n_1, n'_1} \sum_{n_2, n'_2} H_{0, n'_2} G_{n_1, n'_1}^{\Sigma \dagger} \Gamma_{n_2, n_1}^R G_{n_2, n'_2}^{\Sigma} H_{n'_1, 0} \quad (2.34)$$

In order to consider all electrons tunneling into the right electrode from all incoming electrons from the left with energy E , we need to multiply Eq. (2.34) by the density of states of the left electrode,

$$\rho_L(E) = \sum_l \delta(E - E_l) = \sum_l \delta(E - H_{l, l}), \quad (2.35)$$

where we exploit that the functions $|l\rangle$ are (orthonormal) eigenstates of an effective single-particle Hamiltonian for the left electrode, with energy E_l . The flux per energy is now obtained as

$$\begin{aligned} \left(\frac{\partial J_{L \rightarrow R}(E)}{\partial E} \right)_{E=E_0} &= \frac{|c_0|^2}{2\pi\hbar} \sum_l 2\pi \delta(E - H_{l, l}) \\ &\times \sum_{n_1, n'_1} \sum_{n_2, n'_2} H_{l, n'_2} G_{n'_2, n_2}^{\Sigma \dagger} \Gamma_{n_2, n_1}^R G_{n_1, n'_1}^{\Sigma} H_{n'_1, l}, \end{aligned} \quad (2.36)$$

and exploiting Eq. (2.33) leads to

$$\begin{aligned} \left(\frac{\partial J_{L \rightarrow R}(E)}{\partial E} \right)_{E=E_0} &= \frac{|c_0|^2}{2\pi\hbar} \sum_{n_1, n'_1} \sum_{n_2, n'_2} \Gamma_{n'_1, n'_2}^L G_{n'_2, n_2}^{\Sigma \dagger} \Gamma_{n_2, n_1}^R G_{n_1, n'_1}^{\Sigma} \\ &= \frac{|c_0|^2}{2\pi\hbar} \underbrace{\text{Tr} \left[\mathbf{\Gamma}^L \mathbf{G}^{\Sigma \dagger} \mathbf{\Gamma}^R \mathbf{G}^{\Sigma} \right]}_{\mathcal{T}(E_0)}. \end{aligned} \quad (2.37)$$

The population of the incoming state $|c_0\rangle^2$ can be described by the Fermi–Dirac distribution,

$$|c_0|^2 = f_L(E_0) = (e^{(E_0 - E_{FL})/k_B T} + 1)^{-1}, \quad (2.38)$$

with the local Fermi energy of the left electrode $E_F^L = E_F - \frac{eV}{2}$ (V being the bias voltage, e the unit charge and E_F the Fermi energy of the electrodes in equilibrium (assuming chemically equivalent electrodes and a symmetric voltage drop across the

junction). Inserting Eq. (2.38) into Eq. (2.37) and multiplying by 2 (for one spin-up and one spin-down electron per single particle level) yields

$$\left(\frac{\partial J_{L \rightarrow R}(E)}{\partial E} \right)_{E=E_0} = \frac{1}{\pi \hbar} \mathcal{T}(E_0) f_L(E_0). \quad (2.39)$$

Finally, we multiply Eq. (2.39) by $-e$, take the difference between the current from left to right and from right to left and integrate over all energies. The net current I through the junction from left to right is then

$$I(V) = \frac{e}{\pi \hbar} \int_{-\infty}^{\infty} dE \mathcal{T}(E) [f_R(E) - f_L(E)]. \quad (2.40)$$

At a temperature of 0 K, we finally get the equation [213]

$$I(V) = \frac{2e}{h} \int_{E_F - \frac{eV}{2}}^{E_F + \frac{eV}{2}} dE \mathcal{T}(E, V), \quad (2.41)$$

where we have indicated in writing the transmission as a function of V that the electronic structure depends on the bias voltage, which may affect the transmission (and result in phenomena such as rectification). For small bias voltages as considered in this thesis, this dependence may be neglected.

2.2. Analytical transmission function for a single-level system

We will illustrate the calculation of the transmission function for the simple case of a single level $|1\rangle$ with energy ε_1 between two electrodes (see Fig. 2.3).

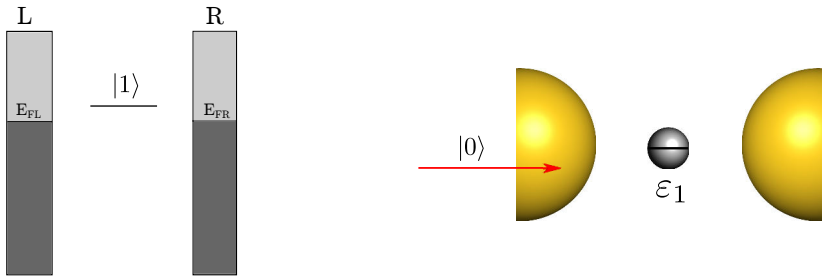


Figure 2.3.: *Left:* Energy scheme for a single level $|1\rangle$ between two electrodes (L,R) represented by their continua with the Fermi level in equilibrium denoted by E_F . *Right:* A system represented by a single level with energy ε_1 is coupled to two semi-infinite electrodes.

Using Eq. (2.37), the transmission in terms of Green's functions for a single level can be written as

$$\mathcal{T}(E) = \Gamma_{1,1}^L G_{1,1}^{\Sigma\dagger}(E) \Gamma_{1,1}^R G_{1,1}^{\Sigma}(E). \quad (2.42)$$

We obtain the Green's function defined by Eq. (2.21) in the form

$$G_{1,1}^{\Sigma}(E) = \frac{1}{E - H_{1,1} - \Sigma_{1,1}} = \frac{1}{E - \varepsilon_1 + \frac{i}{2}\Gamma_{1,1}}, \quad (2.43)$$

where the energy of the resonance level is defined such that it already incorporates the shift due to the electrodes, $\varepsilon_1 = E_1 - \Lambda_{1,1} = H_{1,1} - \Lambda_{1,1}$. The coupling function can be expressed as

$$\Gamma_{1,1}(E) = \Gamma_{1,1}^L(E) + \Gamma_{1,1}^R(E). \quad (2.44)$$

with (compare Eq. (2.32) and Eq. (2.33), $K = R, L$),

$$\Gamma_{1,1}^K(E) = 2\pi \sum_k |H_{1,k}|^2 \delta(E - E_k). \quad (2.45)$$

Using Eq. (2.18), we get

$$\begin{aligned} \Gamma_{1,1}^K(E) &= 2\pi \int_{-\infty}^{\infty} dE_k |H_{1,k}(E_k)|^2 \delta(E - E_k) \rho_K(E_k) \\ &= 2\pi \left(\overline{|H_{1,k}(E_k)|^2} \right)_{E=E_k} \rho_K(E), \end{aligned} \quad (2.46)$$

where we average over all matrix elements $H_{1,k}$ for a given energy. In order to further simplify $\Gamma_{1,1}^K$, we assume that the term is energy-independent. This assumption is referred to as the wide-band-limit (WBL) approximation, which leads to

$$\Gamma_{1,1}^K = 2\pi \overline{|H_{1,k}|^2} \rho_K. \quad (2.47)$$

If we now substitute Eq. (2.43) into Eq. (2.42), the transmission is given by

$$\begin{aligned} \mathcal{T}(E) &= \frac{\Gamma_{1,1}^L \Gamma_{1,1}^R}{(E - \varepsilon_1 - \frac{i}{2}\Gamma_{1,1})(E - \varepsilon_1 + \frac{i}{2}\Gamma_{1,1})} \\ &= \frac{\Gamma_{1,1}^L \Gamma_{1,1}^R}{(E - \varepsilon_1)^2 + (\frac{1}{2}\Gamma_{1,1})^2}. \end{aligned} \quad (2.48)$$

For symmetric barriers (*e. g.*, electrode L and R are composed of the same material and structure), the coupling functions can be approximated by

$$\Gamma_{1,1}^R = \Gamma_{1,1}^L, \quad (2.49)$$

so that Eq. (2.48) can be rewritten in the form

$$\mathcal{T}(E) = \frac{(\Gamma_{1,1}^R)^2}{(E - \varepsilon_1)^2 + (\Gamma_{1,1}^R)^2}, \quad (2.50)$$

where the shape of the transmission curve depends on the parameters $\Gamma_{1,1}^R$ and ε_1 . The dependence of \mathcal{T} on these parameters is illustrated in Figure 2.5: a maximum Lorentzian at peak energy is obtained ε_1 and with its half-width determined by $\Gamma_{1,1}^R$ (that is, the larger the electronic coupling, the broader the peak).

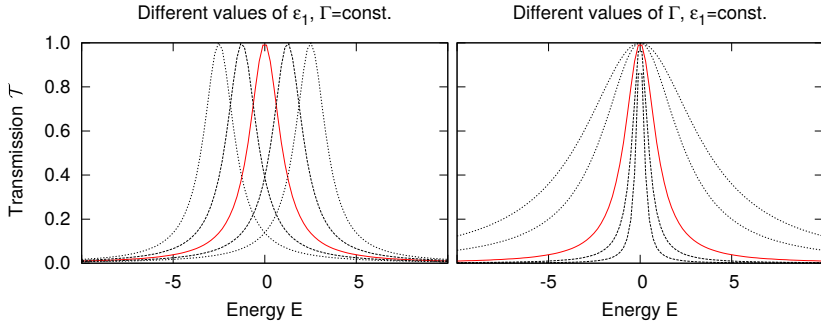


Figure 2.4.: Transmission functions for a single level system. The position of the peak is dependent on (left) the energy value ε_1 and (right) the width of the function is determined by $\Gamma_{1,1}^R$.

2.3. Analytical transmission function for a two-level system

As a more realistic example, we now consider a 2-level system as shown on the left hand side of Fig. 2.5.

This would be the case for a hydrogen molecule with the 1s-levels of each hydrogen atom as single-particle basis functions⁵ (see right panel of Fig. 2.5) or alternatively the π system of an ethylene molecule.

We will again start by writing the transmission function in terms of Green's functions,

$$\mathcal{T}(E) = \text{Tr} \left[\Gamma^L \mathbf{G}^{\Sigma \dagger} \Gamma^R \mathbf{G}^{\Sigma} \right] = \text{Tr} \left[(\mathbf{G}^{\Sigma} \Gamma^L) (\mathbf{G}^{\Sigma \dagger} \Gamma^R) \right]. \quad (2.51)$$

Note that trace is invariant under cyclic permutations. In the basis of the atomic orbitals localized on the hydrogen atoms, $\{|1\rangle, |2\rangle\}$, the matrix Green's function adopts the following form,

$$\mathbf{G}^{\Sigma} = \begin{pmatrix} E - H_{1,1} - \Sigma_{1,1} & H_{1,2} \\ H_{2,1} & E - H_{2,2} - \Sigma_{2,2} \end{pmatrix}^{-1}, \quad (2.52)$$

⁵Note that we shift from a (molecular) orbital basis to a localized basis, which is mathematically equivalent and has the advantage of being easier to combine with standard quantum chemistry electronic structure approaches.

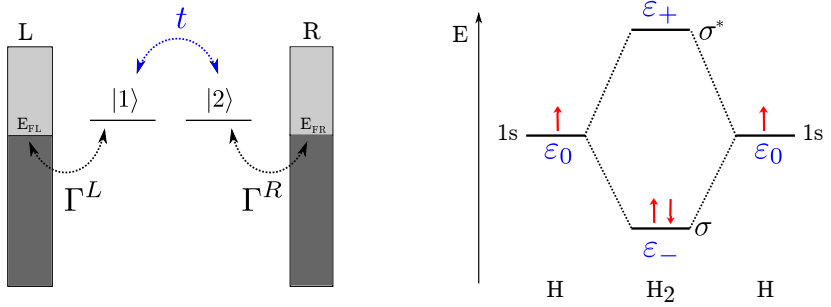


Figure 2.5.: *Left:* A 2-level system between two electrodes. The coupling of the respective level to the neighboring electrode is described by Γ^K ($K = L, R$) and the coupling among the levels is denoted by t . *Right:* Molecular orbital diagram for a hydrogen molecule. As each hydrogen atom has a singly occupied 1s atomic orbital (AO) with energy ϵ_0 , a bonding (σ) and an antibonding (σ^*) orbital with energies ϵ_- and ϵ_+ , respectively, are formed by interaction between these two AOs.

with the site energies ϵ_0 and the coupling between the two sites t given by

$$\epsilon_0 = H_{1,1} = H_{2,2}, \quad (2.53)$$

and

$$t = H_{1,2} = H_{2,1}. \quad (2.54)$$

We assume that the self energy is dominated by its imaginary part (in other words, the shift of single-particle energies is neglected or incorporated into the definition of ϵ_0), so the matrix Green's function now reads

$$\mathbf{G}^\Sigma = \begin{pmatrix} E - \epsilon_0 + \frac{i}{2}\Gamma & t \\ t & E - \epsilon_0 + \frac{i}{2}\Gamma \end{pmatrix}^{-1}. \quad (2.55)$$

Recalling that a matrix is invertible⁶ if the determinant of the matrix is different from zero, we have

$$\mathbf{G}^\Sigma = \frac{1}{(E - \epsilon_0 + \frac{i}{2}\Gamma)^2 - t^2} \begin{pmatrix} E - \epsilon_0 + \frac{i}{2}\Gamma & -t \\ -t & E - \epsilon_0 + \frac{i}{2}\Gamma \end{pmatrix}. \quad (2.56)$$

If we now follow the steps that have lead from Eq. (2.45) to Eq. (2.47), we get

$$\Gamma_{i,j}^L = 2\pi H_{i,l} H_{l,j} \rho, \quad (2.57)$$

$$\Gamma_{i,j}^R = 2\pi H_{i,r} H_{r,j} \rho, \quad (2.58)$$

⁶ $\mathbf{A} = \begin{pmatrix} a & b \\ c & d \end{pmatrix} \Rightarrow \mathbf{A}^{-1} = \frac{1}{\det|\mathbf{A}|} \begin{pmatrix} d & -b \\ -c & a \end{pmatrix}$

where we assume that the coupling to all electrode states is equal and that the density of states are constant ($\rho = \text{const}$). The matrix elements $H_{i,j}$ are defined as

$$H_{1,l} = H_{l,1} \neq 0 \quad (2.59)$$

$$H_{2,l} = H_{l,2} = 0 \quad (2.60)$$

$$H_{1,r} = H_{r,1} = 0 \quad (2.61)$$

$$H_{2,r} = H_{r,2} \neq 0 \quad (2.62)$$

As a result, the matrix coupling functions are given by

$$\mathbf{\Gamma}^L = \begin{pmatrix} 2\pi\rho H_{1,l}H_{l,1} & 0 \\ 0 & 0 \end{pmatrix} = \begin{pmatrix} \Gamma & 0 \\ 0 & 0 \end{pmatrix}, \quad (2.63)$$

$$\mathbf{\Gamma}^R = \begin{pmatrix} 0 & 0 \\ 0 & 2\pi\rho H_{2,r}H_{r,2} \end{pmatrix} = \begin{pmatrix} 0 & 0 \\ 0 & \Gamma \end{pmatrix}. \quad (2.64)$$

If we now multiply the respective matrix Green's function with Eq. (2.63) or Eq. (2.64), we obtain the following expressions for the two parts in parentheses within the trace of Eq. (2.51),

$$\begin{aligned} (\mathbf{G}^\Sigma \mathbf{\Gamma}^L) &= \frac{1}{(E - \varepsilon_0 + \frac{i}{2}\Gamma)^2 - t^2} \begin{pmatrix} E - \varepsilon_0 + \frac{i}{2}\Gamma & -t \\ -t & E - \varepsilon_0 + \frac{i}{2}\Gamma \end{pmatrix} \begin{pmatrix} \Gamma & 0 \\ 0 & 0 \end{pmatrix} \\ &= \frac{1}{(E - \varepsilon_0 + \frac{i}{2}\Gamma)^2 - t^2} \begin{pmatrix} (E - \varepsilon_0 + \frac{i}{2}\Gamma)\Gamma & 0 \\ -t\Gamma & 0 \end{pmatrix}, \end{aligned} \quad (2.65)$$

$$\begin{aligned} (\mathbf{G}^{\Sigma\dagger} \mathbf{\Gamma}^R) &= \frac{1}{(E - \varepsilon_0 - \frac{i}{2}\Gamma)^2 - t^2} \begin{pmatrix} E - \varepsilon_0 - \frac{i}{2}\Gamma & -t \\ -t & E - \varepsilon_0 - \frac{i}{2}\Gamma \end{pmatrix} \begin{pmatrix} 0 & 0 \\ 0 & \Gamma \end{pmatrix} \\ &= \frac{1}{(E - \varepsilon_0 - \frac{i}{2}\Gamma)^2 - t^2} \begin{pmatrix} 0 & -t\Gamma \\ 0 & (E - \varepsilon_0 - \frac{i}{2}\Gamma)\Gamma \end{pmatrix}. \end{aligned} \quad (2.66)$$

The transmission matrix can then be expressed as

$$\begin{aligned}
 \mathbf{T} &= \frac{1}{[E - \varepsilon_0 - \frac{i}{2}\Gamma]^2 - t^2} \frac{1}{[(E - \varepsilon_0 + \frac{i}{2}\Gamma)^2 - t^2]} \\
 &\times \begin{pmatrix} (E - \varepsilon_0 + \frac{i}{2}\Gamma)\Gamma & 0 \\ -t\Gamma & 0 \end{pmatrix} \begin{pmatrix} 0 & -t\Gamma \\ 0 & (E - \varepsilon_0 - \frac{i}{2}\Gamma)\Gamma \end{pmatrix} \\
 &= \frac{1}{[(E - \varepsilon_0 - \frac{i}{2}\Gamma)^2 - t^2][(E - \varepsilon_0 + \frac{i}{2}\Gamma)^2 - t^2]} \\
 &\times \begin{pmatrix} 0 & -(E + \varepsilon_0 + \frac{i}{2}\Gamma)\Gamma^2 t \\ 0 & t^2\Gamma^2 \end{pmatrix}. \tag{2.67}
 \end{aligned}$$

Thus, the transmission function as the trace over the transmission matrix is given by

$$\mathcal{T}(E) = \text{Tr}(\mathbf{T}) = \frac{t^2\Gamma^2}{[(E - \varepsilon_0 - \frac{i}{2}\Gamma)^2 - t^2][(E - \varepsilon_0 + \frac{i}{2}\Gamma)^2 - t^2]}. \tag{2.68}$$

The denominator⁷ of Eq. (2.68) can be rewritten as

$$\mathcal{T}(E) = \frac{t^2\Gamma^2}{[(E - \varepsilon_+)^2 + 1/4\Gamma^2][(E - \varepsilon_-)^2 + 1/4\Gamma^2]}, \tag{2.69}$$

with $\varepsilon_{\pm} = \varepsilon_0 \pm t$.

Fig. 2.6 shows the transmission function for a 2-level system (left) and the resulting I - V curve obtained by integrating over the transmission (right). Two peaks are obtained, located at the molecular orbital energies ε_+ and ε_- , with their width again determined by Γ . It is clear from the right-hand side of Figure 2.6 why the quantized nature of the two-level system leads to nonohmic (but rather stepwise) behavior of the $I - V$ curve.

⁷ The denominator in Eq. (2.68) can be reformulated as follows, with $a = E - \varepsilon_0$ and $b = \frac{\Gamma}{2}$:

$$\begin{aligned}
 [(a - ib)^2 - t^2][(a + ib)^2 - t^2] &= [a^2 - 2iab - b^2 - t^2][a^2 + 2iab - b^2 - t^2] \\
 &= [(a^2 - b^2 - t^2) - i2ab][(a^2 - b^2 - t^2) + i2ab] \\
 &= (a^2 - b^2 - t^2)^2 + 4a^2b^2 \\
 &= (a^2 - b^2)^2 - 2(a^2 - b^2)t^2 + t^4 + 4a^2b^2 \\
 &= a^4 - 2a^2b^2 + b^4 - 2a^2t^2 + 2b^2t^2 + t^4 + 4a^2b^2 \\
 &= a^4 + b^4 + t^4 + 2a^2b^2 - 2a^2t^2 + 2b^2t^2 \\
 &= a^4 + 2a^3t + a^2t^2 + a^2b^2 - 2a^3t - 4a^2t^2 - 2at^3 \\
 &\quad - 2atb^2 + a^2t^2 + 2at^3 + t^4 + b^2t^2 + a^2b^2 \\
 &\quad + 2atb^2 + b^2t^2 + b^4 \\
 &= [(a - t)^2 + b^2][(a + t)^2 + b^2].
 \end{aligned}$$

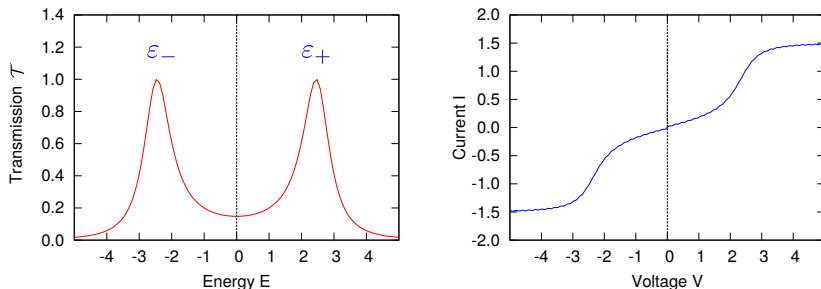


Figure 2.6.: Integrating over the transmission function leads to the current as a function of voltage. The two peaks that occur in the transmission function for a 2-level system correspond to the (renormalized) energies of the highest occupied molecular orbital (HOMO) with ϵ_- and the lowest unoccupied molecular orbital (LUMO) with ϵ_+ .

2.4. A first-principles approach and its implementation in ARTAIOS

ARTAIOS is a computer program for postprocessing output from electronic structure calculations, which computes electron transport properties of molecular junctions [206]. The transport approach implemented in ARTAIOS is based on a combination of the Landauer approximation with a Green’s function formalism, as described above. Instead of single-particle eigenfunctions of the electrodes and the central region, the single-particle basis functions are chosen to be the atom-centered Gaussian-type orbitals usually employed in quantum chemistry. Since these functions are nonorthogonal, the algorithm needs to be changed slightly (see Ref. [177] and below). Note that defining interfaces between electrodes and the central region within a space of spatially overlapping functions is not necessarily physically reasonable [214]. Given the complexity of molecular junctions, striving for qualitative agreement with the experiment is usually all that can be hoped for. For this purpose, the overlap of the basis functions across the interface may be considered negligible. It should be made sure, however, that ghost transmission does not affect the calculated transmission (see Section 3.2.1 and Ref. [215]).

The mode of operation of ARTAIOS shall only be briefly summarized. The relevant equations which are implemented in the ARTAIOS code to calculate the transport properties are summarized in Fig. 2.8. The schematic picture demonstrates that the transport code only needs the overlap matrix \mathbf{S} and the one-particle Hamiltonian matrix (i.e., the Fock matrix) \mathbf{H} from a previous electronic structure calculation on a gold-cluster–molecule–gold-cluster system, along with the information which

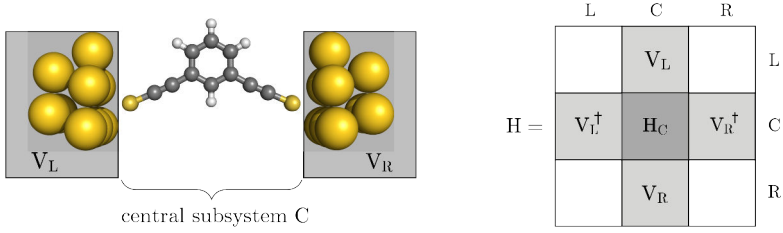


Figure 2.7.: *Left:* Partitioning of the electrode–molecule–electrode system into central subsystem (C) and left and right electrodes (L and R). The central subsystem only comprises the molecule. For quantitative accuracy, it would be essential to incorporate as many electrode atoms into the central region as are necessary to ensure bulk properties at both sides of the interface. *Right:* Definition of the central subsystem Hamiltonian and the coupling matrices as submatrices of the full one-particle Hamiltonian (see Ref. [215] for further details). The same partitioning is applied to the overlap matrix.

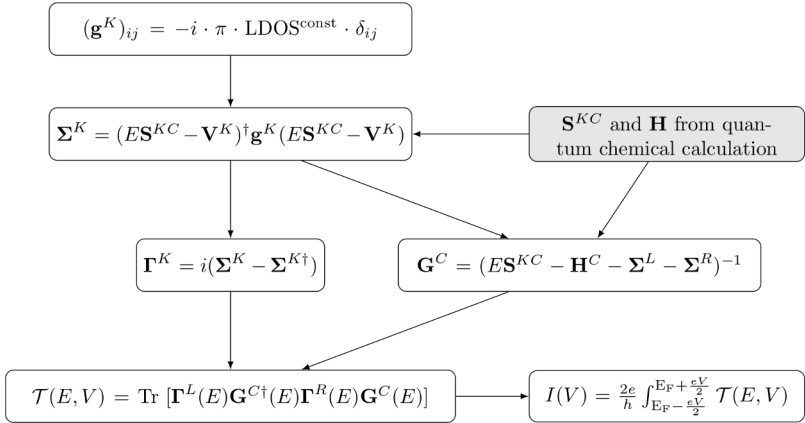


Figure 2.8.: The main equations evaluated in transport calculations by ARTAIOS.

basis functions belong to the right and left electrodes and to the central subsystem (see Fig. 2.7). The bulk Green’s functions of the electrodes \mathbf{g}^K are calculated in the WBL approximation, which is appropriate for gold with its flat local density of states (LDOS) around the Fermi energy E_F . Note that for quantitative accuracy, the effects of having an open system under bias voltage on the electronic structure would need to be taken into account. In view of all the other approximations that cannot be circumvented in practice (*e.g.*, Landauer approximation, approximate

exchange–correlation functional, Kohn–Sham eigenstates rather than many-electron states, neglect of molecular dynamics/statistics, and the effect of solvent and adsorbate molecules on the properties of the system), incorporating these effects on the electronic structure alone would hardly lead to the desired accuracy. For our purposes of qualitatively understanding molecular junctions, it does therefore not seem worth the considerable effort.

For better understanding the connection between molecular structure and conductance, ARTAIOS offers the possibility to decompose the transmission into local contributions [196, 216, 217],

$$\mathcal{T}(E) = \sum_{A \in L, B \in R} \mathcal{T}_{AB}(E), \quad (2.70)$$

where $\mathcal{T}_{AB}(E)$ is the transmission for electrons between atomic centers A and B , and A the sum is over all pairs of atoms which have one atom on the left and one on the right side of an arbitrarily chosen interface through which the current shall be evaluated. Fig. 2.9 shows the local transmissions for a 1,3-benzenedithiol molecule at different energies.

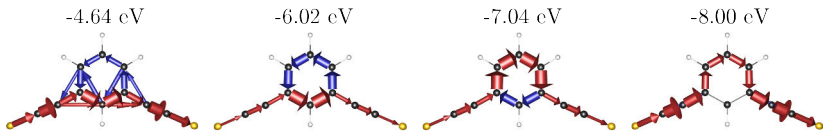


Figure 2.9.: Local transmissions at different energies through 1,3-benzenedithiol. The diameter of the arrows is defined by the value of the local transmission for the atom pairs, normalized to the largest contribution. Local transmission contributions in the same (opposite) direction as the total current are indicated by red (blue) arrows, respectively. Only contributions to the transmission larger than 10 % of the largest local transmission are shown.

Furthermore, the subsystem molecular orbitals (MOs) can be obtained from solving the subsystem’s secular equations [206, 215],

$$\mathbf{H}^C \mathbf{C}^C = \mathbf{S}^C \mathbf{C}^C \boldsymbol{\varepsilon}_C, \quad (2.71)$$

where \mathbf{H}^C and \mathbf{S}^C correspond to the Fock and overlap matrix blocks of the total system where both basis functions are located on the central subsystem (indicated by index C , see right-hand side of Figure 2.7). \mathbf{C}^C are the subsystem MO coefficients and $\boldsymbol{\varepsilon}_C$ is a diagonal matrix containing the central subsystem MO energies. Central subsystem molecular orbital energies are where the peaks in the transmission function should be located. They are thus another important means for understanding structure–conductance relationships.

3. Analyzing and predicting force and conductance measurements using static density functional theory

3.1. Introduction

In order to implement and exploit desirable functionalities of molecules in molecular devices, it is crucial to control the molecular structure and the relevant forces that occur at the molecule–electrode interface. Simultaneous measurements of forces and conductances by combined STM/AFM and c-AFM have provided new insights into the correlation between mechanical and electrical properties and the influence of mechanical strain on force–conductance variations, in particular molecule stiffnesses [218, 219], bond rupture forces [153, 220], and bonding energies [221]. However, our understanding of the junction formation is limited since we often know little or nothing about the junction configuration from experiments. For example, measured conductance values for 1,4-benzenedithiol (BDT) sandwiched between two gold electrodes were found to vary by at least two orders of magnitude [37, 48, 222–224]. This can (to some extent) be attributed to the unknown binding structures in junctions and indicates that several stable Au–S contact configurations exist [225]. For electron transport calculations, the lack of knowledge about the metal–molecule–metal structure and its evolution during transport has posed a major challenge in finding a method to quantitatively reproduce experimental conductance values and their wide distributions [226, 227].

In theoretical models, the molecular junction is often described by an idealized metal–molecule–metal structure, in which typically a straight molecular binding configuration to planar contacts is assumed [228–232]. Such a simplified model and the fact that most studies do not account for the statistics resulting from the molecules’ flexibility and multiple binding modes, partly explains the large discrepancies between theory and experiment that have been found even for simple molecules [233]. For instance, DFT calculations considerably overestimate¹ the

¹Note that a better agreement with experimental conductance values can be achieved using self-interaction correction schemes [234, 235], semiempirical methods (*e. g.*, DFT+ Σ) [40, 236] or self-consistent GW approximations [226, 227, 237].

experimentally measured conductance for gold–BDT–gold junctions [238–240]. A proper theoretical treatment of the structural fluctuations and bond rupture forces under mechanical stress usually requires the use of MD simulations [42,241] or Monte Carlo approaches [242–244]. Furthermore, combining MD simulations of molecular junction formation and elongation with electron transport calculations using, *e. g.* the DFT-based nonequilibrium Green’s-function approach [153, 170, 245–247] has helped to resolve the gap between theoretical and experimental predictions and provided new insight into structural changes and their effect on the conductance of mechanically stretched molecules. Snapshots of gold–BDT–gold junction configurations extracted from MD simulations have demonstrated that the S–Au bond is even stronger than the Au–Au bond itself [248, 249] and thus mechanical stretching of a single thiolate molecule can result in pulling a gold nanowire out of the gold electrode with subsequent Au–Au bond breaking [225, 250]. Although MD simulations provide richer information about structural variations, they are typically much more computationally demanding than static approaches (for a given method of calculating energies and forces) and will usually not correctly reproduce experiments performed at large time scales (*e. g.*, seconds) due to practical limitations on simulation time in the range of $10^{-15} - 10^{-9}$ s. Therefore, considering a number of different representative initial configurations (*i. e.* different adsorption sites or molecule-to-metal alignments) of a gold–molecule–gold junction using static DFT calculations [251, 252] may be desirable in order to circumvent a computationally intensive MD simulation. Moreover, anchoring groups such as amines [49], pyridines [108] or platform moieties (*e. g.*, tripod-shaped molecules [253, 254]) with well-defined binding structures to metals can reduce the number of relevant junction configurations in contrast to the thiol case or reduce the dependence of transport properties on the adsorption site and configuration [255–257]. Recently, triazatriangulenium (TATA) platform molecules have received much interest for the preparation of adlayers and their possible use as binding groups in metal–molecule–metal junctions [258–265]. The TATA platforms adsorb flat on a surface and can be functionalized at the center or at the edges, providing high stability and a good compromise between electronic decoupling and a relatively low contact resistance. In this part of the thesis, we will present force and conductance simulations of platform-mounted molecules under stress using static DFT and extend the method to incorporate other molecules of interest.

3.2. A mechanically flexible platform-based Zn-porphyrin complex

Porphyrins are of particular interest for various applications such as photovoltaics, photocatalysis, and electronics due to their light-harvesting and charge transport properties [266–270]. If adsorbed on metal surfaces, porphyrins lie parallel to the surface [271] which results in reduced photoreactivity due to strong interaction with the surface [272–274]. In order to maintain the desired properties of porphyrins when connected to metals, it is thus mandatory to reduce the molecule–surface coupling by introducing spacers with proper anchoring groups, while ensuring that the coupling is still sufficiently large to allow current to flow [275]. Thiols [276–278] and pyridines [277, 279, 280] are commonly used to reduce electronic coupling of porphyrin molecules from the metal surface. In molecular junctions based on self-assembled arrays, however, these anchors lead to closely stacked porphyrins, where transport is dominated by intermolecular interactions [281, 282]. In order to mount molecules in an upright orientation on surfaces with a well-defined molecule–molecule spacing, triazatriangulenium (TATA) cations have been proposed [258]. Furthermore, these molecular platforms offer sufficient electronic decoupling from the substrate while providing, as it turned out during the course of this thesis and in a related work performed during the same time, a high conductivity [263, 265, 283].

Recently, combined STM/AFM measurements on Zn-porphyrin-triazatriangulenium (Por-TATA) junctions by Hauptmann *et al.*, in which Zn-porphyrin molecules are attached to a molecular platform (TATA) via an ethynyl spacer (see Fig. 3.1a), showed an unusual non-monotonous variation of both force and conductance [283]. To understand this unusual behavior and to check the interpretation of the experimental findings, we have performed force and conductance simulations by combining constrained molecular structure optimizations using static Kohn–Sham DFT and the Landauer–Imry–Büttiker approach. Our model system consists of a pyramidal Au₂₀ cluster mimicking the STM tip, which was placed above the middle H-atom of the Por-TATA. The octyl chains attached to the nitrogen atoms of the TATA platform were replaced with methyl groups to reduce computational costs. A series of model structures were optimized first with no constraint and subsequently with the constraint that the coordinates of three hydrogen atoms of the TATA platform² (see Fig. 3.1b, circled in red) and the topmost slab of the tip were held fixed. The structure obtained from an unconstrained optimization has an internuclear Au–H distance³ of $d_{\text{Au-H}} = 1.30 \text{ \AA}$. The force was approximated as the negative of

²For the constrained optimizations and subsequent force calculations the gold surface was neglected.

³Note that the distance between the Au and H nuclei is not the same as the tip–molecule distance d , which represents the displacement along the tip–TATA platform direction.

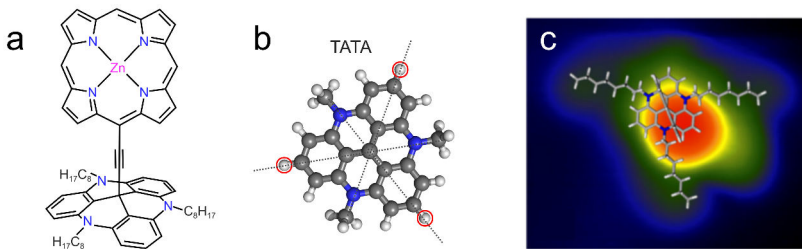


Figure 3.1.: (a) Lewis structure of *tri-octyl*-triazatriangulenium functionalized with Zn-porphyrin (*tri-octyl*-Por-TATA); (b) Optimized structure of TATA (Alkyl chains were replaced by methyl groups for in the calculation for the sake of computational efficiency). The red circled atoms were held fixed in the constrained optimizations using DFT; (c) STM image of a single Por-TATA with an overlaid molecular sketch (-0.44 V, 13 pA, (3.5×2.8) nm²) [283].

the numerical derivative of the energy values with respect to the tip–molecule distance d (d is defined as the height of the whole tip–Por-TATA system minus the height of the fully optimized structure that corresponds to $d = 0.00$ Å). For electron transport calculations, the TATA platform of the optimized Por-TATA was replaced by a TATA platform which was previously optimized on four layers of Au (PBE-D2/SVP) [284]. The Por-TATA was then attached to a single gold layer (20 atoms) with N–Au distances of 3.20 Å, as optimized in Ref. [284]. The resulting finite-cluster system was divided into tip (left electrode), surface (right electrode), and Por-TATA molecule (central subsystem). All gold atoms were assigned to the electrodes.

Table 3.1.: Comparison of the HOMO–LUMO gaps (in eV) obtained from the experiment [283] with the calculated gap energies for the Por-TATA subsystem, the isolated Por-TATA and Zn-Porphyrin using two different functionals and basis sets, respectively.

System		Functional/Basis set	HOMO–LUMO gap (eV)
Por-TATA	Exp. [283]	–	2.80(5)
	Subsystem	B3LYP/LANL2DZ	2.67
	Isolated	B3LYP/LANL2DZ	2.60
		B3LYP-D2/def-TZVP	2.55
Zn-Porphyrin	Isolated	BP86-D2/def-TZVP	1.56
		B3LYP-D2/def-TZVP	3.05
		BP86-D2/def-TZVP	2.07

The central subsystem molecular orbital (MO)s of the Por-TATA were calculated by solving the central subsystem’s secular equations (see Sec. 2.4, Eq. (2.71) and Ref. [215]) and assigned by comparing its shape with the MOs of the isolated Por-TATA (see Fig. 3.2a). The calculated gap between the HOMO and the LUMO of the Por-TATA agrees reasonably well with the experimental result. Of course HOMO-LUMO gaps cannot directly be related to the gaps between peaks in the dI/dV curves, but it is still reassuring that the two are in the same range. This value is only slightly larger than the calculated gap of isolated Por-TATA using the same exchange-correlation functional with dispersion correction (2.60 eV). Although quantitative differences occur using a pure functional (BP86-D2), the MO energies are qualitatively in the same order as when calculated with B3LYP.

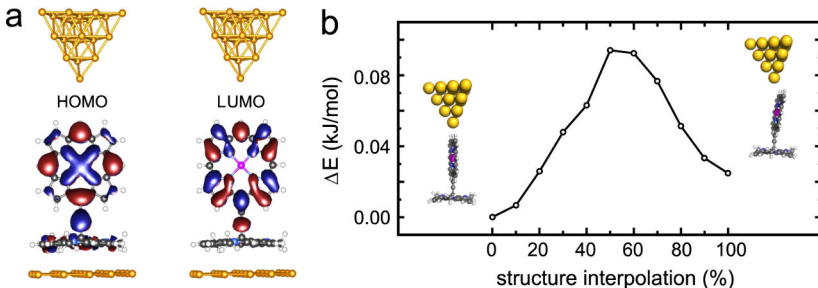


Figure 3.2.: (a) Isosurface plots of the frontier central subsystem molecular orbitals of Por-TATA (isovalue 0.02). (b) Potential energy surface scan between straight and bent Por-TATA structures with a Au_{20} tip using the linear synchronous transit method in internal coordinates. The relative tip–molecule distance of $d = 1.47 \text{ \AA}$ was chosen because here the energy difference between the two structures is minimal.

The STM image of a single Por-TATA molecule (see Figure 3.1d) indicates that the Zn-porphyrin is not centered on the *tri-octyl*-TATA platform. From an interpolation between a straight (S_i) and a bent (S_f , 6.7°) structure for a given tip–molecule distance, we find a fairly flat potential energy surface (PES) with two almost degenerate minima (Fig. 3.2b). They correspond to straight and bent structures of the central ligand and are separated by a barrier well below the error margin of DFT. We estimate an effective stiffness of $k = 0.6 \text{ N/m}$. Owing to this low stiffness and to the flat PES, the Por-TATA is assumed to be quite flexible. Thus, bending of the Zn-porphyrin is likely to occur.

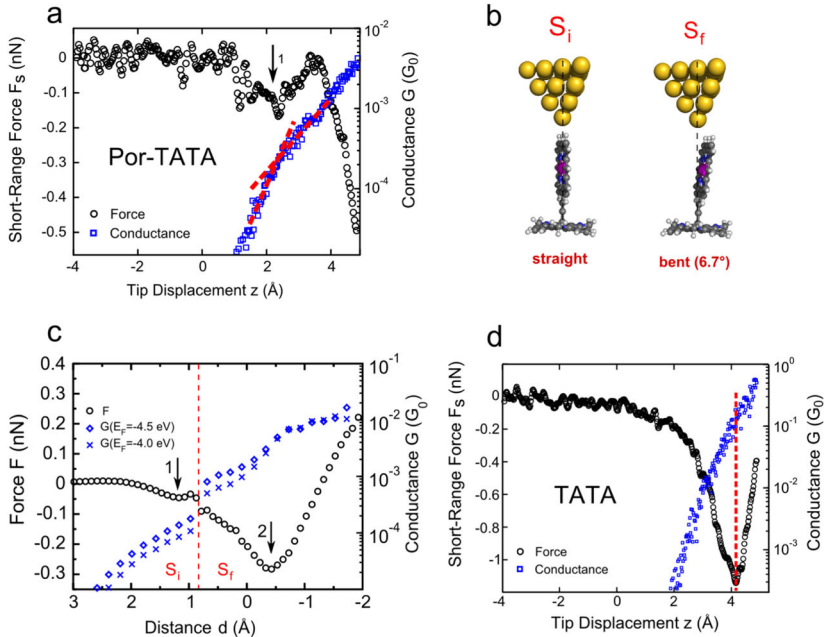


Figure 3.3.: (a) Simultaneously measured short-range force (circles, left axis) and conductance (squares, right axis) for a Por-TATA at the location of the Zn-porphyrin (with 0.1 V applied to the sample). The arrow indicates the shallow force minimum. (b) Snapshots of constrained-optimized model structures for the structures S_i (straight) and S_f (bent, 6.7°). (c) Calculated force (left axis) and conductance⁴ (right axis) as a function of the relative tip–molecule distance for different values of the Fermi energy. The dashed line indicates the change of the minimum-energy molecular structure (from S_i to S_f). Arrows mark force minima 1 and 2. $d = 0$ Å was set to the structure obtained from an unconstrained optimization of the tip–molecule system (Au–H internuclear distance of 1.3 Å). (d) Simultaneously measured force (circles, left axis) and conductance (squares, right axis) on a *tri-octyl*-TATA molecule at $V = 50$ mV.

⁴The conductance values are corrected for ghost transmissions (see Sec. 3.2.1).

Fig. 3.3a shows the experimental results for simultaneously measured short-range forces F_s and conductances G with respect to the tip–molecule distance. A shallow minimum of the force (arrow 1 in Fig. 3.3a) occurs with a maximally attractive force $F_{\max} = 0.2(1)$ nN. The measured conductance G increases monotonously. At the point of maximal attraction, a kink in the conductance curve is observed and a contact conductance of $G_c = (2 \pm 1) \cdot 10^{-4} G_0$ is determined. The contact conductance is within the range ($10^{-3} - 10^{-5} G_0$) that was measured for a similar junction (Zn-porphyrin with two thiolphenyl linkers) using MCBJ techniques [277, 285, 286]. Fig. 3.3d shows a high conductance for the TATA platform itself – making it a suitable linker for molecule–metal interfaces.

The constrained optimizations using BP86-D2/def-TZVP were started from structure S_i (straight, Fig. 3.3b). The tip–molecule distance d was elongated and reduced by steps of 0.20 Å over a range of 5.00 Å, starting with an elongation of 3.00 Å. Fig. 3.3c shows the calculated forces and conductances. For distances $d > 0.80$ Å, the porphyrin position remains qualitatively unchanged after the relaxation. For smaller distances, the structure S_i undergoes an abrupt change to a more bent shape S_f (see Fig. 3.3b). This change corresponds to the transition from the left to the right minimum in Fig. 3.2b, which is presumably less abrupt in the experiment due to fluctuations of the molecule.

Upon further approaching of the tip, the Por-TATA structure is even more bent (13.2° for a tip–molecule distance of $d = -1.70$ Å). It should be noted that the bent structure does not converge to the straight structure when used as the initial structure (even for large tip–molecule distances). However, using the bent structure as the initial structure for the constrained optimizations leads to energetically more favorable converged structures for distances $d < 0.80$ Å compared with the straight structure. Therefore, S_i -type structures are used for distances $d > 0.80$ Å. Structures of the type S_f are used as the initial guess for smaller distances for the calculations shown in Fig. 3.3c, in which this structure is consistently more stable than the straight one. The force exhibits two minima (arrows 1 and 2) that correspond to maximal attraction. The first shallow maximum occurs when the tip contacts the middle H-atom of the porphyrin ring, while the second one reflects the interaction of the Au tip with carbon atoms from the porphyrin macrocycle.

As the barrier between a straight and a bent Por-TATA is well below the estimated error margin of the DFT calculations ($0.1 \text{ kJ}\cdot\text{mol}^{-1}$, Fig. 3.2b), the same procedure as for the tip straight above the porphyrin (S_i and S_f) has been applied for the structures B_i and B_f (see Fig. 3.4a). The B_i structure corresponds to S_f (bent, 6.7°), but the tip is laterally displaced so that the tip atom is placed above the middle H atom of the porphyrin macrocycle. The B_f structure (bent, 14.7°) is obtained for smaller distances, where stronger bending occurs. Fig. 3.4b

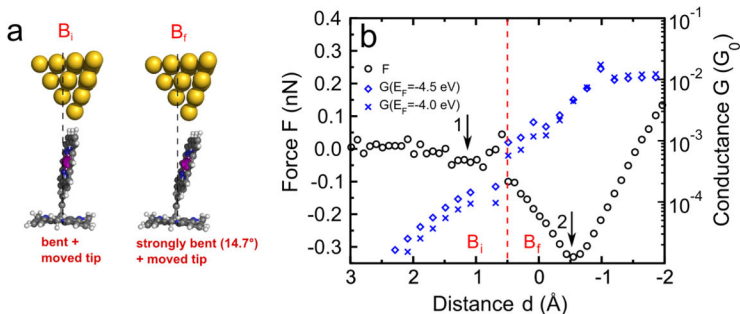


Figure 3.4.: (a) Snapshots of constrained-optimized model structures B_i (6.7°) and B_f (14.7°). (b) Calculated force (left axis) and conductance⁴ (right axis) as a function of the relative tip–molecule distance for different values of the Fermi energy. The dashed line indicates the change of the minimum-energy molecular structure (from B_i to B_f). Arrows mark force minima 1 and 2.

shows that this results in virtually the same shapes of the force and conductance curves (compare Fig. 3.3c). We have verified that the calculated conductances are independent of the choice of the Fermi energy E_F over the range from -4.0 eV to -4.5 eV. Moreover, no transmission peaks are present near the Fermi energy for all examined tip–molecule distances (see lower panel of Fig. 3.6), which suggests that the Landauer formalism is a good description of electron transport through the junction [195]. To conclude, the calculated forces and conductances⁵ reproduce the essential features of the experimental data. The forces exhibit a similar shallow attractive well and the deeper second force minimum, which is obtained in the calculation. Also, the absolute values of the forces are in reasonable agreement with the experiment.

3.2.1. A closer look at the conductance curve

In Ref. [215] it has been shown that sometimes an artificially high transmission is observed using the Landauer approach in combination with large nonorthogonal atom-centered basis sets, i.e. triple-zeta quality basis sets with polarization functions. This problem is referred to as ghost transmission. In such cases, transport is still present even though all atomic nuclei and electrons of the central subsystem are removed and only the associated atom-centered basis functions remain.

⁵We note that the quantitative agreement of the conductances observed at the position of the first attractive force maximum may be due to a favorable cancellation of errors. The qualitative agreement however is interpreted as supporting our interpretation of the experimental results, *i. e.*, the Por-TATA being intact and upright on the surface

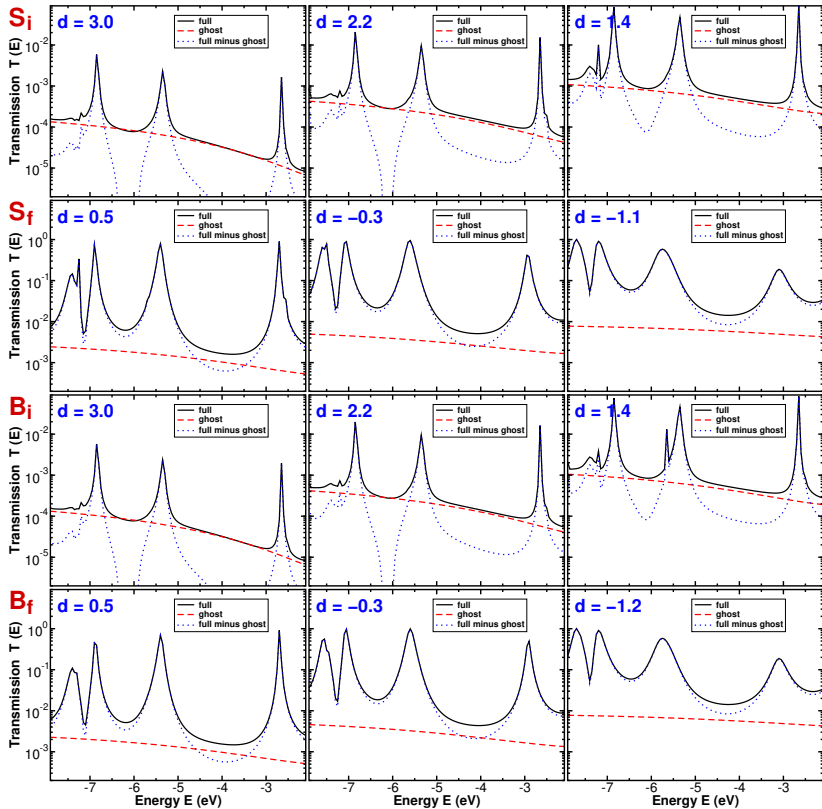


Figure 3.5.: Full (black solid lines) and ghost transmission (red dashed lines) as a function of energy for representative structures at a tip–molecule distance d in Å. Transmission curves were corrected in a pragmatic approach by subtracting ghost transmission (blue dotted lines). DFT(B3LYP)/LANL2DZ.

Figure 3.5 shows representative transmission functions for the system under study which correspond to the conductance values of the “full” transport calculation within the Landauer approach in Figure 3.6 (red symbols). The plotted energy range around the HOMO-LUMO gaps includes reasonable choices for the Fermi energy of gold electrodes (-3.0 to -5.0 eV), since the Fermi function of bulk gold (-5.5 eV [287]) may be shifted using the finite metal cluster approach and by the presence of the molecular adsorbates. Even though we used the double-zeta quality basis set LANL2DZ to avoid ghost transmission, the flat regions of the transmission curves – in particular for structures with large tip–molecule distances – indicate

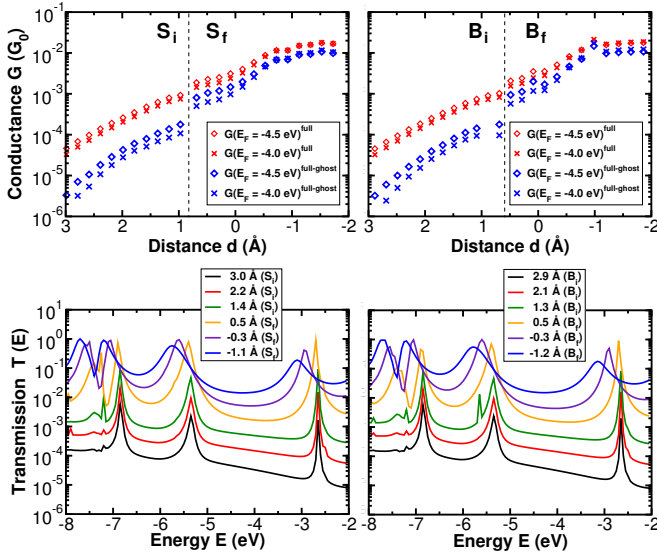


Figure 3.6.: *Upper panel:* Calculated conductance obtained from a full transport calculation (red) and corrected by ghost transmission (blue) as a function of energy for all Por-TATA structures under study. *Lower panel:* Total transmission as a function of energy for representative structures. For structure B_i at a tip–molecule distance of $d = 0.90$ Å, no ghost transmission could be obtained due to convergence problems. DFT(B3LYP)/LANL2DZ.

that exactly those may occur. Therefore, ghost transmission calculations were performed considering the same structures as in the full transport calculation, except that all atoms of the central region were replaced by their basis functions only. Figure 3.5 shows that ghost transmission is a non-negligible contribution to the full transmission and that the curves are nearly constant over the considered energy range. Subtracting the ghost from the full transmission results in a much lower transmission curve in the energy range of the expected Fermi energy. The full conductance in comparison with the one corrected by ghost transmission is shown in Figure 3.6. The corrected values (plotted in Fig. 3.3c and Fig. 3.4b) deviate strongly for large and slightly for small tip–molecule distances compared with the conductance values obtained from full transport calculations. The stronger significance of ghost transmission at larger distances may be because ghost transmission falls off more slowly with increasing distance than “real” transmission.

3.2.2. Platform contribution to the conductance

To estimate the contribution of the TATA platform to the conductance of the Por-TATA molecule, we have calculated the local transmissions (see Eq. (2.70) in Sec. 2.4) for Por-TATA and TATA including the four lowest gold atoms of the tip into the central region (see Fig. B.2 and Fig. B.1 in Sec. B.1 of the Appendix, respectively). Comparing the sum of local transmissions that can be assigned to either contributions from the "contact H" atom or contributions from the platform, the platform contributions are significantly higher for TATA than for the Por-TATA system (as expected from the smaller distance between platform and tip). Thus, direct tunneling from the tip to the platform contributes, as expected, more to transmission than for the Por-TATA system.

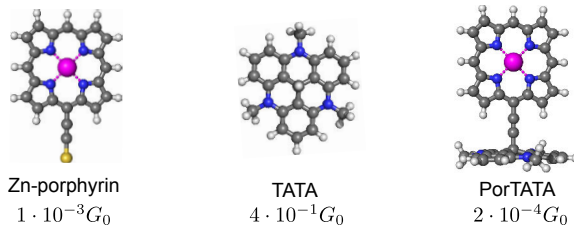


Figure 3.7.: Illustrations of Por-TATA and its subunits, namely a Zn-porphyrin (with an ethynyl thiolate linker) and a TATA platform with the respective conductance⁴ $G(E_F = 4.5 \text{ eV})$. The product of the transmissions of the subunits results in a value which is close to the total transmission of the Por-TATA system. B3LYP/LANL2DZ.

In the Landauer model of coherent transport, the total transmission is the product of the transmissions of the subunits [21]. This implies that the contact conductance of Por-TATA ($2 \cdot 10^{-4} G_0$) may be attributed to the combined effects of the platform and the Zn-porphyrin unit⁶, which were estimated from calculations on TATA functionalized with an H atom ($10^{-1} G_0$) and Zn-porphyrin with an ethynyl thiolate spacer ($\approx 10^{-3} G_0$), respectively, as illustrated in Fig. 3.7.

⁶Of course this comparison is limited by the need to introduce a thiol anchor group for the "platformless" porphyrin, but it may still serve for illustrating that the platform is not the bottleneck for transport.

3.3. Functionalized trioxotriangulenium platforms

Driven by the structural and electronic advantages of the TATA binding group, trioxotriangulenium (TOTA) derivatives have been studied with respect to surface functionalization [288–292]. Similar to TATA, TOTA and its derivatives reduce the coupling to metal surfaces compared to molecules adsorbed lying flat on a surface and have the additional advantage of a higher thermal stability compared to TATA [288, 289].

Recent STM measurements of various TOTA derivatives showed that the conductance increases monotonously as a function of the tip displacement [293]. However, a non-monotonous variation in the conductance has been observed within the contact range for hydroxyl- and propinyl-functionalized TOTA molecules. At a contact conductance of approximately $10^{-4} G_0$, the conductance suddenly decreases (over a range of 1 Å) and then increases again.

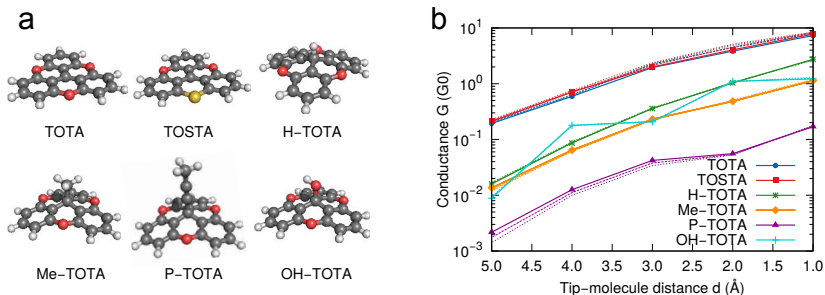


Figure 3.8.: (a) Optimized structures of isolated TOTA derivatives using BP86-D2/def-TZVP. (b) Calculated conductance G of functionalized TOTA molecules as a function of the relative tip–molecule distance for different values of the Fermi energy (solid line: $E_F = -5.0$ eV, dashed line: $E_F = -4.5$ eV, dotted line: $E_F = -4.0$ eV) using B3LYP/LANL2DZ.

In order to gain a deeper insight into the conductive behavior of functionalized TOTA molecules, we take first steps towards simulating the platforms used in the above mentioned STM studies, including a functionalization with hydrogen (H-TOTA), methyl (Me-TOTA), propinyl (P-TOTA), hydroxyl (OH-TOTA) as well as replacing one oxygen atom by a sulfur atom (TOSTA). Fig. 3.8a shows the optimized structures of the isolated TOTA derivatives under study. Our model systems consist of a TOTA derivative on a one-layered Au_{20} cluster with a tetrahedral Au_{20} tip placed above the center of the platform. As indicated by the experimental findings, all TOTA molecules were oriented with the oxygen atoms in the top position on the Au(111) surface using the experimentally estimated O–Au distance of 3.0 Å,

except for TOSTA which was oriented in the hollow position. We calculated the conductance as a function of different tip–molecule distances⁷ without optimizing the structures at each distance. Fig. 3.8b shows the obtained conductance curves for different values of the Fermi energy. Note that it is difficult to determine the exact contact distance from the STM measurements. Thus, a quantitative comparison of the calculated conductances values with the measured ones would have to be interpreted with caution. However, the conductance curves are qualitatively in good agreement with the experiment, except for P-TOTA and OH-TOTA. For these two TOTA derivatives, we could not fully reproduce the experimentally observed variation in the conductance curve. This was to be expected since we neglected any structural changes in our calculations which are likely to be particularly important for hydroxyl and propinyl functional groups (as they might not be as rigid as the other platforms). Conceivable in this regard would be an out-of-plane deformation of the TOTA core or a tilting of the functional group due to the presence of the tip similar to the Por-TATA system discussed in the previous section.

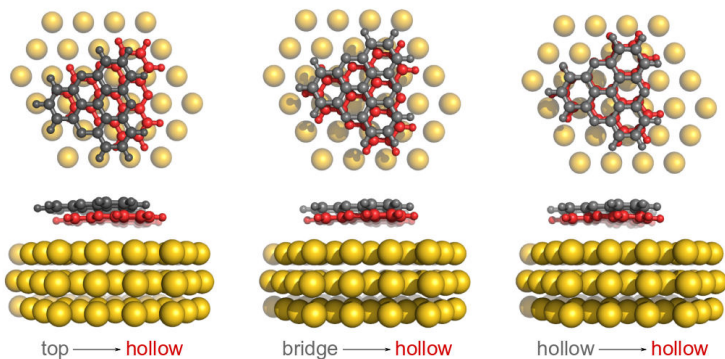


Figure 3.9.: Initial (gray) and optimized (red) TOTA on a three-layered Au₉₀ cluster (all gold atoms were held fixed) based on different initial adsorption sites (top, bridge and hollow) using BP86-D3(BJ)/SVP. All structures converged to the hollow site.

As a first step towards a more comprehensive picture of current as a function of tip–sample distance, we study the adsorption structure in more detail. Therefore, we optimized TOTA on a three-layered Au₉₀ cluster starting from different adsorption sites (top, bridge and hollow). Figure 3.9 illustrates that the hollow site is the most favored adsorption position for TOTA when using BP86-D3(BJ)/SVP. Such discrepancies between calculated and measured site-preference are known for non-

⁷In case of Me-TOTA, the tip–molecule distance d denotes the distance from the tip apex Au atom to the center of the triangle formed by the three H atoms of the methyl group.

covalently bound systems and are attributed to the fact that GGA functionals do not properly account for dispersion interactions [294]. Since we described dispersion interactions using Grimmes' D3 correction scheme, the problem here is more likely due to modeling the surface using a cluster rather than periodic methods, and possibly also to the rather small basis set used for this exploratory study. Further steps would include series of constraint relaxations similar to the ones conducted for the Por-TATA system. However, the more complicated current–distance curves observed in the experiment for the TOTA derivatives suggest a considerable computational effort for such studies, which was beyond the time frame of this thesis.

3.4. Mechanical manipulation of spin states in manganocene

In the field of molecular electronics, new opportunities arise for molecular storage of information when combined with the ideas and the advantages of spintronics at the single molecule level [158, 295–298]. In this context, single-molecule magnets⁸ (SMMs) [299–302] and spin crossover (SCO) molecules [303–305] have been the subject of intensive research attempting to control the spin states of individual magnetic molecule (or of the transported electrons). The frequently observed bistability of such compounds enables switching between magnetic properties of the two states [306], which often has direct impact on the transport behavior. It has proven difficult to incorporate SMMs into electronic devices, and the success of such approaches is often tied to ultralow temperatures [307, 308]. In contrast, SCO compounds show bistability near room temperature [309]. These materials can undergo a transition between a low-spin (LS) and a high-spin (HS) configuration through changes in, *e. g.*, pressure or temperature [310]. Widely studied examples of SCO compounds are Fe(II) terpyridine or structurally related complexes [305, 309, 311, 312]. Recently, a mechanically controlled spin transition for such a complex has been demonstrated in a single-molecule junction, where the mechanical change was induced by an applied voltage [162].

Furthermore, manganocene (MnCp_2) and some of its derivatives are SCO compounds [313]. They are members of the metallocene family ($\text{M}(\text{C}_5\text{R}_5)_2$) [314–316], which has found promising potential applications in the field of molecular electronics [317–327]. At room temperature, MnCp_2 is almost entirely in its high-spin state. By substituting the cyclopentadienyl (Cp) rings of manganocene with sterically demanding electron-donating ligands (*e. g.*, methyl), a low-spin state is supported [328]. This is attributed to electronic factors, which are overriding the steric effects (which due to Mn–C bond elongation should favor a high-spin state).

⁸SMMs are compounds whose magnetic hysteresis at low temperatures originates from a single molecule.

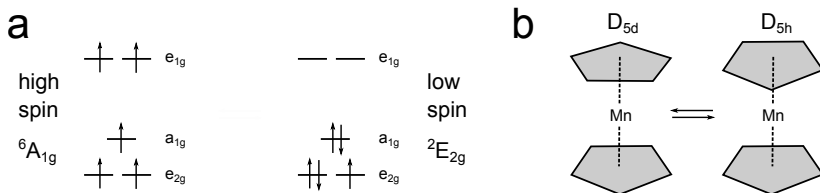


Figure 3.10.: (a) Energy level diagram for the high-spin (${}^6A_{1g}$) and the low-spin (${}^2E_{2g}$) state of MnCp_2 (D_{5d} notation). (b) Two conformations of the manganocene: eclipsed (D_{5d}) and staggered (D_{5h}).

Introducing even more bulky isopropyl ligands overcomes the electronic effects of the methyl substituents and leads to a high-spin ground state despite the electron-donating character of the substituents. The change from a HS ($S = \frac{5}{2}$) to a LS ($S = \frac{1}{2}$) ground state (see Fig. 3.10a) correlates with shorter and more covalent Mn–C bonds, compared to high-spin complexes. This metal-to-ring distance dependence on the spin state of the molecule suggests a potential to control the spin state of manganocene mechanically (similar to the Fe(II) complex mentioned above). As illustrated in Figure 3.10b, manganocene can adopt two conformations, an eclipsed (D_{5d}) and a staggered (D_{5h}) one, which are both accessible through Cp ring rotation in the gas phase [316]. The energy difference between those two conformations is small, with the D_{5h} structures being slightly more stable than the D_{5d} structures (at least for the high-spin state).

In order to assess whether mechanical stress can, in principle, be used to induce a spin crossover, we stretched and compressed an isolated manganocene molecule first. To this end, we optimized the molecule in D_{5h} symmetry and in its HS and LS states, respectively. Figure 3.11 shows the molecular orbital (MO) diagrams for high-spin and low-spin manganocene within the energy range of the $3d$ orbitals of manganese. The energy gaps between the LUMO $^\alpha$ and the HOMO $^\alpha$ are 3.42 (4.97) eV for the high-spin and 2.73 (4.53) eV for the low-spin state using BP86-D2 (B3LYP-D2). Note that orbital energies are highly sensitive to the functional used, but irrespective of the functional the MO energies are qualitatively in the same order here. Table 3.2 shows the calculated structural and vibrational parameters obtained with the two different functionals and compared to the experimental data available. As mentioned before, the low-spin state is promoted by methylation of the Cp rings. The corresponding experimental data is shown in Table 3.3 and compared to the calculated bond lengths. The calculated Mn–C and C–C bond lengths agree well with the experimental ones for both functionals.

Table 3.2.: Calculated bond lengths d (in Å), vibrational wavenumbers $\tilde{\nu}$ (in cm^{-1}), force constants f (in $N \cdot \text{cm}^{-1}$), and the HOMO–LUMO energy difference E_{gap} (α and β , in eV) for high-spin and low-spin manganocene using a def-TZVP basis set and two different functionals with Grimmes’ (-D2) correction scheme. Bond lengths of high-spin manganocene are compared to experimental findings.

Prop.	high-spin (HS)			low-spin (LS)	
	BP86-D2	B3LYP-D2	Exp. [329]	BP86-D2	B3LYP-D2
Mn–Cp	2.06	2.09	2.046(8)	2.05	1.95
Mn–C	2.39	2.42	2.380(6)	2.38	2.18
C–C	1.43	1.42	1.429(8)	1.44	1.43
C–H	1.09	1.08	1.125(10)	1.09	1.08
$\tilde{\nu}$	213	213	–	262	265
f	15	15	–	40	23
E_{gap}^{α}	3.42	4.97	–	2.73	4.53
E_{gap}^{β}	2.87	4.94	–	0.44	3.84

Table 3.3.: Calculated Mn–C and C–C bond lengths d (in Å) for high-spin and low-spin decamethylmanganocene using a def-TZVP basis set and two different functionals with Grimmes’ (-D2) correction scheme. Bond lengths of low-spin decamethylmanganocene are compared to experimental findings. Note that the Cp rings of high-spin decamethylmanganocene are tilted, resulting in different Mn–C bond lengths, thus a range is obtained.

Prop.	high-spin (HS)		low-spin (LS)		
	BP86-D2	B3LYP-D2	BP86-D2	B3LYP-D2	Exp. [330]
Mn–C	2.25–2.48	2.32–2.44	2.15	2.17	2.105(2)–2.118(2)
C–C	1.43	1.42	1.43	1.43	1.411(2)–1.434(2)

A series of constrained optimizations have then been performed with the restriction that all carbon atoms of the Cp rings were held fixed. The distance between the Cp ligands was reduced and elongated by steps of 0.10 Å over a range of -0.50 Å to 0.50 Å compared to the equilibrium distance. The optimized structures for manganocene in the HS state at maximum elongation and compression using BP86-D2/def-TZVP are shown in Fig. 3.4a. As can be seen from Fig. 3.4b, B3LYP-D2 predicts the HS state at 127.9 kJ/mol below the LS ground state at $d = 0$ Å,

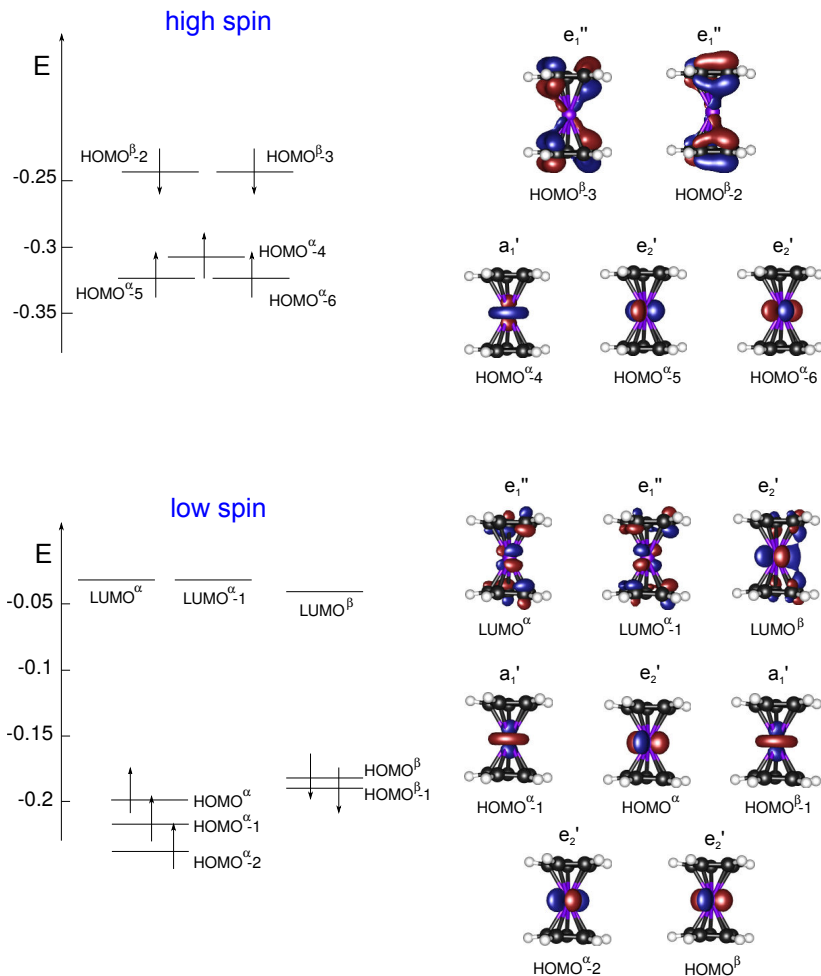


Figure 3.11.: Calculated molecular orbital (MO) energy level diagram for HS and LS manganocene and isosurface plots of low-spin MOs with a_1' , e_1'' , and e_2' symmetry (D_{5h} notation) using B3LYP-D2/def-TZVP. The isosurface value is set to 0.05.

while the corresponding value for BP86-D2 is 48.3 kJ/mol. It is well known that hybrid functionals tend to overestimate the stability of the HS state with respect to the LS state [331,332]. A HS to LS transition in the range of 0.2 Å (BP86, pure functional) to 0.4 Å (B3LYP, hybrid functional, 20 % exact exchange) compression can be obtained, which suggests that such a transition would be conceivable in an

AFM setup (provided that the MnCp_2 is compressible by the tip).

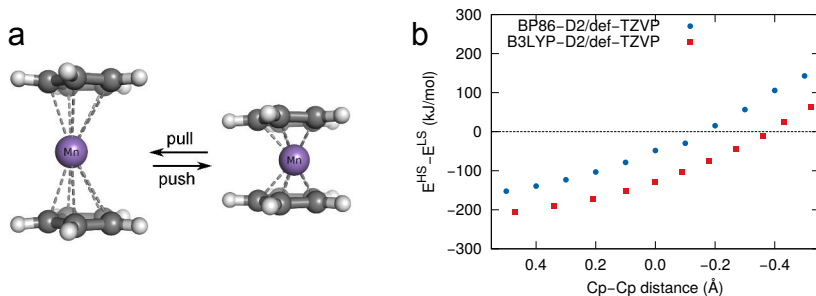


Figure 3.12.: (a) Optimized high-spin structures of an isolated manganocene upon maximum elongation and compression using B3LYP-D2/def-TZVP. (b) Calculated spin state energy differences ($E^{\text{HS}} - E^{\text{LS}}$) as a function of the Cp-Cp distance (measured as the height of MnCp_2) using a def-TZVP basis set and two different exchange-correlation functionals.

To estimate the relative stiffness of tip and molecule, we calculated the infrared (IR) vibrational wavenumbers for both spin states of manganocene and for a tip-shaped Au_{20} cluster within the harmonic approximation (see Fig. B.4 in Sec. B.2 of the Appendix). Figure 3.13 shows selected vibrational normal mode displacements

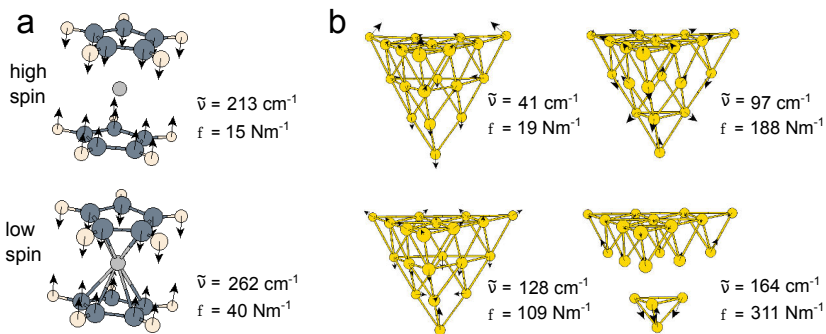


Figure 3.13.: Selected normal mode displacements for (a) HS and LS manganocene and (b) a Au_{20} cluster. BP86-D2/def-TZVP.

which may be attributed to a breathing mode. The corresponding force constants for these modes in the harmonic approximation are in the range of 15 to $40 \text{ N}\cdot\text{m}^{-1}$ for manganocene and approximately $20 - 300 \text{ N}\cdot\text{m}^{-1}$ for Au_{20} . This suggests that the tip is stiffer than manganocene and might be used in principle to compress the

molecule.

To test the compressibility of MnCp_2 by a gold tip in more detail, a model system consisting of a single manganocene with an Au_{20} tip was optimized with BP86-D2/def-TZVP – first with no constraint and subsequently with the restriction that the five carbon atoms of the lower Cp ring as well as the topmost slab of the Au tip were held fixed. The results show a distortion of the manganocene due to strong deformation of the upper cyclopentadienyl ring (see Fig. 3.14). Whether or not this is a result of the restriction of the molecule’s movement in its lateral degrees of freedom depends on the molecule–surface interactions, which points out that it is important to take those into account molecule–surface interactions in further studies.

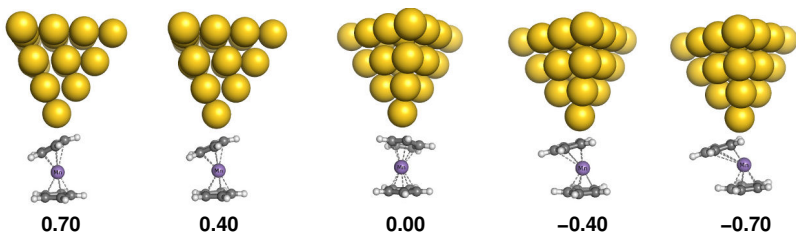


Figure 3.14.: Constrained optimized structures of manganocene with a Au_{20} tip. The five carbon atoms of the lower cyclopentadienyl ring as well as the topmost slab of the Au tip were held fixed during relaxation. The structures were generated based on the constraint optimized structures for the high-spin state. BP86/def-TZVP.

These results suggest that while mechanically induced spin crossover should be in principle possible, but may be prevented by lateral distortions. Furthermore, DFT calculations indicate that high-spin manganocene will partially transfer its spin to the gold surface [333]. Thus, introducing ligands or insulating layers for electronic decoupling from the surface may also be required for realizing such experiments.

3.5. Detecting the dipole moment of carbon monoxide on different surfaces

The adsorption of carbon monoxide on metal surfaces has been extensively studied because it is a fundamental step in many catalytic reactions [334]. Furthermore, functionalization of AFM tips with carbon monoxide has helped increasing the resolution of AFM images drastically and, therefore, improved the interpretation of the obtained AFM images [335–342]. Recently, non-contact AFM studies of CO molecules adsorbed on different surfaces – in particular $\text{Mn}/\text{W}(001)$, $\text{NiO}(100)$, and

Cu(111) – showed a bright ring with a dark center (donut) in the AFM image at a certain tip–molecule distance [343]. A change in the dipole–dipole interaction between the adsorbed CO and the metallic Cr tip is suggested to be responsible for this behavior *e. g.*, it is conceivable that a change in the dipole moment occurs upon shifting the molecule to another adsorption position with the tip. In the theoretical community, carbon monoxide is well known because of the “CO puzzle”, which expresses the failure of common exchange–correlation functionals to describe the correct adsorption site of CO on surfaces [294].

In this section, we focus on detecting the dipole moment of CO at different adsorption sites. CO possesses a dipole moment with its positive pole at the oxygen atom, contrary to what would be expected from the relative electronegativities [344]. Schneider *et al.* found opposite signs of the CO dipole moment depending on the adsorption site using plane-wave based DFT calculations for CO adsorbed on a Pt(111) surface [345]. They have calculated the z -component of the total dipole moment including the Pt(111) surface (μ_z) as the first moment of the spatial charge distribution (z being the direction normal to the Pt surface). Their GGA corrected results show a positive top CO dipole moment (0.43 D) corresponding to $C^{\delta-}-O^{\delta+}$ and negative dipole moments if adsorbed at bridge (-0.24 D) and hollow (-0.38 D) sites corresponding to $C^{\delta+}-O^{\delta-}$.

We have calculated the dipole moment of the CO molecule on Pt(111)⁹ in top, bridge and fcc hollow position using a plane-wave based method in combination with the BADER AIM program and LOCALDIP. The latter has been developed within the framework of this thesis and provides an interface for grid-based AIM methods by relying on internal reference points instead of bond critical points (see Sec. 4.3 and 4.4 for more information). The results are given in Figure 3.15a. Optimized Pt–C (C–O) distances are 1.86 Å (1.15 Å) for the top, 1.48 Å (1.17 Å) for the bridge and 1.36 Å (1.19 Å) for the fcc hollow position. Bader charge transfer for different adsorption sites is in good agreement with the one calculated by Schneider *et al.* [345]. However, the obtained CO dipole moments are negative ($C^{\delta+}-O^{\delta-}$) for all the adsorption sites investigated, even for the top site. Furthermore, the dipole moment increases with increasing coordination (top < bridge < fcc). When comparing our results with electrostatic potential plots (see Fig. 3.15c), we observe the same trend as the change in the CO dipole moment from top to higher coordinated sites. Subsequently, we suggest that our results are physically reasonable and that it is vital to calculate the adsorbates’ local dipole moment instead of solely the total dipole moment in one direction.

In order to gain further insight into the adsorption behavior of CO and for evaluat-

⁹The Pt(111) surface was modeled using 4 layers of 2×2 Pt atoms, comparable to the unit cell used in Ref. [345]

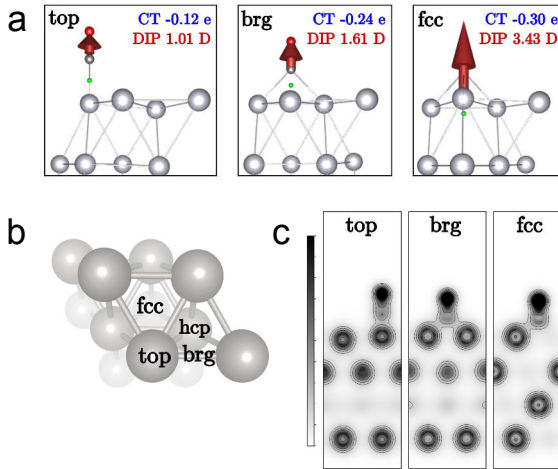


Figure 3.15.: (a) Calculated local dipole moments of CO on Pt(111) in different adsorption positions using LOCALDIP (see Sec. 4.4 for more information) in combination with the AIM analysis program BADER. Structure optimizations were performed using PAW-PBE-D2. The dipole moments are indicated as red arrows pointing towards the negative part (δ^-). The length of the dipole moment is specified in Debye (multiplied by a scaling factor of 2 for visualization). The internal reference points are indicated as small green dots between CO and the Cu(111) surface. The total dipole moment of an isolated CO molecule with the same settings is $\mu(\text{CO}) = 0.09$ D. (b) Schematic representation of adsorption positions on a Pt(111) surface: top, bridge (brg), fcc hollow and hcp hollow. (c) Electrostatic potential plots (isosurface value 0.05).

ing the importance of describing surfaces under periodic boundary conditions, we have studied the adsorption structure of CO on a Cu(111) surface using two different methods: a plane-wave periodic-boundary (PB) model and a cluster approach employing a localized single-particle basis. To get an impression of the differences between the adsorption positions, CO was placed in top and hcp hollow position on a Cu(111) surface (the bridge position was not considered in any detail here). The optimized structures are shown in Fig. 3.16. The CO molecule adsorbs in an upright orientation with the oxygen atom pointing away from the surface using both methods when including dispersion corrections. Bond lengths, angles, partial charges, and local dipole moments are given in Table 3.4. The method used has only a minor influence on the structural properties (except for the O–C–Cu angle). C–O and C–Cu distances are in good agreement with the calculated ones in Ref. [346]

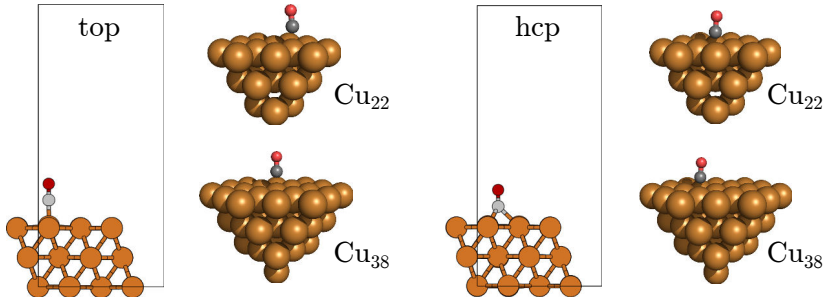


Figure 3.16.: Optimized structures of CO on Cu(111) for the top and the hollow adsorption positions using a plane wave approach with periodic-boundary conditions and a cluster approach with two different cluster sizes.

(PW91 functional) and similar to those calculated for CO on Pt(111). In case of CO on a Cu_{22} cluster, top-CO is slightly tilted by an angle of 7° in contrast to CO on the hcp hollow site. For a larger cluster size, hcp-CO is slightly tilted by an angle of 5° and top-CO is almost in an upright position. The calculated dipole moment of CO on top and hcp hollow site is shown in the left panel of Fig. 3.17. Similar to CO/Pt(111), we obtain a dipole moment pointing away from the surface ($\text{C}^{\delta+}-\text{O}^{\delta-}$) and an increase in its magnitude if we go from the top to the hcp hollow site to about > 3 D.

Upon approaching a CO molecule by a pyramidal Cu_{10} tip with either lateral or no displacement (see right panel of Fig. 3.17), the force was approximated as the negative of the numerical derivative of the energy values with respect to the tip displacement z . The starting point, $z = 0$, denotes a Au-O distance of $d = 2 \text{ \AA}$ (which is the same as from top-CO to the copper surface). Fig. 3.18 shows repulsive interactions for top-CO (left panel) and attractive interactions for hcp-CO (right panel) at a tip-molecule distance of -0.02 nm (red).

Table 3.4.: C–O and C–Cu distance d (in Å), O–C–Cu angle θ (in °), AIM partial charge q_{CO} (in unit charges) and local dipole moment μ_{CO} (in Debye) of a CO molecule on a Cu(111) surface for the top and the hcp hollow (hcp) adsorption positions using a periodic-boundary (PB) and a cluster approach with a Cu_{22} and a Cu_{38} cluster (Basis set: def2-TZVP).

Position	Method	Functional	$d_{\text{C-O}}$	$d_{\text{C-Cu}}^{\text{a}}$	$\theta_{\text{O-C-Cu}}$	q_{CO}	μ_{CO}
top	PB	PAW-PBE-D2	1.15	1.86	179.9	-0.16	0.99
	Cu_{22}	PBE-D3(BJ)	1.15	1.92	172.7	-0.17	1.07
	Cu_{38}	PBE-D3(BJ)	1.15	1.92	180.0	-0.18	1.12
hcp	PB	PAW-PBE-D2	1.18	1.41	179.7	-0.41	4.33
	Cu_{22}	PBE-D3(BJ)	1.18	1.43	178.5	-0.35	3.56
	Cu_{38}	PBE-D3(BJ)	1.18	1.43	175.1	-0.39	4.05

^a The C–Cu distance denotes the height of the CO molecule above the copper surface.

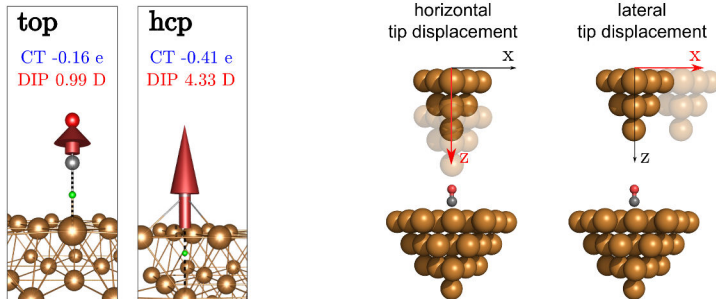


Figure 3.17.: *Left:* Calculated dipole moment of CO on Cu(111) for top and hollow adsorption position using BADER in combination with LOCALDIP. The dipole moment is indicated as a red arrow pointing towards the negatively charged part. Internal reference coordinates (marked as green dots) were used to determine COs' dipole moment within the theory of AIM. Structure optimizations were performed using a plane wave approach (PAW-PBE-D2). *Right:* Schematic representation of constrained optimizations while moving the tip horizontally and vertically.

Although we can qualitatively confirm the observations in the AFM experiments, much shorter distances between tip and molecule were necessary to achieve similar results in our simulations. In experiments, the occurrence of the donut shaped images was observed at tip–CO distances of up to 5 Å [343]. At such large distances

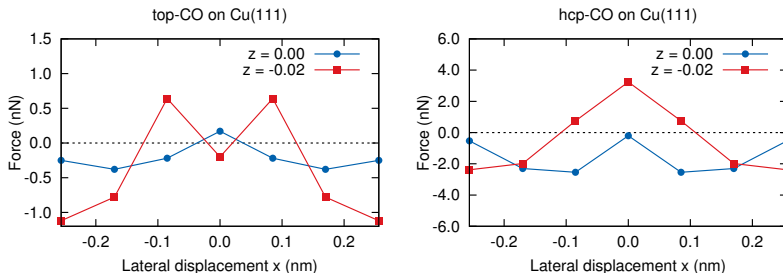


Figure 3.18.: Calculated forces as a function of lateral dip displacement for different tip–molecule distances.

long-range interactions play a much larger role than the short-range interactions which we studied. For CO on NiO(100), Shluger *et al.* proposed that the Cr tip has a permanent electric dipole moment with its positive end oriented toward the sample [347]. By representing the metallic tip as a point dipole, they conclude the importance of a long-range dipole–dipole interaction between the tip and the molecule in good quantitative agreement with experimental results. Although this has been contradicted by recent investigations [348]. Nonetheless, it has been demonstrated that using clusters rather than a periodic tip model with (at least five) pyramidal atomic layers on top of a surface may lead to incorrect predictions [349]. These findings support the assumption that our cluster-based model is not able to represent the tip structure in AFM experiments accurately, especially if we are interested in long-range interactions. For this purpose, computationally demanding calculations with more surface layers and potentially larger tips will be necessary, which were beyond the scope of this thesis.

3.6. Conclusion

Controlling and understanding molecular structure and all relevant inter- and intramolecular forces is crucial for improving and guiding the design of nanoscopic devices with advanced functionalities. Using a low-temperature scanning probe microscope, Hauptmann *et al.* measured the force and conductance of model junctions comprising a triazatriangulenium (TATA) platform, an ethynyl spacer, and an upright Zn-porphyrin (Por-TATA) as a function of tip-sample distance. In order to characterize the fairly complex and mechanically flexible Por-TATA molecule, MD simulations may achieve a comprehensive understanding. However, since the measurements have been performed at time scales of up to one minute, even these computationally demanding MD simulations may not correctly reproduce the ex-

periment due to practical limitations on simulation time in the femto- to nanosecond range. Therefore, we performed computationally less expensive constrained optimizations using static DFT calculations at different tip-sample distances. To account for the flexibility of the Por-TATA-platform system (as suggested by the flat potential energy surface when bending the porphyrin to the side), we started from a straight (S_i) and a bent (S_f) structure, respectively. Our calculations further revealed that the variations in force and conductance curves result from an induced tilting of the porphyrin due to the presence of the STM tip. Two force minima are assigned to tip-hydrogen and tip-carbon interactions. The calculated forces are in remarkably close agreement with the experimental data which suggests that it is indeed standing upright on the surface. The transport calculations showed an artificially high transmission in the energy range of the expected Fermi energy caused by so called “ghost transmission”. After subtracting the ghost transmission, the calculated conductance curves are similar to the experimental results. Furthermore, the contact conductance of Por-TATA may be attributed to the combined effects of the platform and the Zn-porphyrin subunits. Because the static DFT results obtained with only two “boundary” configurations agree so well with the experiment, we applied the constrained optimization approach to other molecular systems of interest.

Inspired by measurements of molecules based on a related platform, trioxotriangulenium (TOTA), with and without various functional groups attached to the center (see Sec. 3.3), which showed unexpected kinks in the conductance curves of some of the molecules, we carried out single-point calculations combined with the Landauer approach in order to obtain more detailed information on the molecules’ conductance. The results qualitatively reproduce the linear increase of conductance when approaching the tip. On the other hand, we could not confirm the sudden decrease in the contact region. In order to test if the kinks are the result of a deformation of the molecule (or the tip), as in Section 3.2, it is important to allow the molecules to relax when attached to the surface. This was done by studying the adsorption structure of TOTA on a three-layered gold cluster. In contrast to top site adsorption found in the experiments, the calculations predict that TOTA prefers the hollow site when attached to gold. This site-preference problem of GGA functionals is well known for non-covalently bound systems where van der Waals forces play a major role [294]. Although we used Grimme’s correction scheme to describe dispersion interactions (which is considered to improve solving this problem [350, 351]), we could not reproduce the correct adsorption structure. This may also be due to the cluster approach employed for describing the surface, which suggests that more computationally demanding computations under periodic boundary conditions may be required.

In Section 3.4, we extended the system of interest towards a single magnetic molecule

to assess the possibility of a mechanically-induced spin-crossover. Constrained optimizations of an isolated manganocene suggest that a transition between a high-spin and a low-spin state can, in principle, be achieved by stretching and compressing the molecule. The estimated stiffness of a Au_{20} tip compared to a manganocene also indicates that the mechanical strain can be applied in an AFM/STM setup. However, initial force simulations on a manganocene with a sharp Au_{20} tip did not lead to the desired spin-crossover. Instead of a controlled vertical elongation/compression of the molecular structure, the manganocene was artificially distorted accompanied by a lateral displacement of the upper cyclopentadienyl ring. This is most likely due to the restriction of the molecule movement in its lateral degrees of freedom since we neglected the surface in the simulation. As in the TOTA case, future investigations would require an accurate description of manganocenes' adsorption structure on surfaces. Apart from that, it is likely that the pyramidal-shaped Au_{20} cluster does not represent the dimensions of a STM tip accurately and that one has to use broader shapes and tip materials to realize a mechanically-induced spin transition.

In the images of non-contact AFM experiments, the occurrence of "donuts" led to the assumption that CO molecules could possibly change their adsorption sites with concurrent changes in the dipole-dipole interactions with the tip. Therefore, in Section 3.5, we studied different adsorption sites of CO on a Pt(111) and a Cu(111) surface with respect to changes in the molecular dipole moment using two different DFT methodologies. Contrary to the suggestions in the literature, we did not observe a reversal of the dipoles' direction due to adsorption on different adsorption sites. This may be due to the use of a more well-defined local dipole approach in our studies. As we could not reproduce the long-range dipole interactions observed in AFM experiments with the three metal atom layers employed, more computationally demanding approaches involving up to seven layers should be used in follow-up studies for an accurate modeling of tip-sample interactions, which will help in elucidating the relation between local dipole moments and observed AFM data. For the same reason, larger representations of the tip may be needed.

4. Charge transfer and dipole effects in functionalized carbon nanotubes (CNTs)

In the previous chapter, we have investigated tip–molecule interactions of single molecules on surfaces and demonstrated how changes in the molecular structure can affect the conductance. In this part of the thesis, we focus on molecules that have an indirect impact on the conductance of another system involved in transport, namely: carbon nanotubes (CNTs). Their unique properties make carbon nanotubes promising candidates for nanotechnological applications. In particular, functionalization of CNTs (*e. g.*, adsorption of molecules of the nanotubes surface) may serve as a switchable unit to alter the conductance of the CNTs in response to external stimuli and has important advantages for sensing applications.

4.1. Introduction

The quasi one-dimensional structure of a single-walled carbon nanotube (CNT) can be thought of as a graphene sheet rolled into a (theoretically infinite) cylinder [352]. Thus, their electronic structure is usually described in terms of the graphene band structure. Fig. 4.1 shows a carbon nanotube unit cell mapped on the honeycomb structure of a graphene sheet. The structure of a carbon nanotube can be uniquely described by its circumferential (also referred to as “chiral”) vector,

$$\mathbf{c} = n\mathbf{a}_1 + m\mathbf{a}_2, \quad (4.1)$$

where the integers n and m denote the number of unit vectors, \mathbf{a}_1 and \mathbf{a}_2 , along two directions in the crystal lattice of graphene. This vector is described by the angle θ of the graphene helix around the tube. If $2n + m$ is a multiple of 3, the nanotube is metallic (otherwise it is a semiconducting tube). Nanotubes with chirality $(n, 0)$ are called zigzag carbon nanotubes ($\theta = 0^\circ$), and tubes with chirality (n, n) are called armchair nanotubes ($\theta = 30^\circ$). All the remaining examples, for which $0 < \theta < 30^\circ$, belong to the class of chiral nanotubes [353]. The allowed electronic wave vector k_{\parallel} parallel to the nanotube axis is continuous since the tube can be considered infinitely long. Furthermore, the electrons in the π orbitals obey periodic boundary conditions (finite circumference) which causes quantization of the waves perpendicular to the

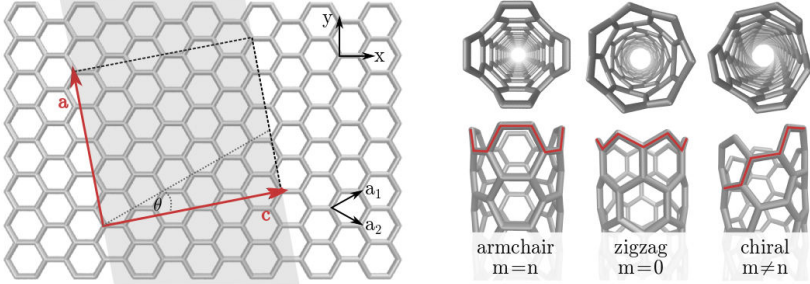


Figure 4.1.: Construction of carbon nanotubes by folding the honeycomb structure of a graphene sheet. The vector along the tube axis \mathbf{a} and the circumferential vector \mathbf{c} are indicated as red arrows. The chiral angle θ can vary within $0 < \theta < 30^\circ$. Armchair ($m = n$) and zigzag ($m = 0$) tubes are rolled up along a high symmetry direction (0° and 30° , respectively). Chiral tubes, on the other hand can be rolled up along any other angle. The gray area represents the part of the sheet used to roll up a (4,2) CNT.

axis [353]. Fig. 4.2 shows the Brillouin zones of a (5,5) and a (8,0) carbon nanotube (red lines). This quantization creates $q = 2n$ lines (red) parallel to the tube axis in the first Brillouin zone separated by $\Delta k_\perp \propto 1/d$, where the diameter d depends on the indices n and m as

$$d = \frac{a}{\pi} \sqrt{(n^2 + nm + m^2)}, \quad (4.2)$$

where a is the length of the unit vectors ($a = |\mathbf{a}_1| = |\mathbf{a}_2|$). Now, two possible scenarios can be formulated as illustrated in Fig. 4.2 for a (5,5) and a (8,0) carbon nanotube. In the case of the (5,5) CNT, an allowed k_\parallel vector contains a K point and, thus, the tube becomes metallic. In the (8,0) CNT, however, the K point is not covered by any allowed k vectors and consequently the tube is semiconducting with a band gap at the Γ point.

At the Fermi energy, the density of states (DOS) is finite for a metallic and zero for a semi-conducting tube. Figure 4.3 exemplarily shows the electronic DOS and the conductance for a metallic (5,5) single-walled CNT. The sharp peaks in the DOS appear due to the quasi one-dimensional character of the CNTs and are known as van Hove singularities [356]. The spacing between the spikes reflects the tube's optical absorption and emission properties.

Since the intrinsic properties of carbon nanotubes (CNTs) can be tuned through interaction with other chemical species, their chemical functionalization has been the subject of intensive research in the past few years [357,358], aiming at creating nanotubes with new functionalities [359,360]. Due to strong tube-tube van der

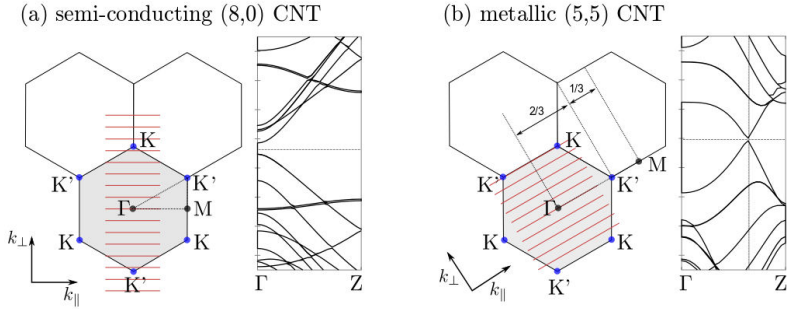


Figure 4.2.: First Brillouin zone and band structure for a (a) semi-conducting (8,0) and (b) metallic (5,5) carbon nanotube. The black hexagons define the first Brillouin zone of graphene with three high-symmetry points Γ , K , and M , where the blue dots in the corners are the K points. Allowed k_{\perp} wave vectors within the first Brillouin zone are represented by red lines perpendicular to the nanotube axis along k_{\parallel} . When these lines cross a K point, the nanotube is metallic and the “band gap” lies at two third from Γ to Z . If this is not the case, the nanotube is semi-conducting with a band gap at the Γ point ($k = 0$). The Z point represents the allowed k_{\parallel} vector along the tube axis at (b) $k_{\parallel} = 2\pi/\sqrt{3}a$ and (a) $k_{\parallel} = 2\pi/a$. The band structures were calculated using PAW-PBE-D2. The horizontal dotted lines mark the Fermi energy E_F .

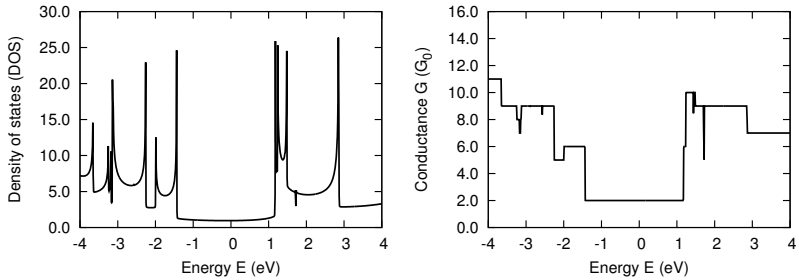


Figure 4.3.: Calculated electronic density of states (DOS) and conductance as a function of the energy for a metallic (5,5) carbon nanotube based on maximally-localized Wannier functions [354, 355] using PBE, ultrasoft pseudo potentials, a 20-atom unit cell, 5 k points, 30 Ry (240 Ry) plane-wave cutoff for wavefunctions (charge density), and 0.03 Ry of cold smearing.

Waals interactions, CNTs tend to form bundles. This aggregation often results in deteriorated optical and electronic properties of the tube, but can be avoided by separating the tubes through functionalization [361, 362]. Functionalization of CNTs can be achieved using covalent or non-covalent interactions. In non-covalent functionalization the van der Waals force becomes the dominant interaction between the adsorbate and the CNT. Therefore, the atomic structure of the CNTs is not significantly perturbed in contrast to covalent functionalization [363, 364].

A reliable theoretical approach with truly predictive capabilities of such complex transistor configurations would require a multi-scale description ideally combined with ensemble methods such as molecular dynamics or Monte Carlo methods [365, 366]. In this work, we focus on a basic step in such an approach, the interaction between a CNT and an adsorbate, and the resulting changes in the CNT properties, for a selected set of adsorption configurations. We will focus on the comparison of two different density functional theory (DFT) methodologies which are commonly used to describe the supramolecular interactions between adsorbates and CNTs: A periodic boundary (PB) model (which in practice is often based on plane waves and pseudopotentials)¹ and a truncated approach (in practice often combined with a localized basis), both of which have their advantages and disadvantages.

The PB model is the method of choice in theoretical solid state and surface physics to account for the extended nature of the system under study. When studying the influence of an adsorbate on a nanotube, interactions between adsorbates in adjacent unit cells are often not desired. This may require a large unit cell. The same holds for large adsorbates such as a lanthanide ion sandwiched between two organic phthalocyanine units (TbPc₂), as investigated by Ruben, Balestro and co-workers with regards to their single-molecule magnet behavior [307, 372, 373]. An even more crucial point is the (in practice) often limited choice of pseudopotentials in plane-wave codes (and thus the limited choice of exchange–correlation functionals). This is particularly relevant for hybrid functionals, which are computationally much more expensive than pure ones in this context. On the other hand, a truncated approach based on atom-centered basis functions allows treating interactions between molecules and nanotubes or surfaces (involving capping atoms such as hydrogen, where necessary) within the typical language of chemistry. This approach can take advantage of a well-developed pool of diverse exchange–correlation functionals, which is in some cases essential even for an accurate qualitative description and allows for easy interfacing with various quantum chemical analysis tools. The most serious error source of the truncated approximation is the choice of a too small CNT size, which may lead to a preferred adsorption at the edge (“edge effects”) and usually wrong binding energies. Choosing an inappropriate CNT size can also

¹Of course, there are also some electronic-structure codes which combine periodic boundary conditions with localized basis functions such as CP2K [367], ADF [368–370], and GAUSSIAN [371].

lead to inaccurate structural properties. Moreover, truncating the nanotube produces discrete single-particle levels (“molecular orbitals”) rather than bands, and the number of these levels decreases with the tubes’ decreasing length, thus leading to an electronic structure less suitable for the approximation of band structures.

In this part of the thesis, we determine (among others) under which conditions the truncated approach based on localized, atom-centered single-particle basis functions and the PB model using plane waves produce similar results, thus functioning as a benchmark study, on the basis of which the reliability of the truncated approach can be evaluated. On the basis of these benchmark studies, we investigate the link between changes in the transistor characteristics and changes in the adsorbates’ properties, in particular charge transfer and dipole effects.

Probing changes in local electric dipole moments helps to understand several phenomena important for nanoscience, such as tip–molecule interactions in atomic force microscopy as outlined in Section 3.5 and Refs. [347, 374, 375]. Adsorption of molecules on solid surfaces may lead to a significant charge redistribution. The resulting difference in magnitude as well as orientation of the molecular dipole moments in comparison to their isolated forms may create surface dipoles, affecting the local electrostatic environment [376]. The effect of the solvent environment on the electron transport of single-molecule junctions, for example, has been recently suggested to result from solvent-induced dipoles (“solvent gating”) changing the electrostatic potential at the junction [377]. Similarly, single molecule magnets [307, 373] or molecular switches [141, 142, 378–380] adsorbed on single-walled carbon nanotube transistors have been found to induce significant changes of the nanotubes’ conductivity (“chemical gating”). Changes in the adsorbates’ dipole moments have been suggested as causing this effect. Modifications in local dipole moments during vibrational motions are also relevant for understanding infrared intensities [381, 382], and local electric (static) polarizabilities are usually obtained from local dipole moments [383–385].

While it is straightforward to calculate the total dipole moment of a system, the local dipole moment of a subsystem (*e. g.*, an adsorbed molecule on a surface) is not uniquely defined. This is similar to population analysis [207, 386–391] and local properties in general [392–397]. When defining local dipole moments, an additional difficulty arises, as fragments of molecular or supramolecular systems are usually (partially) charged, and dipole moments of charged systems depend on the choice of origin. Inspired by previous work based on Bader’s atoms-in-molecules (AIM) partitioning, we will derive a definition of fragment dipole moments which achieves origin-independence by relying on internal reference points. Instead of bond critical points as in existing approaches, we use as few as possible reference points, which are located between the fragment and the remainder(s) of the system and may be

chosen based on chemical intuition. This allows our approach to be used with AIM implementations that circumvent the calculation of critical points for reasons of computational efficiency, for cases where no bond critical points are found due to large interfragment distances, and with local partitioning schemes other than AIM which do not provide bond critical points.

4.2. Local dipole moments within the theory of Atoms-In-Molecules

Local partitioning of molecular properties has a long tradition in quantum chemistry [392], which started with partial charges [207, 386–391, 398], and was later extended to various properties such as electron spins [394–397, 399–402], electric dipole moments [344, 403–413], and local (static) electric polarizabilities [383–385, 393]. The advantage of assigning properties to atoms or groups of atoms (fragments) in a molecule is that it allows us to structure our thinking about molecules and other nanostructures. Since the “borders” of atoms in molecules, molecular fragments or individual molecules interacting with their surroundings (*e. g.*, on a surface) are not uniquely defined, various local partitioning schemes have been developed. Unlike approaches based on atom-centered one-particle basis functions, such as the Mulliken [386] and Löwdin [387] population analysis, partitioning schemes of the charge density ρ are not highly sensitive to the basis set used in the electronic structure calculation [393, 414]. Commonly used methods based on real space are Voronoi [415], Bader’s Atoms-In-Molecules (AIM) [207, 416–420] and Hirshfeld [421] partitioning. Here, we will focus on Bader partitioning because several available postprocessing tools make it quite broadly applicable [209], although one may apply the following definition of dipole moments of atoms or groups of atoms to any method which defines atomic basins in three dimensional space. For more informations about Hirshfeld partitioning and a comparison between Hirshfeld and Bader charges for a large series of diatomic molecules see Refs. [422] and [423], respectively.

Beyond the general difficulty of local properties being arbitrarily defined, the simulation of local dipole effects is challenging since (1) modeling interfaces — in particular molecule–metal ones — is a difficult task for electronic-structure methods [294, 424], and (2) dipole moments of charged entities (such as local subsystems having a nonzero partial charge, which is usually the case) are dependent on the location of the Cartesian coordinate origin. As they are most relevant in the scientific context discussed above, we will discuss different ways of defining local dipole moments briefly for the case of a molecule (whose local dipole moment is of interest) adsorbed on a (*e. g.*, metallic) surface. A simple model for approximating individual molecular dipole moments is to subtract the charge density of the surface and to

integrate over the remaining charge density distribution [345]. However, this does not resolve the origin-dependence problem. Estimating the local dipole from a set of atomic charges is a rough approximation as it ignores dipolar contributions arising from the atomic polarizations. In simulations for periodic systems, maximally localized Wannier functions based on the Berry-phase approach are usually employed for calculating the local electronic dipole moments [405, 406]. Recently, subsystem DFT-based embedding approaches [407–410] as well as an approach using the Voronoi tessellation of the electron density [411, 412] for the calculation of local electric dipole moments for supramolecular (periodic) systems have been presented. These approaches are limited to non-covalently bound systems so far. According to the quantum theory of Atoms-In-Molecules, Bader and Matta presented another way of calculating local contributions to the molecular dipole moment using bond critical points (BCPs) [344, 413]. Based on this approach, Keith suggested to reformulate the atomic charges into so-called bond charges, thus creating additional dipolar terms [425] in order to cancel the origin dependent terms. In other words, origin-independence is achieved by using BCPs as references rather than an arbitrarily chosen origin. The need for bond critical points restricts this approach to subsystems/fragments which are chemically bound to the remainder of the system.

In general, the electric dipole moment $\boldsymbol{\mu}$ of a molecular or supramolecular system is defined as,

$$\boldsymbol{\mu} = - \int \mathbf{r} \rho(\mathbf{r}) d\mathbf{r} + \sum_A Z_A \mathbf{X}_A, \quad (4.3)$$

where \mathbf{r} represents a vector describing any point in space, Z_A the nuclear charge, \mathbf{X}_A the nuclear coordinate of atom A and ρ the electron density. Within the AIM theory, a total property P such as the charge, dipole moment, multipole moment or energy, is equal to the sum of atomic contributions to that property, $P = \sum_A P_A$ [207]. Therefore, the dipole moment of a system can be expressed as a sum of atomic dipole moments,

$$\boldsymbol{\mu} = \sum_A \boldsymbol{\mu}_A = \sum_A \left[- \int_A \mathbf{r} \rho(\mathbf{r}) d\mathbf{r} + Z_A \mathbf{X}_A \right], \quad (4.4)$$

where the integrals are taken over the atomic basins. These local dipole moments will depend on the choice of origin if local subsystems are (partially) charged, as is generally the case. By introducing coordinates relative to the atomic nuclear coordinates in each of these integrals, $\mathbf{r}_A = \mathbf{r} - \mathbf{X}_A$, we can rewrite Eq. (4.4) as

$$\begin{aligned} \boldsymbol{\mu} &= \sum_A \left[- \int_A (\mathbf{r}_A + \mathbf{X}_A) \rho(\mathbf{r}) d\mathbf{r} + Z_A \mathbf{X}_A \right] \\ &= \sum_A \left[- \int_A \mathbf{r}_A \rho(\mathbf{r}) d\mathbf{r} + \left(Z_A - \int_A \rho(\mathbf{r}) d\mathbf{r} \right) \mathbf{X}_A \right]. \end{aligned} \quad (4.5)$$

Since the net charge of an atom A is $q_A = Z_A - N_A = Z_A - \int_A \rho(\mathbf{r})d\mathbf{r}$, N_A being the electron population of atom A , the second term in Eq. (4.5) can be expressed as

$$\boldsymbol{\mu} = \sum_A \left[- \int_A \mathbf{r}_A \rho(\mathbf{r})d\mathbf{r} + q_A \mathbf{X}_A \right] \quad (4.6)$$

The first term in parentheses represents the atomic polarization contribution $\underline{\boldsymbol{\mu}}_A^p$ and the second term, $\underline{\boldsymbol{\mu}}_A^c$, results from the transfer of electronic charge between the atoms. Note that origin-dependent terms are underlined. Thus, the total dipole moment is given by the sum of a polarization $\boldsymbol{\mu}^p$ and a charge transfer $\boldsymbol{\mu}^c$ contribution [413,425],

$$\boldsymbol{\mu} = \sum_A \left[\underline{\boldsymbol{\mu}}_A^p + \underline{\boldsymbol{\mu}}_A^c \right] = \boldsymbol{\mu}^p + \boldsymbol{\mu}^c. \quad (4.7)$$

Both terms are important in the description of a molecular dipole moment [426]. In order to overcome the origin-dependence of the charge transfer term, Keith [425] suggested to reformulate the atomic charges q_A in terms of bond charges $q(A|B)$,

$$q_A = \sum_B q(A|B), \quad (4.8)$$

where the sum runs only over atoms B sharing an interatomic surface with atom A . Each bond charge is the negative of the one corresponding to charge transfer in the opposite direction,

$$q(A|B) = -q(B|A). \quad (4.9)$$

Furthermore, for each atom A which belongs to a ring, the sum of bond charges within the ring must be equal to zero,

$$\sum_{A \in \text{ring}} q(A|A+1) = 0. \quad (4.10)$$

Using Eqs. (4.8), (4.9), and (4.10), we get a set of $N_{\text{Atoms}} + N_{\text{BCP}} + N_{\text{RCP}}$ linearly independent equations which determine the bond charges. N_{Atoms} , N_{BCP} , and N_{RCP} denote the number of atoms, bond critical points (BCPs) and ring critical points (RCPs), respectively. Note that we need to subtract one redundant equation in order to account for a neutral system ($q = 0$) and one redundant Eq. (4.10) for each cage critical point (CCP) from the number of independent equations [207], $N_{\text{Atoms}} + N_{\text{BCP}} + N_{\text{RCP}} - N_{\text{CCP}} - 1$. The charge transfer term can then be written as,

$$\boldsymbol{\mu}^c = \sum_A \mathbf{X}_A q_A = \sum_A \left[\mathbf{X}_A \sum_B q(A|B) \right]. \quad (4.11)$$

² $\boldsymbol{\mu}^c$ is called a charge transfer term in the literature, even though it may contain no explicit expression for charge transfer between atoms. However, for a neutral system, the partial charges contributing to this simplest formulation of $\boldsymbol{\mu}^c$ are indeed resulting from charge transfer (or "charge rearrangement") within the molecule.

If we now reformulate the nuclear coordinates with respect to BCPs $\mathbf{X}^c(A|B)$ between atoms A and B , $\mathbf{X}_A = \sum_B [\mathbf{X}_A - \mathbf{X}^c(A|B)] + \sum_B \mathbf{X}^c(A|B)$, the origin-dependent term of the charge transfer contribution disappears [403, 404],

$$\boldsymbol{\mu}^c = \underbrace{\sum_A \sum_B [\mathbf{X}_A - \mathbf{X}^c(A|B)] q(A|B)}_{\boldsymbol{\mu}_A^c} + \underbrace{\sum_A \sum_B \mathbf{X}^c(A|B) q(A|B)}_{=0, \text{ since } q(A|B) = -q(B|A) \text{ and } \mathbf{X}^c(A|B) = \mathbf{X}^c(B|A)} \quad (4.12)$$

Thus, the origin-independent atomic dipole moment of atom A can be defined as,

$$\boldsymbol{\mu}_A = [\boldsymbol{\mu}_A^p + \boldsymbol{\mu}_A^c] = \boldsymbol{\mu}_A^p + \sum_B [\mathbf{X}_A - \mathbf{X}^c(A|B)] q(A|B), \quad (4.13)$$

which is implemented in the program POLABER [384]. Note that in POLABER, a bond weighting factor (reciprocal bond strengths) is assigned to the bond charge in Eq. (4.10) to counteract any unrealistic changes in the intramolecular and intermolecular bond paths.

As discussed above, we are often interested in the dipole moment of a group of atoms (molecular fragment F). The fragment dipole moment can be expressed as

$$\boldsymbol{\mu}_F = \sum_{A \in F} \boldsymbol{\mu}_A = \sum_{A \in F} \left\{ \boldsymbol{\mu}_A^p + \sum_B [\mathbf{X}_A - \mathbf{X}^c(A|B)] q(A|B) \right\}. \quad (4.14)$$

Commonly used implementations of the Bader partitioning schemes provide atomic properties, such as atomic charges and polarizations. In order to obtain the bond charges $q(A|B)$ in Eq. (4.14), an explicit critical point (CP) search is needed – a feature which is not implemented in some AIM codes for reasons of computational efficiency [427–429], and which may not be available at all when a different local partitioning scheme is employed or when nonbonded fragments are studied.

4.3. Derivation of a generalized approach to calculate local dipole moments

In this section, we present an alternative way of calculating fragment dipole moments that requires only specific bond critical points (or more generally, internal reference points (IRPs) that need not be BCPs) between the fragment and the residual groups. Our approach is inspired by Bader and Laidig’s exemplary presentation of calculating the charge transfer contribution of methyl and methylen groups [404]. Based on these examples, a derivation of a general description for fragment dipole moments is provided in Section B.3 in the Appendix. However, their approach requires critical points as well for achieving origin-independence, and it is necessary

to define a fragment atom which shares an interatomic surface with the residual group. The latter is usually not well defined for systems that are partitioned into more than two fragments unless all residual groups are bonded to one fragment atom.

Here, we focus on calculating fragment dipole moments without the need for a previous critical point search, and tailored towards systems where an arbitrary number and arrangement of residual groups calls for a flexible choice of internal reference points (IRPs) [430]. A schematic representation of partitioning a system into a fragment and residual groups is given in Figure 4.4.

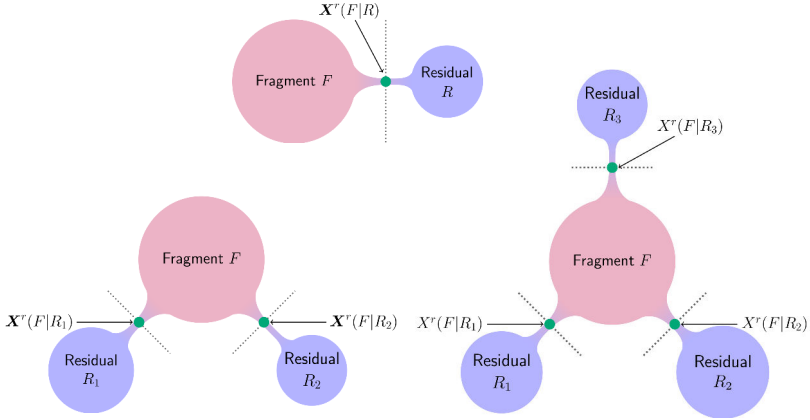


Figure 4.4.: Partitioning of a system into subsystems, namely fragment F and one or more residual group(s) R . The internal reference point $\mathbf{X}^r(F|R)$ connecting the subsystems is indicated as a green dot.

First, the charge transfer contribution is divided into fragment F and n residual group R_i contributions (with $i = 1, 2, \dots, n$),

$$\boldsymbol{\mu}^c = \sum_A \mathbf{X}_A q_A = \sum_{A \in F} \mathbf{X}_A q_A + \sum_{i=1}^n \sum_{A \in R_i} \mathbf{X}_A q_A. \quad (4.15)$$

All nuclear coordinates \mathbf{X}_A are reformulated with respect to an internal reference point between the fragment F and the respective residual groups R_i , $\mathbf{X}^r(F|R_i)$,

$$\begin{aligned} \boldsymbol{\mu}^c &= \sum_{A \in F} [\mathbf{X}_A - \mathbf{X}^r(F|R_n)] q_A + \mathbf{X}^r(F|R_n) q_F + \sum_{i=1}^n \mathbf{X}^r(F|R_i) q_{R_i} \\ &+ \sum_{i=1}^n \sum_{A \in R_i} [\mathbf{X}_A - \mathbf{X}^r(F|R_i)] q_A, \end{aligned} \quad (4.16)$$

In order to demonstrate that μ^c does not depend on the choice of the origin, we insert $q_F = -\sum_{i=1}^n q_{R_i}$,

$$\begin{aligned} \mu^c &= \sum_{A \in F} [\mathbf{X}_A - \mathbf{X}^r(F|R_n)] q_A + \sum_{i=1}^{n-1} [\mathbf{X}^r(F|R_i) - \mathbf{X}^r(F|R_n)] q_{R_i} \\ &+ \sum_{i=1}^n \sum_{A \in R_i} [\mathbf{X}_A - \mathbf{X}^r(F|R_i)] q_A. \end{aligned} \quad (4.17)$$

In Eq. (4.17), the second term is a difference between IRPs (Note that it vanishes if $i = n$) and, thus, origin-independent. If we define local dipole moments, this term either needs to be assigned to the fragment or to the residual contribution. Here, the former is used to get the following expression for the dipole moment of a fragment F ,

$$\mu_F = \sum_{A \in F} \mu_A^p + \sum_{A \in F} [\mathbf{X}_A - \mathbf{X}^r(F|R_n)] q_A + \sum_{i=1}^{n-1} [\mathbf{X}^r(F|R_i) - \mathbf{X}^r(F|R_n)] q_{R_i}. \quad (4.18)$$

The first term of the charge transfer contribution represents the intrafragment charge transfer and the second term represent the interfragment charge transfer. This expression of the fragment dipole moment is origin-independent, but it depends on the arbitrary numbering of the respective residual groups unless, of course, there is only one remainder. In practice, a different numbering of the residual groups (especially R_n) has a rather small effect on the fragment dipole moments [208]) and, moreover, in nanoscience applications, we often only have to deal with two subsystems (e.g. adsorbate and surface or adsorbate and nanotubes).

4.4. Implementation in GenLocDip

Having developed a generalized approach to for calculating local electric dipole moments for fragments of (supra)molecular systems, we are now going to present the main steps implemented in the program GENLOCIP (available online at https://www.chemie.uni-hamburg.de/ac/herrmann/software/genlocdip_e.html), followed by benchmark calculations on small isolated and intramolecular systems. This includes a study on how the fragment dipole moment depends on the internal reference points and on the numbering of the residual groups, and how it compares with previous local dipole definitions from the literature. Furthermore, an example for a non-covalently bonded molecule–surface system is given to demonstrate the capabilities of the program.

Two different technical approaches for Bader partitioning are available: A wavefunction approach (based on wavefunction files, e.g. files containing the molecular

orbital coefficients of a Kohn–Sham or Hartree–Fock Slater determinant) and an electronic-density-on-a-grid approach (often based on so-called cube files). Using the wavefunction approach, the gradient of the charge density with respect to Cartesian coordinates \mathbf{r} can be calculated from derivatives of an analytic wavefunction (implemented in early AIM programs, e.g. AIMPAC [431–433]). First, the algorithm finds stationary points (hereinafter referred to as critical points) in the charge density by following trajectories along the density gradient until the path terminates at a nucleus where the electron density exhibits its local maximum. Gradient paths originate at saddle points or local minima, for example between atom pairs which are connected by a chemical bond (bond critical points). Within the theory [207, 420], an atom is defined as an open system bounded by interatomic surfaces which cannot be crossed by any trajectories in applying the zero flux condition, $\nabla\rho(\mathbf{r}) \cdot \mathbf{n} = 0$, \mathbf{n} being the unit vector perpendicular to the dividing surface. Thus, integrating over volumes assigned to individual atoms (atomic basins) yields atomic charges or well-defined atomic energies. However, it has been criticized [422, 428, 434] that the method is computationally expensive and not robust enough to be applied to large molecules or to complex bonding geometries. Instead of explicitly representing the interatomic surfaces, the grid-based approach assigns each volume element of the system to an atomic volume by tracing an approximate electron density gradient vector trajectory from the center of the volume element back to an atomic nucleus, and assigns the volume element to that atom [427]. Since the most time-consuming step (searching for critical points) is bypassed, this approach is well suited for large solid-state physical systems and for plane-wave based DFT calculations. The computational time depends only on the size of the three-dimensional grid used to represent the electron density, and scales linearly with the total number of grid points [427]. The accuracy of the method depends on the grid spacing, hence it is necessary to check for convergence. An overview of different software packages available for the analysis of the electron density according to the theory of AIM is given in Table B.1 in Section B.3 of the Appendix.

The starting point of GENLOC-DIP [209] is the electron density which can be generated from a Kohn–Sham determinant in a DFT calculation [435]. In general, the following steps are necessary:

1. Perform an electronic structure calculation using software such as GAUSSIAN [371], TURBOMOLE [436] or QUANTUM ESPRESSO [437].
2. Generate a wavefunction (`.wfn/.wfx`), a formatted checkpoint (`.fchk`) or a density-on-a-grid (`.cube`) file.
3. Run a local dipole calculation by typing `localdip` and choose an AIM program which will be started automatically (GENLOC-DIP currently interfaces to AIMALL [438], MULTIWFN [439] and BADER [427]).

4. The relevant information from the AIM analysis is extracted: Cartesian atomic coordinates \mathbf{X}_A , partial charges q_A and atomic polarizations $\boldsymbol{\mu}_A^p$.
If a wavefunction-based AIM program is selected, coordinates of the BCPs, RCPs and CCPs are read as well and the bond charges $q(A|B)$ are calculated numerically. Furthermore, the atomic dipole moments $\boldsymbol{\mu}_A$ are calculated using Eq. (4.14), with the fragment F being a single atom A .
5. The molecular system is partitioned into subsystems based on the user input (see Sec. B.3 of the Appendix for examples of GENLOCDIP prompts and user response).
6. Choose an option to define the internal reference point(s) (IRPs) between the fragment and the residual group(s). Available options are shown in Table 4.1.

Table 4.1.: Different options to choose an IRP between a fragment and a residual group.

Keyword	Description
<code>man X Y Z atomF atomR</code>	<code>man</code> : manually type in IRP coordinates between fragment and residual group <code>X,Y,Z</code> : coordinates of the IRP (in Bohr) <code>atomF,atomR</code> : fragment and residual atom number
<code>sel BCPnum</code>	<code>sel</code> : select a BCP from a previous BCP search <code>BCPnum</code> : number of the BCP
<code>bond atomF atomR fac</code>	<code>bond</code> : guess an IRP between fragment and residual group along the bond of atom pairs <code>atomF,atomR</code> : fragment and residual atom number <code>fac</code> : shifting factor ($0 < \text{fac} < 1$), e.g. <code>fac = 0.5</code> corresponds to the midpoint of atom pairs
<code>aprx atomF atomR</code>	<code>aprx</code> : check which grid point of the Bader volume of the fragment is closest to <code>atomR</code> , and drop a perpendicular from this point to the straight line connecting <code>atomF</code> and <code>atomR</code> . <code>atomF,atomR</code> : fragment and residual atom number

7. A fragment dipole moment is calculated using Eq. (4.18).
8. An output file containing a summary of the calculation and a POVRAY input file illustrating the coordinates of the studied system, BCPs/IRPs between the fragment and residual groups, as well as the fragment dipole moment are written.

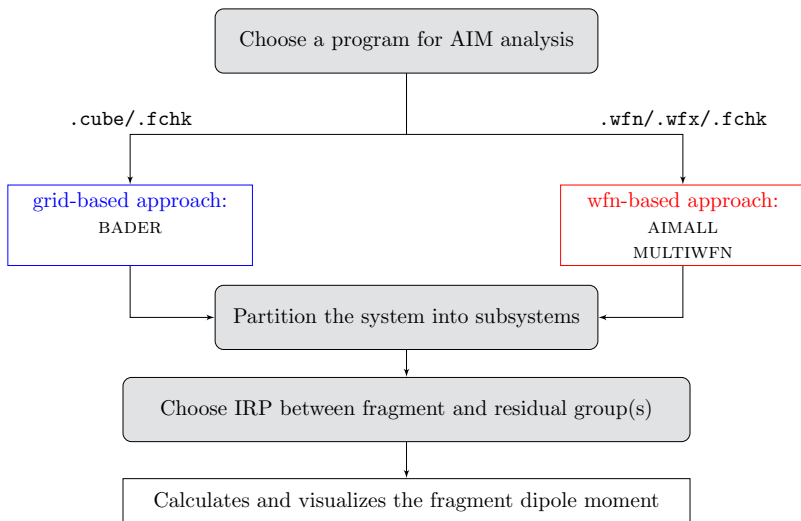


Figure 4.5.: Schematic picture of the main steps in a calculation of the fragment dipole moment using the program GENLOCDIP.

Figure 4.5 shows the main steps in a calculation of the fragment dipole moment as implemented in the GENLOCDIP code [209]. The code is written in FORTRAN90 and was compiled using the gfortran 4.8.2 compiler on an Ubuntu 14.4 operating system with eight 64-bit Intel Xeon CPUs. Furthermore, GENLOCDIP has been successfully installed on a 64-bit Mac OS X 10.7.5 system with a 2.0 GHz Intel Core i7 processor using gfortran 4.6.2. In principle, it can be installed on any machine with access to an FORTRAN compiler (and POVRAY if a graphical representation is desired).

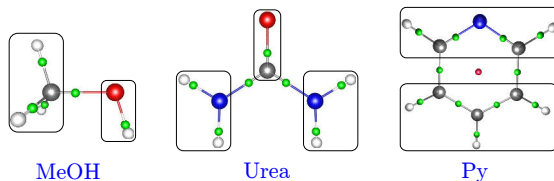


Figure 4.6.: Optimized structures of methanol (MeOH), urea and pyridine (Py) using G09(BP86)/TZVP. The bond critical points were calculated using AIMALL and are marked as green dots. The molecules are partitioned into the framed fragments.

We start with calculations on isolated molecules of methanol, urea and pyridine. The first two molecules were chosen based on the examples given in the FRAGDIP

(methanol) and the POLABER (urea) manual, and pyridine as an example for an aromatic molecule (containing a ring critical point). The optimized structures are shown in Fig. 4.6 and partitioned into fragments as illustrated. A comparison of the total dipole moment with the fragment sums ($\mu = \sum_F \mu_F$, where μ_F is defined by Eq. (4.18)) using different electronic-structure and AIM programs is shown in the graphs below. Figure 4.7 shows the results obtained using wavefunction-based AIM methods. It is evident that the summed-up fragment dipoles obtained using TURBOMOLE 6.6 (TM6.6) deviate strongly from the reference values. This happens when wavefunction files fail the normalization check of AIMALL [438] (which according to AIMALL output may be due to an “orientation inconsistency”). The dipole moments obtained using GAUSSIAN 09 (G09) in combination with the two AIM programs investigated, however, are quite good ($< 3\%$). Although the errors using MULTIWFN do not differ significantly from those using AIMALL, care must be taken when using MULTIWFN because it is sometimes difficult to find all critical points, especially for complex systems.

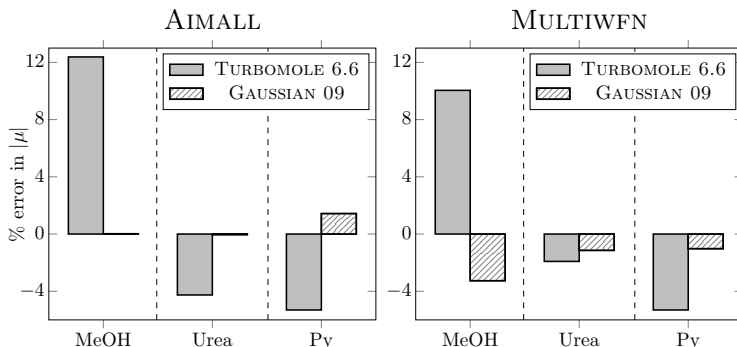


Figure 4.7.: Deviation of the total dipole moment from the fragment sums $\mu = \sum_F \mu_F$ (where μ_F is defined by Eq. (4.18)) in % for isolated test systems using different quantum chemical electronic structure packages and wavefunction-based AIM programs and choosing the `se1` option in order to set the IRP.

The results obtained using the grid-based program BADER are plotted in Figure 4.8. Again, the errors obtained using TM are huge, at least for small grid sizes³. This is due to the fact that already the fragment charges differ heavily (see Sec. B.3, Fig. B.6 in the Appendix). However, the accuracy of the TM dipoles scales nearly linearly with the total number of grid points leading to results that are sufficiently well

³Note that the default setting in TM represents a grid spacing of 0.02 Bohr, which shows a deviation of up to 10 % in Figure 4.8.

converged, which applies also to G09 and QUANTUM ESPRESSO 5.0 (QE5.0). It should be stressed that the errors reported in Figures 4.7 and 4.8 indicate that care should be taken to prevent numerical issues on the level of electronic structure and AIM programs, and does not indicate a failure of the GENLOCDIP program.

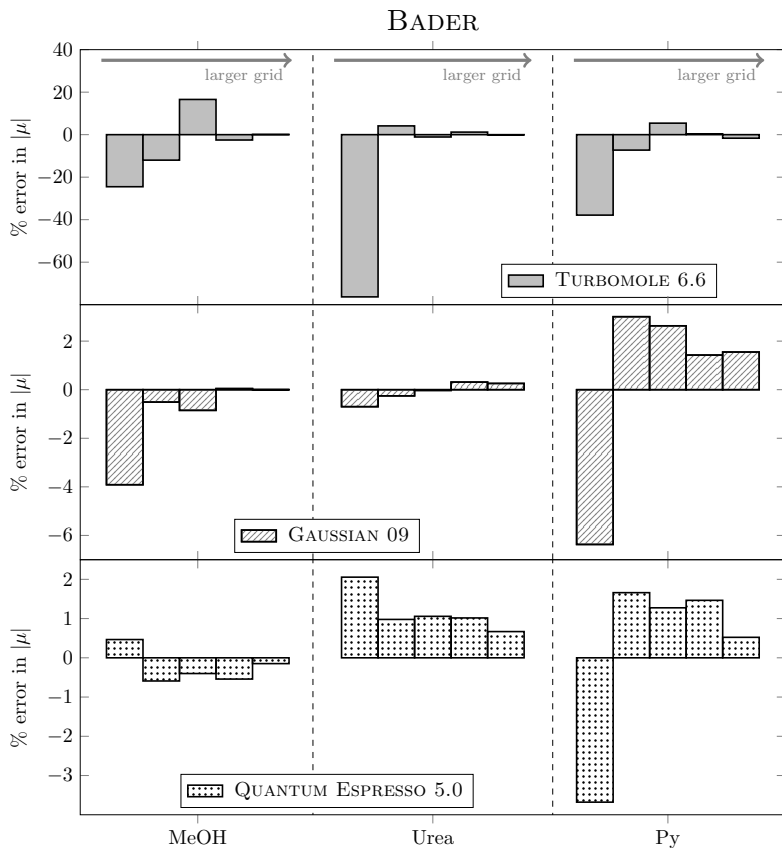


Figure 4.8.: Deviation of the total dipole moment from the fragment sums $\mu = \sum_F \mu_F$ (where μ_F is defined by Eq. (4.18)) in % for isolated test systems using different quantum chemical electronic structure packages in combination with a grid-based AIM program and choosing the `aprx` option in order to set the IRP. Each volume element of the grid is 0.30, 0.20, 0.15, 0.10, and 0.05 Bohr wide (from left to right).

In order to illustrate the influence of intermolecular interactions, we will first consider two water molecules with different intermolecular distances. The left panel of Fig. 4.9 shows water dimers interacting through a $\text{H}\cdots\text{O}$ hydrogen bond. The dipole of one water molecule induces a change in the dipoles of the nearby water molecule, thus, both water molecules are polarized. If the distance between the two water molecules is sufficiently large, no BCP can be determined as shown in the right panel of Fig. 4.9. In such a case, wavefunction-based AIM programs fail because the Poincaré–Hopf relationship [207], which states that $N_{\text{Atoms}} - N_{\text{BCP}} + N_{\text{RCP}} - N_{\text{CCP}} - 1 = 1$, can not be met (and the bond charges are not defined). Therefore, the dipole moment of each H_2O was calculated using the grid-based method as implemented in the BADER program in combination with IRPs (defined as the midway between both oxygen atoms) leading to magnitudes of the local dipole moments that are approximately the same for both molecules.

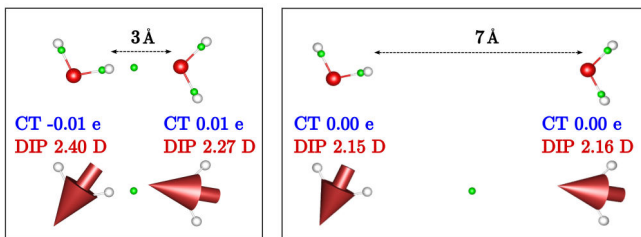


Figure 4.9.: Left: Two optimized water molecules using G09(BP86-D3(BJ))/TZVP separated by a small distance ($d(\text{O1-O2}) = 3 \text{ \AA}$). AIM analysis was performed using AIMALL. The respective water dipole moment was calculated with respect to the intermolecular BCP as IRP. Right: Single point calculation using G09(BP86-D3(BJ))/TZVP of two water molecules separated by a large distance ($d(\text{O1-O2}) = 7 \text{ \AA}$). AIM analysis has been performed using BADER. The IRP was set midway between both water molecules. The total dipole moment of an isolated water molecule with the same settings is $\mu^{\text{tot}}(\text{H}_2\text{O}) = 2.13 \text{ D}$. Local dipole moments were evaluated according to Eq. (4.18).

Dependence on the choice of internal reference point

Figure 4.10 shows that several critical points are found between pyridine and benzene and that the fragment dipole moment (at least for noncovalent molecular interactions) is not highly sensitive to which BCP (RCP) was chosen as an IRP.

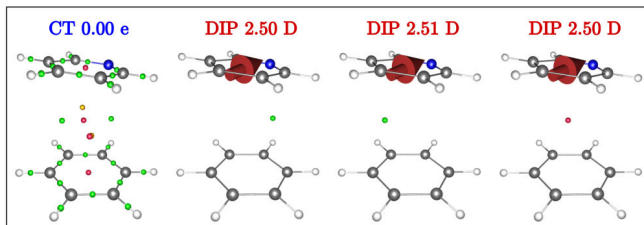


Figure 4.10.: Optimized structures of a benzene stacked with pyridine in a parallel offset conformation using G09(BP86-D3(BJ))/TZVP separated by an interplane distance of $d_{\text{plane}} = 3 \text{ \AA}$. AIM analysis has been performed using AIMALL. The pyridine dipole moments were calculated with respect to three different bond (ring) critical points as IRPs. The total dipole moment of an isolated pyridine molecule with the same settings is $\mu^{\text{tot}}(\text{pyridine}) = 2.28 \text{ D}$. Local dipole moments were evaluated according to Eq. (4.18).

Dependence on the numbering of the residual groups

Figure 4.11 shows the dependence on the arbitrary numbering of the respective residual groups of the fragment dipole moment (as implemented in the program GENLOC DIP) for methanol. For the partitioning examples considered here, a different numbering of the residual groups produces an error in the range of 0.05 – 0.15% of the value of the fragment dipole moments compared to the summed-up atomic dipole moments in the fragment.

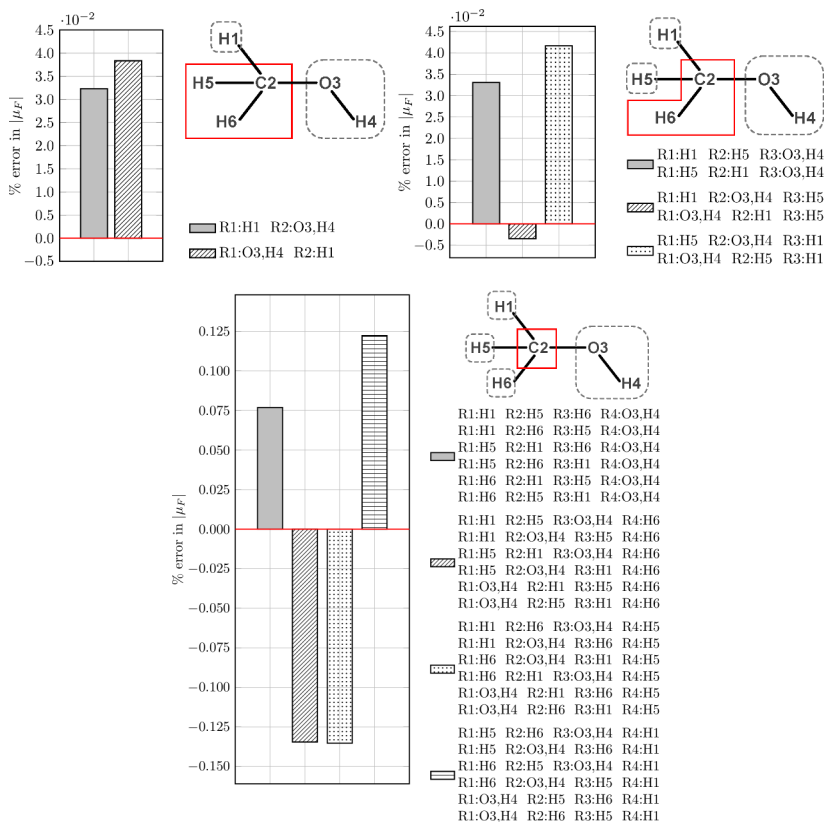


Figure 4.11.: Comparison of the fragment dipole moment calculated using GENLOC DIP with the summed-up atomic dipole moments in the fragment (% error in $|\mu_F|$) for methanol. Settings: G09(BP86-D3(BJ))/def-TZVP in combination with AIMAll. Local dipole moments were evaluated according to Eq. (4.18).

A comparison with fragment dipole definitions in the literature

In the following, we will compare our approach with different definitions of the fragment dipole moment which can be found in the literature (see Table 4.2). As we have mentioned in the beginning of Section 4.3, one can derive a more general expression from the examples provided in Refs. [404] and [403] (see Sec. B.3 in the Appendix for details). Starting from Eq. (4.15), we reformulate all nuclear coordinates \mathbf{X}_A that correspond to the fragment and residual contribution, with respect to an atom A^R and bond critical points between F and R_i ,

$$\begin{aligned} \boldsymbol{\mu}^c = & \sum_{A \neq A^R \in F} \left[\mathbf{X}_A - \mathbf{X}(A^R) \right] q_A + \mathbf{X}(A^R) q_F + \sum_{i=1}^n \mathbf{X}^c(F|R_i) q_{R_i} \\ & + \sum_{i=1}^n \sum_{A \in R_i} \left[\mathbf{X}_A - \mathbf{X}^c(F|R_i) \right] q_A, \end{aligned} \quad (4.19)$$

where $\mathbf{X}(A^R)$ indicates the nuclear coordinate of an atom A which has a common interatomic surface with the residual group(s) and q_{R_i} denotes the charge of the residual group i . Rewriting the third term with respect to $\mathbf{X}^r(F|R_n)$, then leads to

$$\begin{aligned} \boldsymbol{\mu}^c = & \sum_{A \neq A^R \in F} \left[\mathbf{X}_A - \mathbf{X}(A^R) \right] q_A + \mathbf{X}(A^R) q_F + \mathbf{X}^c(F|R_n) \sum_{i=1}^n q_{R_i} \\ & + \sum_{i=1}^{n-1} \left[\mathbf{X}^c(F|R_i) - \mathbf{X}^c(F|R_n) \right] q_{R_i} \\ & + \sum_{i=1}^n \sum_{A \in R_i} \left[\mathbf{X}_A - \mathbf{X}^c(F|R_i) \right] q_A. \end{aligned} \quad (4.20)$$

Inserting $q_F = -\sum_{i=1}^n q_{R_i}$ (as the system has neutral charge) into Eq. (4.20), results in an origin-independent expression for the charge transfer contribution,

$$\begin{aligned} \boldsymbol{\mu}^c = & \sum_{A \neq A^R \in F} \left[\mathbf{X}_A - \mathbf{X}(A^R) \right] q_A + \left[\mathbf{X}(A^R) - \mathbf{X}^c(F|R_n) \right] q_F \\ & + \sum_{i=1}^{n-1} \left[\mathbf{X}^c(F|R_i) - \mathbf{X}^c(F|R_n) \right] q_{R_i} + \sum_{i=1}^n \sum_{A \in R_i} \left[\mathbf{X}_A - \mathbf{X}^c(F|R_i) \right] q_A. \end{aligned} \quad (4.21)$$

Finally, assigning the second term to the fragment contribution, we obtain a general definition of fragment dipole moments of which Eqs. (B.3) and (B.5) are special cases,

$$\begin{aligned} \boldsymbol{\mu}_F^c = & \sum_{A \neq A^R \in F} \left[\mathbf{X}_A - \mathbf{X}(A^R) \right] q_A + \left[\mathbf{X}(A^R) - \mathbf{X}^c(F|R_n) \right] q_F \\ & + \sum_{i=1}^{n-1} \left[\mathbf{X}^c(F|R_i) - \mathbf{X}^c(F|R_n) \right] q_{R_i}. \end{aligned} \quad (4.22)$$

In what follows, we demonstrate that Eq. (4.22) can be reformulated in such a way that $\mathbf{X}(A^R)$ vanishes and an equation results which is equivalent to our approach provided that BCPs are chosen as IRPs in the latter.

$$\begin{aligned}
 & \sum_{A \neq A^R \in F} \left[\mathbf{X}_A - \mathbf{X}(A^R) \right] q_A + \left[\mathbf{X}(A^R) - \mathbf{X}^c(F|R_n) \right] q_F \\
 = & \sum_{A \neq A^R \in F} \mathbf{X}_A q_A - \sum_{A \neq A^R \in F} \mathbf{X}(A^R) q_A + \mathbf{X}(A^R) q_F - \mathbf{X}^c(F|R_n) q_F \\
 = & \sum_{A \neq A^R \in F} \mathbf{X}_A q_A - \underbrace{\sum_{A \neq A^R \in F} \mathbf{X}(A^R) q_A + \sum_{A \in F} \mathbf{X}(A^R) q_A - \mathbf{X}^c(F|R_n) q_F}_{\mathbf{X}(A^R) q_{A^R}} \\
 = & \sum_{A \in F} \mathbf{X}_A q_A - \mathbf{X}^c(F|R_n) q_F = \sum_{A \in F} [\mathbf{X}_A - \mathbf{X}^c(F|R_n)] q_A \quad (4.23)
 \end{aligned}$$

From this follows that Eq. (4.22) equals Eq. (4.18) if the IRPs in Eq. (4.18) are defined as BCPs.

Table 4.2.: Calculated partial charges q_F (in unit charges), local dipole vectors $\boldsymbol{\mu}_F$ in three dimensions (x, y, z) and local dipole magnitudes $|\boldsymbol{\mu}_F|$ (in Debye) for methanol fragments (framed in red) using different definitions^a for the fragment dipole moment.

Equation	Fragment properties				
		2 subsystems.	3 subsystems.	4 subsystems.	5 subsystems.
	q_F	0.4611991	0.4257206	0.4193291	0.4129384
Eq. (4.14)	$\mu_F(x)$	0.1002744	0.2127758	0.1431273	0.0734792
	$\mu_F(y)$	-0.2192165	-0.1760974	-0.1133782	-0.0506587
	$\mu_F(z)$	-0.0001752	-0.0001739	0.1202053	-0.0001742
Eq. (4.18)	$ \boldsymbol{\mu}_F $	0.6127183	0.7020184	0.5556455	0.2268503
	$\mu_F(x)$	0.1002685	0.2127791	0.1431264	0.0734740
	$\mu_F(y)$	-0.2193552	-0.1762333	-0.1135103	-0.0507870
	$\mu_F(z)$	-0.0001752	-0.0001739	0.1202132	-0.0001742
	$ \boldsymbol{\mu}_F $	0.6130327	0.7022451	0.5558292	0.2270248

^a Note that when a fragment of interest is part of a ring (*i. e.*, a residual group is attached to it via two bonds), Eq. (4.14) has a natural advantage due to using bond charges. In Eqs. (4.22), one would need to decide for one of the two possible BCPs in that case. In our approach (Eq. (4.18)), rings can be treated if a suitable internal reference point is chosen.

Application to noncovalently bonded supramolecular systems

For the chiral-selective synthesis of single-walled carbon nanotubes (SWCNTs) using in-solution techniques, it is crucial to control and understand the effect of remaining water on the conductivity of a carbon nanotube. Experimental studies have obtained contradictory results [249, 440–442]. Recently, the long-range electron density redistribution effects of a single water molecule adsorbed on metallic and semi-conducting SWCNTs have been investigated theoretically using plane-wave based DFT [443]. Mostofi *et al.* have found that the charge transfer between SWCNT and water is negligible, which indicates that water has a rather weak effect on the conductivity of the nanotubes. Furthermore, they showed that the dipole moment of water induces a long-ranged polarization of the electronic charge density of the CNT which is strongly dependent of the orientation of the adsorbed water molecule.

In order to investigate how the dipole moment of the water molecule depends on the adsorption structure, we have calculated the dipole moment of a single water molecule adsorbed on a metallic (5,5) SWCNT using a plane-wave based method in combination with the BADER AIM program and GENLOCIP. Figure 4.12 shows different orientations of the water molecule and the obtained adsorbate dipole moments. Our results confirm that the Bader charge transfer between SWCNT and water is negligible. The magnitudes of the local dipole moments increases with larger orientation angles ($0^\circ < 45^\circ < 90^\circ < 180^\circ$).

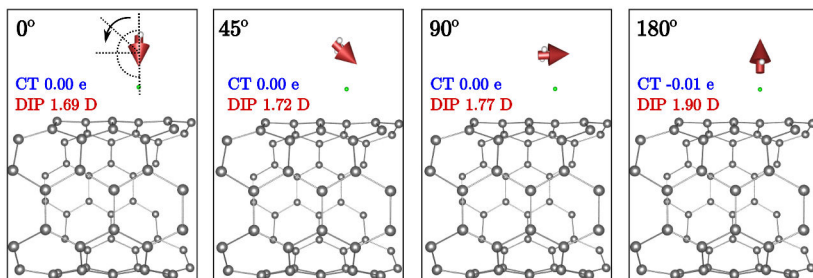


Figure 4.12.: Structures of water molecules adsorbed on a metallic (5,5) single-walled carbon nanotube with four different angles between the water C2 axis and the normal to the carbon nanotube surface (0° , 45° , 90° , and 180°). Single point calculations are done using QE5.0/PAW-PBE-D2. AIM analysis has been performed using BADER. The total dipole moment of an isolated H_2O molecule with the same settings is $\mu^{\text{tot}}(\text{H}_2\text{O}) = 1.81$ D. Local dipole moments were evaluated according to Eq. (4.18).

4.5. Effects of truncating a carbon nanotube on simulating adsorbate-induced property changes

Since the first reports on detecting gaseous molecules with individual single-walled carbon nanotubes⁴, published in 2000 [444, 445], the effect of adsorption on the conductivity of CNTs has been the subject of several experimental [446–450] and theoretical studies [451–459]. Kong *et al.* showed experimentally that a large shift of transistor characteristics towards lower gate voltages is caused by NH_3 adsorption, whereas NO_2 adsorption leads to a large shift towards higher gate voltages. However, the mechanism by which the transport properties of the nanotube is affected has been controversially discussed in the literature [448, 457, 460–463]. In this regard, there are several aspects that have to be taken into account. In transistors, the nanotube is contacted by (typically) metallic electrodes acting as a source and a drain [464]. Thus, gas adsorption may occur on the metal surface, on the nanotube surface, as well as at the interface between the nanotube and the metal contacts [59, 465]. In order to assess which of these adsorption mechanisms is responsible for the changes in the conductance, the transistor characteristics have been experimentally studied by selectively masking different parts of the device. However, the reported results are ambiguous depending on the passivation materials and environmental conditions used in the experiments. For instance, Bradley *et al.* proposed that NH_3 mainly adsorbs on the nanotube surface [466], while Zhang *et al.* had doubts about an on-tube adsorption mechanism. Based on the long response times and small current changes as a result of poly(methyl methacrylate) (PMMA)-passivated contacts, they rather assumed that adsorption takes place at the metal contacts [448]. This is consistent with studies using Si_3N_4 as the passivation material [467] and with investigations that cover the effect of the electrode material on NO_2 detection [468].

Theoretical studies have mainly focused on understanding the adsorbate–nanotube interactions within the channel region. Goldoni *et al.* attributed the process of NO_2 gas adsorption to a chemical reaction on the CNT surface forming NO_3 and NO [446, 447, 469]. Such a dissociative adsorption was supported by evidence of strong binding energies for NO_3 by Peng *et al.* [461], which were later challenged by Dai *et al.* [470, 471]. Furthermore, a charge transfer mechanism (NH_3 molecules acting as donors and NO_2 molecules acting as acceptors) has been considered by many theoretical studies [451–453, 472–474]. For NH_3 -CNT systems, however, very little or no charge transfer from the NH_3 to the tube has been observed [451–453, 459]. Electron transport calculations of NO_2 -CNT systems by Sadrzadeh *et al.* suggested that a strong electric dipole moment of the gas molecules might be responsible for

⁴Unless stated otherwise, “carbon nanotubes” always refers to single walled carbon nanotubes.

shifts in the conductance curve [457]. Moreover, the impact of NO_2 concentration on the transport characteristics has been studied [457], indicating that an increase of the NO_2 concentration leads to a shift of the density of states to lower energies. Recent investigations by Li *et al.* using a multiscale approach have provided new insights on the adsorption–conductance relation by explicitly taking the CNT–electrode interface into account [475]. They showed that NH_3 and NO_2 physisorb on the CNT and chemisorb at the contact region, while the latter is suggested to be the dominant mechanism affecting the conductance.

Given the – sometimes contradictory – statements in the literature and the broad range of calculated adsorption energies (0.01–1.80 eV) that have been reported for on-tube adsorption of NH_3 and NO_2 , we systematically compare structures, adsorption energies, local charges and dipole moments between a description under periodic boundary (PB) conditions and an approach using truncated nanotubes of two different lengths. Specifically, our goal is to evaluate whether the truncated model based on localized, atom-centered single-particle basis functions, whose advantages have been pointed out in Section 4.1, can yield data consistent with the periodic-boundary approach. We focus on NH_3 as an example of a “simple” physisorbed molecule and on NO_2 providing a more challenging test case due to its open-shell nature and its potential for chemisorption, on the basis of which the reliability of the truncated approach can be evaluated.

Adsorption energies and structures of NH_3 and NO_2 on CNTs

Since several reports on the adsorption mechanism of NH_3 and NO_2 on CNTs showed that the binding energy is quite insensitive to the orientation with respect to the tube surface [451, 453, 461] (within a given method), only one orientation of the attached molecule was studied here (see Figure 4.13). At the beginning of each structure relaxation, the respective adsorbate is placed in an upright position on top of a carbon atom. Considering the adsorption configuration, the NO_2 molecule stays perpendicular to the CNT surface (with the oxygen atoms pointing away from it). The NH_3 molecule is adsorbed such that the hydrogen atoms are pointing towards the nanotube. Structural and local properties are given in Table 4.3 and 4.4 for NH_3 and NO_2 adsorption, respectively. Further figures of optimized adsorption structures using PBE-D2 are provided in Sec. B.4 of the Appendix. Both – NO_2 and NH_3 – molecules adsorb with the nitrogen on top of a carbon atom in an upright orientation using the PB approach when including (see Figure 4.13a) or not including dispersion correction. If not explicitly mentioned, the following refers to calculations including dispersion correction (using the D2 and D3 versions of Grimme’s empirical approach [198, 476]).

Table 4.3.: N–H and N–C distance d (in Å), H–N–H angle θ (in °), adsorption energy E_a (in eV), AIM partial charge q_{NH_3} (in unit charges) and local dipole moment μ_{NH_3} (in Debye) of a NH_3 molecule on a single-walled CNT using a periodic-boundary (PB) code and a truncated approach (Basis set: def-TZVP) with different tube lengths (short: 8 Å and long: 19 Å). The preferred adsorption sites: T (top of a carbon atom), H (center of a carbon hexagon), and B (center of C–C bond) and orientations: \uparrow (upright) and \nearrow (tilted) are indicated by arrows.

	Method	Functional	Position	$d_{\text{N-H}}$	$d_{\text{N-C}}$	θ	E_a	q_{NH_3}	μ_{NH_3}
metallic (5,5) CNT	PB	PBE	T \uparrow	1.02	3.90	106.4	0.00	0.00	1.55
		PBE-D2	T \uparrow	1.02	3.38	105.8	-0.08	0.00	1.69
	Trunc. (short)	PBE-D2	H \nearrow	1.02	3.33	105.7	-0.18	0.02	1.82
		PBE-D3	T \nearrow	1.02	3.53	105.9	-0.15	-0.02	2.05
	Trunc. (long)	BP86-D3	B \uparrow	1.02	3.40	105.6	-0.15	0.00	1.92
		B3LYP-D3	T \nearrow	1.01	3.52	106.7	-0.13	0.00	1.91
		PBE-D2	T \uparrow	1.02	3.41	105.9	-0.13	-0.03	2.10
		PBE-D3	T \uparrow	1.02	3.49	106.0	-0.13	0.01	1.78
		BP86-D3	T \uparrow	1.02	3.41	105.9	-0.14	-0.02	2.04
		B3LYP-D3	T \uparrow	1.01	3.52	106.9	-0.12	-0.02	2.02
semi-conducting (8,0) CNT	PB	PBE	T \uparrow	1.02	3.92	106.4	0.00	0.00	1.54
		PBE-D2	T \uparrow	1.02	3.23	106.0	-0.07	0.00	1.69
	Trunc. (short)	PBE-D2	H \nearrow	1.02	3.38	106.1	-0.17	-0.01	1.98
		PBE-D3	H \nearrow	1.02	3.50	106.2	-0.16	0.01	1.77
	Trunc. (long)	BP86-D3	H \nearrow	1.02	3.45	106.0	-0.33	0.00	1.89
		B3LYP-D3	H \nearrow	1.02	3.53	107.1	-0.30	-0.02	1.96
		PBE-D2	H \uparrow	1.02	2.97	106.0	-0.16	0.01	1.83
		PBE-D3	H \uparrow	1.02	3.11	106.2	-0.16	0.00	1.84
		BP86-D3	T \uparrow	1.02	3.34	106.0	-0.13	0.00	1.90
		B3LYP-D3	T \uparrow	1.01	3.41	106.9	-0.22	0.01	1.79
isolated NH_3	PB	PBE	- -	1.02	-	106.4	-	0.00	1.49
		PBE-D2	- -	1.02	-	106.5	-	0.00	1.48
	Trunc.	PBE-D2	- -	1.02	-	107.1	-	0.00	1.75
		PBE-D3	- -	1.02	-	107.0	-	0.00	1.76
		BP86-D3	- -	1.02	-	107.1	-	0.00	1.76
		B3LYP-D3	- -	1.01	-	107.8	-	0.00	1.74

Table 4.4.: N–O and N–C distance d (in Å), O–N–O angle θ (in °), adsorption energy E_a (in eV), AIM partial charge q_{NO_2} (in unit charges) and local dipole moment μ_{NO_2} (in Debye) of a NO_2 molecule on a single-walled CNT using a periodic-boundary (PB) code and a truncated approach (Basis set: def-TZVP) with different tube lengths (short: 8 Å and long: 19 Å). The preferred adsorption sites: T (top of a carbon atom), H (center of a carbon hexagon), and B (center of C–C bond) and orientations: \uparrow (upright) and \nearrow (tilted) are indicated by arrows.

	Method	Functional	Position	$d_{\text{N-O}}$	$d_{\text{N-C}}$	θ	E_a	q_{NO_2}	μ_{NO_2}	
metallic (5,5) CNT	PB	PBE	T	\uparrow	1.22	3.30	129.4	-0.43	-0.21	2.16
		PBE-D2	T	\uparrow	1.22	2.96	129.2	-0.53	-0.22	2.16
	Trunc. (short)	PBE-D2	T	\nearrow	1.22	2.97	129.1	-0.25	-0.25	2.39
		PBE-D3	T	\nearrow	1.22	2.99	129.1	-0.25	-0.21	1.98
	Trunc. (long)	BP86-D3	T	\nearrow	1.22	2.95	128.7	-0.27	-0.30	2.85
		B3LYP-D3	T	\nearrow	1.20	3.00	131.4	-0.18	-0.12	1.36
		PBE-D2	T	\nearrow	1.22	2.87	130.0	-0.20	-0.19	1.84
		PBE-D3	T	\nearrow	1.22	2.92	130.0	-0.20	-0.17	1.64
		BP86-D3	T	\nearrow	1.22	2.84	129.6	-0.22	-0.16	1.61
		B3LYP-D3 ^a	T	\nearrow	–	–	–	–	–	–
semi-conducting (8,0) CNT	PB	PBE	T	\uparrow	1.22	3.44	130.7	-0.08	-0.14	1.63
		PBE-D2	T	\uparrow	1.22	2.95	130.6	-0.17	-0.16	1.66
	Trunc. (short)	PBE-D2	T	\uparrow	1.23	1.58	126.4	-2.08	-0.42	3.35
		PBE-D3	T	\uparrow	1.23	1.58	126.4	-2.07	-0.41	3.22
	Trunc. (long)	BP86-D3	T	\uparrow	1.23	1.58	126.4	-2.08	-0.38	3.12
		B3LYP-D3	T	\uparrow	1.22	1.58	126.0	-2.71	-0.41	3.30
		PBE-D2	T	\uparrow	1.22	1.77	127.6	-0.74	-0.29	2.66
		PBE-D3	T	\uparrow	1.22	1.75	127.6	-0.71	-0.29	2.68
		BP86-D3	T	\uparrow	1.22	1.77	127.5	-0.77	-0.30	2.69
		B3LYP-D3	T	\uparrow	1.21	1.67	126.8	-1.64	-0.41	3.30
isolated NO_2	PB	PBE	–	–	1.21	–	134.1	–	0.00	0.27
		PBE-D2	–	–	1.21	–	134.1	–	0.00	0.27
	Trunc.	PBE-D2	–	–	1.21	–	133.9	–	0.00	0.21
		PBE-D3	–	–	1.21	–	133.9	–	0.00	0.21
		BP86-D3	–	–	1.21	–	133.8	–	0.00	0.21
		B3LYP-D3	–	–	1.19	–	134.3	–	0.00	0.31

^a The results of the B3LYP-D3 calculation are not shown due to convergence problems.

First, we focus on the results obtained using a plane-wave method under periodic boundary conditions. For NH_3 adsorption, the length of an N–H bond and the H–N–H angle near the nanotube has not changed compared with 1.02 Å and 106° for the isolated NH_3 molecule when optimized with the same computational settings. The adsorption energy calculated including dispersion correction is very small, independent of the electronic nature of the nanotube (metallic: -0.08 eV; semi-conducting: -0.07 eV). If Grimme’s D2 dispersion correction is not included in the calculations, there is no binding of the NH_3 to the nanotube at all.

For NO_2 adsorption, the length of an N–O bond is 1.22 Å, which is a little longer than for an isolated NO_2 molecule (1.21 Å). The O–N–O angle is around 130° and, thus, slightly smaller than for the isolated NO_2 molecule (134°). The adsorption energy calculated including dispersion correction for NO_2 on a metallic (5,5) CNT is stronger than for NH_3 and twice as high (-0.53 eV) as for their semi-conducting counterpart (-0.17 eV), which has also been observed in Ref. [309]. The interaction between the NO_2 molecule and the CNT is weaker if dispersion correction is not included in the calculations.

The truncated approach is considered next. For short truncated nanotube lengths, despite starting from the same initial structure, we obtain different adsorption sites (at the top of a carbon atom, at the center of a hexagon or at the center of a C–C bond) for NH_3 molecules on a metallic CNT depending on the functional and dispersion correction used. For NH_3 adsorption on a semi-conducting tube, NH_3 molecules adsorb at the center of the hexagon and they are slightly tilted to one side. For no functional or dispersion correction scheme (D2 or D3) the same adsorption structure as for the PB (PBE-D2) calculation is obtained for the short truncated nanotube. Extending the nanotubes’ lengths leads to NH_3 adsorption above a carbon atom in an upright orientation on a metallic and semi-conducting tube (except for the NH_3 –(8,0) CNT system using PBE), in agreement with the PBE-D2 PB calculation. For NH_3 , the structural parameters of the truncated model are in very good agreement with the PB approach. All adsorption energies are within the range of -0.12 to -0.33 eV, which is higher than the binding energies obtained using the PB model. This is in line with the frequently observed necessity to have sufficiently extended structures (e.g. through PB conditions and sufficiently thick slabs when modeling surfaces) for quantitative adsorption energies.

For both truncated metallic tube lengths, NO_2 molecules are adsorbed in top position, however, they are slightly tilted to one side (30°–40°) in contrast with the PB description. The binding energies are calculated to be between -0.16 and -0.33 eV, which is smaller than the energy obtained with the PB approach (-0.53 eV).

The optimized structures of NO_2 molecules on semi-conducting CNTs with different tube lengths is shown on the left hand side of Figure 4.13 (blue: 8 Å; red: 19 Å).

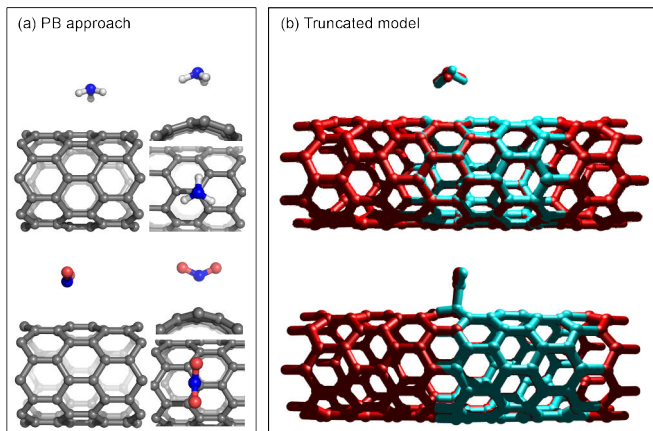


Figure 4.13.: Optimized structures of NH_3 (upper panel) and NO_2 (lower panel) adsorption on a semi-conducting (8,0) CNT using a PB model (left; PAW-PBE-D2) and a truncated approach (right; PBE-D2/def-TZVP) with two different tube lengths (blue: 8 Å; red: 19 Å).

In contrast to the proposed physisorption mechanism in the literature and to the relaxed structures using the PB approach (see right hand side of Figure 4.13), we obtain very short N–C distances for short and longer tube lengths (1.58 Å and 1.77 Å, respectively) and large binding energies in the range of chemisorption ($E_a \leq -0.80$ eV).

Thus, while NH_3 adsorption structures on CNTs can be described correctly by a truncated model provided that the tube is long enough, NO_2 adsorption structures cannot be predicted this way. This may be related to the NO_2 's capability of chemisorption, as opposed to the NH_3 being able to bind only through a physisorption mechanism. Adsorption energies, as expected, are not reliable when obtained from a truncated model up to the length considered here.

Changes in local properties due to adsorption

In Figure 4.14, the charge transfer between adsorbates and nanotubes and the adsorbates' dipole moments obtained from AIM analysis in combination with the PB approach are depicted. Additional Mulliken and Löwdin partial charges are provided in Table B.2 of Sec. B.4 in the Appendix. The calculated partial charges show fairly little charge transfer from the NH_3 to the nanotube in agreement with the literature [451–453, 459]. The local dipole moment of the NH_3 molecule does

not change for different tube chiralities (1.69 D) and is a little larger than the self-consistent field (SCF) dipole moment for an isolated NH_3 molecule (1.49 D to 1.73 D depending on the method).

For the NO_2 -CNT system, the total charge transfer from the metallic (semi-conducting) tube to the NO_2 molecule is 0.22 (0.16) unit charges for PBE-D2 under PB conditions. Thus, it can be deduced that NO_2 acts as an acceptor, which is in agreement with the density of states (see Fig. B.15 of Sec. B.4 in the Appendix). The NO_2 molecules' dipole moment increases strongly due to adsorption compared to the SCF dipole moment of an isolated molecule (0.2 D to 0.3 D). Furthermore, the local dipole moment of NO_2 on a metallic CNT is about 0.5 D larger than the one of NO_2 on a semi-conducting CNT (1.66 D).

The truncated approach also indicates that the charge transfer between NH_3 molecules and nanotubes is negligible. The NH_3 molecules' dipole moments are within the range of 1.77 – 2.10 D depending on the tube chirality and length, which is a little larger compared to the ones obtained with the PB approach. The PBE-D2 results for the shorter semi-conducting nanotube deviate more from the PB PBE-D2 data than the PBE-D2 values for the longer tube, but both are quite close to the PB data. Moreover, both truncated tube lengths indicate that the semi-conducting versus metallic nature of the tube barely affects the adsorbate dipoles, which suggests that these dipole moments may be interpreted qualitatively.

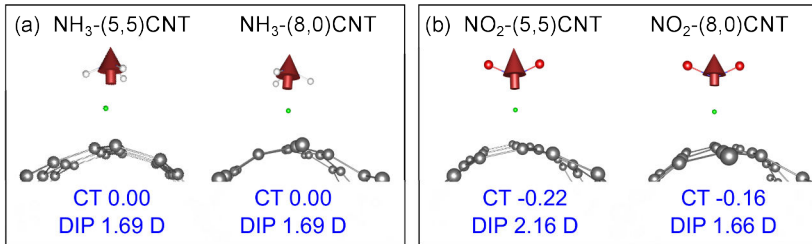


Figure 4.14.: Local dipole moments (in Debye) and charge transfer (in unit charges) of (a) NH_3 and (b) NO_2 molecules adsorbed on a metallic and a semi-conducting nanotube, respectively. Optimized structures were obtained using PAW-PBE(-D2) (PB approach). The dipole moment is indicated as a red arrow pointing towards the negatively charged part. Internal reference coordinates (marked as green dots) were used to determine the adsorbates' dipole moment within the theory of AIM.

The AIM analysis shows large charge transfer from the nanotube to the NO_2 molecule (about -0.20 unit charges) for NO_2 adsorption on truncated metallic

nanotubes and an even larger charge transfer (-0.30 to -0.42 unit charges) for semi-conducting nanotubes. In the latter case, these deviations from the PB description are a result of the strong binding of NO_2 to the truncated (8,0) CNT whereas for the metallic CNT, the deviations from the PB approach are small, indicating that tilting of the adsorbate does not influence its electronic structure significantly. This is consistent with the molecular orbital diagrams for the isolated subsystems (see Figs. B.17 and B.18 of Sec. B.4 in the Appendix) showing that the lowest unoccupied molecular orbital (LUMO) is energetically close to the HOMO-LUMO gap of the truncated carbon nanotube. The local dipole moment of NO_2 molecules on truncated (5,5) CNTs scatters between 1.36 D and 2.85 D, depending on the functional and the dispersion correction used, again showing reasonable agreement with the PB values for PBE-D2. On semi-conducting nanotubes, the NO_2 molecular dipole moment is calculated to be around 3.00 D, consistent with a large change in binding compared with the PB approach. This suggested that the dipole effect on the transistor characteristics is similar for both NO_2 and NH_3 adsorption. Thus, if we consider only on-tube adsorption, the changes in the conductance can be attributed to a dipolar mechanism (with the positive part of the dipole moment pointing towards the CNT). In case of NO_2 , an additional contribution occurs through charge transfer from the CNT to the NO_2 . However, as stated in Ref. [475], physisorption mediated adsorbate-CNT interactions have only a minor impact on changes in the conductance. Regardless of the chemical gating effect, we conclude that the length of metallic nanotubes can be fairly small (as this does not significantly affect the adsorption structure) when studying adsorbate-CNT interactions. Semi-conducting nanotubes on the other hand tend to be affected more severely by truncating the nanotube.

4.6. Noncovalent functionalization of carbon nanotubes by diarylethene photoswitches

One widely studied class of photochromic molecular switches are diarylethene (DAE) derivatives [118,120] which can undergo a ring-opening or a ring-closing reaction by illumination with ultra-violet ($\lambda < 400$ nm) or visible ($\lambda = 400 - 700$ nm) light, respectively (see Figure 4.15). The conjugation extends across the molecule in the closed form, whereas it is broken in the open form. In particular, cyclopentene-bridged DAE switches (lower panel of Fig. 4.15) with different substituents (e.g., halogens [120], pyridines [477], porphyrins [106], and ferrocenes [478,479]) or introduced into supramolecular systems [480,481], have been studied intensively in the literature over the past decades [482]. Recently, Steenbock *et al.* showed that the switching behavior of cyclohexene-bridged DAE switches (upper panel of Fig. 4.15) is comparable to the cyclopentene counterpart and that they offer the advantage of

allowing for chiral modification of the cyclohexene unit [483].

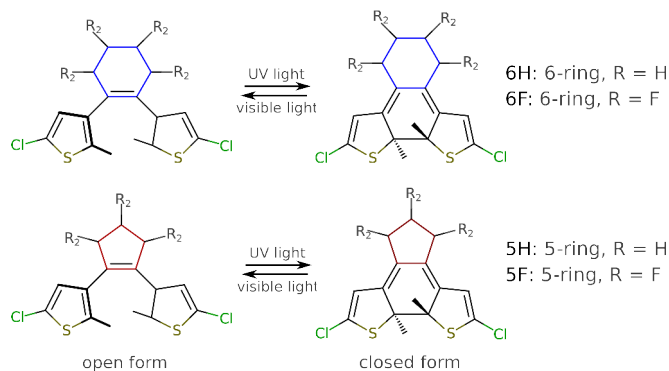


Figure 4.15.: Photoreactivity of dithienylcyclohexene (upper panel) and dithienylcyclopentene (lower panel) derivatives. By illumination with ultra-violet ($\lambda < 400$ nm) light the closed form is obtained and reversed to the open form under visible light ($\lambda = 400 - 700$ nm).

The overall length of DAE molecules does not change significantly during the isomerization process, which suggests that the mechanical freedom of conformational changes is preserved when sandwiched between electrodes. Inserting a DAE molecule in a molecular device would enable the switching between two conductance states: a high- (closed) and a low-conductance (open) state. The design of switchable devices typically requires an interface between molecules and metals, which is a rather difficult task since it is not self-evident that the molecule retains its functionality when attached to electrodes. Experimental studies showed that switching from the closed to the open state is irreversible for thiophene-substituted DAE molecules in a Au-DAE-Au junction [117, 122], presumably because of the strong covalent bond between sulfur and gold [484, 485]. Studies using CNTs as electrodes showed that DAE can only be converted from the open to the closed state [486–488] (contrary to what was observed for gold electrodes). In order to overcome the strong electronic coupling to the electrodes, the photoswitching behavior of DAE has been investigated using insulating spacers and/or other anchoring groups (e.g., pyridine, amide and pyrrole) [121, 486, 489–494]. However, decreasing the molecule–electrode coupling is often accompanied by a reduced closed (“on”) state conductivity [495]. In order to compensate poor conductivity, arrays of nanoparticles with connecting DAE switches have been used increasing the number of photoactive units [72, 496]. Another approach based on a single-walled carbon nanotube network and DAE polymers has been presented by Sciascia [497].

Recently, Wurl *et al.* investigated the non-covalent functionalization of single-walled carbon nanotubes with different DAE derivatives, namely 1,2-bis(5-chloro-2-methylthien-3-yl)cyclohexene (6H), 1,2-bis(5-chloro-2-methylthien-3-yl)cyclopentene (5H), and 1,2-bis(5-chloro-2-methylthien-3-yl)perfluorocyclopentene (5F) [498, 499], by means of current–voltage ($I - V_g$) measurements in a carbon nanotube field-effect transistor (CNTFET) configuration. They observed a shift in the transistor characteristics upon photoswitching the DAEs.

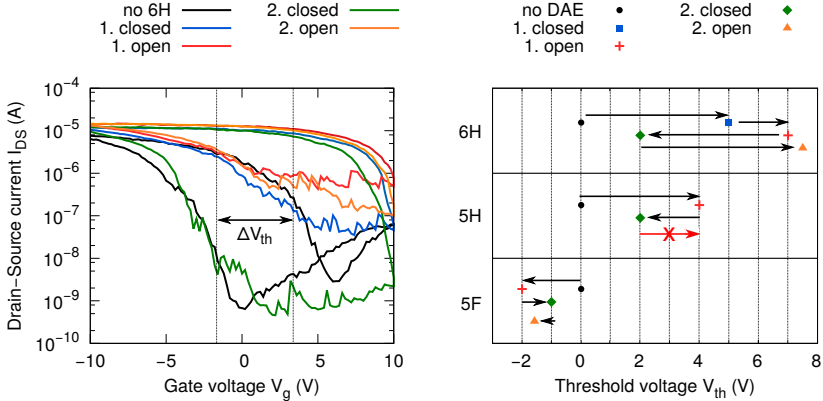


Figure 4.16.: *Left:* The transistor characteristics of a carbon nanotube field-effect transistor (CNTFET) at $V_{DS} = -1$ V before (black) and after incubation (blue) with the closed form of the 6H switch and after photoswitching from the closed to the open form (red). The first and second switching from the closed to the open form (respectively vice versa) of the DAEs are indicated by the numbers 1. and 2., respectively. The area between the dotted lines represents the shift of the threshold voltage ΔV_{th} due to the incubation of the closed form. *Right:* Schematic representation of the shifts in the threshold voltage for the systems under study. The shifts refer to the forward sweeps of the hysteresis, which may be regarded as more reproducible because no charges have been accumulated on the device yet (at least in the first iteration). Note that the pristine nanotube voltages have been shifted to zero for the sake of clarity.

The left panel of Figure 4.16 exemplarily shows the current I_{DS} as a function of the gate voltage V_g before and after functionalization with 6H using a drain–source voltage of $V_{DS} = -1$ V. The current–voltage forward and backward sweeps are not identical showing a typical hysteresis of CNTFETs attributed to charging and discharging of the system in the contact region. The shifts in the threshold

voltage⁵ (V_{th}) are schematically shown in the right panel of Figure 4.16. As can be seen, functionalization with (c)-6H (closed form) leads to a positive threshold shift ($\Delta V_{th} = +5$ V) compared to the pristine CNT. Under visible light, an additional shift of $\Delta V_{th} = +2$ V in the same direction is observed and attributed to a ring-opening process. The shifts due to irradiation with UV light ($\Delta V_{th} = -5$ V) and subsequent ring-opening ($\Delta V_{th} = +5.5$ V) demonstrate that the photocyclization of 6H is, to some extent, reversible. Functionalization with (o)-5H shows a positive shift of $\Delta V_{th} = +4$ V and closing the cyclopentene ring using UV light results in a subsequent negative shift ($\Delta V_{th} = -2$ V). In contrast to 6H, the photocyclization of 5H is irreversible since a subsequent ring-opening could not be achieved. In case of 5F, functionalization with the open form shows a negative shift of $\Delta V_{th} = -2$ V and ring-opening a positive shift ($\Delta V_{th} = +1$ V). A reversible photocyclization of the open form to the closed form was partly achieved as indicated by a slightly negative shift (-0.5 V). Thus, an opposite effect is observed for the perfluorinated DAE switch compared to the perhydrated ones as the ring-opening and ring-closing results in a negative and a positive shift, respectively.

For similar noncovalently functionalized CNTFETs, different mechanisms that explain the observed threshold shifts have been proposed in the literature, including a partial electron transfer to or from the nanotube [460, 466, 500, 501] and a change in the dipole moment concurrent with an isomerization process [141, 142, 380].

In order to determine the mechanism by which the DAE–nanotube interactions change the nanotube conductance, we studied the chemical gating effect of four DAE derivatives: 6H, 6F, 5H, and 5F (Fig. 4.15 illustrates the notation used). Table 4.5 summarizes the results obtained using a plane-wave periodic boundary (PB) DFT methodology. Mulliken and Löwdin partial charges, which are provided in Table B.3 of Sec. B.4 in the Appendix. Figure 4.17 and Figure 4.18 show the optimized structures of the perhydrated and perfluorinated DAE derivatives, respectively, on a (5,5) single-walled carbon nanotube with parallel (upper panel) and perpendicular (lower panel) orientation of the thiophene units with respect to the nanotube axis. It should be noted that the DAE derivatives were attached to metallic nanotubes, instead of semi-conducting ones as used in the experiments. However, the local properties of the adsorbates are quite insensitive to the tube chirality as we have demonstrated in Sec. 4.5.

The adsorption energy for 6H in the parallel configurations is -0.53 eV (open form) and 0.53 eV (closed form), which is slightly smaller (about $0.03 - 0.04$ eV) than for the perpendicular ones. For 6F, the most favorable binding interaction occurs when the DAE is oriented parallel to the nanotube axis (the binding energies are

⁵The threshold voltage V_{th} is defined as the minimum voltage applied between gate and source, which is required to create a conducting channel.

Table 4.5.: Shortest distance between the cyclopentene/cyclohexene ring and the CNT surface d (in Å), adsorption energy E_a (in eV), Bader partial charge q (in unit charges) and local dipole moment μ (in Debye) of a DAE photoswitch on a metallic (5,5) SWCNT using a plane wave method with periodic boundary conditions (PAW-PBE-D2). The thiophene units of the DAE molecules are oriented parallel and perpendicular to the nanotube surface as shown in Figure 4.19. Note that the dipole moments of the perfluorinated switches have opposite orientations with respect to the perhydrated ones. The dipole moments for the isolated DAE molecules are obtained using a localized single-particle basis (BP86-D3(BJ)/def-TZVP). Results for the perpendicular structures of (o)-5H and (c)-5F are not shown due to convergence problems.

Properties	6H		5H		6F		5F	
	open	closed	open	closed	open	closed	open	closed
parallel								
d	3.77	3.64	3.34	3.53	4.13	3.88	3.65	3.90
E_a	-0.53	-0.51	-0.70	-0.56	-0.61	-0.60	-0.69	-0.68
q	-0.16	0.04	0.00	0.00	-0.03	-0.04	-0.04	-0.03
μ	3.95	2.95	1.66	3.04	3.78	4.38	4.35	4.08
perpendicular								
d	4.02	4.07	—	3.59	4.20	4.88	3.80	—
E_a	-0.56	-0.55	—	-0.52	-0.52	-0.45	-0.50	—
q	-0.18	0.02	—	0.02	-0.03	-0.03	-0.02	—
μ	4.65	3.40	—	3.33	4.01	4.65	4.40	—
isolated DAEs								
μ	2.69	3.59	2.04	3.56	3.08	4.08	3.88	3.80

about 0.10 eV larger compared to the perpendicular ones). Furthermore, (c)-5H and (o)-5F favor the parallel configuration. Possibly, the preference for the same adsorption mode in both the open and closed configuration for 6H could explain its reversible switching behavior.

The AIM partial charges of the DAE molecules (see Table 4.5) suggest that the charge transfer between the DAE switches and the CNT is negligible (< 0.04). An exception is (o)-6H, which shows charge transfer from the nanotube to the DAE by about 0.20 unit charges. Thus, it acts as an acceptor which would correlate with the observed shift in the threshold voltage towards positive values. As shown in

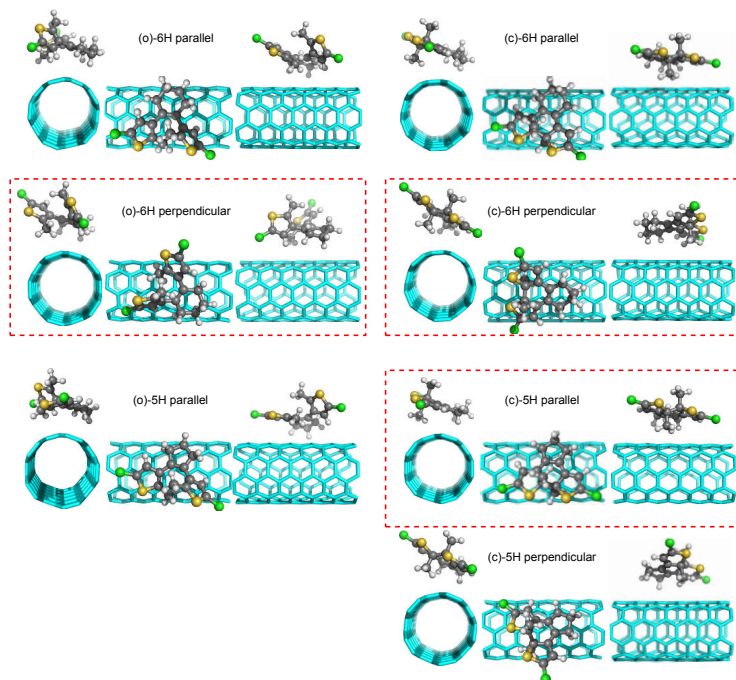


Figure 4.17.: Optimized structures of a metallic (5,5) CNT functionalized with the open and the closed form of 5H and 6H using PAW-PBE-D2. The thiophene units are oriented parallel and perpendicular to the nanotube surface, respectively. The preferred orientations are bordered in red. Note that the optimized structure of (o)-5H with perpendicular orientation to the CNT surface could not be obtained due to convergence problems.

Figure 4.19, the dipole moments of the perhydrated DAE molecules are oriented with the positive center on the thiophene unit and opposite orientations for the perfluorinated DAE switches. For 6H, the dipole moment increases upon photo-switching from the closed to the open form with the positive partial charge closer to the nanotube. This would result in a shift of the threshold voltage towards negative values as it acts as a positive gate, contradictory to what is suggested by charge transfer and experimental findings. In case of 5H, the dipole moment increases if we go from the open to the closed form, which might be responsible for the observed shifts. The relatively small changes in the dipole moment of the perfluorinated DAEs upon photoswitching and its parallel orientation to the nanotube surface correlate with the less pronounced shifts of the threshold voltage. However,

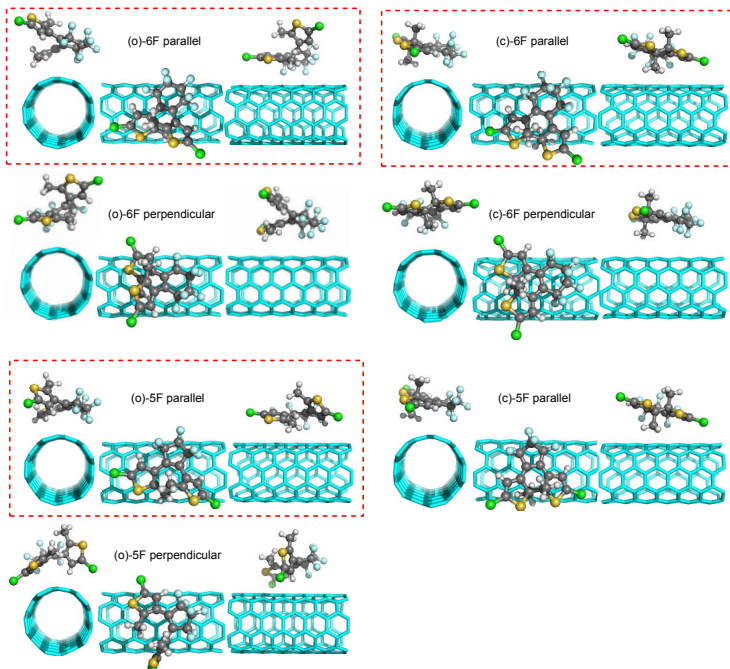


Figure 4.18.: Optimized structures of a metallic (5,5) CNT functionalized with the open and the closed form of a 5F and b 6F using PAW-PBE-D2. The thiophene units are oriented parallel and perpendicular to the nanotube surface, respectively. The preferred orientations are bordered in red. The optimized structure of (c)-5F with perpendicular orientation could not be obtained due to convergence problems.

these changes do not explain the ΔV_{th} shift in negative direction (observed for 5F). To conclude, we cannot yet make any reliable predictions whether a change in the dipole moment or a charge transfer effect is responsible for the observed shifts in the transport characteristics.

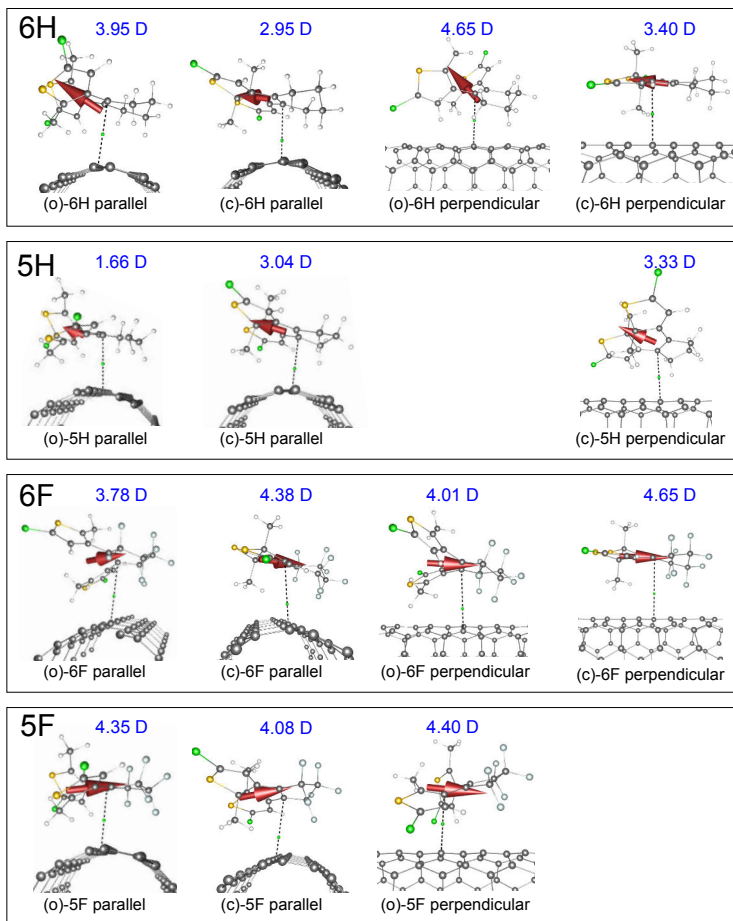


Figure 4.19.: Calculated local dipole moments of DAE derivatives. The dipole moments are indicated as red arrows pointing towards the negative part (δ^-). The length of the dipole moment is specified in Debye (multiplied by a scaling factor of 2 for visualization). The internal reference points (small green dots on dotted line) between CNT–DAE atom pairs (aprx option) were used to determine the DAE’s dipole moment as implemented in GENLOCDIP. The AIM analyses were performed using BADER.

4.7. Conclusion

Local dipole moments for fragments of molecular or supramolecular systems are important for understanding various phenomena in nanoscience, such as solvent effects on the conductance of single molecules in break junctions or the interaction between the tip and the adsorbate in atomic force microscopy. Therefore, we derived a definition of fragment dipole moments which achieves origin-independence by relying on internal reference points. Instead of bond critical points as in existing approaches, we use as few as possible reference points, which are located between the fragment and the remainder(s) of the system and may be chosen based on chemical intuition. This approach is implemented in the GENLOC-DIP program which uses the Bader electron density partitioning scheme to define the atomic boundaries and acts as a post-processing tool for AIM programs. Because our approach does not require the location of bond critical points, GENLOC-DIP can also be used as an interface for grid-based AIM programs (*e. g.*, BADER) in combination with plane-wave electronic structure calculations, when AIM fails to locate bond critical points between, *e. g.*, distant noncovalently bound molecular fragments, or when a local partitioning scheme other than AIM is employed which does not provide critical points.

Furthermore, we have described the supramolecular interaction between metallic and semi-conducting carbon nanotubes (CNTs) and adsorbates using two different density functional theory approaches, namely a periodic-boundary (PB) code based on plane-wave single-particle basis functions and pseudopotentials, and a truncated approach based on a localized basis set, where the CNTs were cut and capped by hydrogen atoms. The latter approach has proven to be very useful in practice because a large number of postprocessing quantum-chemical methods and exchange–correlation functionals are available for finite systems. On the downside, the results of truncated model calculations can be affected considerably by the choice of the model size, in terms of optimized structures as well as electronic properties. Since well-established adsorption structures exist for metallic and semi-conducting SWCNTs functionalized with NH_3 and NO_2 , respectively, these were used as benchmark systems. For NH_3 adsorption, optimized adsorption structures and binding energies E_a (the error in E_a is ≈ 0.05 eV) for the truncated nanotubes qualitatively and to a good extent also quantitatively agree with the PB model on condition that the finite tube length is sufficiently large (19 Å). Both models suggest a physisorption mechanism and a negligible charge transfer to the nanotube. In case of NO_2 adsorption on a metallic (5,5) CNT, both studied truncated nanotubes’ lengths lead to tilted and sometimes shifted adsorption structures compared to the PB model structures. However, both models suggest that NO_2 is physisorbed and acts as an acceptor. An unexpected chemisorption of NO_2 on a semi-conducting

nanotube surface is obtained for the truncated description, of course affecting the charge transfer and dipole properties. Enlarging the tube length from 8 to 19 Å leads to a less pronounced covalent binding, but still results in an inaccurate description in comparison to the PB description. This leads to the conclusion that one must further enlarge the truncated nanotube or employ PB models in order to produce accurate adsorption structures if a competition between chemisorption and physisorption is possible. Local dipole moments are similar between metallic and semiconducting tubes for physisorbed adsorbates.

Based on current–voltage ($I - V_g$) measurements of non-covalently functionalized single-walled carbon nanotube field-effect transistors (CNTFETs) with diarylethene (DAE) photoswitches, we studied the nanotube–DAE interactions using plane-wave density functional theory. In order to explain the threshold voltage shifts that have been observed in the transistor characteristics and to determine the mechanism by which the DAE–nanotube interactions affect the conductance, we have calculated the charge transfer and the local dipole moments of the DAE molecules with two different orientations on a single-walled (5,5) carbon nanotube. In all cases except for the open form of the perhydrated cyclohexene species, the charge transfer is negligible and consequently plays no significant role in transistor characteristics. In the aforementioned case, charge transfer from the nanotube might be responsible for the shifts in the threshold voltage upon photoswitching from the closed to open form. However, the change in the dipole moment offers grounds for contradictory assumptions. On the other hand, a dipole mechanism would correlate with shifts in the threshold voltage for perhydrated cyclopentene. Although, the changes in dipole moment between open and closed forms of the perfluorinated photoswitches do not explain the shift in negative direction, the relatively small changes and the nearly parallel orientation of the dipole moment with respect to the CNT "surface" do correlate with the less pronounced shifts of the threshold voltage for these compounds. Also, the reversibility of the photoswitching may be related to the preferred adsorption modes for the open and closed forms. Although some of the results coincide with the experimental observations, others are not comparable. A multiscale approach (based on the extraction of local dipole moments) taking into account the metal–CNT contacts may provide a more comprehensive picture of the dipole mechanism.

5. Molecular conductance in competition with energy transfer in nanoparticle arrays

5.1. Introduction

Colloidal quantum dots (QDs) such as CdS nanoparticles with adsorbed organic dyes are a highly promising system for photovoltaics and optoelectronics [502–504]. In such QD–linker–dye systems (see Fig. 5.1a), competing processes can occur, in particular electron transfer and exciton transfer. For a truly predictive theoretical approach towards such devices, a multiscale ansatz would be needed, where transfer rates are extracted from first-principles calculations and plugged into a framework for solving the resulting rate equations. Here one step towards this goal is studied by setting up such a system of rate equations and discussing the resulting populations of states at different moments in time as a function of the (relative) rates. It will also be discussed how their rates can be obtained from a first-principles theory.

As already noted, the conductance of a molecular junction (that is, a molecule between two macroscopic electrodes acting as semi-infinite electron baths) and its electron transfer properties (when the same bridge is linking a donor and an acceptor unit) can be related within the electron tunneling regime [194]. In this section, electron transfer and Förster-type energy transfer processes are introduced, focusing on the relationship between electron transfer in Donor-Bridge-Acceptor (DBA) systems and molecular conductance. The latter allows us to obtain a reliable estimate of transfer rates from transport observables.

In general, the thermally averaged rate constant k for electron/energy transfer from a donor vibronic state $|d, \chi_d\rangle$ to an acceptor vibronic state $|a, \chi_a\rangle$ is given by Fermi's golden rule

$$k_{D \rightarrow A} = \frac{2\pi}{\hbar} \sum_{\chi_d, \chi_a} P_d |\langle d, \chi_d | \hat{V} | a, \chi_a \rangle|^2 \delta(E_{d, \chi_d} - E_{a, \chi_a}), \quad (5.1)$$

where P_d is the Boltzmann distribution of the donor states, \hat{V} is the interstate coupling, and \hbar is the reduced Planck constant. The nuclear states $\chi_{d,a}$ belong to the electronic states d, a and $E_{d, \chi_d}, E_{a, \chi_a}$ are the energies of the donor and acceptor vibrational levels, respectively. Since the Born–Oppenheimer approximation is used

where k_B is the Boltzmann constant and T is the temperature. The reorganization energy E_λ (energy required for “vertical” electron transfer without displacement of the nuclear coordinates) and the driving force E_{AD} (the standard free-energy change for the electron transfer, often referred to as ΔG_0) can be obtained using standard quantum chemistry methods [508]. Furthermore, a number of methods are available to determine the electronic coupling $V_{d,a}$. Approaches based on minimizing the energy of a system are constrained density functional theory as exploited by Voorhis *et al.* [509] and symmetry-broken SCF calculations with external perturbations [510, 511]. Another ansatz is to rotate adiabatic states into charge-localized diabatic states by extending the generalized Mulliken–Hush (GMH) algorithm [512, 513] analogous to Boys localization [514] as described by Subotnik *et al.* [515].

5.1.1. Electron transfer in donor–bridge–acceptor systems and its relation to electron transport in molecular junctions

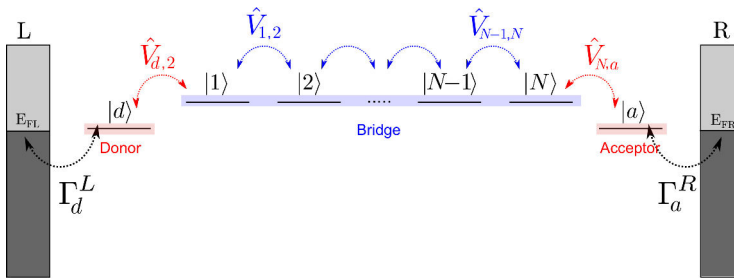


Figure 5.2.: Simple level representation of a Donor–Bridge–Acceptor system between metal leads. The molecular bridge consists of identical subunits and is described by a set of local orbitals. Only the first and the last molecular level in the chain couples to the donor $|d\rangle$ and acceptor $|a\rangle$ state. In turn, the donor and acceptor may be coupled to electronic continua of the metal leads ($\{l\}$ for left, $\{r\}$ for right electrode).

Let us consider a model system in which the molecular bridge is described by a chain of N effective single-particle states, $\{|1\rangle, |2\rangle, \dots, |N\rangle\}$ as shown in Fig. 5.2 (without taking into account the coupling to the leads). Following the derivation in Ref. [194], we assume (1) only nearest-neighbor coupling and (2) that the first state $|1\rangle$ couples to the donor state $|d\rangle$ and the last $|N\rangle$ couples to the acceptor state $|a\rangle$.

The effective single-particle Hamiltonian for such a DBA system is defined as

$$\begin{aligned} \hat{H} = & E_d|d\rangle\langle 1| + \sum_{n=1}^N E_n|n\rangle\langle n| + E_a|a\rangle\langle a| \\ & + V_{d,1}|d\rangle\langle 1| + V_{1,d}|1\rangle\langle d| + V_{a,N}|a\rangle\langle N| + V_{N,a}|N\rangle\langle a| \\ & + \sum_{n=1}^{N-1} \left(V_{n,n+1}|n\rangle\langle n+1| + V_{n+1,n}|n+1\rangle\langle n| \right). \end{aligned} \quad (5.4)$$

We now calculate the eigenstates of the Hamiltonian in the general form $\psi = c_d|d\rangle + c_a|a\rangle + \sum_{n=1}^N c_n|n\rangle$. The secular equation then takes the form

$$\begin{pmatrix} E_d - E & V_{d,1} & 0 & 0 & \cdots & 0 \\ V_{1,d} & E_1 - E & V_{1,2} & 0 & \cdots & 0 \\ 0 & V_{2,1} & E_2 - E & V_{2,3} & & \vdots \\ 0 & 0 & V_{3,2} & \ddots & \ddots & 0 \\ \vdots & \vdots & & \ddots & E_N - E & V_{N,a} \\ 0 & 0 & \cdots & 0 & V_{a,N} & E_a - E \end{pmatrix} \begin{pmatrix} c_d \\ c_1 \\ \vdots \\ c_N \\ c_a \end{pmatrix} = 0. \quad (5.5)$$

Alternatively, Eq. (5.5) can be written as

$$\begin{pmatrix} E_1 - E & V_{1,2} & 0 & \cdots & 0 \\ V_{2,1} & E_2 - E & V_{2,3} & & \vdots \\ 0 & V_{3,2} & \ddots & & 0 \\ \vdots & & & E_{N-1} - E & V_{N-1,N} \\ 0 & \cdots & 0 & V_{N,N-1} & E_N - E \end{pmatrix} \begin{pmatrix} c_1 \\ c_2 \\ \vdots \\ c_{N-1} \\ c_N \end{pmatrix} = - \begin{pmatrix} V_{1,d}c_d \\ 0 \\ \vdots \\ 0 \\ V_{N,a}c_a \end{pmatrix}, \quad (5.6)$$

with

$$(E_d - E)c_d + V_{d,1}c_1 = 0, \quad (5.7)$$

$$(E_a - E)c_a + V_{a,N}c_N = 0. \quad (5.8)$$

In matrix notation, Eq. (5.6) is given by

$$(\mathbf{H}_B - E)\mathbf{c}_B = -\mathbf{u} \quad (5.9)$$

$$\Leftrightarrow \mathbf{c}_B = -\underbrace{\mathbf{u}(\mathbf{H}_B - E)^{-1}}_{-\mathbf{G}^B} = \mathbf{G}^B \mathbf{u}, \quad (5.10)$$

where \mathbf{G}^B is the Green's function matrix of the bridge. From Eq. (5.10), we get the following expressions for the coefficients c_1 and c_N ,

$$c_1 = G_{1,1}^B V_{1,d} c_d + G_{1,N}^B V_{N,a} c_a \quad (5.11)$$

$$c_N = G_{N,1}^B V_{1,d} c_d + G_{N,N}^B V_{N,a} c_a \quad (5.12)$$

Inserting Eq.(5.11) into Eq.(5.7) leads to

$$(E_d - E + V_{d,1} G_{1,1}^B V_{1,d}) c_d + V_{d,1} G_{1,N}^B V_{N,a} c_a = 0 \quad (5.13)$$

$$\Leftrightarrow (\tilde{E}_d - E) c_d + \tilde{V}_{d,a} c_a = 0, \quad (5.14)$$

with the donor energy and donor-acceptor coupling modified by the bridge defined as

$$\tilde{E}_d = E_d + V_{d,1} G_{1,1}^B V_{1,d}, \quad (5.15)$$

$$\tilde{V}_{d,a} = V_{d,1} G_{1,N}^B V_{N,a}. \quad (5.16)$$

If we insert Eq. (5.16) for the coupling \tilde{V} in the golden rule expression, Eq. (5.1), we get the electron transfer rate

$$k^{ET} = \frac{2\pi}{\hbar} |\tilde{V}_{d,a}|^2 \mathcal{F}(E_{AD}) = \frac{2\pi}{\hbar} |V_{d,1} V_{N,a}|^2 |G_{1,N}^B|^2 \mathcal{F}(E_{AD}). \quad (5.17)$$

The effective coupling $\tilde{V}_{d,a}$ depends on the energy E through the Green's function

$$\mathbf{G}^B = (E - \mathbf{H}_B)^{-1}. \quad (5.18)$$

Since we focus on the case where the manifold of bridge levels $\{n\}$ is energetically distinct from the donor and acceptor levels, we can substitute E by the donor/acceptor energy $E_{d/a}$ ($E_{d/a} = E_d = E_a$) in Eq. (5.18) and only the lowest-order term in the Dyson expansion¹ can contribute to the matrix element of the bridge Green's function

$$G_{1,N}^B = \frac{1}{(E_{d/a} - E_1)} V_{1,2} \frac{1}{(E_{d/a} - E_2)} V_{2,3} \cdots \frac{1}{(E_{d/a} - E_{N-1})} V_{N-1,N} \frac{1}{(E_{d/a} - E_N)}. \quad (5.19)$$

If we assume that the bridge consists of identical units, we can define that all coupling elements and energies of the bridge states are equal (hereinafter referenced as V_B and E_B , respectively). This leads to

$$G_{1,N}^B = \frac{1}{V_B} \left(\frac{V_B}{E_{d/a} - E_B} \right)^N, \quad (5.20)$$

¹For example, $\hat{G}(z) = \hat{G}_0(z) + \hat{G}_0(z) \hat{V} \hat{G}(z)$, where $\hat{G}_0(z)$ is the Greens function for the interacting electron system.

and

$$\tilde{V}_{d,a} = \frac{V_{d,1}V_{N,a}}{V_B} \left(\frac{V_B}{E_{d/a} - E_B} \right)^N. \quad (5.21)$$

Now, the DBA complex is sandwiched between two metal electrodes. Note that the donor and acceptor orbitals are only coupled to their adjacent metal contact. Within the tight-binding approximation, the transmission coefficient \mathcal{T} (*cf.* Eq. (2.51)) evaluated at the Fermi energy E_F takes the form

$$\mathcal{T}(E_F) = \text{Tr}[\mathbf{\Gamma}^L \mathbf{G}^{B\dagger}(E_F) \mathbf{\Gamma}^R \mathbf{G}^B(E_F)] = \Gamma_d^L \Gamma_a^R |G_{d,a}^B(E_F)|^2. \quad (5.22)$$

where Γ_d^L and Γ_a^R are, respectively, widths of the donor and acceptor levels due to their coupling to the electrodes (*cf.* Eq. (2.33) and Eq. (2.32), respectively). The Greens function matrix element of the DBA system is given by

$$G_{d,a}^B(E_F) = G_{d,1}^B(E_F) V_{d,1} G_{1,N}^B(E_F) V_{N,a} G_{N,a}^B(E_F), \quad (5.23)$$

with

$$G_{d,1}^B(E_F) = \frac{1}{E_F - E_d + \Sigma^L(E)} = \frac{1}{E_F - \tilde{E}_d + \frac{i}{2}\Gamma_d^L}, \quad (5.24)$$

$$G_{N,a}^B(E_F) = \frac{1}{E_F - E_a + \Sigma^R(E)} = \frac{1}{E_F - \tilde{E}_a + \frac{i}{2}\Gamma_a^R}. \quad (5.25)$$

where $\tilde{E}_{d/a}$ is the donor/acceptor energy shifted by the respective real part of the self energy $\Sigma^{L/R}$ and where the energy-dependence of Γ has been neglected. Eq. (5.22) can be further simplified using the approximations that (1) the renormalized donor and acceptor energies are close to the Fermi energy, so that $E_F = \tilde{E}_d = \tilde{E}_a$, (2) the electronic structure of the bridge does not change significantly upon attaching to the electrodes and (3) the denominators in Eq. (5.24) and Eq. (5.25) are dominated by Γ ,

$$\begin{aligned} \mathcal{T}(E_F) &= \frac{\Gamma_d^L \Gamma_a^R |V_{d,1} V_{N,a}|^2 |G_{1,N}^B(E_F)|^2}{[(E_F - \tilde{E}_d)^2 - (\Gamma_d^L/2)^2][(E_F - \tilde{E}_a)^2 - (\Gamma_a^R/2)^2]} \\ &= \frac{16|V_{d,1} V_{N,a}|^2 |G_{1,N}^B(E_F)|^2}{\Gamma_d^L \Gamma_a^R}. \end{aligned} \quad (5.26)$$

Now, we recall that the conductance² is $G = G_0 \mathcal{T}(E_F)$ (*cf.* Eq. (1.9), with $G_0 = \frac{2e^2}{h}$), insert Eq. (5.26), and compare with Eq. (5.17). In the weak coupling limit of the Landauer formula, we get an approximate expression of G which depends on the electron transfer rate from the donor to the acceptor,

$$G \approx \frac{8e^2}{\pi^2 \Gamma_d^L \Gamma_a^R \mathcal{F}(E_{AD})} k_{D \rightarrow A}. \quad (5.27)$$

²Not to be confused with the Greens function element of the bridge G^B .

Using typical values of $\Gamma_d^L = \Gamma_a^R \approx 0.5$ eV, Eq. (5.27) yields $g \approx 5 \times 10^{-19} k^{ET} \mathcal{F}^{-1}$. At room temperature, Eq. (5.3) yields $\mathcal{F} \approx 3 \cdot 10^{-4}$ (eV) $^{-1}$, with a typical value of the reorganization energy $E_\lambda = 0.9$ eV [516], $E_d = E_a$, and $k_B T = 0.026$ eV.

5.1.2. Fluorescence resonance energy transfer

When the donor is excited by a photon, the excitation energy can be transferred to the acceptor. Fig. 5.3 shows two common mechanisms of energy transfer, namely dipole-induced Förster (or Coulombic) energy transfer [211] and exchange-induced Dexter energy transfer [517]. In this section, we focus on the former mechanism.

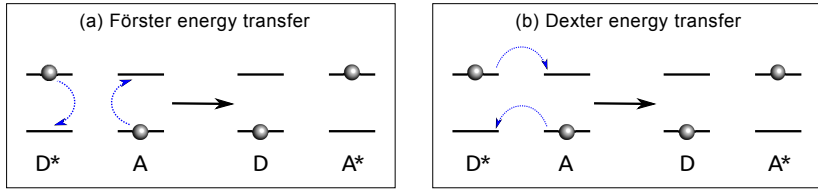


Figure 5.3.: (a) Förster energy transfer and (b) Dexter energy transfer between an excited donor state and an acceptor state (in its ground state), $D^* + A \rightarrow D + A^*$, respectively.

We describe the ground states of the donor and acceptor by their vibronic manifolds $\{|d, \chi_d\rangle\}$, $\{|a, \chi_a\rangle\}$ and the excited states by $\{|d', \chi_{d'}\rangle\}$, $\{|a', \chi_{a'}\rangle\}$, respectively. Note that the zeroth-order wave functions can be defined as products of terms associated with the individual molecules or donor and acceptor parts of the system, *e.g.* $|d\chi_d, a'\chi_{a'}\rangle = |d, \chi_d\rangle|a', \chi_{a'}\rangle$. If we assume that intermolecular coupling is electrostatic and that the extent of the individual molecular charge distributions is much smaller than the intermolecular distance, we can expand the intermolecular coupling \hat{V} between donor D and A in a multipole series. The dominant interaction is the dipole–dipole coupling which is represented by

$$\begin{aligned} \hat{V} &= \frac{\hat{\boldsymbol{\mu}}_A \cdot \hat{\boldsymbol{\mu}}_D - 3(\hat{\boldsymbol{\mu}}_A \cdot \mathbf{u}_R)(\hat{\boldsymbol{\mu}}_D \cdot \mathbf{u}_R)}{R^3} \\ &= \hat{\boldsymbol{\mu}}_A \hat{\boldsymbol{\mu}}_D \cdot \frac{\mathbf{u}_A \cdot \mathbf{u}_D - 3(\mathbf{u}_A \cdot \mathbf{u}_R)(\mathbf{u}_D \cdot \mathbf{u}_R)}{R^3}, \end{aligned} \quad (5.28)$$

where \mathbf{u}_R is a unit vector in the direction from donor to acceptor and R is the distance between them. The dipole operators associated with the donor and acceptor, $\hat{\boldsymbol{\mu}}_A$ and $\hat{\boldsymbol{\mu}}_D$, can be written as unit vectors multiplied by the normalized transition dipole moment, *e.g.* $\hat{\boldsymbol{\mu}}_A = \mathbf{u}_A \hat{\mu}_A$.

In the following, part of the numerator in Eq. (5.28) will be represented by an

orientation factor

$$\kappa = \mathbf{u}_A \cdot \mathbf{u}_D - 3(\mathbf{u}_A \cdot \mathbf{u}_R)(\mathbf{u}_D \cdot \mathbf{u}_R), \quad (5.29)$$

In order to evaluate the golden rule rate, we can write the absolute square of matrix elements in the form

$$\begin{aligned} |\langle d' \chi_{d'} | a \chi_a | \hat{V} | d \chi_d, a' \chi_{a'} \rangle|^2 &= |\langle d' \chi_{d'} | a \chi_a | \hat{\mu}_A \hat{\mu}_D | d \chi_d, a' \chi_{a'} \rangle|^2 \times \frac{\kappa^2}{R^6} \\ &= |\langle d' \chi_{d'} | \hat{\mu}_D | d \chi_d \rangle|^2 |\langle a \chi_a | \hat{\mu}_A | a' \chi_{a'} \rangle|^2 \\ &\quad \times \frac{\kappa^2}{R^6}. \end{aligned} \quad (5.30)$$

Inserting Eq. (5.30) in the golden rule expression of Eq. (5.2) leads to

$$\begin{aligned} k^{XT} &= \frac{2\pi}{\hbar} \frac{\kappa^2}{R^6} \sum_{\chi_a, \chi_{a'}, \chi_d, \chi_{d'}} P_{d'} P_a |\langle d' \chi_{d'} | \hat{\mu}_D | d \chi_d \rangle|^2 |\langle a \chi_a | \hat{\mu}_A | a' \chi_{a'} \rangle|^2 \\ &\quad \times \delta(E_d + E_{a'} - E_{d'} - E_a). \end{aligned} \quad (5.31)$$

Next, we use the relation

$$\delta(E_d + E_{a'} - E_{d'} - E_a) = \int_{-\infty}^{\infty} dE \delta(E + E_a - E_{a'}) \delta(E + E_d - E_{d'}), \quad (5.32)$$

in Eq. (5.31), to obtain the rate expression for energy transfer from the donor to the acceptor as

$$\begin{aligned} k^{XT} &= \frac{\hbar}{2\pi} \frac{\kappa^2}{R^6} \int_{-\infty}^{\infty} dE \frac{2\pi}{\hbar} \underbrace{\sum_{\chi_d, \chi_{d'}} P_{d'} |\langle d' \chi_{d'} | \hat{\mu}_D | d \chi_d \rangle|^2 \delta(E + E_d - E_{d'})}_{k_{d' \rightarrow d}(E)} \\ &\quad \times \underbrace{\sum_{\chi_a, \chi_{a'}} P_a |\langle a \chi_a | \hat{\mu}_A | a' \chi_{a'} \rangle|^2 \delta(E + E_a - E_{a'})}_{k_{a \rightarrow a'}(E)} \\ &= \frac{\hbar}{2\pi} \frac{\kappa^2}{R^6} \int_{-\infty}^{\infty} dE k_{a \rightarrow a'}(E) k_{d' \rightarrow d}(E), \end{aligned} \quad (5.33)$$

where $k_{a \rightarrow a'}$ is the adsorption lineshape of the acceptor and $k_{d' \rightarrow d}$ is the emission lineshape of the donor. Expressed in terms of measurable quantities, the rate constant of energy transfer yields

$$k^{XT} = k_D^0 \left(\frac{R_0}{R} \right)^6 \quad \text{with } R_0^6 = \frac{\hbar}{2\pi} \frac{\kappa^2}{R^6} \int_{-\infty}^{\infty} dE k_{a \rightarrow a'}(E) k_{d' \rightarrow d}(E), \quad (5.34)$$

where k_D^0 is the internal decay rate of the excited donor state (in the absence of transfer) and R_0 is the critical donor–acceptor distance (Förster radius) [518]. At

the distance of the Förster radius, the energy transfer rate is equal to k_D^0 . Typical values of Förster radii for biological donor–acceptor systems are in the range of $R_0 = 8 - 10$ nm [519].

5.2. Excitation pathways as a function of transfer rates

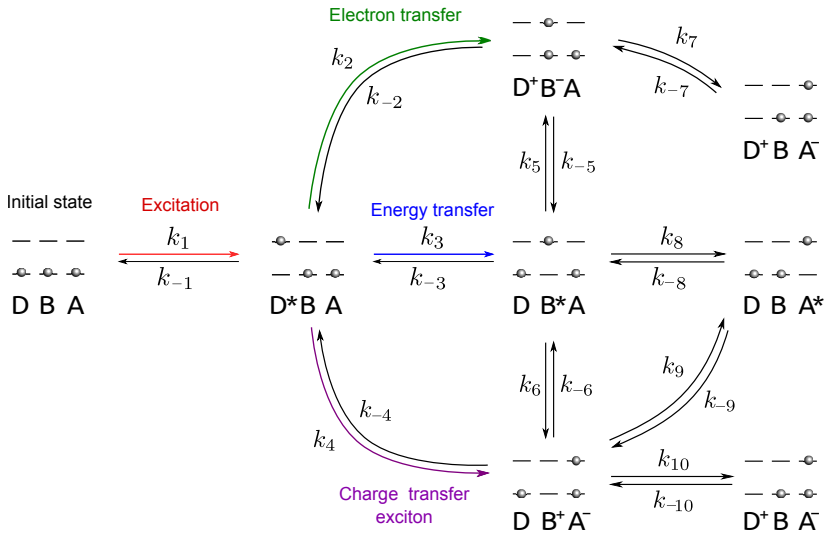


Figure 5.4.: Possible electronic processes in a Donor–Bridge–Acceptor system.

In DBA systems, such as CdSe quantum dot (QD) functionalized with organic dyes, the donor may be excited via optical excitation followed by various transfer processes which can be described by first-order kinetics. Thus, being able to make reliable predictions about the dominant processes and the populations of the different states as a function of time is desirable. We used the open-source program Wxmaxima [520] to analytically solve the master equations for the populations of different states corresponding to possible excitation pathways for different transfer rate constants [212]. Figure 5.4 illustrates possible tunneling pathways in DBA systems and Table 5.1 lists the notations used.

Table 5.1.: Notations used to define the respective states in Fig. 5.4 ($X = D, B, A$).

Notation	Definition
X	Subsystem X is in its ground state.
X^*	Subsystem X is in its excited state.
X^-	An additional electron is introduced to subsystem X .
X^+	An electron is removed from subsystem X .

The corresponding kinetic equations which describe the time evolution of the probabilities in the system lead to Eqs. (5.35)–(5.41).

$$\frac{d[DBA]}{dt} = -k_1[DBA] + k_{-1}[D^*BA] \quad (5.35)$$

$$\begin{aligned} \frac{d[D^*BA]}{dt} = & -(k_{-1} + k_2 + k_3 + k_4)[D^*BA] + k_1[DBA] \\ & + k_{-2}[D^+B^-A] + k_{-3}[DB^*A] + k_{-4}[DB^+A^-] \end{aligned} \quad (5.36)$$

$$\begin{aligned} \frac{d[DB^*A]}{dt} = & -(k_{-3} + k_5 + k_6 + k_8)[DB^*A] + k_3[D^*BA] \\ & + k_{-5}[D^+B^-A] + k_{-6}[DB^+A^-] + k_8[DBA^*] \end{aligned} \quad (5.37)$$

$$\begin{aligned} \frac{d[D^+B^-A]}{dt} = & -(k_{-2} + k_{-5} + k_7)[D^+B^-A] + k_2[D^*BA] \\ & + k_5[DB^*A] + k_{-7}[D^+BA^-] \end{aligned} \quad (5.38)$$

$$\begin{aligned} \frac{d[DB^+A^-]}{dt} = & -(k_{-4} + k_{-6} + k_9 + k_{10})[DB^+A^-] + k_4[D^*BA] \\ & + k_6[DB^*A] + k_{-9}[DBA^*] + k_{-10}[D^+BA^-] \end{aligned} \quad (5.39)$$

$$\frac{d[DBA^*]}{dt} = -(k_{-8} + k_{-9})[DBA^*] + k_8[DB^*A] + k_9[DB^+A^-] \quad (5.40)$$

$$\frac{d[D^+BA^-]}{dt} = -(k_{-7} + k_{-10})[D^+BA^-] + k_7[D^+B^-A] + k_{10}[DB^+A^-] \quad (5.41)$$

Solving the kinetic equations, we obtain populations of the respective states as a function of time as shown in Figure 5.5a. Energy and electron transfer rates in the

right panel of Figure 5.5b were taken from time-resolved experiments by Wachtveitl *et al.*. They have investigated photo-induced interfacial electron transfer from CdSe quantum dots to methylviologen as a function of QD size and the acceptor concentration [521]. More recently, they studied photo-induced fluorescence resonance energy transfer (FRET) dynamics in a perylene diimide derivative attached to a Cd-Se/CdS/ZnS multishell quantum dot also in terms of acceptor concentration [522]. Figure 5.5b shows that the initial state (ground state, blue) is virtually no longer populated after 0.04 ns since the reverse processes of electron and energy transfer are blocked (k_{-2} and k_{-3} are assumed to be negligibly small). At the same time, the electron (green) and the energy (yellow) transfer state approach their limits.

The photoexcited state (red) reaches a maximum at time $t = 0.01$ ns. In order to assess how the population will qualitatively depend on the actual value of the electron and transfer rate constants, we have systematically varied these rate constants in a range of $0 - 200 \text{ ns}^{-1}$ for a given population at a certain time (see Figs. 5.5c-f). Figure 5.5c-d illustrate how the population of the photoexcited state depends on the electron k_{ET} and the energy k_{XT} transfer rate at the time of its (c) maximum ($t = 0.01$ ns) and decrease ($t = 0.04$ ns). With an increase of both electron and energy transfer rates, the photoexcited state decreases uniformly toward zero. Figure 5.5e-f illustrate that we obtain a 50:50 population for the electron and the energy transfer state if their transfer rate constants are equal.

5.3. Conclusion

The approximate relation between electron transfer rate constants and molecular conductance derived by Nitzan [194] provides a reliable basis for comparing estimates of both observables involving the same molecular system [523]. The well established donor-bridge-acceptor model can be applied to nanoscopic systems in which the donor/acceptor may function as a molecule or molecular subunit, but also as a molecule (or subunit) attached to an electrode. In the latter case, the vibronic bath is replaced by the electronic bath (continuum of states of a metal electrode). In practice, a remarkably good agreement (within about one order of magnitude) between Eq. (5.27) and experimental values has been found [516] considering the number of assumptions made (*e. g.*, the electronic structure of a molecule does not change significantly when incorporated in a junction and D/A levels are near the Fermi energy). Thus, the approach presented here may provide a good basis for a multiscale description of population dynamics in colloidal quantum dot systems since (estimated) rate constants of electron transfer and other competing processes (*i. e.* energy transfer) can be entered in this rather simple kinetic model to facilitate identifying the dynamics of state populations.

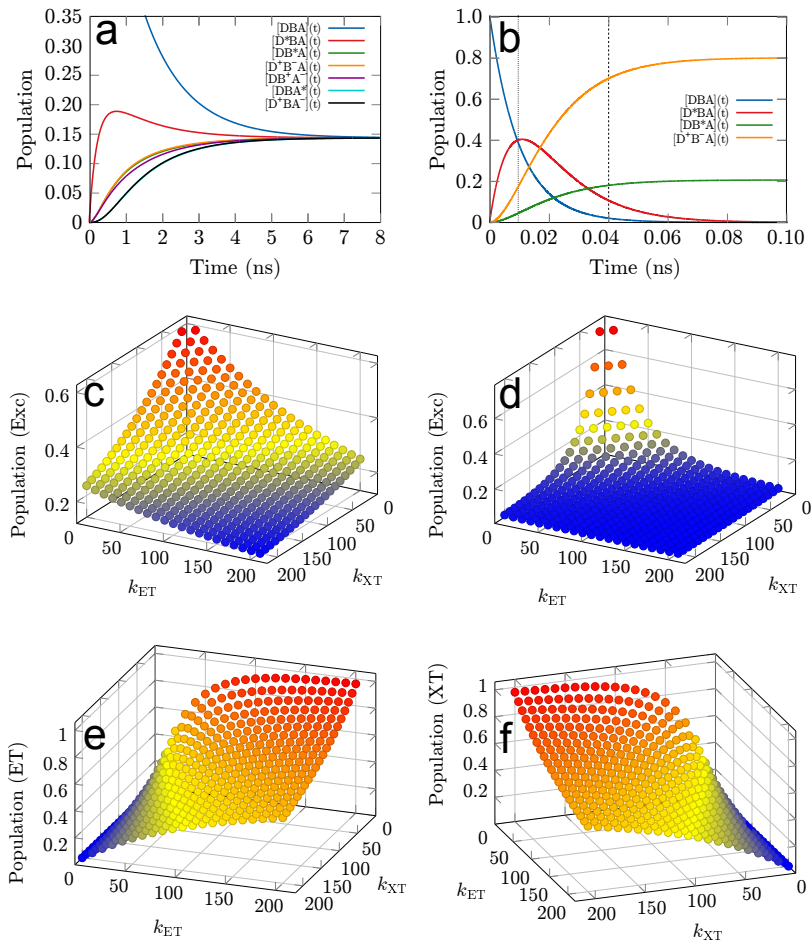


Figure 5.5.: (a-b) Populations of different states (shown in Figure 5.4) as a function of time. (a) All transfer rates were set to 1 ns^{-1} . (b) All transfer rates were set to zero, except for the photoexcitation/relaxation ($k_1 = 10^2 \text{ ns}^{-1} / k_{-1} = 1 \text{ ns}^{-1}$), the electron ($k_2 = 17 \text{ ns}^{-1}$ [521]), and the energy ($k_3 = 66 \text{ ns}^{-1}$ [522]) transfer rates from the initial photoexcited state. (c-f) Population of different states as a function of the electron k_{ET} (k_2) and the energy k_{XT} (k_3) transfer rate, respectively. Population of the photoexcited state at (c) time $t = 0.01 \text{ ns}$ (dotted vertical line in b) and (d) time $t = 0.04 \text{ ns}$ (dashed vertical line in b). Population of the (e) electron transfer and (f) energy transfer state at time $t = 0.04 \text{ ns}$.

6. Conclusion and Perspective

Modeling molecular electronic devices requires computational methods that cover a broad range of time and length scales in order to combine the proper treatment of *e. g.*, macroscopic metal contacts and the nanoscopic system. To account for such large length scales, the systems must be simplified and/or the theoretical methods must be coarse-grained, focusing only on the relevant properties. A possible way to link methods for different scales is to use data from accurate calculations on small subunits of the system to parametrize a coarse-grained model at larger scales [524]. However, multiscale approaches are still under development and the exact calculation of the respective parameters is often difficult and depends highly on the system under study, especially when the properties in the nanoscopic system are, as in our case, manipulated chemically or mechanically.

The aim of this thesis was twofold: to understand the mechanisms for mechanically and photochemically induced changes in the transport properties of nanoscale junctions and, for this purpose, to introduce new approaches towards coarse gained methods.

6.1. Summary

We simulated STM and AFM processes by combining constrained optimizations using DFT and Landauer-type electron transport calculations in order to investigate structural and electronic properties of various molecular systems under mechanical stress (see Chapter 3). Given the flexibility of the platform-mounted Zn-porphyrin molecule discussed in Section 3.2, a MD simulation would probably be indispensable to achieve a comprehensive understanding of the structural changes. However, by taking two important configurations into account, we were able to reproduce and explain the major features observed in the experiment using static DFT. In applying this approach to other systems of interest such as (1) trioxotriangulenium-based platforms (Section 3.3) and (2) manganocene as an example for investigating mechanically-induced spin crossover phenomena (Section 3.4), we had to face the lack of an accurate description with regards to non-covalently bound systems using a cluster rather than models employing periodic boundary conditions. Still, we could show that conductance curves for the platforms depend on chemical func-

tionalization in rough agreement with the experiment, and that for manganocene, cyclopentadienyl rings slipping sideways under mechanical stress may prevent the desired spin crossover from happening. In Section 3.5, the importance of local dipole moments in atomic force microscopy experiments was pointed out. In this context, we could show that a truncated cluster approach has its limitations when it comes to modeling experimental tip structures. For an adequate description of tip–molecule interactions, calculating local dipole moments of periodic slabs instead of finite clusters is desirable, and thick slabs in combination with large tip representations may be required for describing long-range tip–sample interactions. Still, a new approach to local dipole moments developed during this thesis suggests that inversions of local dipole moments depending on the adsorption position may have been overestimated in previous studies.

Following this idea, we showed in Chapter 4 which challenges and hurdles can be encountered when calculating local dipole moments of both physisorbed and chemisorbed adsorbates and their chemical gating effect on the nanotubes' electronic properties. To address these challenges, we developed a flexible approach for calculating local electric dipole moments for fragments of molecular or supramolecular systems and implemented it in the new post-processing computer program LOCALDIP. In Section 4.5 we investigated the effect of truncating a carbon nanotube on local properties. To this end, we systematically compared two different density functional theory methodologies: a plane-wave periodic boundary model and a truncated approach employing a localized single-particle basis. Our results suggest that truncated CNTs provide a good description of non-covalent adsorbate–CNT interactions, thus allowing to use the broad variety of quantum chemical methods implemented in non-periodic electronic-structure codes for future studies of such systems. In order to understand the underlying mechanism of photoswitchable molecules interacting with single-walled CNTs, we studied charge transfer and dipole effects in Section 4.6. However, although there is correlation between the experimental findings and calculations, we cannot yet give any final conclusions with regards to the dipole moment and charge transfer effect on the transport characteristics of carbon nanotube-based transistors. To gain a comprehensive picture of the relevant adsorption mechanisms, a multiscale approach (based on the extraction of local dipole moments) taking into account the metal–CNT contacts should be considered in successive investigations.

Chapter 5 presents an ansatz to integrate electron transfer rate constants and those of competing processes (*e. g.*, energy transfer) into a coarse grained model. As shown by Nitzan [149], electron transfer rate constants can be approximated using calculated conductance values of donor–bridge–acceptor systems. This allows to predict the transfer dynamics of state populations corresponding to possible excitation pathways in *e. g.*, cadmium selenite quantum dots functionalized with organic

dyes which may be relevant for *e. g.*, solar cells, lasers, and light-emitting diodes.

6.2. Outlook

Building on the insights and implementations provided in this thesis, further investigations may involve a coarse grained description of (more) complicated systems:

- The postprocessing tool presented in Sec. 4.4 makes the calculation of local dipole moments more accessible for a variety of applications, such as chemical gating and solvent effects in nanoelectronics, interpretations of atomic force microscopy data, and vibrational infrared absorption intensities. While first steps towards these applications have been taken in this work, the general applicability of such an approach remains to be tested in future work.
- Program packages such as NANOTCAD VIDES [171, 172] are promising for simulating functionalized carbon nanotube-based field effect transistors. The coarse grained description based on maximally localized Wannier functions enables to combine plane-wave electronic structure codes with the Greens function approach. It has not been systematically tested for molecule-based nanodevices yet. Alternatively, it would also be conceivable to establish quantum-chemical local projection operators for a coarse grained description of subsystems (*e. g.*, similar to population analysis).
- Since the analytical method developed in Sec. 5.2 allows to determine the dominant transfer pathway in Donor–Bridge–Acceptor systems, it would be particularly intriguing to apply this model to a realistic system and therefore to calculate electron transfer and exciton dynamics of *e. g.* CdSe quantum dots functionalized with organic dyes based on first-principles input.
- Our transport code ARTAIOS may be extended towards a flexible multiscale simulation package in order to describe electron transport of various nanoscale devices such as gold nanoparticle (NP) arrays based on similar ideas as introduced in Ref. [75], and possibly extended by, *e. g.*, the effect of molecular adsorbates on dielectric properties (see below), and taking local dipole effects (see Section 4.3) into account. The current through an array of nanoparticles can be expressed by an Arrhenius-type activated tunneling model [77, 525]

$$G \propto \exp(-\beta\delta)\exp\left(\frac{-E_{\text{act}}}{k_B T}\right), \quad (6.1)$$

where β is the tunneling decay constant, δ is the interparticle distance, k_B is the Boltzmann constant, and T is the temperature. The thermal activation

energy E_{act} of the nanoparticles can be described by Marcus theory [526]

$$E_{\text{act}} = \frac{E_{\lambda}}{4} = \frac{e^2}{16\pi\epsilon_0} \left(\frac{1}{\epsilon_{op}} - \frac{1}{\epsilon_s} \right) \left(\frac{1}{2r_1} + \frac{1}{2r_2} - \frac{1}{d} \right), \quad (6.2)$$

where E_{λ} is the “outer-sphere” reorganization energy, r_1 and r_2 are radii of neighboring NPs (ideally equal), d is the center-to-center distance between nanoparticles, ϵ_0 is the vacuum permittivity and ϵ_{op} and ϵ_s are the medium optical and static dielectric constants, respectively. Thus, the response of conductance in nanostructured films to adsorbate molecules (*e.g.* for sensor applications) can be characterized by two opposing effects: an increase in spacing between NPs due to swelling and an increase in the permittivity of the organic matrix, which result in a decrease and increase of conductance, respectively. In order to assess the analyte’s contribution to the permittivity of the ligand shells, it would be interesting to explore how the analyte molecules are sorbed into the film using MD simulations. Furthermore, calculating dielectric constants for different analytes using first-principles methods (*e.g.*, Quantum Espresso) will allow for gaining further important insights.

7. Acknowledgments

First and foremost, I thank my supervisor, Prof. Dr. Carmen Herrmann, for her support and the great effort she put into guiding me throughout my scientific research. During my tenure, Carmen encouraged me in presenting my work at various conferences, assisted me by proof reading reports (*i. e.*, manuscripts, proposals, and this thesis), and gave me the opportunity to join the very last Sostrup Summer School as well as the Ratner Group at the Northwestern University (Evanston, United States).

Additionally, I would like to thank my PhD committee members PD Dr. Christian Klinke, Dr. Tobias Vossmeier, and Prof. Dr. Gabriel Bester for their interest in my work.

The results presented in this thesis would not have been accomplished without the help and support of fellow group members and collaborators. In particular, my colleagues Martin Zöllner, Philipp Bahlke, Michael Deffner and Alexander Voigt provided a friendly and cooperative atmosphere at work and also useful feedback and insightful comments on my work. Martin provided a great introduction to plane wave electronic structure methods that greatly assisted my research. I thank Philipp for the stimulating discussions and for his knack for helping to solve practical difficulties. I am thanking both of them for proof reading chapters of this thesis and other manuscripts. Michael, I would like to thank for the company on the way to the institute and during long office hours. I am grateful to Michael and Alex for their support and valuable hints that greatly improved my scripting and programming skills. I like to thank our former group member, Jonny Proppe (now at the ETH Zurich), for his great help solving mathematical problems and the introduction in the program MAXIMA.

During my two week internship at the Northwestern University, I had the privilege to meet with Prof. Abraham Nitzan (University of Tel Aviv, Israel) and Prof. Mark A. Ratner. They deserve the credit for initiating the transfer pathways project and patiently taught me much about various transfer processes. I gained a lot from their vast knowledge and scientific curiosity.

Furthermore, I would like to thank our collaboration partners Dr. Nadine Hauptmann, Dr. Torben Jasper-Tönnies, Prof. Dr. Richard Berndt, PD Dr. Christian

Klinke, Dr. Annette Wurl and Dr. Alexander Schwarz for the great help in understanding the experiments and interpreting the theoretical results. Dr. Christian Mück-Lichtenfeld of the WWU Münster provided insightful discussions and suggestions while I worked on the local dipole project.

Moreover, special thanks are directed to the IT service of the chemistry department for their extensive help in technical and software problems. In particular, Christian Schmidt and Sören Ziehe provided immediate support for any technical problems we encountered.

I also thank the University of Hamburg High Performance Computing Centre (RRZ) and the North-German Supercomputing Alliance (HLRN) for computational resources. In particular, I wish to thank Thomas Orgis and Dr. Hinnerk Stüben for setting up and taking care of the old and the new high-performance computer cluster and software in Hamburg and Simone Knief in her function as contact person of the HLRN for assistance with software issues.

In addition, I would like to acknowledge the financial, academic and technical support of the University of Hamburg. In particular, I am grateful to Beate Susemihl and Katrin Brüggmann, who helped me a lot with administrative questions and issues. I thank the University (Dept. of International Affairs/International University Cooperations) for co-funding of my two-weeks research project at the NWU. Furthermore, additional financial support from the Deutsche Forschungsgemeinschaft (SFB 668) is gratefully acknowledged.

Finally, I would like to acknowledge my friends and family who supported me not only in my PhD time. In particular, I would like to thank my friend Nico for proof reading most parts of this thesis, offering me advice, and supporting me throughout the hard times.

A. Computational methodology

Density functional theory (DFT) is often described as the “workhorse” of electronic-structure calculations, because it provides a good compromise between accuracy and computational costs. In view of the relatively large number of atoms involved in most of our model systems, all calculations were carried out using Kohn–Sham DFT. Today, a variety of DFT-based quantum chemical program packages is available, each of which having its pros and cons with regards to *e. g.*, area/range of application and performance, and postprocessing/analysis methods implemented. The majority of the existing computer codes can be divided into two types, using either (1) a basis set of localized orbitals or (2) (augmented) plane waves as a basis set. The plane wave (PW) model is often used in theoretical solid state and surface physics where periodic boundary conditions are employed, implemented *e. g.* in the codes VASP [527] or QUANTUM ESPRESSO (QE) [437]. A drawback is the (in practice) often limited choice of pseudopotentials in PW codes (and thus the limited choice of exchange–correlation functionals). Codes based on atom-centered basis functions can most often take advantage of a well-developed pool of diverse exchange–correlation functionals, which is in some cases essential even for an accurate qualitative description, and allow for easy interfacing with various quantum chemical analysis tools. A linear combination of Gaussian-type orbitals is implemented (among many others) in the program packages GAUSSIAN 09 (G09) [371] and TURBOMOLE (TM) [528]. Of course there are also codes such as CP2K [367] which are flexible with respect to using both atom-centered basis functions and plane waves under periodic boundary conditions.

Electronic structure calculations

All finite-system structure optimizations were performed using TURBOMOLE (Version 6.0, 6.5, and 6.6), because it provides a fast and stable implementation of DFT. The convergence criterion in the self-consistent field algorithm was a change of energy below 10^{-7} hartree. The convergence criterion in the structure optimization was a gradient below 10^{-4} a.u. As a standard, the gradient-corrected density functional BP86 [184, 185] and a triple- ζ quality [529] all-electron basis set with polarization functions on all atoms (def-TZVP) were employed. Additional molecular

structure optimizations were performed using the PBE functional [186,530] and the B3LYP hybrid functional [191,531], with 20% of exact exchange admixture. For all pure functionals (BP86 and PBE) we used the resolution-of-the-identity (RI) approximation [532,533]. In Sections 3.3 and 3.5, a def-SVP [534] and a def2-TZVP [535] basis set were employed, respectively.

Most exchange–correlation functionals describe dispersion interactions poorly. Therefore, dispersion interactions were taken into account via Grimme’s empirical correction according to versions D2 [476] and D3 [198] with Becke-Johnson (BJ) damping [536]. In this correction schemes, an empirical dispersion term E_{disp} is added to the (conventional) DFT energy,

$$E_{\text{disp}} = -s_6 \sum_{A < B} \frac{C_6^{AB}}{R_{AB}^6} f_{\text{dmp}}(R_{AB}), \quad (\text{A.1})$$

where s_6 is a global scaling factor that only depends on the functional used and R_{AB} is the distance between the atoms A and B . The damping parameter f_{dmp} ensures the correct behavior for small distances. The C_6^{AB} dispersion coefficient of the atom pair AB is calculated from the C_6 coefficients as $C_6^{AB} = \sqrt{C_6^A C_6^B}$ (where the C_6^A coefficients are fitted parameters). Note that in Turbomole 6.0 no C_6 parameters are available for gold.

Spin-unrestricted calculations were performed for NO_2 (Sec. 4.5) and MnCp_2 (Sec. 3.4) systems. NO_2 has formally one unpaired electron, and the high-spin and low-spin state of MnCp_2 have five and two unpaired electrons, respectively.

Optimized molecular structures under periodic boundary conditions were obtained using the open-source electronic structure code QUANTUM ESPRESSO 5.0, which uses plane waves to account for the valence electrons and pseudopotentials for treating nuclei plus core electrons. Projector-augmented plane-wave pseudopotentials generated with GGA-PBE (PAW-PBE) [537] with Grimme’s empirical correction (D2) [476] were employed. In Table A.2, the settings for the respective model systems are shown. A Monkhorst-Pack-Grid with a Marzari-Vanderbilt smearing of 0.01 – 0.02 Ry to sample the Brillouin zone was used.

Given that it is not relevant for plane-wave calculations, and given the relatively large size of the employed atom-centered basis set, the basis superposition error was assumed to be negligible. The density functionals and basis sets used for the structure optimizations, frequency analyses and calculations of molecular properties are summarized in Table A.1.

Table A.1.: Computational settings used for the structure optimizations, vibrational frequency analyses and calculations of molecular properties using TURBOMOLE (TM) and QUANTUM ESPRESSO (QE) in the various sections of this thesis. Curly braces indicate constrained optimizations in which parts of the system were held fixed.

Sec.	System	Functional	Basis set	Prog.
3.2	{Au ₂₀ tip}+Por-TATA	BP86-D2	def-TZVP	TM6.0
	Por-TATA	BP86-D2, B3LYP-D2	def-TZVP	TM6.0
	Zn-porphyrin	BP86-D2, B3LYP-D2	def-TZVP	TM6.0
3.3	TOTA derivatives	BP86-D2, B3LYP-D2	def-TZVP	TM6.0
	TOTA+{3L Au ₉₀ }	BP86-D3(BJ)	def-SVP	TM6.5
3.4	MnCp ₂	BP86-D2, B3LYP-D2	def-TZVP	TM6.0
	Au ₂₀	BP86-D2	def-TZVP	TM6.0
	{Au ₂₀ tip}+MnCp ₂	BP86-D2	def-TZVP	TM6.0
3.5	CO+4L Pt(111)	PAW-PBE		QE5.0
	CO+{3L Cu ₂₂ }/{4L Cu ₃₈ }	BP86-D3(BJ)	def2-TZVP	TM6.6
	CO+3L Cu(111)	PAW-PBE		QE5.0
	{Cu ₁₀ tip}+CO+{4L Cu ₃₈ }	PBE-D3(BJ)	def2-TZVP	TM6.6
4.4	H ₂ O+(5,5)CNT	PAW-PBE-D2		QE5.0
4.5	NH ₃ /NO ₂	BP86-D3(BJ)	def-TZVP	TM6.6
		B3LYP-D3(BJ)	def-TZVP	TM6.6
		PBE-D3(BJ), PBE-D2	def-TZVP	TM6.6
		PAW-PBE-D2, PAW-PBE		QE5.0
	PAW-PBE-D2		QE5.0	
	NH ₃ /NO ₂ +(5,5)/(8,0)CNT	BP86-D3(BJ)	def-TZVP	TM6.5
		B3LYP-D3(BJ)	def-TZVP	TM6.5
PBE-D3(BJ), PBE-D2		def-TZVP	TM6.5	
	PAW-PBE-D2, PAW-PBE		QE5.0	
4.6	6 H/5 H/6 F/5 F	BP86-D3(BJ)	def-TZVP	TM6.5
		PAW-PBE-D2		QE5.0
	6 H/5 H/6 F/5 F+(5,5)CNT	BP86-D3(BJ)	def-TZVP	TM6.5
		PAW-PBE-D2		QE5.0

Table A.2.: Dimensions of the unit cells, minimum plane-wave cutoff for wavefunctions (E^{cut}) and charge density (ρ^{cut}), and k point settings for the model systems studied under periodic boundary conditions.

System	Cell dimensions (\AA^3)	E^{cut} (Ry)	ρ^{cut} (Ry)	k points
CO, NO ₂ , NH ₃	50 × 50 × 50	47	264	Γ point
(5,5) CNT	25 × 25 × 6.89	47	264	1 × 1 × 16
(8,0) CNT	25 × 25 × 8.86	47	264	1 × 1 × 16
H ₂ O + (5,5) CNT	20 × 20 × 7.39	50	800	1 × 1 × 16
NH ₃ /NO ₂ + (5,5) CNT	25 × 25 × 6.89	47	264	1 × 1 × 16
NH ₃ /NO ₂ + (8,0) CNT	25 × 25 × 8.86	47	264	1 × 1 × 16
6 H/5 H + (5,5) CNT	30 × 35 × 14.83	50	800	1 × 1 × 16
6 F/5 F + (5,5) CNT	30 × 35 × 14.83	50	800	1 × 1 × 16
CO + 4 layers Pt(111)	5.54 × 4.80 × 18.11	50	800	6 × 6 × 1
CO + 3 layers Cu(111)	7.67 × 8.85 × 20	50	800	4 × 4 × 1

Electron transport calculations

The transmission functions, conductance at zero-voltage, central subsystem MOs, and local transmissions were calculated using the post-processing tool ARTAIOS [206, 215]. In order to obtain the overlap and Fock matrices, single-point calculations using the G09 quantum chemistry program package [371] with the B3LYP functional and the Los Alamos (LANL2DZ) effective core potentials with matching basis sets [538–541] were employed. A small basis set was chosen to reduce ghost transmission [215], and B3LYP to bypass convergence problems occasionally encountered with BP86. The central subsystem MOs were calculated by solving the central subsystem’s secular equations and assigned by comparing their shape with the MOs of the isolated molecular bridges [542].

Molecular structures and local properties

The structures were generated with AVOGADRO [543], oriented with MODCO 1.2 written by J. Neugebauer (University of Münster) and mainly visualized with PYMOL [544]. The (subsystem) MOs were visualized with MOLDEN.

The adsorption energy (E_a) is defined as the difference between the energy of the total adsorbate–surface (or CNT) system ($E^{\text{ads-surf}}$) and the summed-up energy of the surface (E^{surf}) alone and the isolated adsorbate (E^{ads}),

$$E_a = E^{\text{ads-surf}} - (E^{\text{surf}} + E^{\text{ads}}). \quad (\text{A.2})$$

Mulliken and Löwdin partial charges were calculated using a locally modified version of MOLOCH [396]. Bader charges and atomic polarizations were obtained using AIMALL [438], MULTIWFN [439], and BADER [427, 429, 545]. The grid-based BADER tool written by the Henkelman group is well suited for large solid-state physical systems due to its computational efficiency. Each volume element of the three-dimensional grid was 0.10 Bohr wide, unless otherwise stated. Reference points and dipole moments were calculated using the LOCALDIP tool presented in Sec. 4.4. Dipole moments and local transmissions were visualized with a tool written by G. C. Solomon (University of Copenhagen) for modifying POVRAY files.

For the calculation of molecular vibrations, the MOVIPAC code [546] was employed using TM gradients. JMWL [547] and VMD [548] were used for the graphical representation of the normal modes and the electrostatic potential, respectively. The calculated data was plotted using GNUPLOT [549] and figures were illustrated using INKSCAPE [550].

B. Additional data

B.1. Local transmissions

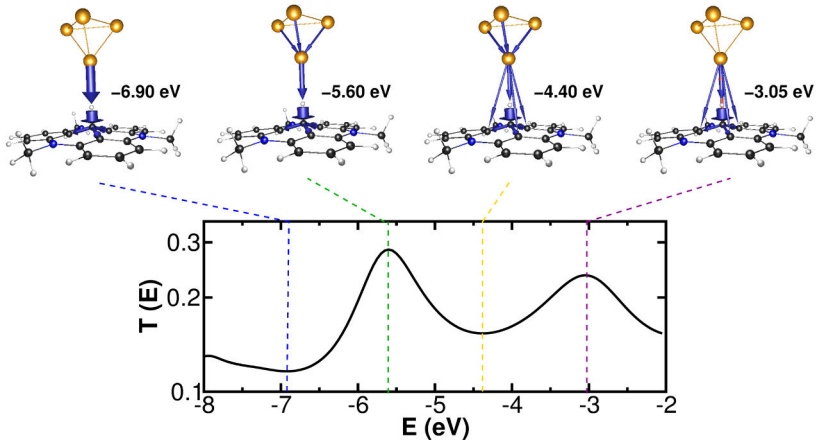


Figure B.1.: Representative local transmission plots for the TATA platform at an internuclear Au-H distance of $d_{Au-H} = 2.70$ Å. The diameter of the arrows is defined by the value of the local transmission for the atom pairs normalized to the largest contribution. Local transmission contributions in the same or opposite direction as the total current are indicated by blue and red arrows, respectively. Only contributions to the transmission larger than 10 % of the largest local transmission are shown. B3LYP/LANL2DZ.

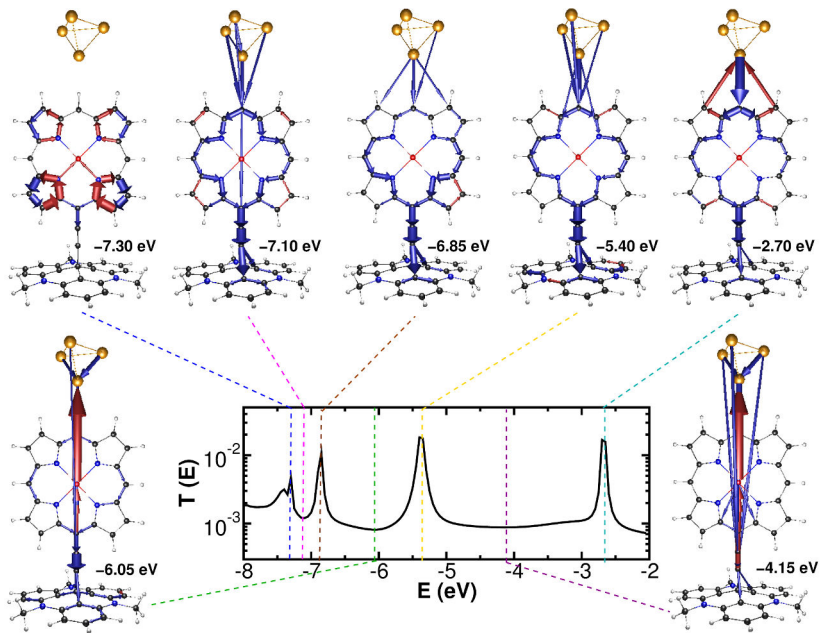


Figure B.2.: Representative local transmission plots for the Por-TATA at an internuclear Au-H distance of $d_{Au-H} = 2.70$ Å (corresponding to a tip-molecule distance of $d = 1.00$ Å). The diameter of the arrows are defined by the value of the local transmission for the atom pairs normalized to the largest contribution. Local transmission contributions in the same or opposite direction as the total current are indicated by blue and red arrows, respectively. Only contributions to the transmission larger than 10 % of the largest local transmission are shown. Note that the local transmission plots to the left and to the right of the graph at energies of -6.05 eV and -4.15 are affected by ghost transmission. B3LYP/LANL2DZ.

B.2. Infrared spectra

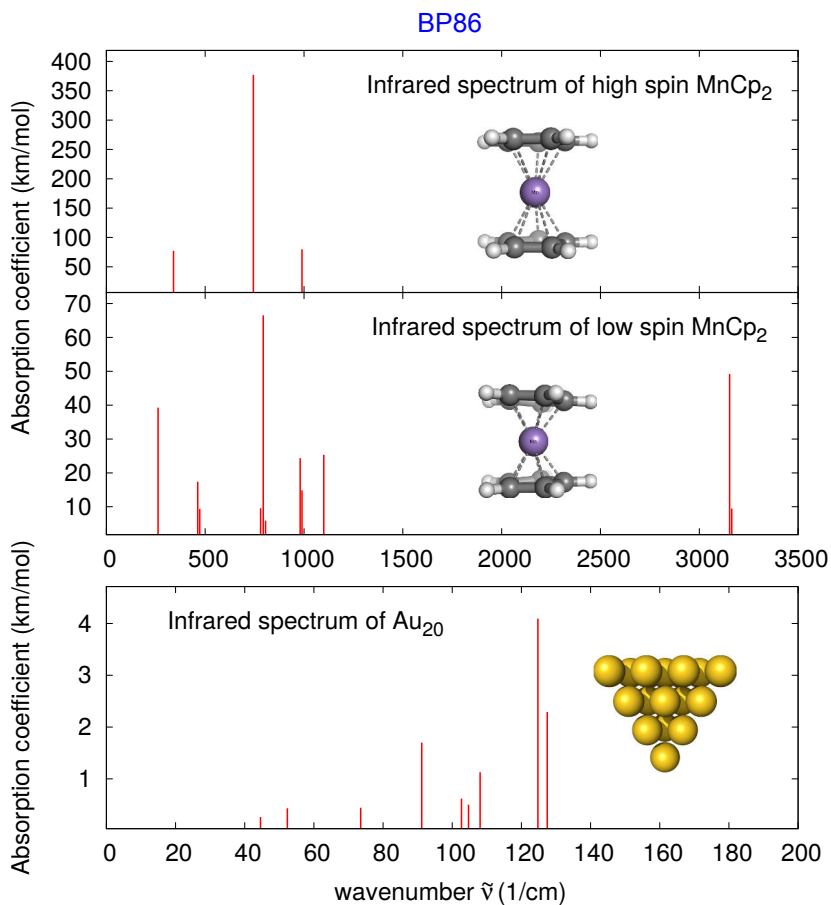


Figure B.3.: Infrared line spectra of manganocene (upper panel) and Au₂₀ (lower panel). BP86/def-TZVP.

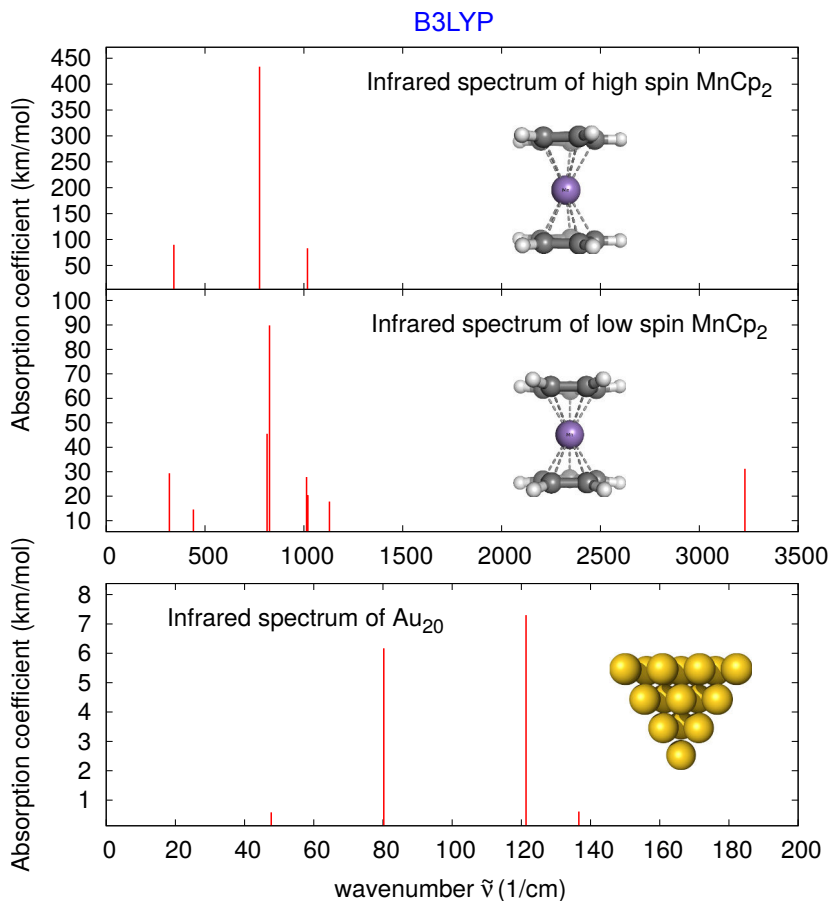


Figure B.4.: Infrared line spectra of manganocene (upper panel) and Au_{20} (lower panel). B3LYP/def-TZVP.

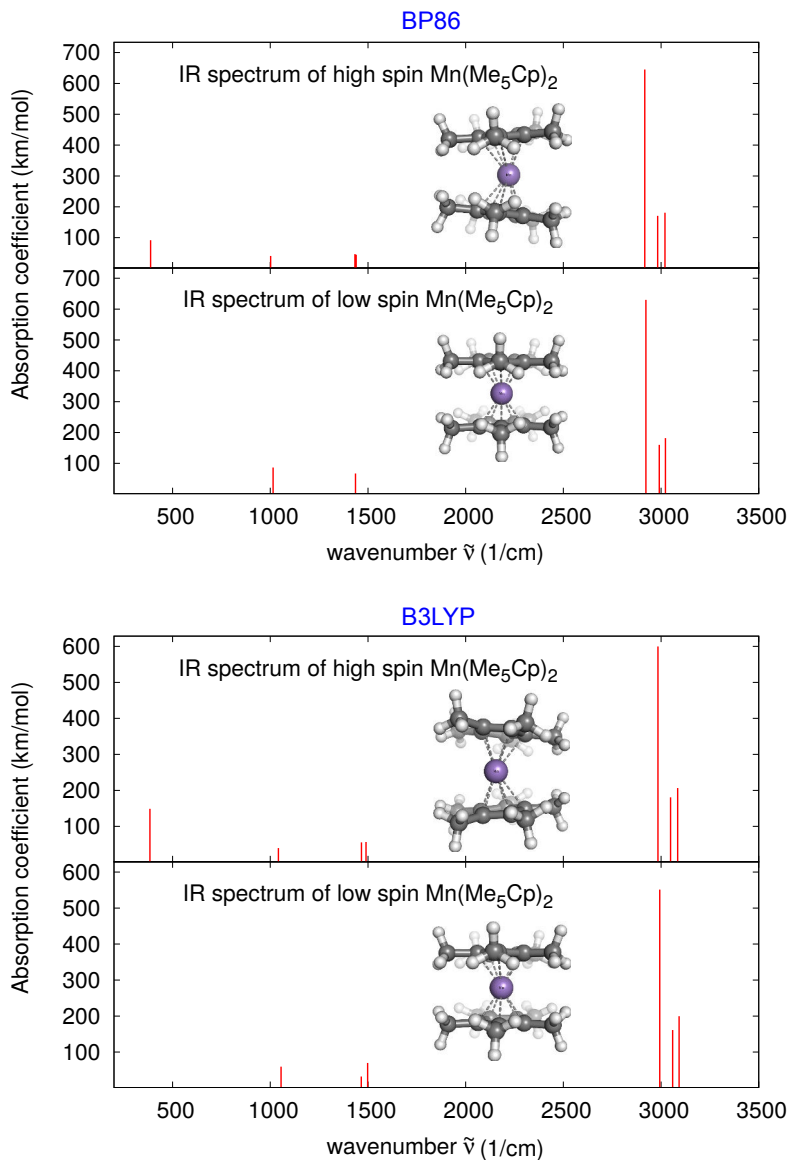


Figure B.5.: Infrared line spectra of decamethylmanganocene using BP86/def-TZVP (upper panel) and B3LYP/def-TZVP (lower panel).

B.3. Additional data on local dipole moments

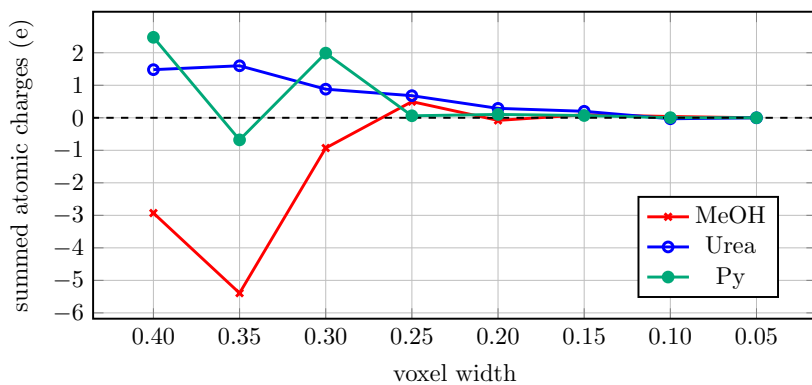


Figure B.6.: Summed atomic charges of methanol (MeOH), urea and pyridine (Py) as a function of the width of each grid volume element (in Bohr). Atomic charges are calculated using TURBOMOLE 6.6 in combination with the BADER tool.

Available software packages available for the analysis of the electron density

An overview of different software packages available for the analysis of the electron density according to the theory of AIM is given in Table B.1. No claim is made to completeness, timeliness, and accuracy.

Table B.1.: An overview of different software packages available for the analysis of the electron density according to the theory of Atoms-In-Molecules.

	AIMPAC [431–433]	AIMAll [438]	AIM2000 [551, 552]	Multiwfn [439]	Bader [427–429]	ADF [368]	XAIM [553]	DGrid [554]	XD2006 [555]	Horton [556]	PAMoC [557]	TopChem [558]	TopMoD [559]	DensToolKit [560]	MORPHY [561, 562]
Type of license															
Open source	×			×	×		×	×		×	×	×	×	×	×
Free demo		×	×												
Commercial		×	×			×			×						
Operating system															
Windows		×	×	×	×				×						
Linux	×	×		×	×	×	×	×	×	×	×	×	×		×
Mac OS X		×		×	×				×						
Input format															
.wfn/.wfx	×	×	×	×		×	×	×		×		×	×	×	×
.cube				×	×			×		×		×			
Other						×			×						
AIM properties															
Critical points	×	×	×	×		×	×	×	×	×	×		×	×	×
Atomic charges	×	×	×	×	×	×			×	×	×	×			
Atomic polarizations	×	×	×	×	×	×			×		×	×			

Examples of GenLocDip prompts and user response*Wavefunction-based AIM program*

```

-----
>> Choose Bader AIM program (default=aimall)
-----
multiwfn (m) : needs .wfn/.wfx/.fchk input file
aimall   (a) : needs .wfn/.wfx/.fchk input file
bader    (b) : needs .cube/.fchk input file
-----
a
-----
>> Name of input file (.wfn|.wfx|.fchk|.cube):
-----
waterdimer.wfn
-----
>> List of atoms in fragment   1
    (i.e. 1-5,12,34-55) ?
-----
1-3
-----
>> How many residual groups are connected to fragment 1? default=1
-----
1
-----
>> BCP b/w fragment 1 and residual 1 (default= sel Bcpnum)
-----
man <X Y Z> <atomF> <atomR>  - type in BCP coordinates manually
sel <Bcpnum>                  - select a BCP from a previous BCP search

  1  2.1476832246893700E-008  0.25979566099244700  3.0054016182053100  01  H5

bond <atomF> <atomR> <fac>    - guess a BCP along the bond of atom pairs
                                (0 < fac < 1)
aprx <atomF> <atomR>         - approximate a BCP from summed Bader volumes
                                of the fragment
-----
sel 1
-----
>> Do you want to continue (y/n)? default: n
-----
n

```

Grid-based AIM program

```

-----
>> Choose Bader AIM program (default=aimall)
-----
multiwfn (m) : needs .wfn/.wfx/.fchk input file
aimall   (a) : needs .wfn/.wfx/.fchk input file
bader    (b) : needs .cube/.fchk input file
-----
bader
-----
>> Name of input file (.wfn|.wfx|.fchk|.cube):
-----
waterdimer.cube
-----
>> List of atoms in fragment   1
    (i.e. 1-5,12,34-55) ?
-----
1-3
-----
>> How many residual groups are connected to fragment 1? default=1
-----
1
-----
>> BCP b/w fragment 1 and residual 1 (default= sel Bcpnum)
-----
man <X Y Z> <atomF> <atomR> - type in BCP coordinates manually
sel <Bcpnum>                - select a BCP from a previous BCP search
bond <atomF> <atomR> <fac>  - guess a BCP along the bond of atom pairs
                           (0 < fac < 1)
aprx <atomF> <atomR>        - approximate a BCP from summed Bader volumes
                           of the fragment
-----
aprx 1 4
-----
>> Do you want to continue (y/n)? default: n
-----
n

```

A closer look at charge transfer contributions

Here, we will take a closer look at some crucial equations derived by Laidig, Keith, Gough and Bader in Refs. [403] and [404], where it is suggested to express the charge transfer contribution to the dipole moment $\boldsymbol{\mu}^c$ as a sum of origin-independent terms, indicated as Eq. (16) in Ref. [403] and Eq. (12) in Ref. [404], respectively,

$$\boldsymbol{\mu}^c = \sum_{i=1}^n q_i \mathbf{X}_i = \sum_{i=1}^{n-1} q'_i (\mathbf{X}_i - \mathbf{X}_{i+1}), \quad (\text{B.1})$$

with q'_i being the net charge of a group of atoms i , $q'_i = \sum_{j=1}^i q_j$ (atom $j = 1, 2, \dots, i$). In what follows, Eq. (B.1) is verified with additional intermediate steps, and examples are discussed. We reformulate Eq. (B.1) as

$$\begin{aligned} \sum_{i=1}^n q_i \mathbf{X}_i &= \sum_{i=1}^{n-1} \sum_{j=1}^i q_j (\mathbf{X}_i - \mathbf{X}_{i+1}) \\ &= \sum_{i=1}^{n-1} \sum_{j=1}^i q_j \mathbf{X}_i - \sum_{i=1}^{n-1} \sum_{j=1}^i q_j \mathbf{X}_{i+1} \\ &= \sum_{i=1}^{n-1} \sum_{j=1}^i q_j \mathbf{X}_i - \sum_{i=2}^n \sum_{j=1}^{i-1} q_j \mathbf{X}_i \\ &= (q_1 \mathbf{X}_1 + \sum_{i=2}^{n-1} \sum_{j=1}^i q_j \mathbf{X}_i - \sum_{i=1}^{n-1} \sum_{j=1}^{i-1} q_j \mathbf{X}_i - \sum_{j=1}^{n-1} q_j \mathbf{X}_n) \\ &= q_1 \mathbf{X}_1 - \sum_{j=1}^{n-1} q_j \mathbf{X}_n + \sum_{i=2}^{n-1} \left(\sum_{j=1}^i q_j \mathbf{X}_i - \sum_{j=1}^{i-1} q_j \mathbf{X}_i \right) \\ &= q_1 \mathbf{X}_1 - \sum_{j=1}^{n-1} q_j \mathbf{X}_n + \sum_{i=2}^{n-1} q_i \mathbf{X}_i \\ &= q_1 \mathbf{X}_1 + \sum_{i=2}^{n-1} q_i \mathbf{X}_i + q_n \mathbf{X}_n \\ &= \sum_i^n q_i \mathbf{X}_i. \end{aligned} \quad (\text{B.2})$$

Furthermore, the charge transfer contribution to the dipole moment of a methyl group $\mu^c(\text{CH}_3)$ connected to a residual group is given as an example, indicated as Eq. (18) in Ref. [403] and Eq. (14) in Ref. [404], respectively,

$$\mu^c(\text{CH}_3) = \sum_{k=1}^3 [\mathbf{X}_{\text{H}_k} - \mathbf{X}_\text{C}] q_{\text{H}_k} + [\mathbf{X}_\text{C} - \mathbf{X}^c(\text{CH}_3|\text{R})] q_{\text{CH}_3}, \quad (\text{B.3})$$

where index C and H_k ($k = 1, 2, 3$) denote the carbon atom and the hydrogen atoms, respectively, and $\mathbf{X}^c(\text{CH}_3|\text{R})$ is the bond critical point between the methyl group and the remainder R . The carbon atom is singled out the atom within the fragment which makes the chemical bond to the remainder of the system.

In the following equation, we show that the methyl group dipole moment derived in Eq. (B.3) is consistent with the expression one can derive starting from the total charge transfer contribution of a $\text{CH}_3\text{-R}$ system which is given by

$$\begin{aligned} \mu^c(\text{CH}_3 - \text{R}) &= \sum_{k=1}^3 q_{\text{H}_k} \mathbf{X}_{\text{H}_k} + q_\text{C} \mathbf{X}_\text{C} + q_\text{R} \mathbf{X}_\text{R} \\ &= \sum_{k=1}^3 q_{\text{H}_k} [\mathbf{X}_{\text{H}_k} - \mathbf{X}_\text{C}] + q_\text{R} \mathbf{X}_\text{R} + q_\text{C} \mathbf{X}_\text{C} + \underbrace{\sum_{k=1}^3 q_{\text{H}_k} \mathbf{X}_\text{C}}_{q_{\text{CH}_3} \mathbf{X}_\text{C}} \\ &= \sum_{k=1}^3 q_{\text{H}_k} [\mathbf{X}_{\text{H}_k} - \mathbf{X}_\text{C}] + q_\text{R} [\mathbf{X}_\text{R} - \mathbf{X}^c(\text{CH}_3|\text{R})] \\ &\quad + q_{\text{CH}_3} [\mathbf{X}_\text{C} - \mathbf{X}^c(\text{CH}_3|\text{R})] + \underbrace{q_\text{R} \mathbf{X}^c(\text{CH}_3|\text{R}) + q_{\text{CH}_3} \mathbf{X}^c(\text{CH}_3|\text{R})}_{=0, \text{ since } q_\text{R} = -q_{\text{CH}_3}} \\ &= \underbrace{\sum_{k=1}^3 q_{\text{H}_k} [\mathbf{X}_{\text{H}_k} - \mathbf{X}_\text{C}] + q_{\text{CH}_3} [\mathbf{X}_\text{C} - \mathbf{X}^c(\text{CH}_3|\text{R})]}_{\text{CT contribution from CH}_3, \text{ equals Eq. (B.3)}} \\ &\quad + \underbrace{q_\text{R} [\mathbf{X}_\text{R} - \mathbf{X}^c(\text{CH}_3|\text{R})]}_{\text{CT contribution from R}}. \end{aligned} \quad (\text{B.4})$$

As another example, the charge transfer contribution to the dipole moment of a methylene group $\boldsymbol{\mu}^c(\text{CH}_2)$ connected to two residual groups is defined, indicated as Eq. (16) in Ref. [404],

$$\begin{aligned} \boldsymbol{\mu}^c(\text{CH}_2) &= \sum_{k=1}^2 q_{\text{H}_k} [\mathbf{X}_{\text{H}_k} - \mathbf{X}_{\text{C}}] + q_{\text{CH}_2} [\mathbf{X}_{\text{C}} - \mathbf{X}^c(\text{CH}_2|\text{R}')] \\ &\quad + q_{\text{R}} [\mathbf{X}^c(\text{CH}_2|\text{R}) - \mathbf{X}^c(\text{CH}_2|\text{R}')], \end{aligned} \quad (\text{B.5})$$

where $\mathbf{X}^c(\text{CH}_2|\text{R})$ and $\mathbf{X}^c(\text{CH}_2|\text{R}')$ are the bond critical points that correspond to the remainder R and R', respectively. Eq. (B.6) shows that the methylene group dipole moment derived in Eq. (B.5) is as well consistent with the expression one can derive starting from the total charge transfer contribution of a R – CH₂ – R' system. The latter can be expressed as

$$\begin{aligned} \boldsymbol{\mu}^c(\text{R} - \text{CH}_2 - \text{R}') &= \sum_{k=1}^2 q_{\text{H}_k} \mathbf{X}_{\text{H}_k} + q_{\text{C}} \mathbf{X}_{\text{C}} + q_{\text{R}} \mathbf{X}_{\text{R}} + q_{\text{R}'} \mathbf{X}_{\text{R}'} \\ &= \sum_{k=1}^2 q_{\text{H}_k} [\mathbf{X}_{\text{H}_k} - \mathbf{X}_{\text{C}}] + q_{\text{R}} \mathbf{X}_{\text{R}} + q_{\text{R}'} \mathbf{X}_{\text{R}'} \\ &\quad + \underbrace{q_{\text{C}} \mathbf{X}_{\text{C}} + \sum_{k=1}^2 q_{\text{H}_k} \mathbf{X}_{\text{C}}}_{q_{\text{CH}_2} \mathbf{X}_{\text{C}}} \\ &= \sum_{k=1}^2 q_{\text{H}_k} [\mathbf{X}_{\text{H}_k} - \mathbf{X}_{\text{C}}] + q_{\text{R}} \mathbf{X}_{\text{R}} + q_{\text{R}'} \mathbf{X}_{\text{R}'} \\ &\quad + q_{\text{CH}_2} [\mathbf{X}_{\text{C}} - \mathbf{X}^c(\text{CH}_2|\text{R}')] + q_{\text{CH}_2} \mathbf{X}^c(\text{CH}_2|\text{R}') \\ &= \sum_{k=1}^2 q_{\text{H}_k} [\mathbf{X}_{\text{H}_k} - \mathbf{X}_{\text{C}}] + q_{\text{R}} \mathbf{X}_{\text{R}} \\ &\quad + q_{\text{R}'} [\mathbf{X}_{\text{R}'} - \mathbf{X}^c(\text{CH}_2|\text{R}')] + q_{\text{CH}_2} [\mathbf{X}_{\text{C}} - \mathbf{X}^c(\text{CH}_2|\text{R}')] \\ &\quad + \underbrace{q_{\text{CH}_2} \mathbf{X}^c(\text{CH}_2|\text{R}') + q_{\text{R}'} \mathbf{X}^c(\text{CH}_2|\text{R}')}_{= -q_{\text{R}} \mathbf{X}^c(\text{CH}_2|\text{R}'), \text{ since } q_{\text{CH}_2} + q_{\text{R}'} = -q_{\text{R}}} \end{aligned}$$

$$\begin{aligned}
 &= \sum_{k=1}^2 q_{H_k} [\mathbf{X}_{H_k} - \mathbf{X}_C] + q_R [\mathbf{X}_R - \mathbf{X}^c(\text{CH}_2|\text{R})] \\
 &\quad + q_{R'} [\mathbf{X}_{R'} - \mathbf{X}^c(\text{CH}_2|\text{R}')] + q_{\text{CH}_2} [\mathbf{X}_C - \mathbf{X}^c(\text{CH}_2|\text{R}')] \\
 &\quad + \underbrace{q_R \mathbf{X}^c(\text{CH}_2|\text{R}) - q_R \mathbf{X}^c(\text{CH}_2|\text{R}')}_{=q_R [\mathbf{X}^c(\text{CH}_2|\text{R}) - \mathbf{X}^c(\text{CH}_2|\text{R}')] } \\
 &= \sum_{k=1}^2 q(H_k) [\mathbf{X}_{H_k} - \mathbf{X}_C] + q_R [\mathbf{X}_R - \mathbf{X}^c(\text{CH}_2|\text{R})] \\
 &\quad + q_{R'} [\mathbf{X}_{R'} - \mathbf{X}^c(\text{CH}_2|\text{R}')] + q_{\text{CH}_2} [\mathbf{X}_C - \mathbf{X}^c(\text{CH}_2|\text{R}')] \\
 &\quad + q_R [\mathbf{X}^c(\text{CH}_2|\text{R}) - \mathbf{X}^c(\text{CH}_2|\text{R}')] . \tag{B.6}
 \end{aligned}$$

Based on these examples, we now derive a general expression for the dipole moment of a fragment within Bader and Laidig's approach.

The charge transfer contribution is divided into fragment F and n residual group R_i contributions (with $i = 1, 2, \dots, n$),

$$\boldsymbol{\mu}^c = \sum_A \mathbf{X}_A q_A = \sum_{A \in F} \mathbf{X}_A q_A + \sum_{i=1}^n \sum_{A \in R_i} \mathbf{X}_A q_A . \tag{B.7}$$

We reformulate all nuclear coordinates \mathbf{X}_A , that correspond to the fragment contribution, with respect to an atom A^R within the fragment, sharing an interatomic surface with the remaining group(s) of the system,

$$\boldsymbol{\mu}^c = \sum_{A \neq A^R \in F} [\mathbf{X}_A - \mathbf{X}(A^R)] q_A + \mathbf{X}(A^R) q_F + \sum_{i=1}^n \sum_{A \in R_i} \mathbf{X}_A q_A \tag{B.8}$$

and all \mathbf{X}_A coordinates of the second term (contributions of residual group) with respect to an bond critical point between the fragment F and the respective residual groups R_i , $\mathbf{X}^c(F|R_i)$,

$$\begin{aligned}
 \boldsymbol{\mu}^c &= \sum_{A \neq A^R \in F} [\mathbf{X}_A - \mathbf{X}(A^R)] q_A + \mathbf{X}(A^R) q_F + \sum_{i=1}^n \mathbf{X}^c(F|R_i) q_{R_i} \\
 &\quad + \sum_{i=1}^n \sum_{A \in R_i} [\mathbf{X}_A - \mathbf{X}^c(F|R_i)] q_A, \tag{B.9}
 \end{aligned}$$

By reformulating the third term with respect to $\mathbf{X}^r(F|R_n)$, we get

$$\begin{aligned}
 \boldsymbol{\mu}^c &= \sum_{A \neq A^R \in F} \left[\mathbf{X}_A - \mathbf{X}(A^R) \right] q_A + \mathbf{X}(A^R) q_F + \mathbf{X}^c(F|R_n) \sum_{i=1}^n q_{R_i} \\
 &+ \sum_{i=1}^{n-1} [\mathbf{X}^c(F|R_i) - \mathbf{X}^c(F|R_n)] q_{R_i} \\
 &+ \sum_{i=1}^n \sum_{A \in R_i} [\mathbf{X}_A - \mathbf{X}^c(F|R_i)] q_A. \tag{B.10}
 \end{aligned}$$

In Eq. B.10, we can insert $q_F = -\sum_{i=1}^n q_{R_i}$ (as the system has neutral charge) which leads us to an origin independent expression for the charge transfer contribution,

$$\begin{aligned}
 \boldsymbol{\mu}^c &= \sum_{A \neq A^R \in F} \left[\mathbf{X}_A - \mathbf{X}(A^R) \right] q_A + \left[\mathbf{X}(A^R) - \mathbf{X}^c(F|R_n) \right] q_F \\
 &+ \sum_{i=1}^{n-1} [\mathbf{X}^c(F|R_i) - \mathbf{X}^c(F|R_n)] q_{R_i} \\
 &+ \sum_{i=1}^n \sum_{A \in R_i} [\mathbf{X}_A - \mathbf{X}^c(F|R_i)] q_A, \tag{B.11}
 \end{aligned}$$

Finally, assigning the second term to the fragment contribution, we obtain a general definition of fragment dipole moments,

$$\begin{aligned}
 \boldsymbol{\mu}_F^c &= \sum_{A \neq A^R \in F} \left[\mathbf{X}_A - \mathbf{X}(A^R) \right] q_A + \left[\mathbf{X}(A^R) - \mathbf{X}^c(F|R_n) \right] q_F \\
 &+ \sum_{i=1}^{n-1} [\mathbf{X}^c(F|R_i) - \mathbf{X}^c(F|R_n)] q_{R_i}. \tag{B.12}
 \end{aligned}$$

B.4. Additional data on noncovalent functionalization of CNTs

Molecular structures

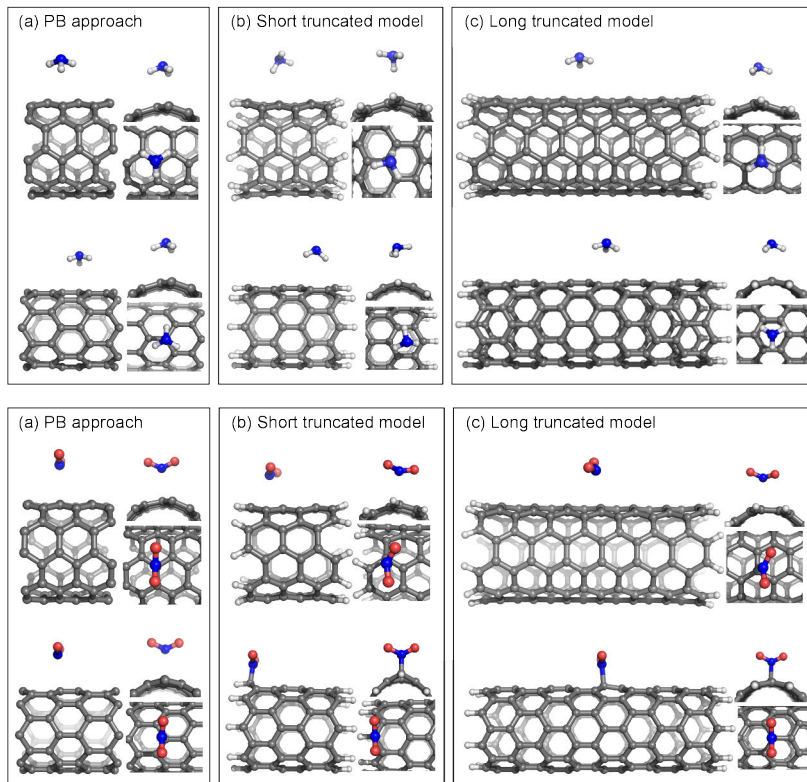


Figure B.7.: Optimized structures of a metallic (5,5) and a semi-conducting (8,0) single-walled CNT functionalized with NH₃ (upper panel) and NO₂ (lower panel) using (a) a periodic boundary (PB) approach (PAW-PBE-D2), a (b) short and (c) long truncated model (PBE-D2/def-TZVP).

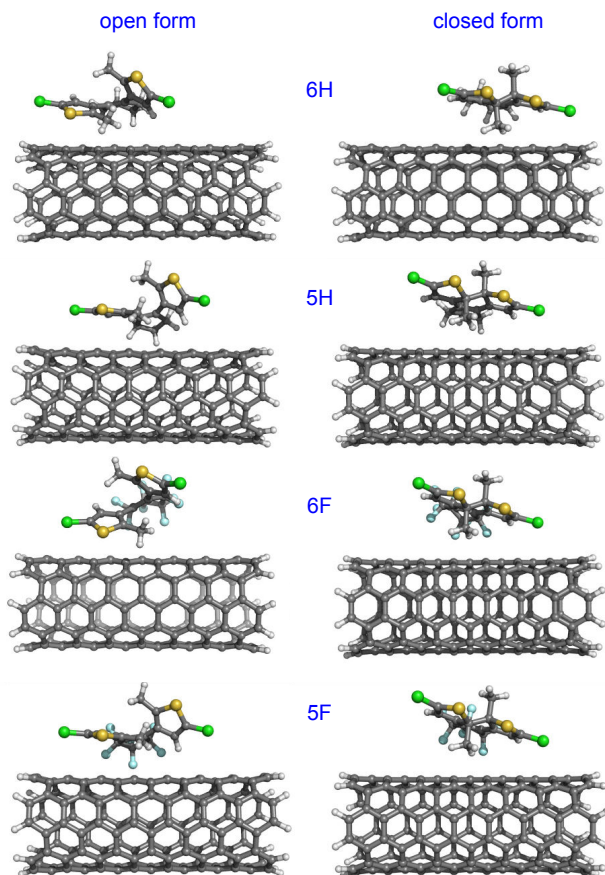


Figure B.8.: Optimized structures of DAE-functionalized metallic (5,5) CNTs using a truncated model (19 Å tube length). The thiophene groups are oriented parallel to the nanotube axis. BP86-D3(BJ)/def-TZVP.

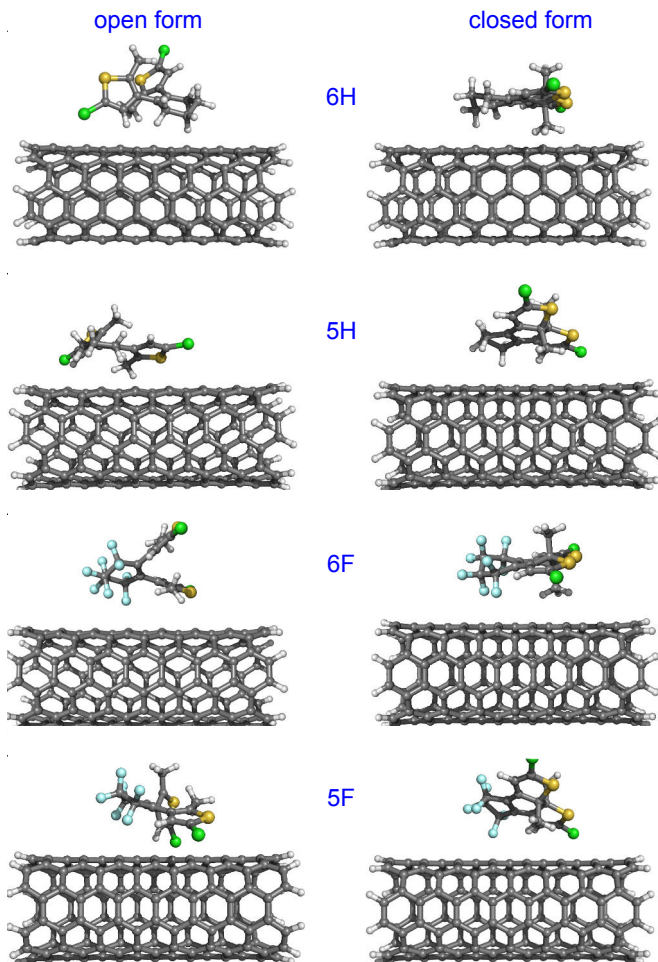


Figure B.9.: Optimized structures of DAE-functionalized metallic (5,5) CNTs using a truncated model (19 Å tube length). The thiophene groups are oriented perpendicular to the nanotube axis. BP86-D3(BJ)/def-TZVP.

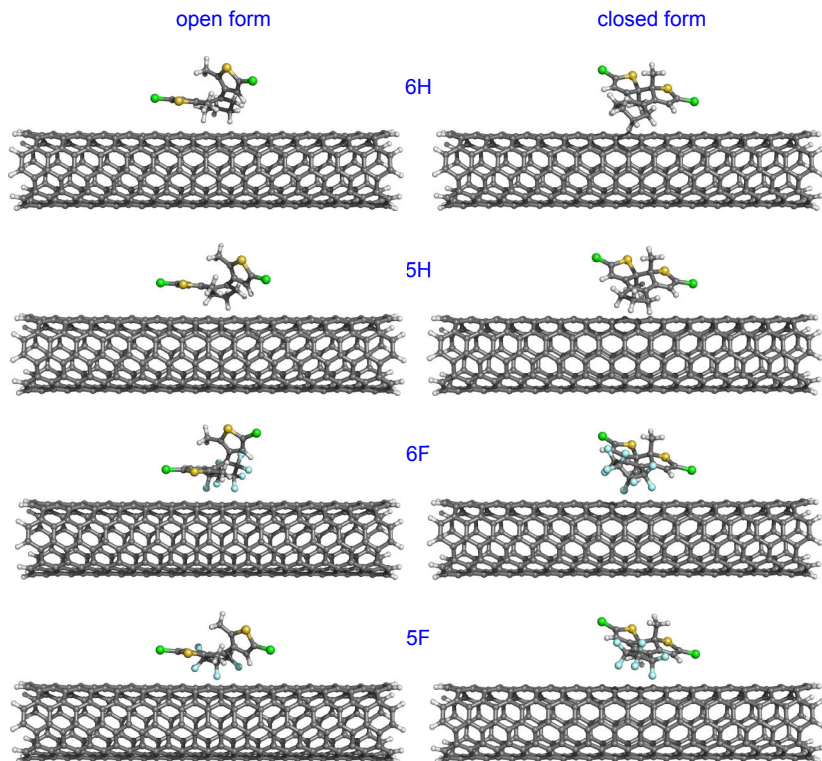


Figure B.10.: Optimized structures of DAE-functionalized metallic (5,5) CNTs using a truncated model (36 Å tube length). The thiophene groups are oriented parallel to the nanotube axis. BP86-D3(BJ)/def-TZVP.

Löwdin and Mulliken charges

Table B.2.: Partial Mulliken and Löwdin charges (in unit charges) of a NH_3 and a NO_2 molecule on a metallic (5,5) CNT and a semi-conducting (8,0) CNT using a periodic-boundary code and a truncated approach (Basis set: def-TZVP) with two different tube lengths (short: 8 Å and long: 19 Å).

Method	Functional	Mulliken		Löwdin	
		(5,5) CNT	(8,0) CNT	(5,5) CNT	(8,0) CNT
NH_3 molecule					
Periodic-boundary	PBE	–	–	0.15	0.03
	PBE-D2	–	–	0.15	0.06
Short truncated	PBE-D2	0.05	0.05	0.04	0.04
	PBE-D3	0.02	0.04	0.02	0.03
	BP86-D3	0.04	0.05	0.03	0.03
	B3LYP-D3	0.02	0.02	0.02	0.02
Long truncated	PBE-D2	0.04	0.05	0.03	0.04
	PBE-D3	0.03	0.04	0.03	0.04
	BP86-D3	0.04	0.05	0.03	0.03
	B3LYP-D3	0.03	0.03	0.02	0.02
NO_2 molecule					
Periodic-boundary	PBE	–	–	0.04	0.10
	PBE-D2	–	–	0.02	0.09
Short truncated	PBE-D2	–0.21	–0.05	–0.17	–0.12
	PBE-D3	–0.21	–0.05	–0.17	–0.12
	BP86-D3	–0.22	–0.06	–0.18	–0.13
	B3LYP-D3	–0.12	–0.09	–0.09	–0.14
Long truncated	PBE-D2	–0.16	–0.11	–0.12	–0.13
	PBE-D3	–0.16	–0.10	–0.12	–0.13
	BP86-D3	–0.17	–0.11	–0.13	–0.14
	B3LYP-D3 ^a	–	–0.11	–	–0.15

^a The results for the NO_2 -(5,5) CNT system using B3LYP-D3 are not shown due to convergence problems.

Table B.3.: Partial Mulliken and Löwdin charges (in unit charges) of DAE molecules on a metallic (5,5) CNT using a periodic-boundary code and a truncated approach (Basis set: def-TZVP) with two different tube lengths (short: 19 Å and long: 36 Å). The thiophene groups are oriented either parallel (||) or perpendicular (⊥) to the nanotube axis.

Method	Functional	6H		5H		6F		5F	
		o	c	o	c	o	c	o	c
Mulliken									
Short	BP86-D3(BJ)	0.00	0.04	0.02	0.04	-0.02	0.00	0.12	0.00
	⊥ BP86-D3(BJ)	0.01	0.05	0.03	0.03	-0.01	0.01	0.09	0.03
Long	BP86-D3(BJ)	0.00	0.03	0.03	0.04	-0.02	0.01	0.00	0.00
Löwdin									
PB	PBE	1.28	1.24	1.22	1.18	1.58	1.51	1.44	1.38
	PBE-D2	1.19	1.39	1.28	1.32	1.64	1.57	1.49	1.44
	⊥ ^a PBE-D2	1.20	1.34	—	1.27	1.64	1.57	—	1.51
Short	BP86-D3(BJ)	0.12	0.12	0.13	0.12	0.12	0.11	0.30	0.10
	⊥ BP86-D3(BJ)	0.12	0.13	0.13	0.11	0.12	0.05	0.31	0.11
Long	BP86-D3(BJ)	0.14	0.13	0.13	0.12	0.13	0.12	0.14	0.10

^a The results for (o)-5H and (c)-5F with perpendicular orientation could not be obtained due to convergence problems.

Electrostatic potentials

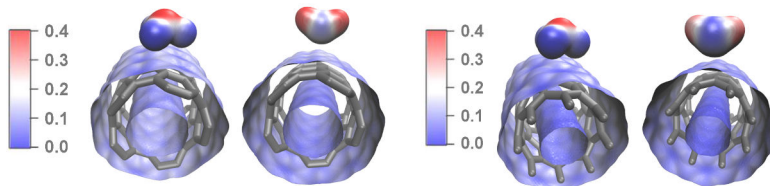


Figure B.11.: Total electrostatic potential of a NH_3 and a NO_2 molecule on a metallic (5,5) CNT (left) and a semi-conducting (8,0) CNT (right) using a periodic boundary code (PAW-PBE-D2). Sliced perpendicular to the nanotube axis and passing through the adsorbate. The contour value is 0.00 to 0.05 au.

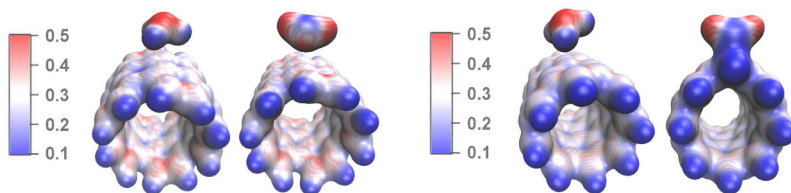


Figure B.12.: Total electrostatic potential of a NH_3 and a NO_2 molecule on a metallic (5,5) CNT (left) and a semi-conducting (8,0) CNT (right) using a short truncated model (PBE-D2/def-TZVP). Sliced perpendicular to the nanotube axis and passing through the adsorbate. The contour value is 0.00 to 0.05 au.

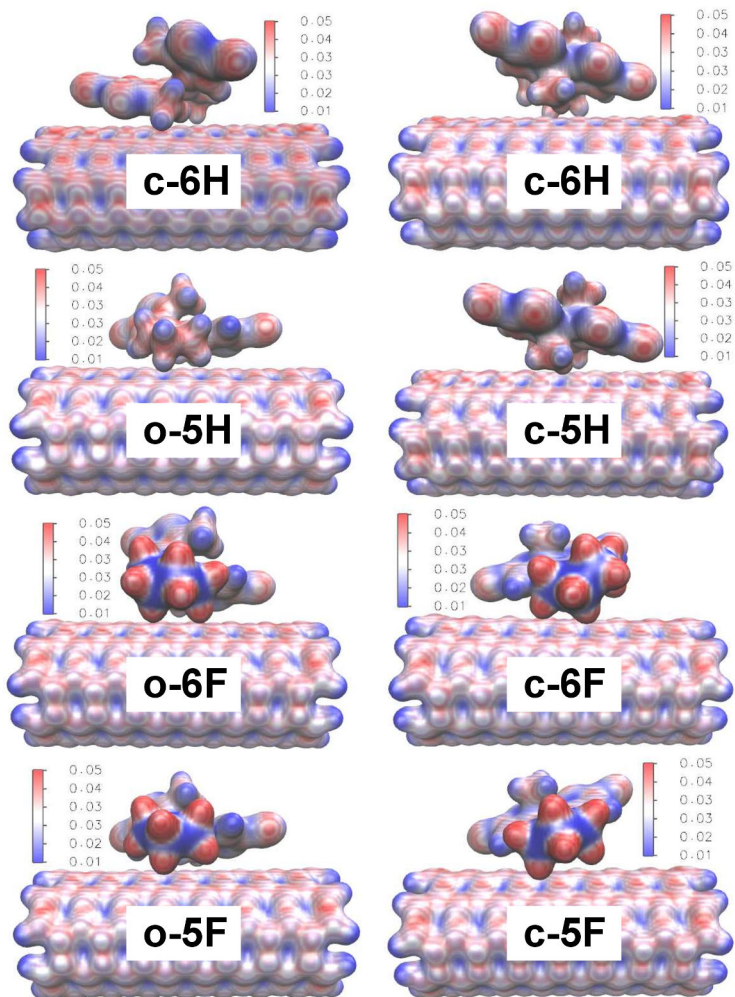


Figure B.13.: Total electrostatic potential of DAE molecules on a metallic (5,5) CNT using a short truncated model (BP86-D3(BJ)/def-TZVP). The thiophene units are oriented parallel to the nanotube axis. The contour value is 0.01 to 0.05 au.

Density of states

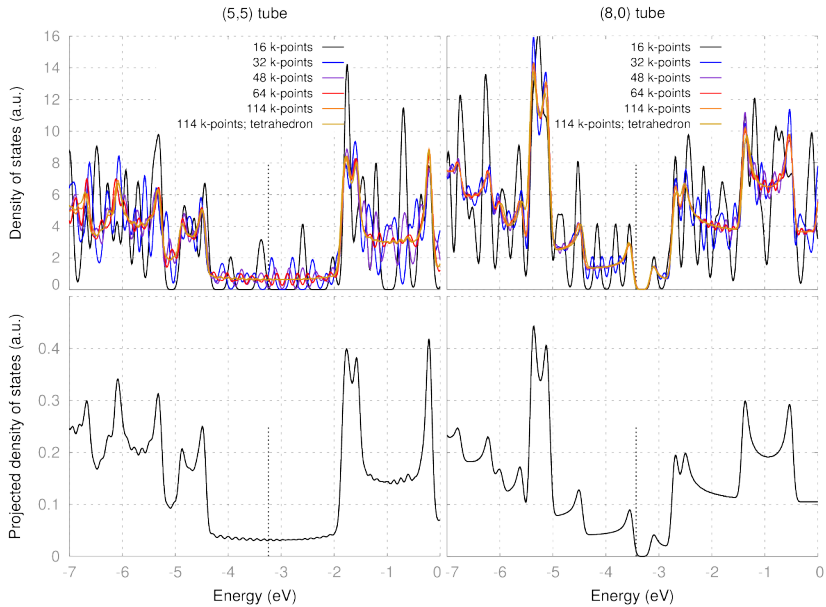


Figure B.14.: Upper panel: Total DOS plots for a metallic (5,5) and a semiconducting (8,0) carbon nanotube depending on the number of k points in z -dimension $M_z = 16, 32, 48, 64, 114$. Lower panel: p contributions of the projected DOS using 114 k points along the tube axis (s contributions are neglected). The unit cell of a pristine semiconducting (8,0) consists $25 \times 25 \times 4.44 \text{ \AA}^3$ (32 atoms) or a metallic (5,5) $25 \times 25 \times 2.48 \text{ \AA}^3$ (20 atoms) carbon nanotube. Settings: PAW-PBE-D2. The vertical dotted line marks the Fermi energy E_F .

In the upper panel of Figure B.14, the total densities of states (DOS) for a metallic (5,5) and a semiconducting (8,0) CNT using different numbers of k points in z -dimension, $M_z = 16, 32, 48, 64, 114$ (and the tetrahedron method for $M_z = 114$), are plotted against the energy. The projected DOS (PDOS) are plotted in the lower panel of Figure B.14 for a metallic (5,5) and semiconducting (8,0) CNT, respectively. Since the PDOS is determined by the p contributions, the s contributions are neglected.

Using a low number of k points results in a DOS equal to zero even for a metallic CNT, which would lead to an artificial band gap near the Fermi energy. The DOS starts to oscillate around the expected one upon increasing the number of k points, leading to accurate results with a number of k points of $M_z = 114$. For a (5,5)

metallic CNT, the density of states at the Fermi energy is constant as a function of energy, while there is a energy gap for a (8,0) semiconducting CNT. The DOS for both nanotubes show van Hove singularities of one-dimensional systems.

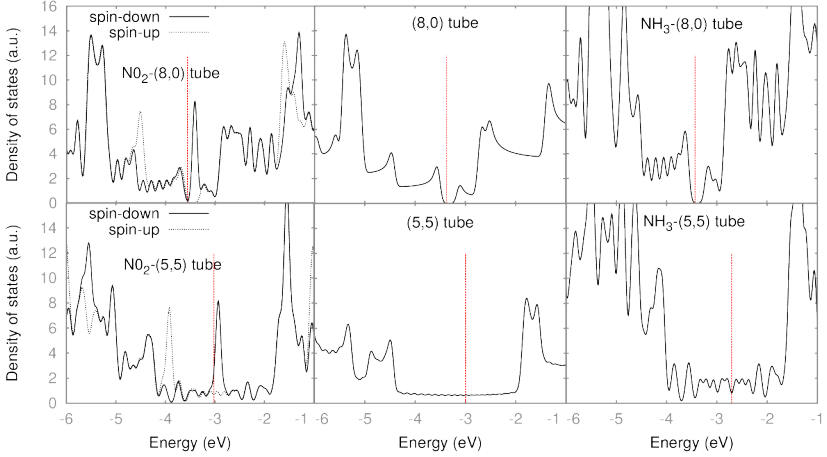


Figure B.15.: Density of states (DOS) of a semi-conducting (8,0) CNT (upper panel) and a metallic (5,5) CNT (lower panel) functionalized with NO_2 (left) and with NH_3 (right) compared with a pristine nanotube (middle) using the PB model (PAW-PBE-D2, tetrahedron method). A higher value of k points in z -dimension is used for the pure nanotube ($M_z = 114$) in comparison to the functionalized tubes ($M_z = 16$). The vertical dotted (red) line marks the Fermi energy E_F .

To further elucidate the changes in the electronic structure due to gas adsorption, analyses of the density of states (DOS) were performed using the PB model. DOS diagrams of a (5,5) CNT and a (8,0) CNT before and after the gas adsorption are shown in Figure B.15. For NH_3 adsorption, there is no hybridization and only little interaction between orbitals of the gas molecule and the CNT is visible. Thus, the charge transfer to the nanotube is expected to be negligible. It is important to note that lower values of k points in z -dimension are used for the functionalized nanotubes ($M_z = 16$) in comparison to the pure tubes ($M_z = 114$), as the unit cell is smaller in that direction for the latter. Therefore, artificial fluctuations in the DOS at the Fermi energy (vertical dotted line) occur. The left panel of Figure B.15 shows that an additional peak around the Fermi energy appears for “spin-down” electrons in the NO_2 case. This state is missing for the “spin-up” electrons. The lowest unoccupied molecular orbital (LUMO) is energetically close to the Fermi level of the pristine carbon nanotube. This indicates a large charge transfer from the nanotube to the NO_2 molecule.

Band structures

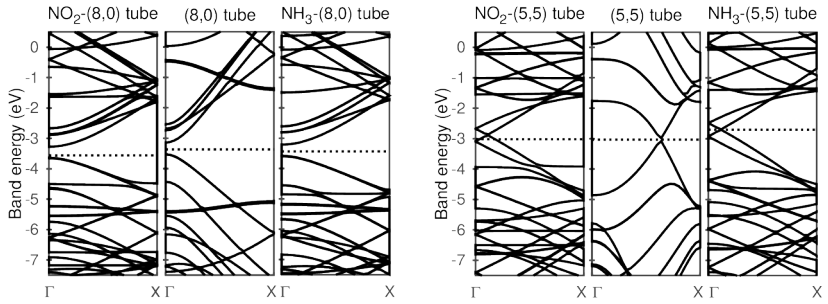


Figure B.16.: Electronic band structures of a semi-conducting (8,0) (left) and a metallic (5,5) (right) CNT functionalized with NO_2 and with NH_3 compared with the pristine nanotubes using the PB model (PAW-PBE-D2). The dotted line marks the Fermi energy E_F .

Molecular orbital diagram

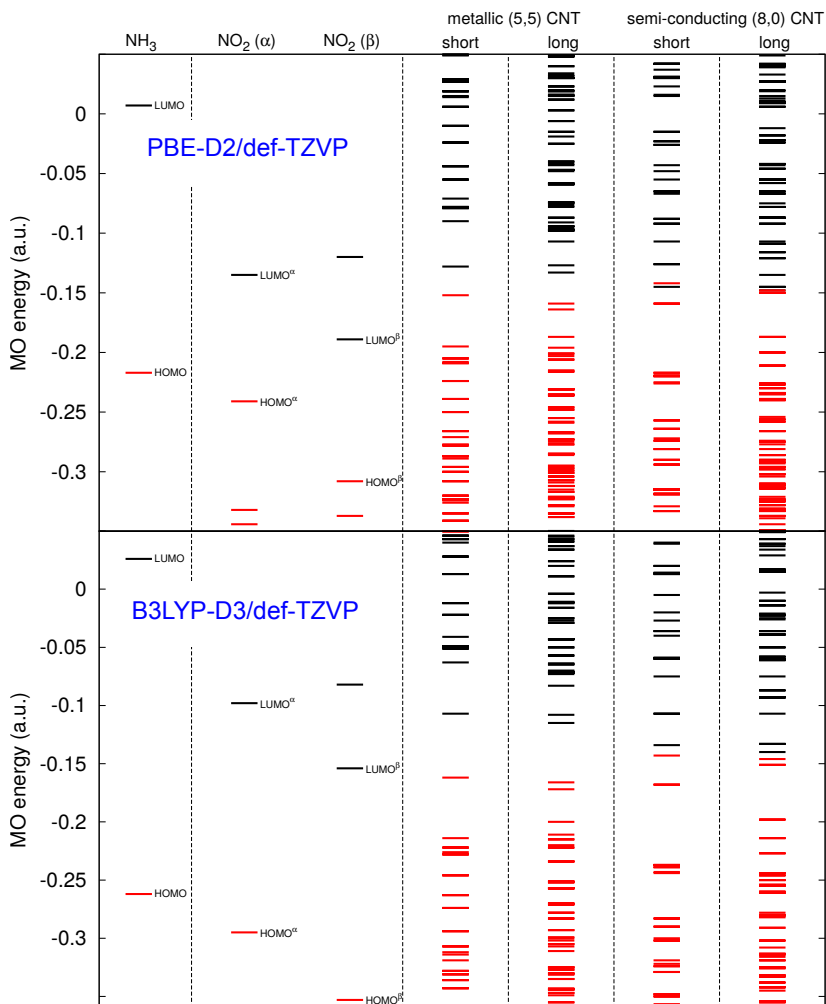


Figure B.17.: Calculated molecular orbital (MO) diagrams for isolated subsystems: NH₃, NO₂, (5,5) and (8,0) single-walled CNTs using PBE-D2/def-TZVP (upper panel) and B3LYP-D3(BJ)/def-TZVP (lower panel).

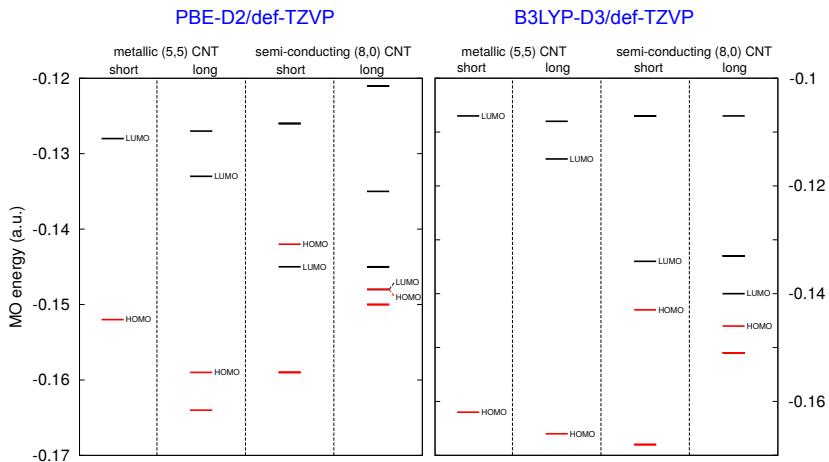


Figure B.18.: Enlarged section from Fig. B.17 for truncated (5,5) and (8,0) single walled CNTs of different length using PBE-D2/def-TZVP (left panel) and B3LYP-D3(BJ)/def-TZVP (right panel).

C. List of notations

A acceptor. 103

\mathbf{a} vector along the carbon nanotube axis. 57

\mathbf{c} circumferential (“chiral”) vector. 57

$\chi_{d,a}$ nuclear states of donor and acceptor state. 97

C coefficient. 16

d diameter. 58

d distance. 34, 53

D donor. 103

e unit charge. 9

E_a adsorption energy. 81

E_{ee} electron–electron interaction energy. 10

E_0 ground state energy. 10

E energy eigenvalue. 9

E_F Fermi energy. 11, 12, 21

E_{gap} HOMO-LUMO energy gap. 46

$\varepsilon_{\chi_d}, \varepsilon_{\chi_a}$ nuclear energies of donor and acceptor state. 98

ε level energy, molecular orbital energy. 25

η decay rate. 17

E_{xc} exchange–correlation functional. 10

f Fermi–Dirac distribution. 21

F_{HK} Hohenberg–Kohn functional. 10

- F fragment. 66
- \mathcal{F} thermally averaged Franck Condon weighted density of nuclear states. 98
- G conductance. 12
- G_0 conductance quantum. 13
- Γ Gamma point. 59
- Γ level broadening. 18
- G Greens function. 19
- \mathbf{g}^K Greens function of the electrode K . 29
- h Planck constant. 13, 102
- \hat{H} Hamiltonian. 9, 16
- \hat{H}_e electronic Hamiltonian. 9
- \hbar reduced Planck constant. 16
- I electric current. 12
- I_{DS} drain–source voltage. 88
- J classical contribution to the potential energy. 10
- J flux. 20
- K K point. 59
- k_B Boltzmann constant. 21, 98
- k_D^0 decay rate of the excited donor state. 104
- k force constant. 35
- k^{ET} electron transfer rate constant. 101
- k^{XT} energy transfer rate constant. 104
- Λ level shifting. 18
- E_λ reorganization energy. 99
- L left electrode. 15

m_e mass of an electron. 9

$\boldsymbol{\mu}$ dipole vector. 63

$\boldsymbol{\mu}^c$ charge transfer contribution to the dipole moment. 64

μ magnitude of dipole moment. 50

$\boldsymbol{\mu}^p$ polarization contribution to the dipole moment. 64

n barrier state. 18

N_A electron population of atom A . 64

∇^2 Laplace operator dependent on the three spatial coordinates. 9

$\tilde{\nu}$ vibrational wavenumber. 46

P Boltzmann distribution. 97

PP Cauchy principal part. 18

Ψ wave function. 9, 16

q partial charge. 53

$q(A|B)$ bond charge (charge transfer from atom A to atom B). 64

q quantization. 58

R_0 Förster radius. 104

R residual group(s). 66

ρ charge density. 10

R right electrode. 15

\mathbf{S} overlap matrix. 28

Σ self energy. 18

t coupling between molecular levels. 25

T temperature. 99

θ angle. 53

\hat{T} kinetic energy. 9

Tr trace. 21

\mathcal{T} transmission function. 12, 13

\mathbf{T} transmission matrix. 27

\mathcal{T}_{AB} local transmission for electrons between atomic centers A and B . 30

T_S kinetic energy of the non-interacting fermions. 10

\hat{V} coupling matrix. 103

V bias voltage. 12

$\tilde{V}_{d,a}$ effective coupling. 101

V_{DS} drain–source current. 88

\hat{V}_{ee} Coulomb interaction between electrons. 9

V_g gate voltage. 88

\hat{V}_{Ne} Coulomb interaction between electron and nuclei. 9

ΔV_{th} threshold voltage. 88

\mathbf{X} nuclear coordinate. 63

\mathbf{X}^c bond critical point. 65

\mathbf{X}^r internal reference point. 66

Z nuclear charge. 63

D. List of abbreviations

5F 1,2-bis(5-chloro-2-methylthien-3-yl)perfluorocyclopentene. 88, 89

5H 1,2-bis(5-chloro-2-methylthien-3-yl)cyclopentene. 88, 89

6H 1,2-bis(5-chloro-2-methylthien-3-yl)cyclohexene. 88, 89

AFM atomic force microscope. 2, 31, 33, 48–50, 53, 54

AIM atoms in molecules. 14, 50, 53, 62, 65, 85, 90

BCPs bond critical points. 64, 65

BDT 1,4-benzenedithiol. 31, 32

BOA Born–Oppenheimer approximation. 9

CCP cage critical point. 64

CNT carbon nanotube. 57, 58, 60, 79, 83, 85–87, 90, 93

CNTFET carbon nanotube field-effect transistor. 88

CP critical point. 65

Cp cyclopentadienyl. 44, 46, 49

DAE diarylethene. 6, 86–91, 93, 95

DBA Donor–Bridge–Acceptor. 97, 100, 102, 105

DFT density functional theory. 9, 10, 13, 14, 31, 32, 35, 55, 63

DFT-MD density functional theory-based molecular dynamics. 8

DOS density of states. 58

FRET fluorescence resonance energy transfer. 107

G09 GAUSSIAN 09. 115, 118

- GGA** generalized gradient approximation. 11
- GMH** generalized Mulliken–Hush. 99
- HF** Hartree–Fock. 11
- HOMO** highest occupied molecular orbital. 5, 11, 12, 28, 35, 39
- HS** high-spin. 44–47
- IR** infrared. 48
- IRPs** internal reference points. 65
- LDA** local density approximation. 11
- LDOS** local density of states. 29
- LS** low-spin. 44–47
- LUMO** lowest unoccupied molecular orbital. 5, 11, 12, 28, 35, 39
- MCBJ** mechanically controllable break junction. 2, 4, 37
- MD** molecular dynamics. 8, 32, 54, 109
- MO** molecular orbital. 35, 45
- NEGF** non-equilibrium Green’s function. 9
- PB** periodic-boundary. 51, 80, 84, 85, 89
- PES** potential energy surface. 35
- Por-TATA** Zn-porphyrin-triazatriangulenium. 33–37, 41, 54, 55, 122
- QD** quantum dot. 105, 107
- QDs** quantum dots. 97
- QE** QUANTUM ESPRESSO. 115, 117
- RCPs** ring critical points. 64
- RI** resolution-of-the-identity. 116
- SCF** self-consistent field. 85, 99

SCO spin crossover. 7, 44

STM scanning tunnelling microscope. 2, 4, 7, 31, 33–35, 42, 55

STM-BJ STM-based break junction. 4

TATA triazatriangulenium. 32–35, 37, 41, 42, 54, 121

TDSE time-dependent Schrödinger equation. 16, 20

TM TURBOMOLE. 115, 117

TOTA trioxotriangulenium. 42, 43, 55

WBL wide-band-limit. 23, 29

E. List of publications originating from this work

1. N. Hauptmann, L. Groß, K. Buchmann, K. Scheil, C. Schütt, F. L. Otte, R. Herges, C. Herrmann, and R. Berndt. High-conductance surface-anchoring of a mechanically flexible platform-based porphyrin complex. *New. J. Phys.* **17** (2015) 013012.
2. L. Groß and C. Herrmann. GENLOCDIP: A program to calculate and visualize local electric dipole moments via Atoms-In-Molecules analysis. *J. Comput. Chem.*, *in press*, 2016.
3. L. Groß and C. Herrmann. Local electric dipole moments: a generalized approach. *J. Comput. Chem.*, *under revision*, 2016.
4. L. Groß, C. Klinke, and C. Herrmann. Effects of truncating a carbon nanotube on simulating adsorbate-induced property changes., *submitted*, 2016.

In Preparation:

5. L. Groß, A. U. Wurl, A. Escribano, J. Heck, C. Klinke, and C. Herrmann. Noncovalent functionalization of carbon nanotubes by diarylethene molecules. *in preparation*.
6. L. Groß, C. Herrmann, A. Nitzan, and M. A. Ratner. Electron and excitation energy transfer in colloidal quantum dots, *in preparation*.
7. L. Groß and C. Herrmann. Mechanically induced spin-crossover in manganocene, *in preparation*.
8. L. Groß, A. Köhler, M. S. Zöllner, A. Schwarz, and C. Herrmann. Local dipole moments in noncontact atomic force microscopy, *in preparation*.

F. List of Chemicals

No hazardous compounds according to the GHS (Globally Harmonized System of Classification and Labeling of Chemicals) regulation have been used within the scope of this thesis.

G. Bibliography

- [1] J. C. Cuevas and E. Scheer. *Molecular Electronics: An Introduction to Theory and Experiment*. World Scientific, Singapore, 2010.
- [2] A. Aviram and M. Ratner, Eds. *Molecular Electronics: Science and Technology*, Volume 852 of *Ann. N. Y. Acad. Sci.* The New York Academy of Sciences, New York, 1998.
- [3] A. Szent Gyorgyi. Towards a new biochemistry? *Science*, **93**(2426) (1941) 609–611.
- [4] R. S. Mulliken. Molecular complexes and their spectra. VI. Some problems and new developments. *Rec. Trav. Chim.*, **75**(7) (1956) 845–852.
- [5] R. S. Mulliken and W. B. Person. Donor-Acceptor Complexes. *Annu. Rev. Phys. Chem.*, **13**(1) (1962) 107–126.
- [6] R. S. Mulliken and W. B. Person. Molecular compounds and their spectra. XXI. Some general considerations. *J. Am. Chem Soc.*, **91**(13) (1969) 3409–3413.
- [7] B. Mann and H. Kuhn. Tunneling through Fatty Acid Salt Monolayers. *J. Appl. Phys.*, **42**(11) (1971) 4398.
- [8] H. Kuhn and D. Möbius. Systems of Monomolecular Layers—Assembling and Physico-Chemical Behavior. *Angew. Chem. Int. Ed. Engl.*, **10**(9) (1971) 620–637.
- [9] A. Aviram and M. Ratner. Molecular Rectifiers. *Chem. Phys. Lett.*, **29**(2) (1974) 277–283.
- [10] K. W. Hipps. Molecular electronics: It’s All About Contacts. *Science*, **294**(5542) (2001) 536–537.
- [11] G. Binnig, H. Rohrer, Ch. Gerber, and E. Weibel. Tunneling through a controllable vacuum gap. *Appl. Phys. Lett.*, **40**(2) (1982) 178.
- [12] G. Binnig, H. Rohrer, C. Gerber, and E. Weibel. Surface Studies by Scanning Tunneling Microscopy. *Phys. Rev. Lett.*, **49**(1) (1982) 57–61.
- [13] G. Binnig and H. Rohrer. Scanning tunneling microscopy. *Surf. Sci.*, **126**(1-

- 3) (1983) 236–244.
- [14] C. Muller, J. van Ruitenbeek, and L. de Jongh. Experimental observation of the transition from weak link to tunnel junction. *Physica C: Superconductivity*, **191**(3-4) (1992) 485–504.
- [15] R. M. Metzger. Electrical Rectification by a Molecule: The Advent of Unimolecular Electronic Devices. *Acc. Chem. Res.*, **32**(11) (1999) 950–957.
- [16] M. Elbing, R. Ochs, M. Koentopp, M. Fischer, C. von Hsch, F. Weigend, F. Evers, H. B. Weber, and M. Mayor. A single-molecule diode. *Proc. Natl. Acad. Sci. USA*, **102**(25) (2005) 8815–8820.
- [17] B. W. Smith, M. Monthieux, and D. E. Luzzi. Carbon nanotube encapsulated fullerenes: a unique class of hybrid materials. *Chem. Phys. Lett.*, **315**(1-2) (1999) 31–36.
- [18] B. W. Smith and D. E. Luzzi. Formation mechanism of fullerene peapods and coaxial tubes: a path to large scale synthesis. *Chem. Phys. Lett.*, **321**(1-2) (2000) 169–174.
- [19] J. Liao, S. Blok, S. J. van der Molen, S. Diefenbach, A. W. Holleitner, C. Schönenberger, A. Vladyka, and M. Calame. Ordered nanoparticle arrays interconnected by molecular linkers: electronic and optoelectronic properties. *Chem. Soc. Rev.*, **44**(4) (2015) 999–1014.
- [20] Y. Xue, S. Datta, and M. A. Ratner. First-principles based matrix Green’s function approach to molecular electronic devices: general formalism. *Chem. Phys.*, **281** (2002) 151.
- [21] A. Nitzan, Eds. *Chemical Dynamics in Condensed Phases: Relaxation, Transfer, and Reactions in Condensed Molecular Systems*. Oxford University Press, Oxford, 2006.
- [22] R. Wiesendanger. *Scanning Probe Microscopy and Spectroscopy*. Cambridge University Press (CUP), 1994.
- [23] J. Tersoff and D. R. Hamann. Theory of scanning tunneling microscope. *Phys. Rev. B*, **31** (1985) 805.
- [24] J. Tersoff and D. M. Hamann. Theory and Application for the Scanning Tunneling Microscope. *Phys. Rev. Lett.*, **50**(25) (1983) 1998–2001.
- [25] J. K. Gimzewski and R. Möller. Transition from the tunneling regime to point contact studied using scanning tunneling microscopy. *Phys. Rev. B*, **36**(2) (1987) 1284–1287.
- [26] C. Joachim, J. K. Gimzewski, R. R. Schlittler, and C. Chavy. Electronic

-
- Transparency of a Single C₆₀ Molecule. *Phys. Rev. Lett.*, **74**(11) (1995) 2102–2105.
- [27] R. Temirov, A. Lassise, F. B. Anders, and F. S. Tautz. Kondo effect by controlled cleavage of a single-molecule contact. *Nanotechnology*, **19**(6) (2008) 065401.
- [28] G. Binnig, C. F. Quate, and C. Gerber. Atomic Force Microscope. *Phys. Rev. Lett.*, **56**(9) (1986) 930–933.
- [29] B. Xu, X. Xiao, and N. J. Tao. Measurements of Single-Molecule Electromechanical Properties. *J. Am. Chem. Soc.*, **125**(52) (2003) 16164–16165.
- [30] N. Agraït, A. L. Yeyati, and J. M. van Ruitenbeek. Quantum properties of atomic-sized conductors. *Phys. Rep.*, **377**(2-3) (2003) 81–279.
- [31] G. Rubio, N. Agraït, and S. Vieira. Atomic-Sized Metallic Contacts: Mechanical Properties and Electronic Transport. *Phys. Rev. Lett.*, **76**(13) (1996) 2302–2305.
- [32] J. K. J. van Duren, X. Yang, J. Loos, C. W. T. Bulle Lieuwma, A. B. Sieval, J. C. Hummelen, and R. A. J. Janssen. Relating the Morphology of Poly(p-phenylene vinylene)/Methanofullerene Blends to Solar-Cell Performance. *Adv. Funct. Mater.*, **14**(5) (2004) 425–434.
- [33] D. J. Wold and C. D. Frisbie. Formation of Metal–Molecule–Metal Tunnel Junctions: Microcontacts to Alkanethiol Monolayers with a Conducting AFM Tip. *J. Am. Chem. Soc.*, **122**(12) (2000) 2970–2971.
- [34] J. Moreland and J. W. Ekin. Electron tunneling experiments using Nb-Sn “break” junctions. *J. Appl. Phys.*, **58**(10) (1985) 3888.
- [35] D. Xiang, H. Jeong, T. Lee, and D. Mayer. Mechanically Controllable Break Junctions for Molecular Electronics. *Adv. Mater.*, **25**(35) (2013) 4845–4867.
- [36] M. A. Reed, C. Zhou, C. J. Muller, T. P. Burgin, and J. M. Tour. Conductance of a Molecular Junction. *Science*, **278** (1997) 252–254.
- [37] M. A. Reed, C. Zhou, M. R. Deshpande, C. J. Muller, T. P. Burgin, L. Jones II, and J. M. Tour. The Electrical Measurement of Molecular Junctions. *Ann. N. Y. Acad. Sci.*, **852** (1998) 133–144.
- [38] M. Mayor and H. B. Weber. Statistical Analysis of Single-Molecule Junctions. *Angew. Chem. Int. Ed.*, **43**(22) (2004) 2882–2884.
- [39] M. Dreher, F. Pauly, J. Heurich, J. C. Cuevas, E. Scheer, and P. Nielaba. Structure and conductance histogram of atomic-sized Au contacts. *Phys. Rev. B*, **72** (2005) 075435.

-
- [40] S. Y. Quek, L. Venkataraman, H. J. Choi, S. G. Louie, M. S. Hybertsen, and J. B. Neaton. Amine-Gold Linked Single-Molecule Circuits: Experiment and Theory. *Nano Lett.*, **7**(11) (2007) 3477–3482.
- [41] D. Q. Andrews, R. P. Van Duyne, and M. A. Ratner. Stochastic Modulation in Molecular Electronic Transport Junctions: Molecular Dynamics Coupled with Charge Transport Calculations. *Nano Lett.*, **8**(4) (2008) 1120–1126. PMID: 18351748.
- [42] M. Paulsson, C. Krag, T. Frederiksen, and M. Brandbyge. Conductance of Alkanedithiol Single-Molecule Junctions: A Molecular Dynamics Study. *Nano Lett.*, **9**(1) (2009) 117–121.
- [43] E. Lörtscher, H. B. Weber, and H. Riel. Statistical Approach to Investigating Transport through Single Molecules. *Phys. Rev. Lett.*, **98** (2007) 176807.
- [44] S. K. Nielsen, M. Brandbyge, K. Hansen, K. Stokbro, J. M. van Ruitenbeek, and F. Besenbacher. Current-Voltage Curves of Atomic-Sized Transition Metal Contacts: An Explanation of Why Au is Ohmic and Pt is Not. *Phys. Rev. Lett.*, **89**(6) (2002) 066804.
- [45] M. T. González, S. Wu, R. Huber, S. J. van der Molen, C. Schönenberger, and M. Calame. Electrical Conductance of Molecular Junctions by a Robust Statistical Analysis. *Nano Lett.*, **6**(10) (2006) 2238–2242.
- [46] L. Venkataraman, J. E. Klare, I. W. Tam, C. Nuckolls, M. S. Hybertsen, and M. L. Steigerwald. Single-Molecule Circuits with Well-Defined Molecular Conductance. *Nano Lett.*, **6**(3) (2006) 458–462.
- [47] W. Haiss, H. van Zalinge, D. Bethell, J. Ulstrup, D. J. Schiffrin, and R. J. Nichols. Thermal gating of the single molecule conductance of alkanedithiols. *Faraday Discuss.*, **131** (2006) 253–264.
- [48] J. Ulrich, D. Esrail, W. Pontius, L. Venkataraman, D. Millar, and L. H. Doerr. Variability of Conductance in Molecular Junctions. *J. Phys. Chem. B*, **110**(6) (2006) 2462–2466. PMID: 16471840.
- [49] M. Kamenetska, M. Koentopp, A. C. Whalley, Y. S. Park, M. L. Steigerwald, C. Nuckolls, M. S. Hybertsen, and L. Venkataraman. Formation and Evolution of Single-Molecule Junctions. *Phys. Rev. Lett.*, **102**(12) (2009) 126803.
- [50] P. Darancet, J. R. Widawsky, H. J. Choi, L. Venkataraman, and J. B. Neaton. Quantitative Current–Voltage Characteristics in Molecular Junctions from First Principles. *Nano Letters*, **12**(12) (2012) 6250–6254. PMID: 23167709.
- [51] P. D. Williams and M. G. Reuter. Level Alignments and Coupling Strengths

-
- in Conductance Histograms: The Information Content of a Single Channel Peak. *J. Phys. Chem. C*, **117**(11) (2013) 5937–5942.
- [52] R. Quan, C. S. Pitler, M. A. Ratner, and M. G. Reuter. Quantitative Interpretations of Break Junction Conductance Histograms in Molecular Electron Transport. *ACS Nano*, **9** (2015) 7704–7713. PMID: 26168212.
- [53] B. Xu and N. J. Tao. Measurement of Single-Molecule Resistance by Repeated Formation of Molecular Junctions. *Science*, **301**(5637) (2003) 1221–1223.
- [54] R. M. Metzger and D. L. Mattern. Unimolecular Electronic Devices. In R. M. Metzger, Eds., *Unimolecular and Supramolecular Electronics II*, Volume 313 of *Topics in Current Chemistry*, p. 39–84. Springer Berlin Heidelberg, 2012.
- [55] M. D. Fischbein and M. Drndić. Sub-10 nm Device Fabrication in a Transmission Electron Microscope. *Nano Lett.*, **7**(5) (2007) 1329–1337.
- [56] P. Avouris. Molecular Electronics with Carbon Nanotubes. *Acc. Chem. Res.*, **35**(12) (2002) 1026–1034. PMID: 12484790.
- [57] P. Avouris and J. Chen. Nanotube electronics and optoelectronics. *Mater. Today*, **9**(10) (2006) 46–54.
- [58] Xi Chen, Ying-Shuang Fu, Shuai-Hua Ji, Tong Zhang, Peng Cheng, Xu-Cun Ma, Xiao-Long Zou, Wen-Hui Duan, Jin-Feng Jia, and Qi-Kun Xue. Probing Superexchange Interaction in Molecular Magnets by Spin-Flip Spectroscopy and Microscopy. *Phys. Rev. Lett.*, **101** (2008) 197208.
- [59] S. Heinze, P. Kurz, D. Wortmann, G. Bihlmayer, and S. Blügel. Complex-magnetism in ultra-thin films: atomic-scale spin structures and resolution by the spin-polarized scanning tunneling microscope. *Appl. Phys. A*, **75** (2002) 25–36.
- [60] S. Datta, W. Tian, S. Hong, R. Reifenberger, J. I. Henderson, and C. P. Kubiak. Current-Voltage Characteristics of Self-Assembled Monolayers by Scanning Tunneling Microscopy. *Phys. Rev. Lett.*, **79** (1997) 2530–2533.
- [61] R. P. Andres, J. D. Bielefeld, J. I. Henderson, D. B. Janes, V. R. Kola-gunta, C. P. Kubiak, W. J. Mahoney, and R. G. Osifchin. Self-Assembly of a Two-Dimensional Superlattice of Molecularly Linked Metal Clusters. *Science*, **273**(5282) (1996) 1690–1693.
- [62] C. Xu, H. v. Zalinge, J. L. Pearson, a. Glidle, J. M. Cooper, D. R. S. Cumming, W. Haiss, J. Yao, D. J. Schiffrin, M. Proupín Pérez, R. Cosstick, and R. Nichols. A combined top-down bottom-up approach for introducing nanoparticle networks into nanoelectrode gaps. *Nanotechnology*, **17**(14) (2006) 3333–3339.

- [63] D. B. Robinson, J. R. Funamura, A. A. Talin, and R. J. Anderson. Spectroscopic observation of chemical change during molecular electronics experiments. *Appl. Phys. Lett.*, **90** (2007) 083119.
- [64] K. Matsuda, H. Yamaguchi, T. Sakano, M. Ikeda, N. Tanifuji, and M. Irie. Conductance Photoswitching of Diarylethene–Gold Nanoparticle Network Induced by Photochromic Reaction. *J. Phys. Chem. C*, **112**(43) (2008) 17005–17010.
- [65] G. Markovich, C. P. Collier, and J. R. Heath. Reversible Metal-Insulator Transition in Ordered Metal Nanocrystal Monolayers Observed by Impedance Spectroscopy. *Phys. Rev. Lett.*, **80** (1998) 3807–3810.
- [66] G. Markovich, C. Patrick Collier, S. E. Henrichs, F. Remeacle, R. D. Levine, and J. R. Heath. Architectonic Quantum Dot Solids. *Acc. Chem. Res.*, **32**(5) (1999) 415–423.
- [67] J. Liao, L. Bernard, M. Langer, C. Schönenberger, and M. Calame. Reversible Formation of Molecular Junctions in 2D Nanoparticle Arrays. *Adv. Mater.*, **18**(18) (2006) 2444–2447.
- [68] V. Santhanam, J. Liu, R. Agarwal, and R. P. Andres. Self-Assembly of Uniform Monolayer Arrays of Nanoparticles. *Langmuir*, **19**(19) (2003) 7881–7887.
- [69] J. Liao, M. A. Mangold, S. Grunder, M. Mayor, C. Schönenberger, and M. Calame. Interlinking Au nanoparticles in 2D arrays via conjugated dithiolated molecules. *New J. Phys.*, **10**(6) (2008) 065019.
- [70] T. Dadosh, J. Sperling, G. W. Bryant, R. Breslow, T. Shegai, M. Dyshel, G. Haran, and I. Bar Joseph. Plasmonic Control of the Shape of the Raman Spectrum of a Single Molecule in a Silver Nanoparticle Dimer. *ACS Nano*, **3**(7) (2009) 1988–1994.
- [71] W. Cheng, M. J. Campolongo, J. J. Cha, S. J. Tan, C. C. Umbach, D. A. Muller, and D. Luo. Free-standing nanoparticle superlattice sheets controlled by DNA. *Nat. Mater.*, **8**(6) (2009) 519–525.
- [72] S. J. van der Molen, J. Liao, T. Kudernac, J. S. Agustsson, L. Bernard, M. Calame, B. J. van Wees, B. L. Feringa, and C. Schönenberger. Light-Controlled Conductance Switching of Ordered Metal–Molecule–Metal Devices. *Nano Lett.*, **9**(1) (2009) 76–80.
- [73] L. Bernard, Y. Kamdzhilov, M. Calame, S. J. van der Molen, J. Liao, and C. Schönenberger. Spectroscopy of Molecular Junction Networks Obtained by Place Exchange in 2D Nanoparticle Arrays. *J. Phys. Chem. C*, **111**(50)

(2007) 18445–18450.

- [74] D. Natelson, Y. Li, and J. B. Herzog. Nanogap structures: combining enhanced Raman spectroscopy and electronic transport. *Phys. Chem. Chem. Phys.*, **15**(15) (2013) 5262.
- [75] C. George, I. Szeleifer, and M. Ratner. Multiple-Time-Scale Motion in Molecularly Linked Nanoparticle Arrays. *ACS Nano*, **7**(1) (2013) 108–116.
- [76] A. Nitzan. The relationship between electron transfer rate and molecular conduction 2. The sequential hopping case. *Isr. J. Chem.*, **42**(2-3) (2002) 163–166.
- [77] Y. Joseph, B. Guse, T. Vossmeier, and A. Yasuda. Gold Nanoparticle/Organic Networks as Chemiresistor Coatings: The Effect of Film Morphology on Vapor Sensitivity. *J. Phys. Chem. C*, **112**(32) (2008) 12507–12514.
- [78] N. Olichwer, E. W. Leib, A. H. Halfar, A. Petrov, and T. Vossmeier. Cross-Linked Gold Nanoparticles on Polyethylene: Resistive Responses to Tensile Strain and Vapors. *ACS App. Mater. Interfaces*, **4** (2012) 6151.
- [79] H. Park, a. K. L. Lim, A. P. Alivisatos, J. Park, and P. L. McEuen. Fabrication of metallic electrodes with nanometer separation by electromigration. *Appl. Phys. Lett.*, **75**(2) (1999) 301.
- [80] W. Liang, M. P. Shores, M. Bockrath, J. R. Long, and H. Park. Kondo resonance in a single-molecule transistor. *Nature*, **417** (2002) 725–729.
- [81] Q. Qing, F. Chen, P. Li, W. Tang, Z. Wu, and Z. Liu. Finely Tuning Metallic Nanogap Size with Electrodeposition by Utilizing High-Frequency Impedance in Feedback. *Angew. Chem. Int. Ed.*, **44**(47) (2005) 7771–7775.
- [82] J. G. Kushmerick, J. Naciri, J. C. Yang, and R. Shashidhar. Conductance Scaling of Molecular Wires in Parallel. *Nano Lett.*, **3**(7) (2003) 897–900.
- [83] B. de Boer, M. M. Frank, Y. J. Chabal, W. Jiang, E. Garfunkel, and Z. Bao. Metallic Contact Formation for Molecular Electronics: Interactions between Vapor-Deposited Metals and Self-Assembled Monolayers of Conjugated Mono- and Dithiols. *Langmuir*, **20**(5) (2004) 1539–1542.
- [84] H. Haick, J. Ghabboun, and D. Cahen. Pd versus Au as evaporated metal contacts to molecules. *Appl. Phys. Lett.*, **86**(4) (2005) 042113.
- [85] S. Kubatkin, A. Danilov, M. Hjort, J. Cornil, J.-L. Brédas, N. Stuhr Hansen, P. Hedegård, and T. Bjørnholm. Single-electron transistor of a single organic molecule with access to several redox states. *Nature*, **425**(6959) (2003) 698–701.

- [86] M. A. Rampi, O. J. A. Schueller, and G. M. Whitesides. Alkanethiol self-assembled monolayers as the dielectric of capacitors with nanoscale thickness. *Appl. Phys. Lett.*, **72**(14) (1998) 1781.
- [87] N. S. Hush. An Overview of the First Half-Century of Molecular Electronics. *Ann. N.Y. Acad. Sci.*, **1006** (2003) 1–20.
- [88] N. J. Tao. Electron transport in molecular junctions. *Nat. Nanotechnol.*, **1**(3) (2006) 173–181.
- [89] X. Chen and R. H. Victora. Effect of pinholes in magnetic tunnel junctions. *Appl. Phys. Lett.*, **91**(21) (2007) 212104.
- [90] N. Prokopuk and K.-A. Son. Alligator clips to molecular dimensions. *J. Phys.: Condens. Matter*, **20** (2008) 374116.
- [91] G. C. Solomon, C. Herrmann, and M. A. Ratner. Molecular Electronic Junction Transport: Some Pathways and Some Ideas. *Top. Curr. Chem.*, **313** (2012) 1–38.
- [92] S. V. Aradhya and L. Venkataraman. Single-molecule junctions beyond electronic transport. *Nat. Nanotechnol.*, **8**(6) (2013) 399–410.
- [93] L. Xiang, T. Hines, J. L. Palma, X. Lu, V. Mujica, M. A. Ratner, G. Zhou, and N. Tao. Non-exponential Length Dependence of Conductance in Iodide-Terminated Oligothiophene Single-Molecule Tunneling Junctions. *J. Am. Chem Soc.*, **138**(2) (2016) 679–687.
- [94] S. Ho Choi, B. Kim, and C. D. Frisbie. Electrical Resistance of Long Conjugated Molecular Wires. *Science*, **320**(5882) (2008) 1482–1486.
- [95] J. He, F. Chen, S. Lindsay, and C. Nuckolls. Length dependence of charge transport in oligoanilines. *Appl. Phys. Lett.*, **90** (2007) 072112.
- [96] V. B. Engelkes, J. M. Beebe, and C. D. Frisbie. Length-Dependent Transport in Molecular Junctions Based on SAMs of Alkanethiols and Alkanedithiols: Effect of Metal Work Function and Applied Bias on Tunneling Efficiency and Contact Resistance. *J. Am. Chem Soc.*, **126**(43) (2004) 14287–14296. PMID: 15506797.
- [97] M. R. Wasielewski, W. B. Davis, W. A. Svec, and M. A. Ratner. Molecular-wire behaviour in *p*-phenylenevinylene oligomers. *Nature*, **396**(6706) (1998) 60–63.
- [98] Q. Lu, K. Liu, H. Zhang, Z. Du, X. Wang, and F. Wang. From Tunneling to Hopping: A Comprehensive Investigation of Charge Transport Mechanism in Molecular Junctions Based on Oligo(*p*-phenylene ethynylene)s. *ACS Nano*, **3**(12) (2009) 3861–3868.

-
- [99] J. Vura Weis, S. H. Abdelwahed, R. Shukla, R. Rathore, M. A. Ratner, and M. R. Wasielewski. Crossover from Single-Step Tunneling to Multistep Hopping for Molecular Triplet Energy Transfer. *Science*, **328**(5985) (2010) 1547–1550.
- [100] L. Luo, S. Ho Choi, and C. D. Frisbie. Probing Hopping Conduction in Conjugated Molecular Wires Connected to Metal Electrodes. *Chem. Mater.*, **23**(3) (2011) 631–645.
- [101] L. A. Zotti, T. Kirchner, J.-C. Cuevas, F. Pauly, T. Huhn, E. Scheer, and A. Erbe. Revealing the Role of Anchoring Groups in the Electrical Conduction Through Single-Molecule Junctions. *Small*, **6**(14) (2010) 1529–1535.
- [102] L. Venkataraman, Y. S. Park, A. C. Whalley, C. Nuckolls, M. S. Hybertsen, and M. L. Steigerwald. Electronics and Chemistry: Varying Single-Molecule Junction Conductance Using Chemical Substituents. *Nano Lett.*, **7**(2) (2007) 502–506.
- [103] D. Dulić, F. Pump, S. Campidelli, P. Lavie, G. Cuniberti, and A. Filoramo. Controlled Stability of Molecular Junctions. *Angew. Chem. Int. Ed.*, **48**(44) (2009) 8273–8276.
- [104] B. S. Kim, J. M. Beebe, Yo. Jun, X.-Y. Zhu, and C. D. Frisbie. Correlation between HOMO Alignment and Contact Resistance in Molecular Junctions: Aromatic Thiols versus Aromatic Isocyanides. *J. Am. Chem. Soc.*, **128**(15) (2006) 4970–4971. PMID: 16608328.
- [105] C.-L. Cheng, J. S. Evans, and T. Van Voorhis. Simulating molecular conductance using real-time density functional theory. *Phys. Rev. B*, **74** (2006) 155112.
- [106] J. J. Parks, A. R. Champagne, G. R. Hutchison, S. Flores Torres, H. D. Abruña, and D. C. Ralph. Tuning the Kondo Effect with a Mechanically Controllable Break Junction. *Phys. Rev. Lett.*, **99** (2007) 026601.
- [107] M. S. Hybertsen, L. Venkataraman, J. E. Klare, A. C. Whalley, M. L. Steigerwald, and C. Nuckolls. Amine-linked single-molecule circuits: systematic trends across molecular families. *J. Phys.:Condens. Matter*, **20**(37) (2008) 374115.
- [108] M. Kamenetska, S. Y. Quek, A. C. Whalley, M. L. Steigerwald, H. J. Choi, S. G. Louie, C. Nuckolls, M. S. Hybertsen, J. B. Neaton, and L. Venkataraman. Conductance and Geometry of Pyridine-Linked Single-Molecule Junctions. *J. Am. Chem. Soc.*, **132**(19) (2010) 6817–6821.
- [109] A. Mishchenko, L. A. Zotti, D. Vonlanthen, M. Bürkle, F. Pauly, J. C. Cuevas,

- M. Mayor, and T. Wandlowski. Single-Molecule Junctions Based on Nitrile-Terminated Biphenyls: A Promising New Anchoring Group. *J. Am. Chem. Soc.*, **133**(2) (2011) 184–187. PMID: 21155561.
- [110] M. Mayor, H. B. Weber, J. Reichert, M. Elbing, C. von Hänisch, D. Beckmann, and M. Fischer. Electric Current through a Molecular Rod – Relevance of the Position of the Anchor Groups. *Angew. Chem. Int. Ed.*, **42**(47) (2003) 5834–5838.
- [111] G. C. Solomon, D. Q. Andrews, T. Hansen, R. H. Goldsmith, M. R. Wasielewski, R. P. Van Duyne, and M. A. Ratner. Understanding quantum interference in coherent molecular conduction. *J. Chem. Phys.*, **129** (2008) 054701.
- [112] G. C. Solomon, D. Q. Andrews, R. P. Van Duyne, and M. A. Ratner. When Things Are Not as They Seem: Quantum Interference Turns Molecular Electron Transfer “Rules” Upside Down. *J. Am. Chem. Soc.*, **130**(25) (2008) 7788–7789.
- [113] G. C. Solomon, D. Q. Andrews, R. P. Van Duyne, and M. A. Ratner. Electron Transport through Conjugated Molecules : When the π System Only Tells Part of the Story. *Chem. Phys. Chem.*, **10** (2009) 257–264.
- [114] T. Hansen, G. C. Solomon, D. Q. Andrews, and M. A. Ratner. Interfering Pathways in Benzene: An Analytical Treatment. *J. Chem. Phys.*, **131** (2009) 194704.
- [115] B. L. Feringa. *Molecular Switches*. Wiley VCH, Hoboken, NJ, 2007.
- [116] T. Kudernac, N. Katsonis, W. R. Browne, and B. L. Feringa. Nano-electronic switches: Light-induced switching of the conductance of molecular systems. *J. Mater. Chem.*, **19**(39) (2009) 7168.
- [117] D. Dulić, S. J. van der Molen, T. Kudernac, H. T. Jonkman, J. J. D. de Jong, T. N. Bowden, J. van Esch, B. L. Feringa, and B. J. van Wees. One-Way Optoelectronic Switching of Photochromic Molecules on Gold. *Phys. Rev. Lett.*, **91** (2003) 207402.
- [118] M. Irie. Diarylethenes for Memories and Switches. *Chem. Rev.*, **100**(5) (2000) 1685–1716.
- [119] H. Tian and S. Yang. Recent progresses on diarylethene based photochromic switches. *Chem. Soc. Rev.*, **33**(2) (2004) 85.
- [120] G. Guirado, C. Coudret, M. Hliwa, and J.-P. Launay. Understanding Electrochromic Processes Initiated by Dithienylcyclopentene Cation-Radicals. *J. Phys. Chem. B*, **109** (2005) 17445–17459.

-
- [121] N. Katsonis, T. Kudernac, M. Walko, S. J. van der Molen, B. J. van Wees, and B. L. Feringa. Reversible Conductance Switching of Single Diarylethenes on a Gold Surface. *Adv. Mater.*, **18**(11) (2006) 1397–1400.
- [122] S. J. van der Molen, H. van der Vegte, T. Kudernac, I. Amin, B. L. Feringa, and B. J. van Wees. Stochastic and photochromic switching of diarylethenes studied by scanning tunnelling microscopy. *Nanotechnology*, **17**(1) (2006) 310.
- [123] Z. F. Liu, K. Hashimoto, and A. Fujishima. Photoelectrochemical information storage using an azobenzene derivative. *Nature*, **347**(6294) (1990) 658–660.
- [124] N. Tamaoki, S. Yoshimura, and T. Yamaoka. A photochromic memory with a non-destructive read-out property. *Thin Solid Films*, **221**(1-2) (1992) 132–139.
- [125] A. Archut, F. Vögtle, L. De Cola, G. C. Azzellini, V. Balzani, P. S. Ramanujam, and R. H. Berg. Azobenzene-Functionalized Cascade Molecules: Photoswitchable Supramolecular Systems. *Chem. Eur. J.*, **4**(4) (1998) 699–706.
- [126] S. Yasuda, T. Nakamura, M. Matsumoto, and H. Shigekawa. Phase Switching of a Single Isomeric Molecule and Associated Characteristic Rectification. *J. Am. Chem. Soc.*, **125**(52) (2003) 16430–16433.
- [127] K. Tamada, H. Akiyama, and T. X. Wei. Photoisomerization Reaction of Unsymmetrical Azobenzene Disulfide Self-Assembled Monolayers Studied by Surface Plasmon Spectroscopy: Influences of Side Chain Length and Contacting Medium. *Langmuir*, **18**(13) (2002) 5239–5246.
- [128] T. Nägele, R. Hoche, W. Zinth, and J. Wachtveitl. Femtosecond photoisomerization of cis-azobenzene. *Chem. Phys. Lett.*, **272**(5-6) (1997) 489–495.
- [129] T. Ishikawa, T. Noro, and T. Shoda. Theoretical study on the photoisomerization of azobenzene. *J. Chem. Phys.*, **115**(16) (2001) 7503.
- [130] T. Hugel, N. B. Holland, A. Cattani, L. Moroder, M. Seitz, and H. E. Gaub. Single-Molecule Optomechanical Cycle. *Science*, **296**(5570) (2002) 1103–1106.
- [131] D. H. Waldeck. Photoisomerization dynamics of stilbenes. *Chem. Rev.*, **91**(3) (1991) 415–436.
- [132] H. Meier. The Photochemistry of Stilbenoid Compounds and Their Role in Materials Technology. *Angew. Chem. Int. Ed. Engl.*, **31**(11) (1992) 1399–1420.
- [133] J. M. Galvin and G. B. Schuster. Preparation and characterization of mixed

- thin films containing spiropyrans and long chain alkyl silanes: towards a command surface for liquid crystal realignment. *Supramolecular Science*, **5**(1-2) (1998) 89–100.
- [134] X. Guo, L. Huang, S. O'Brien, P. Kim, and C. Nuckolls. Directing and Sensing Changes in Molecular Conformation on Individual Carbon Nanotube Field Effect Transistors. *J. Am. Chem. Soc.*, **127**(43) (2005) 15045–15047.
- [135] M. Karcher, C. Rüdert, C. Elsässer, and P. Fumagalli. Switching of nonfunctionalized spiropyran thin films on single crystalline MgO(100). *J. Appl. Phys.*, **102**(8) (2007) 084904.
- [136] S. H. Kawai, S. L. Gilat, R. Ponsinet, and J.-M. Lehn. A Dual-Mode Molecular Switching Device: Bisphenolic Diarylethenes with Integrated Photochromic and Electrochromic Properties. *Chem. Eur. J.*, **1**(5) (1995) 285–293.
- [137] G. M. Tsivgoulis and J.-M. Lehn. Photoswitched and Functionalized Oligothiophenes: Synthesis and Photochemical and Electrochemical Properties. *Chem. Eur. J.*, **2**(11) (1996) 1399–1406.
- [138] A. Fernández Acebes and J.-M. Lehn. Optical Switching and Fluorescence Modulation Properties of Photochromic Metal Complexes Derived from Dithienylethene Ligands. *Chem. Eur. J.*, **5**(11) (1999) 3285–3292.
- [139] S. H. Kawai, S. L. Gilat, and J.-M. Lehn. Photochemical pK_a -Modulation and Gated Photochromic Properties of a Novel Diarylethene Switch. *Eur. J. Org. Chem.*, **1999**(9) (1999) 2359–2366.
- [140] H. Logtenberg and W. R. Browne. Electrochemistry of dithienylethenes and their application in electropolymer modified photo- and redox switchable surfaces. *Org. Biomol. Chem.*, **11**(2) (2013) 233–243.
- [141] J. M. Simmons, I. In, V. E. Campbell, T. J. Mark, F. Léonard, P. Gopalan, and M. A. Eriksson. Optically Modulated Conduction in Chromophore-Functionalized Single-Wall Carbon Nanotubes. *Phys. Rev. Lett.*, **98** (2007) 086802.
- [142] X. Zhou, T. Zifer, B. M. Wong, K. L. Krafcik, F. Léonard, and A. L. Vance. Color Detection Using Chromophore-Nanotube Hybrid Devices. *Nano Lett.*, **9**(3) (2009) 1028–1033.
- [143] M. Alemani, M. V. Peters, S. Hecht, K.-H. Rieder, F. Moresco, and L. Grill. Electric Field-Induced Isomerization of Azobenzene by STM. *J. Am. Chem. Soc.*, **128**(45) (2006) 14446–14447.
- [144] J. Henzl, M. Mehlhorn, H. Gawronski, K.-H. Rieder, and K. Morgenstern. Reversible cis-trans Isomerization of a Single Azobenzene Molecule. *Angew.*

Chem. Int. Ed., **45**(4) (2006) 603–606.

- [145] B.-Y. Choi, S.-J. Kahng, S. Kim, H. Kim, H. W. Kim, Y. J. Song, J. Ihm, and Y. Kuk. Conformational Molecular Switch of the Azobenzene Molecule: A Scanning Tunneling Microscopy Study. *Phys. Rev. Lett.*, **96** (2006) 156106.
- [146] E. Lörtscher, J. W. Ciszek, J. Tour, and H. Riel. Reversible and Controllable Switching of a Single-Molecule Junction. *Small*, **2**(8-9) (2006) 973–977.
- [147] X. H. Qiu, G. V. Nazin, and W. Ho. Mechanismus of Reversible Conformational Transitions in a Single Molecule. *Phys. Rev. Lett.*, **93** (2004) 196806.
- [148] P. Liljeroth, J. Repp, and G. Meyer. Current-Induced Hydrogen Tautomerization and Conductance Switching of Naphthalocyanine Molecules. *Science*, **317**(5842) (2007) 1203–1206.
- [149] A. Nitzan. Electron transmission through molecules and molecular interfaces. *Annu. Rev. Phys. Chem.*, **52**(1) (2001) 681–750.
- [150] J. Chen and O. S. Wenger. Fluoride binding to an organoboron wire controls photoinduced electron transfer. *Chem. Sci.*, **6**(6) (2015) 3582–3592.
- [151] A. A. Kocherzhenko, L. D. A. Siebbeles, and F. C. Grozema. Chemically Gated Quantum-Interference-Based Molecular Transistor. *J. Phys. Chem. Lett.*, **2**(14) (2011) 1753–1756.
- [152] Y. Wang, J. Kröger, R. Berndt, and W. A. Hofer. Pushing and Pulling a Sn Ion through an Adsorbed Phthalocyanine Molecule. *J. Am. Chem. Soc.*, **131**(10) (2009) 3639–3643.
- [153] M. Frei, S. V. Aradhya, M. Koentopp, M. S. Hybertsen, and L. Venkataraman. Mechanics and Chemistry: Single Molecule Bond Rupture Forces Correlate with Molecular Backbone Structure. *Nano Lett.*, **11**(4) (2011) 1518–1523.
- [154] J. Inatomi, S. Fujii, S. Marqués González, H. Masai, Y. Tsuji, J. Terao, and M. Kiguchi. Effect of Mechanical Strain on Electric Conductance of Molecular Junctions. *J. Phys. Chem. C*, **119**(33) (2015) 19452–19457.
- [155] S. Y. Quek, M. Kamenetska, M. L. Steigerwald, H. J. Choi, S. G. Louie, M. S. Hybertsen, J. B. Neaton, and L. Venkataraman. Mechanically controlled binary conductance switching of a single-molecule junction. *Nat. Nanotechnol.*, **4**(4) (2009) 230–234.
- [156] J. Vacek, J. V. Chocholoušová, I. G. Starà, I. Starý, and Y. Dubi. Mechanical tuning of conductance and thermopower in helicene molecular junctions. *Nanoscale*, **7**(19) (2015) 8793–8802.
- [157] P. Gütllich, A. Hauser, and H. Spiering. Thermal and Optical Switching of

- Iron(II) Complexes. *Angew. Chem. Int. Ed. Engl.*, **33**(20) (1994) 2024–2054.
- [158] L. Bogani and W. Wernsdorfer. Molecular spintronics using single-molecule magnets. *Nat. Mater.*, **7**(3) (2008) 179–186.
- [159] I. Šalitroš, N. T. Madhu, R. Boča, J. Pavlik, and M. Ruben. Room-temperature spin-transition iron compounds. *Monatsh. Chem.*, **140**(7) (2009) 695–733.
- [160] P. Gamez, J. S. Costa, M. Quesada, and G. Aromi. Iron Spin-Crossover compounds: from fundamental studies to practical applications. *Dalton Trans.*, **38** (2009) 7845.
- [161] T. Komeda, H. Isshiki, J. Liu, Y.-F. Zhang, N. Lorente, K. Katoh, B. K. Breedlove, and M. Yamashita. Observation and electric current control of a local spin in a single-molecule magnet. *Nat. Comms.*, **2** (2011) 217.
- [162] G. D. Harzmann, R. Frisenda, H. S. J. van der Zant, and M. Mayor. Single-Molecule Spin Switch Based on Voltage-Triggered Distortion of the Coordination Sphere. *Angew. Chem. Int. Ed.*, **54**(45) (2015) 13425–13430.
- [163] T. W. Ebbesen, H. J. Lezec, H. Hiura, J. W. Bennett, H. F. Ghaemi, and T. Thio. Electrical conductivity of individual carbon nanotubes. *Nature*, **382**(6586) (1996) 54–56.
- [164] L. A. Bumm, J. J. Arnold, M. T. Cygan, T. D. Dunbar, T. P. Burgin, L. Jones, D. L. Allara, J. M. Tour, and P. S. Weiss. Are Single Molecular Wires Conducting? *Science*, **271**(5256) (1996) 1705–1707.
- [165] M. Büttiker, Y. Imry, R. Landauer, and S. Pinhas. Generalized many-channel conductance formula with application to small rings. *Phys. Rev. B*, **31**(10) (1985) 6207–6215.
- [166] Y. Meir and N. S. Wingreen. Landauer formula for the current through an interacting electron region. *Phys. Rev. Lett.*, **68** (1992) 2512–2515.
- [167] L. V. Keldysh. *Sov. Phys.-JEW*, **20** (1965) 1018–1026.
- [168] P. Danielewicz. Quantum theory of nonequilibrium processes, I. *Annals of Physics*, **152**(2) (1984) 239–304.
- [169] S. Datta. Proposal for a “spin capacitor”. *Appl. Phys. Lett.*, **87** (2005) 013115.
- [170] I. Franco, C. B. George, G. C. Solomon, G. C. Schatz, and M. A. Ratner. Mechanically Activated Molecular Switch through Single-Molecule Pulling. *J. Am. Chem Soc.*, **133** (2011) 2242.
- [171] G. Fiori and G. Iannaccone. Simulation of Graphene Nanoribbon Field-Effect

-
- Transistors. *Electron Device Letters, IEEE*, **28**(8) (2007) 760–762.
- [172] Y. Yoon, G. Fiori, S. Hong, G. Iannaccone, and J. Guo. Performance Comparison of Graphene Nanoribbon FETs With Schottky Contacts and Doped Reservoirs. *IEEE Transactions on Electron Devices*, **55**(9) (2008) 2314–2323.
- [173] M. Auf der Maur, M. Povolotskyi, F. Sacconi, A. Pecchia, G. Romano, G. Penazzi, and A. Di Carlo. TiberCAD: towards multiscale simulation of optoelectronic devices. *Opt. Quantum. Electron.*, **40**(14) (2009) 1077–1083.
- [174] M. Auf der Maur, M. Povolotskyi, F. Sacconi, G. Romano, E. Petrolati, and A. Carlo. *Simulation of Semiconductor Processes and Devices 2007: SISPAD 2007*, Chapter Multiscale Simulation of Electronic and Optoelectronic Devices with TiberCAD, p. 245–248. Springer Vienna, Vienna, 2007.
- [175] S. Steiger, M. Povolotskyi, H.-H. Park, T. Kubis, and G. Klimeck. NEMO5: A Parallel Multiscale Nanoelectronics Modeling Tool. *IEEE Trans. Nanotechnology*, **10**(6) (2011) 1464–1474.
- [176] J. R. Reimers, G. C. Solomon, A. Gagliardi, A. Bilić, N. S. Hush, T. Frauenheim, A. Di Carlo, and A. Pecchia. The Green’s Function Density Functional Tight-Binding (gDFTB) Method for Molecular Electronic Conduction. *J. Phys. Chem. A*, **111** (2007) 5692–5702.
- [177] M. Brandbyge, J.-L. Mozos, P. Ordejón, J. Taylor, and K. Stokbro. Density-functional method for nonequilibrium electron transport. *Phys. Rev. B*, **65** (2002) 165401.
- [178] R. M. Martin. *Electronic Structure: Basic Theory and Practical Methods (Vol 1)*. Cambridge University Press, April 2004.
- [179] F. Jensen. *Introduction to computational Chemistry*. Wiley, Chichester, 2007.
- [180] P. Hohenberg and W. Kohn. Inhomogenous Electron Gas,. *Phys. Rev.*, **136**(3) (1964) B864–B871.
- [181] W. Kohn and L. J. Sham. Self-Consistent Equations Including Exchange and Correlation Effects,. *Phys. Rev.*, **140**(4) (1965) A1133–A1138.
- [182] C. J. Cramer and D. G. Truhlar. Density functional theory for transition metals and transition metal chemistry. *Phys. Chem. Chem. Phys.*, **11** (2009) 10757–10816.
- [183] S. H. Vosko, L. Wilk, and M. Nusair. Accurate spin-dependent electron liquid correlation energies for local spin density calculations: a critical analysis,. *Can. J. Phys.*, **58** (1980) 1200–1211.
- [184] A. D. Becke. Density-functional exchange-energy approximation with correct

- asymptotic behavior. *Phys. Rev. A*, **38**(6) (1988) 3098–3100.
- [185] J. P. Perdew and Y. Wang. Accurate and simple density functional for the electronic exchange energy: Generalized gradient approximation. *Phys. Rev. B*, **33** (1986) 8800–8802.
- [186] J. P. Perdew, M. Ernzerhof, and K. Burke. Rationale for mixing exact exchange with density functional approximations. *J. Chem. Phys.*, **105** (1996) 9982–9985.
- [187] J. P. Perdew, M. Ernzerhof, K. Burke, and A. Savin. On-Top Pair-Density Interpretation of Spin Density Functional Theory, with Applications to Magnetism. *J. Comput. Chem.*, **61**(2) (1997) 197–205.
- [188] J. Tao, J. P. Perdew, V. N. Staroverov, and G. E. Scuseria. Climbing the Density Functional Ladder: Nonempirical Meta-Generalized Gradient Approximation Designed for Molecules and Solids. *Phys. Rev. Lett.*, **91** (2003) 146401.
- [189] R. G. Parr and W. Yang. *Density-Functional Theory of Atoms and Molecules*, Volume 16 of *International Series of Monographs on Chemistry*. Oxford Science Publications, New York, 1989.
- [190] A. D. Becke. A new mixing of Hartree-Fock and local density-functional theories. *J. Chem. Phys.*, **98** (1993) 1372–1377.
- [191] C. Lee, W. Yang, and R. G. Parr. Development of the Colle-Salvetti correlation-energy formula into a functional of the electron density. *Phys. Rev. B*, **37** (1988) 785–789.
- [192] S. Grimme, J. Antony, T. Schwabe, and C. Mück Lichtenfeld. Density functional theory with dispersion corrections for supramolecular structures, aggregates, and complexes of (bio)organic molecules. *Org. Biomol. Chem.*, **5**(5) (2007) 741.
- [193] M. Di Ventra, S. T. Pantelides, and N. D. Lang. First-Principles Calculation of Transport Properties of a Molecular Device. *Phys. Rev. Lett.*, **84**(5) (2000) 979–982.
- [194] A. Nitzan. A Relationship between Electron-Transfer Rates and Molecular Conduction. *J. Phys. Chem. A*, **105**(12) (2001) 2677–2679.
- [195] A. Nitzan and M. A. Ratner. Electron Transport in Molecular Wire Junctions. *Science*, **300**(5624) (2003) 1384–1389.
- [196] A. Pecchia and A. D. Carlo. Atomistic theory of transport in organic and inorganic nanostructures. *Rep. Prog. Phys.*, **67**(8) (2004) 1497–1561.

-
- [197] S. Grimme. Accurate description of van der Waals complexes by density functional theory including empirical corrections. *J. Comput. Chem.*, **25**(12) (2004) 1463–1473.
- [198] S. Grimme, J. Antony, S. Ehrlich, and H. Krieg. A consistent and accurate ab initio parametrization of density functional dispersion correction (DFT-D) for the 94 elements H-Pu. *J. Chem. Phys.*, **132** (2010) 154104.
- [199] M. Dion, H. Rydberg, E. Schröder, D. C. Langreth, and B. I. Lundqvist. Van der Waals Density Functional for General Geometries. *Phys. Rev. Lett.*, **92** (2004) 246401.
- [200] A. D. Becke and E. R. Johnson. A density-functional model of the dispersion interaction. **123**(15) (2005) 154101.
- [201] A. D. Becke and E. R. Johnson. Exchange-hole dipole moment and the dispersion interaction. *J. Chem. Phys.*, **122** (2005) 154104.
- [202] A. Tkatchenko and M. Scheffler. Accurate Molecular Van Der Waals Interactions from Ground-State Electron Density and Free-Atom Reference Data. *Phys. Rev. Lett.*, **102** (2009) 073005.
- [203] T. Sato and H. Nakai. Density functional method including weak interactions: Dispersion coefficients based on the local response approximation. *J. Chem. Phys.*, **131** (2009) 224104.
- [204] T. Sato and H. Nakai. Local response dispersion method. II. Generalized multicenter interactions. *J. Chem. Phys.*, **133** (2010) 194101.
- [205] C. Herrmann, G. C. Solomon, J. E. Subotnik, V. Mujica, and M. A. Ratner. Ghost transmission: How large basis sets can make electron transport calculations worse. *J. Chem. Phys.*, **132**(2) (2010) 024103.
- [206] C. Herrmann, L. Groß, T. Steenbock, and G. C. Solomon. ARTAIOS — a transport code for postprocessing quantum chemical electronic structure calculations, 2008-2014.
- [207] R. F. W. Bader. *Atoms in Molecules: A Quantum Theory*. Oxford University Press: Oxford, U.K., 1990.
- [208] L. Groß and C. Herrmann. GenLocDip: A program to calculate and visualize local electric dipole moments, in press, 2016.
- [209] L. Groß. GENLOC-DIP — A program to calculate and visualize *local* electric dipole moments via Atoms-In-Molecules analysis, University of Hamburg, 2014-2015.
- [210] R. A. Marcus and N. Sutin. Electron transfers in chemistry and biology.

- Biochim. Biophys. Acta*, **811** (1985) 265–322.
- [211] Th. Förster. Transfer mechanisms of electronic excitation. *Discuss. Faraday Soc.*, **27** (1959) 7–17.
- [212] A. Nitzan. *Chemical Dynamics in Condensed Phases: Relaxation, Transfer, and Reactions in Condensed Molecular Systems*. Oxford University Press, 2006.
- [213] R. Landauer. Electrical resistance of disordered one-dimensional lattices. *Phil. Mag.*, **21**(172) (1970) 863–867.
- [214] M. G. Reuter and R. J. Harrison. Rethinking first-principles electron transport theories with projection operators: The problems caused by partitioning the basis set. *J. Chem. Phys.*, **139**(11) (2013) 114104.
- [215] C. Herrmann, G. C. Solomon, and M. A. Ratner. Local pathways in coherent electron transport through iron porphyrin complexes: A challenge for first-principles transport calculations. *J. Phys. Chem. C.*, **114** (2010) 20813–20820.
- [216] T. N. Todorov. Tight-binding simulation of current-carrying nanostructures. *J. Phys.: Condens. Matter*, **14** (2002) 3049–3084.
- [217] G. C. Solomon, C. Herrmann, T. Hansen, V. Mujica, and M. A. Ratner. Exploring local currents in molecular junctions. *Nat. Chem.*, **2** (2010) 223.
- [218] N. Fournier, C. Wagner, C. Weiss, R. Temirov, and F. S. Tautz. Force-controlling lifting of molecular wires. *Phys. Rev. B*, **84** (2011) 035435.
- [219] N. Hauptmann, F. Mohn, L. Gross, G. Meyer, T. Frederiksen, and R. Berndt. Force and conductance during contact formation to a C_{60} molecule. *New J. Phys.*, **14** (2012) 073032.
- [220] C. Nef, P. L. T. M. Frederix, J. Brunner, C. Schönenberger, and M. Calame. Force–conductance correlation in individual molecular junctions. *Nanotechnology*, **23**(36) (2012) 365201.
- [221] C. Wagner, N. Fournier, F. S. Tautz, and R. Temirov. Measurement of the Binding Energies of the Organic-Metal Perylene-Teracarboxylic-Dianhydride/Au(111) Bonds by Molecular Manipulation Using an Atomic Force Microscope. *Phys. Rev. Lett.*, **109** (2012) 076102.
- [222] S. Ghosh, H. Halimun, A. K. Mahapatro, J. Choi, S. Lodha, and D. Janes. Device structure for electronic transport through individual molecules using nanoelectrodes. *Appl. Phys. Lett.*, **87** (2005) 233509.
- [223] X. Xiao, B. Xu, and N. J. Tao. Measurement of Single Molecule Conductance:

-
- Benzenedithiol and Benzenedimethanethiol. *Nano Lett.*, **4**(2) (2004) 267–271.
- [224] M. Tsutsui, Y. Teramae, S. Kurokawa, and A. Sakai. High-conductance states of single benzenedithiol molecules. *Appl. Phys. Lett.*, **89** (2006) 163111.
- [225] H. C. Nguyen, B. M. Szyja, and N. L. Doltsinis. Electric conductance of a mechanically strained molecular junction from first principles: Crucial role of structural relaxation and conformation sampling. *Phys. Rev. B*, **90** (2014) 115440.
- [226] M. Strange, C. Rostgaard, H. Häkkinen, and K. S. Thygesen. Self-consistent GW calculations of electronic transport in thiol- and amine-linked molecular junctions. *Phys. Rev. B*, **83** (2011) 115108.
- [227] M. Strange and K. S. Thygesen. Towards quantitative accuracy in first-principles transport calculations: The GW method applied to alkane/gold junctions. *Beilstein J. Nanotech.*, **2** (2011) 746–754.
- [228] W. Y. Kim and K. S. Kim. Carbon nanotube, graphene, nanowire, and molecule-based electron and spin transport phenomena using the nonequilibrium Green’s function method at the level of first principles theory. *J. Comput. Chem.*, **29**(7) (2008) 1073–1083.
- [229] F. Zahid, M. Paulsson, E. Polizzi, A. W. Ghosh, L. Siddiqui, and S. Datta. A self-consistent transport model for molecular conduction based on extended Hückel theory with full three-dimensional electrostatics. *J. Chem. Phys.*, **123** (2005) 064707.
- [230] Y. Xue and M. A. Ratner. Theoretical principles of single-molecule electronics: A chemical and mesoscopic view. *Int. J. Quantum Chem.*, **102** (2005) 911–924.
- [231] K. Hirose and N. Kobayashi. Ab initio RTM/NEGF study on electron transport through single molecules. *Physica E: Low-dimensional Systems and Nanostructures*, **40**(2) (2007) 237–240. International Symposium on Nanometer-Scale Quantum Physics.
- [232] J. Tomfohr and O. F. Sankey. Theoretical analysis of electron transport through organic molecules. *J. Chem. Phys.*, **120**(3) (2004) 1542–1554.
- [233] S. M. Lindsay and M. A. Ratner. Molecular Transport Junctions: Clearing Mists. *Adv. Mater.*, **19** (2007) 23–31.
- [234] C. Toher and S. Sanvito. Effects of self-interaction corrections on the transport properties of phenyl-based molecular junctions. *Phys. Rev. B*, **77** (2008) 155402.
- [235] C. Toher and S. Sanvito. Efficient Atomic Self-Interaction Correction Scheme

- for Nonequilibrium Quantum Transport. *Phys. Rev. Lett.*, **99** (2007) 056801.
- [236] D. J. Mowbray, G. Jones, and K. S. Thygesen. Influence of functional groups on charge transport in molecular junctions. *J. Chem. Phys.*, **128** (2008) 111103.
- [237] M. Strange, I. S. Kristensen, K. S. Thygesen, and K. W. Jacobsen. Benchmark density functional theory calculations for nanoscale conductance. *J. Chem. Phys.*, **128** (2008) 114714.
- [238] S. T. D. Pantelides, M. Di Ventra, and N. D. Lang. First-Principles Simulations of Molecular Electronics. *Ann. N. Y. Acad. Sci.*, **960**(1) (2002) 177–183.
- [239] E. G. Emberly and G. Kirczenow. Comment on “First-Principles Calculation of Transport Properties of a Molecular Device”. *Phys. Rev. Lett.*, **87** (2001) 269701.
- [240] F. Evers, F. Weigend, and M. Koentopp. Conductance of molecular wires and transport calculations based on density-functional theory. *Phys. Rev. B*, **69** (2004) 235411.
- [241] Y. Qi, J. Qin, G. Zhang, and T. Zhang. Breaking Mechanism of Single Molecular Junctions Formed by Octanedithiol Molecules and Au Electrodes. *J. Am. Chem. Soc.*, **131**(45) (2009) 16418–16422. PMID: 19902977.
- [242] Q. Pu, Y. Leng, X. Zhao, and P. T. Cummings. Molecular Simulation Studies on the Elongation of Gold Nanowires in Benzenedithiol. *J. Phys. Chem. C*, **114**(23) (2010) 10365–10372.
- [243] W. R. French, C. R. Iacovella, I. Rungger, A. M. Souza, S. Sanvito, and P. T. Cummings. Atomistic simulations of highly conductive molecular transport junctions under realistic conditions. *Nanoscale*, **5** (2013) 3654–3659.
- [244] H. Wang and Y. Leng. Gold/Benzenedithiolate/Gold Molecular Junction: A Driven Dynamics Simulation on Structural Evolution and Breaking Force under Pulling. *J. Phys. Chem. C*, **119**(27) (2015) 15216–15223.
- [245] M. Frei, S. V. Aradhya, M. S. Hybertsen, and L. Venkataraman. Linker Dependent Bond Rupture Force Measurements in Single-Molecule Junctions. *J. Am. Chem. Soc.*, **134**(9) (2012) 4003–4006.
- [246] I. Franco, G. C. Solomon, G. C. Schatz, and M. A. Ratner. Tunneling Currents That Increase with Molecular Elongation. *J. Am. Chem. Soc.*, **133**(39) (2011) 15714.
- [247] S. M. Parker, M. Smeu, I. Franco, M. A. Ratner, and T. Seideman. Molecular Junctions: Can Pulling Influence Optical Controllability? *Nano Lett.*, **14**(8)

(2014) 4587–4591.

- [248] D. Krüger, H. Fuchs, R. Rousseau, D. Marx, and M. Parrinello. Pulling Monatomic Gold Wires with Single Molecules: An *Ab Initio* Simulation. *Phys. Rev. Lett.*, **89** (2002) 186402.
- [249] D. Krüger, R. Rousseau, H. Fuchs, and D. Marx. Towards "Mechanochemistry": Mechanically Induced Isomerizations of Thiolate–Gold Clusters. *Angew. Chem. Int. Ed.*, **42**(20) (2003) 2251–2253.
- [250] B. M. Szyja, H. C. Nguyen, D. Kosov, and N. L. Doltsinis. Conformation-dependent conductance through a molecular break junction. *J. Mol. Model.*, **19**(10) (2013) 4173–4180.
- [251] N. Sergueev, L. Tsetseris, K. Varga, and S. Pantelides. Configuration and conductance evolution of benzene-dithiol molecular junctions under elongation. *Phys. Rev. B*, **82** (2010) 073106.
- [252] R. B. Pontes, A. Reily Rocha, S. Sanvito, A. Fazio, and A. J. Roque da Silva. *Ab Initio* Calculations of Structural Evolution and Conductance of Benzene-1,4-dithiol on Gold Leads. *ACS Nano*, **5**(2) (2011) 795–804. PMID: 21226481.
- [253] Y. Ie, T. Hirose, H. Nakamura, M. Kiguchi, N. Takagi, M. Kawai, and Y. Aso. Nature of Electron Transport by Pyridine-Based Tripodal Anchors: Potential for Robust and Conductive Single-Molecule Junctions with Gold Electrodes. *J. Am. Chem. Soc.*, **133**(9) (2011) 3014–3022. PMID: 21309569.
- [254] T. Hirose, Y. Ie, and Y. Aso. Synthesis of Tripodal-anchor Units Having Pyridine or Amine Functional Groups and Their Adsorption Behavior on Metal Electrodes. *Chem. Lett.*, **40**(2) (2011) 204–205.
- [255] H. Häkkinen. The gold–sulfur interface at the nanoscale. *Nature Chem.*, **4**(6) (2012) 443–455.
- [256] D. Thompson, J. Liao, M. Nolan, A. J. Quinn, C. A. Nijhuis, C. O'Dwyer, P. N. Nirmalraj, C. Schönenberger, and M. Calame. Formation Mechanism of Metal–Molecule–Metal Junctions: Molecule-Assisted Migration on Metal Defects. *J. Phys. Chem. C*, **119**(33) (2015) 19438–19451.
- [257] M. E. Zoloff Michoff, J. Ribas Arino, and D. Marx. Nanomechanics of Bidentate Thiolate Ligands on Gold Surfaces. *Phys. Rev. Lett.*, **114** (2015) 075501.
- [258] B. Baisch, D. Raffa, U. Jung, O. M. Magnussen, C. Nicolas, J. Lacour, J. Kubitschke, and R. Herges. Mounting Freestanding Molecular Functions onto Surfaces: The Platform Approach. *J. Am. Chem. Soc.*, **131**(2) (2009) 442–443.

- [259] U. Jung, S. Kuhn, U. Cornelissen, F. Tucek, T. Strunskus, V. Zaporozhchenko, J. Kubitschke, R. Herges, and O. Magnussen. Azobenzene-Containing Triazatriangulenium Adlayers on Au(111): Structural and Spectroscopic Characterization. *Langmuir*, **27**(10) (2011) 5899–5908.
- [260] U. Jung, C. Schütt, O. Filinova, J. Kubitschke, R. Herges, and O. Magnussen. Photoswitching of Azobenzene-Functionalized Molecular Platforms on Au Surfaces. *J. Phys. Chem. C*, **116**(49) (2012) 25943–25948.
- [261] U. Jung, J. Kubitschke, R. Herges, and O. Magnussen. Studies of the molecular switching of azobenzene-functionalized platform adlayers on Au(111) by chronoamperometry. *Electrochim. Acta*, **112** (2013) 869–880.
- [262] S. Lemke, C.-H. Chang, U. Jung, and O. M. Magnussen. Reversible Potential-Induced Switching of Alkyl Chain Aggregation in Octyl-Triazatriangulenium Adlayers on Au(111). *Langmuir*, **31**(10) (2015) 3115–3124.
- [263] F. L. Otte, S. Lemke, C. Schütt, N. R. Krekieln, U. Jung, O. M. Magnussen, and R. Herges. Ordered Monolayers of Free-Standing Porphyrins on Gold. *J. Am. Chem. Soc.*, **136**(32) (2014) 11248–11251.
- [264] M. Hammerich and R. Herges. Laterally Mounted Azobenzenes on Platforms. *J. Org. Chem.*, **80**(22) (2015) 11233–11236.
- [265] Z. Wei, X. Wang, A. Borges, M. Santella, T. Li, J. K. Sørensen, M. Vanin, W. Hu, Y. Liu, J. Ulstrup, G. C. Solomon, Q. Chi, T. Bjørnholm, K. Nørgaard, and B. W. Laursen. Triazatriangulene as Binding Group for Molecular Electronics. *Langmuir*, **30**(49) (2014) 14868–14876.
- [266] G. Sedghi, V. M. García Suárez, L. J. Esdaile, H. L. Anderson, C. J. Lambert, S. Martín, D. Bethell, S. J. Higgins, M. Elliott, N. Bennett, Macdonald. J. Emyr, and R. J. Nichols. Long-range electron tunnelling in oligo-porphyrin molecular wires. *Nat. Nanotechnol.*, **6**(8) (2011) 517–523.
- [267] J.-H. Kim, Y.-H. Jeong, H.-J. Yoon, H. Tran, L. M. Campos, and W.-D. Jang. Cascade sensing of gold and thiols with imidazole-bearing functional porphyrins. *Chem. Commun.*, **50** (2014) 11500–11503.
- [268] Y.-H. Jeong, M. Son, H. Yoon, P. Kim, D.-H. Lee, D. Kim, and W.-D. Jang. Guest-Induced Photophysical Property Switching of Artificial Light-Harvesting Dendrimers. *Angew. Chem.*, **126**(27) (2014) 7045–7048.
- [269] H. Yoon, J. Min Lim, H.-C. Gee, C.-H. Lee, Y.-H. Jeong, D. Kim, and W.-D. Jang. A Porphyrin-Based Molecular Tweezer: Guest-Induced Switching of Forward and Backward Photoinduced Energy Transfer. *J. Am. Chem. Soc.*, **136**(4) (2014) 1672–1679. PMID: 24401158.

-
- [270] T. Hasobe. Porphyrin-Based Supramolecular Nanoarchitectures for Solar Energy Conversion. *J. Phys. Chem. Lett.*, **4**(11) (2013) 1771–1780. PMID: 26283108.
- [271] J. Brede, M. Linares, R. Lensen, A. E. Rowan, M. Funk, M. Bröring, G. Hoffmann, and R. Wiesendanger. Adsorption and conformation of porphyrins on metallic surfaces. *J. Vac. Sci. Technol. B*, **27** (2009) 799.
- [272] M. Gruyters, T. Pingel, T. G. Gopakumar, N. Néel, Ch. Schütt, F. Köhler, R. Herges, and R. Berndt. Electronic Ground-State and Orbital Ordering of Iron Phthalocyanine on H/Si(111) Unraveled by Spatially Resolved Tunneling Spectroscopy. *J. Phys. Chem. C*, **116**(39) (2012) 20882–20886.
- [273] G. P. Acuna, M. Bucher, I. H. Stein, C. Steinhauer, A. Kuzyk, P. Holzmeister, R. Schreiber, A. Moroz, F. D. Stefani, T. Liedl, F. C. Simmel, and P. Tinnefeld. Distance Dependence of Single-Fluorophore Quenching by Gold Nanoparticles Studied on DNA Origami. *ACS Nano*, **6**(4) (2012) 3189–3195. PMID: 22439823.
- [274] A. Sperl, J. Kröger, and R. Berndt. Electronic Superstructure of Lead Phthalocyanine on Lead Islands. *J. Phys. Chem. A*, **115**(25) (2011) 6973–6978. PMID: 21473640.
- [275] F. Duclairoir and J.-C. Marchon. Anchoring of porphyrins and phthalocyanines on conductors and semiconductors for use in hybrid electronics. In K. M. Kadish, K. M. Smith, and R. Guilard, Eds., *Handbook of Porphyrin Science*, Volume 10, p. 245–311. World Scientific Publishing Co. Pte. Ltd., Singapore, Singapore, 2010.
- [276] Z.-F. Liu, S. Wei, H. Yoon, O. Adak, I. Ponce, Y. Jiang, W.-D. Jang, L. M. Campos, L. Venkataraman, and J. B. Neaton. Control of Single-Molecule Junction Conductance of Porphyrins via a Transition-Metal Center. *Nano Lett.*, **14**(9) (2014) 5365–5370. PMID: 25111197.
- [277] M. L. Perrin, F. Prins, C. A. Martin, A. J. Shaikh, R. Eelkema, J. H. van Esch, T. Briza, R. Kaplanek, V. Kral, v. d. Z. H. S. J. van Ruitenbeek, Jan M., and D. Dulić. Influence of the Chemical Structure on the Stability and Conductance of Porphyrin Single-Molecule Junctions. *Angew. Chem. Int. Ed.*, **50**(47) (2011) 11223–11226.
- [278] Z. Li, T.-H. Park, J. Rawson, M. J. Therien, and E. Borguet. Quasi-Ohmic Single Molecule Charge Transport through Highly Conjugated meso-to-meso Ethyne-Bridged Porphyrin Wires. *Nano Lett.*, **12**(6) (2012) 2722–2727. PMID: 22500812.
- [279] M. L. Perrin, C. A. Martin, F. Prins, A. J. Shaikh, R. Eelkema, J. H. van Esch,

- J. M. van Ruitenbeek, H. S. J. van der Zant, and D. Dulić. Charge transport in a zinc-porphyrin single-molecule junction. *Beilstein J. Nanotech.*, **2** (2011) 714–719.
- [280] Z. Li and E. Borguet. Determining Charge Transport Pathways through Single Porphyrin Molecules Using Scanning Tunneling Microscopy Break Junctions. *J. Am. Chem Soc.*, **134**(1) (2012) 63–66. PMID: 22133080.
- [281] H. Imahori, H. Norieda, Y. Nishimura, I. Yamazaki, K. Higuchi, N. Kato, T. Motohiro, H. Yamada, K. Tamaki, M. Arimura, and Y. Sakata. Chain Length Effect on the Structure and Photoelectrochemical Properties of Self-Assembled Monolayers of Porphyrins on Gold Electrodes. *J. Phys. Chem. B*, **104**(6) (2000) 1253–1260.
- [282] Y. Hong, J. W. Y. Lam, and B. Z. Tang. Aggregation-induced emission. *Chem. Soc. Rev.*, **40** (2011) 5361–5388.
- [283] N. Hauptmann, L. Groß, K. Buchmann, K. Scheil, C. Schütt, F. L. Otte, R. Herges, C. Herrmann, and R. Berndt. High-conductance surface-anchoring of a mechanically flexible platform-based porphyrin complex. *New J. Phys.*, **17**(1) (2015) 013012.
- [284] N. Hauptmann, K. Scheil, T. G. Gopakumar, F. L. Otte, C. Schütt, R. Herges, and R. Berndt. Surface Control of Alkyl Chain Conformations and 2D Chiral Amplification. *J. Am. Chem Soc.*, **135**(24) (2013) 8814–8817.
- [285] A. J. Simbeck, G. Qian, S. K. Nayak, G.-C. Wang, and K. M. Lewis. Gold–sulfur bond breaking in Zn(II) tetraphenylporphyrin molecular junctions. *Surf. Sci.*, **606**(17-18) (2012) 1412–1415.
- [286] X. Qian, J. Li, and S. Yip. Calculating phase-coherent quantum transport in nanoelectronics with *ab initio* quasiatomic orbital basis set. *Phys. Rev. B*, **82** (2010) 195442.
- [287] N. W. Ashcroft and N. D. Mermin. *Solid State Physics*. Holt Rinehart & Winston, Austin, 1976.
- [288] C. Adam, A. Wallabregue, H. Li, J. Guoin, R. Vanel, S. Grass, J. Bosson, L. Bouffier, J. Lacour, and N. Sojic. Electrogenenerated Chemiluminescence of Cationic Triangulene Dyes: Crucial Influence of the Core Heteroatoms. *Chem. Eur. J.*, **21**(52) (2015) 19243–19249.
- [289] S. Kuhn, U. Jung, S. Ulrich, R. Herges, and O. Magnussen. Adlayers based on molecular platforms of trioxatriangulenium. *Chem. Commun.*, **47**(31) (2011) 8880.
- [290] E. Thyrrhaug, T. J. Sørensen, I. Gryczynski, Z. Gryczynski, and B. W.

-
- Laursen. Polarization and Symmetry of Electronic Transitions in Long Fluorescence Lifetime Triangulenium Dyes. *J. Phys. Chem. A*, **117**(10) (2013) 2160–2168.
- [291] T. J. Sørensen and B. W. Laursen. Synthesis and Optical Properties of Trioxatriangulenium Dyes with One and Two Peripheral Amino Substituents. *J. Org. Chem.*, **75**(18) (2010) 6182–6190.
- [292] B. W. Laursen and T. J. Sørensen. Synthesis of Super Stable Triangulenium Dye. *J. Org. Chem.*, **74**(8) (2009) 3183–3185.
- [293] T. Jasper-Tönnies and R. Berndt. unpublished results, 2014.
- [294] P. J. Feibelman, B. Hammer, J. K. Nørskov, F. Wagner, M. Scheffler, R. Stumpf, R. Watwe, and J. Dumesic. The CO/Pt(111) Puzzle. *J. Phys. Chem. B*, **105**(18) (2001) 4018–4025.
- [295] S. Sanvito and A. R. Rocha. Molecular-Spintronics: The Art of Driving Spin Through Molecules. *J. Comput. Theor. Nanosci.*, **3** (2006) 624–642.
- [296] P. Seneor, A. Bernand Mantel, and F. Petroff. Nanospintronics: when spintronics meets single electron physics. *J. Phys.: Condens. Matter*, **19** (2007) 165222.
- [297] S. A. Wolf, D. D. Awschalom, R. A. Buhrman, J. M. Daughton, S. von Molnár, M. L. Roukes, A. Y. Chtchelkanova, and D. M. Treger. Spintronics: A Spin-Based Electronics Vision for the Future. *Science*, **294** (2001) 1488–1495.
- [298] S. A. Wolf, A. Y. Chtchelkanova, and D. M. Treger. Spintronics — A retrospective and perspective. *IBM J. Res. Dev.*, **50**(1) (2006) 101–110.
- [299] A. S. Zyazin, J. W. G. van den Berg, E. A. Osorio, H. S. J. van der Zant, N. P. Konstantinidis, M. Leijnse, M. R. Wegewijs, F. May, W. Hofstetter, C. Danieli, and A. Cornia. Electric Field Controlled Magnetic Anisotropy in a Single Molecule. *Nano Lett.*, **10**(9) (2010) 3307–3311. PMID: 20687519.
- [300] H. B. Heersche, Z. de Groot, J. A. Folk, H. S. J. van der Zant, C. Romeike, M. R. Wegewijs, L. Zobbi, D. Barreca, E. Tondello, and A. Cornia. Electron transport through single Mn₁₂ molecular magnets. *Phys. Rev. Lett.*, **96**(20) (2006) 206801.
- [301] E. Burzurí, A. S. Zyazin, A. Cornia, and H. S. J. van der Zant. Direct Observation of Magnetic Anisotropy in an Individual Fe₄ Single-Molecule Magnet. *Phys. Rev. Lett.*, **109** (2012) 147203.
- [302] M. Karolak, D. Jacob, and A. I. Lichtenstein. Orbital Kondo effect in Cobalt-Benzene sandwich molecules. *Phys. Rev. Lett.*, **107** (2011) 146604.

- [303] E. A. Osorio, K. Moth Poulsen, H. S. J. van der Zant, J. Paaske, P. Hedegård, K. Flensberg, J. Bendix, and T. Bjørnholm. Electrical Manipulation of Spin States in a Single Electrostatically Gated Transition-Metal Complex. *Nano Lett.*, **10**(1) (2010) 105–110.
- [304] V. Meded, A. Bagrets, K. Fink, R. Chandrasekar, M. Ruben, F. Evers, A. Bernard Mantel, J. S. Seldenthuis, A. Beukman, and H. S. J. van der Zant. Electrical control over the Fe(II) spin crossover in a single molecule: Theory and experiment. *Phys. Rev. B*, **83** (2011) 245415.
- [305] E. J. Devid, P. N. Martinho, M. V. Kamalakar, I. Šalitroš, Ú. Prendergast, J.-F. Dayen, V. Meded, T. Lemma, R. González Prieto, F. Evers, T. E. Keyes, M. Ruben, B. Doudin, and S. J. van der Molen. Spin Transition in Arrays of Gold Nanoparticles and Spin Crossover Molecules. *ACS Nano*, **9**(4) (2015) 4496–4507.
- [306] J. S. Miller. Bistable Electrical, Optical, and Magnetic Behavior in a Molecule-Based Material. *Angew. Chem. Int. Ed.*, **42**(1) (2003) 27–29.
- [307] M. Urdampilleta, S. Klyatskaya, J.-P. Cleuziou, M. Ruben, and W. Wernsdorfer. Supramolecular spin values. *Nat. Mater.*, **10** (2011) 502–506.
- [308] S. Sanvito. Organic spintronics: Filtering spins with molecules. *Nat. Mater.*, **10**(7) (2011) 484–485.
- [309] E. Ruiz. Charge transport properties of spin crossover systems. *Phys. Chem. Chem. Phys.*, **16**(1) (2014) 14–22.
- [310] P. Hauke, V. Schünemann, and J. A. Wolny. Progress in Electronic Structure Calculations on Spin-Crossover Complexes. *Eur. J. Inorg. Chem.*, **2013**(5-6) (2013) 628–641.
- [311] D. Aravena and E. Ruiz. Coherent Transport through Spin-Crossover Single Molecules. *J. Am. Chem. Soc.*, **134**(2) (2012) 777–779.
- [312] N. Baadji and S. Sanvito. Giant Resistance Change across the Phase Transition in Spin-Crossover Molecules. *Phys. Rev. Lett.*, **108** (2012) 217201.
- [313] C. Elschenbroich and A. Salzer. *Organometallics: A Concise Introduction*. VCH Weinheim, 1989.
- [314] J. H. Ammeter. EPR of orbitally degenerate sandwich compounds. *Journal of Magnetic Resonance (1969)*, **30**(2) (1978) 299–325.
- [315] J. H. Ammeter, L. Zoller, J. Bachmann, P. Baltzer, E. Gamp, R. Bucher, and E. Deiss. The Influence of Molecular Host Lattices on Electronic Properties of Orbitally (Near-) Degenerate Transition Metal Complexes. *Helv. Chim.*

Acta, **64**(4) (1981) 1063–1082.

- [316] Z.-F. Xu, Y. Xie, W.-L. Feng, and H. F. Schaefer. Systematic Investigation of Electronic and Molecular Structures for the First Transition Metal Series Metallocenes $M(C_5H_5)_2$ ($M = V, Cr, Mn, Fe, Co,$ and Ni). *J. Phys. Chem. A*, **107**(15) (2003) 2716–2729.
- [317] V. Lorenz, S. Blaurock, C. G. Hrib, and F. T. Edelmann. The First Linear, Homoleptic Triple-Decker Sandwich Complex of an f-Element: A Molecular Model for Organolanthanide Nanowires. *Organometallics*, **29**(21) (2010) 4787–4789.
- [318] S. Barlow and D. O’Hare. Metal–Metal Interactions in Linked Metallocenes. *Chem. Rev.*, **97**(3) (1997) 637–670.
- [319] S. Santi, A. Ceccon, A. Bisello, C. Durante, P. Ganis, L. Orian, F. Benetollo, and L. Crociani. Designing Molecules for Metal–Metal Electronic Communication: Synthesis and Molecular Structure of the Couple of Heterobimetallic Isomers $[\nu^6\text{-}(2\text{-Ferrocenyl})\text{indene}]\text{-Cr}(\text{CO})_3$ and $[\nu^6\text{-}(3\text{-Ferrocenyl})\text{indene}]\text{-Cr}(\text{CO})_3$. *Organometallics*, **24**(19) (2005) 4691–4694.
- [320] H. Da, H. M. Jin, K. H. Lim, and S.-W. Yang. Half-Metallic Spintronic Switch of Bimetallic Sandwich Molecular Wire via the Control of External Electrical Field. *J. Phys. Chem. C*, **114**(49) (2010) 21705–21707.
- [321] M. Koleini, M. Paulsson, and M. Brandbyge. Efficient Organometallic Spin Filter between Single-Wall Carbon Nanotube or Graphene Electrodes. *Phys. Rev. Lett.*, **98** (2007) 197202.
- [322] N. Atodiresei, P. H. Dederichs, Y. Mokrousov, L. Bergqvist, G. Bihlmayer, and S. Blügel. Controlling the Magnetization Direction in Molecules via Their Oxidation State. *Phys. Rev. Lett.*, **100** (2008) 117207.
- [323] L. Zhou, S.-W. Yang, M.-F. Ng, M. B. Sullivan, Tan, and L. Shen. One-Dimensional Iron-Cyclopentadienyl Sandwich Molecular Wire with Half Metallic, Negative Differential Resistance and High-Spin Filter Efficiency Properties. *J. Am. Chem. Soc.*, **130**(12) (2008) 4023–4027.
- [324] C. Morari, H. Allmaier, F. Beiuşeanu, T. Jurcuţ, and L. Chioncel. Electronic structure and magnetic properties of metallocene multiple-decker sandwich nanowires. *Phys. Rev. B*, **85** (2012) 085413.
- [325] H. Xiang, J. Yang, J. G. Hou, and Q. Zhu. One-Dimensional Transition Metal–Benzene Sandwich Polymers: Possible Ideal Conductors for Spin Transport. *J. Am. Chem. Soc.*, **128**(7) (2006) 2310–2314.
- [326] Y. Mokrousov, N. Atodiresei, G. Bihlmayer, S. Heinze, and S. Blügel. The in-

- terplay of structure and spin-orbit strength in the magnetism of metalbenzene sandwiches: from single molecules to infinite wires. *Nanotechnology*, **18**(49) (2007) 495402.
- [327] L. Shen, S.-W. Yang, M.-F. Ng, V. Ligatchev, L. Zhou, and Y. Feng. Charge-Transfer-Based Mechanism for Half-Metallicity and Ferromagnetism in one-Dimensional Organometallic Sandwich Molecular Wires. *J. Am. Chem. Soc.*, **130**(42) (2008) 13956–13960.
- [328] M. L. Hays, D. J. Burkey, J. S. Overby, T. P. Hanusa, S. P. Sellers, G. T. Yee, and V. G. Young. Steric Influence on the Structure, Magnetic Properties, and Reactivity of Hexa- and Octaisopropylmanganocene. *Organometallics*, **17**(25) (1998) 5521–5527.
- [329] A. Haaland. The molecular structure of high-spin manganocene, $(n\text{-C}_5\text{H}_5)_2\text{Mn}$, by gas phase electron diffraction: a rerefinement. *Inorganic and Nuclear Chemistry Letters*, **15**(5-6) (1979) 267–269.
- [330] D. P. Freyberg, J. L. Robbins, K. N. Raymond, and J. C. Smart. Crystal and molecular structures of decamethylmanganocene and decamethylferrocene. Static Jahn-Teller distortion in a metallocene. *J. Am. Chem. Soc.*, **101**(4) (1979) 892–897.
- [331] O. Salomon, M. Reiher, and B. A. Hess. Assertion and validation of the performance of the B3LYP* functional for the first transition metal row and the G2 test set. *J. Chem. Phys.*, **117**(10) (2002) 4729.
- [332] M. Swart, A. R. Groenhof, A. W. Ehlers, and K. Lammertsma. Validation of Exchange-Correlation Functionals for Spin States of Iron Complexes. *J. Phys. Chem. A*, **108**(25) (2004) 5479–5483.
- [333] M. S. Zöllner, M. P. Bahlke, A. Bahde, and C. Herrmann. Modeling spin transfer from molecular adsorbates to metal surfaces, in preparation, 2016.
- [334] G. Brodén, T. Rhodin, C. Brucker, R. Benbow, and Z. Hurych. Synchrotron radiation study of chemisorptive bonding of CO on transition metals – Polarization effect on Ir(100). *Surface Science*, **59**(2) (1976) 593–611.
- [335] L. Gross, F. Mohn, N. Moll, P. Liljeroth, and G. Meyer. The Chemical Structure of a Molecule Resolved by Atomic Force Microscopy. *Science*, **325**(5944) (2009) 1110–1114.
- [336] M. Neu, N. Moll, L. Gross, G. Meyer, F. J. Giessibl, and J. Repp. Image correction for atomic force microscopy images with functionalized tips. *Phys. Rev. B*, **89** (2014) 205407.
- [337] B. Schuler, W. Liu, A. Tkatchenko, N. Moll, G. Meyer, A. Mistry, D. Fox,

-
- and L. Gross. Adsorption Geometry Determination of Single Molecules by Atomic Force Microscopy. *Phys. Rev. Lett.*, **111** (2013) 106103.
- [338] L. Gross, F. Mohn, N. Moll, B. Schuler, A. Criado, E. Guitián, D. Peña, A. Gourdon, and G. Meyer. Bond-Order Discrimination by Atomic Force Microscopy. *Science*, **337**(6100) (2012) 1326–1329.
- [339] O. Guillermet, S. Gauthier, C. Joachim, P. de Mendoza, T. Lauterbach, and A. Echavarren. STM and AFM high resolution intramolecular imaging of a single decastarphene molecule. *Chem. Phys. Lett.*, **511**(4–6) (2011) 482–485.
- [340] N. Moll, L. Gross, F. Mohn, A. Curioni, and G. Meyer. The mechanisms underlying the enhanced resolution of atomic force microscopy with functionalized tips. *New J. Phys.*, **12**(12) (2010) 125020.
- [341] N. Moll, B. Schuler, S. Kawai, F. Xu, L. Peng, A. Orita, J. Otera, A. Curioni, M. Neu, J. Repp, G. Meyer, and L. Gross. Image Distortions of a Partially Fluorinated Hydrocarbon Molecule in Atomic Force Microscopy with Carbon Monoxide Terminated Tips. *Nano Lett.*, **14**(11) (2014) 6127–6131. PMID: 25247477.
- [342] B. Schuler, S. Fatayer, F. Mohn, N. Moll, N. Pavliček, G. Meyer, D. Peña, and L. Gross. Reversible Bergman cyclization by atomic manipulation. *Nature Chem.*, Jan 2016) 1–5.
- [343] A. Schwarz, A. Köhler, J. Grenz, and R. Wiesendanger. Detecting the dipole moment of a single carbon monoxide molecule. *Appl. Phys. Lett.*, **105**(1) (2014) 011606.
- [344] C. F. Matta and R. J. Gillespie. Understanding and Interpreting Molecular Electron Density Distributions. *J. Chem. Educ.*, **79**(9) (2002) 1141.
- [345] P. Deshlahra, J. Conway, E. E. Wolf, and W. F. Schneider. Influence of Dipole–Dipole Interactions on Coverage-Dependent Adsorption: CO and NO on Pt(111). *Langmuir*, **28**(22) (2012) 8408–8417.
- [346] M. Gajdoš and J. Hafner. CO adsorption on Cu(111) and Cu(001) surfaces: Improving site preference in DFT calculations. *Surf. Sci.*, **590**(2-3) (2005) 117–126.
- [347] D. Z. Gao, J. Grenz, M. B. Watkins, F. Federici Canova, A. Schwarz, R. Wiesendanger, and A. L. Shluger. Using Metallic Noncontact Atomic Force Microscope Tips for Imaging Insulators and Polar Molecules: Tip Characterization and Imaging Mechanisms. *ACS Nano*, **8**(5) (2014) 5339–5351.
- [348] M. Ellner, N. Pavliček, P. Pou, B. Schuler, N. Moll, G. Meyer, L. Gross, and R. Pérez. The electric field of co tips and its relevance for atomic force

- microscopy. *Nano Lett.*, 2016. PMID: 26840626.
- [349] T. Trevethan, M. Watkins, and A. L. Shluger. Models of the interaction of metal tips with insulating surfaces. *Beilstein J. Nanotech.*, **3** (2012) 329–335.
- [350] I. Grinberg, Y. Yourdshahyan, and A. M. Rappe. CO on Pt(111) puzzle: A possible solution. *J. Chem. Phys.*, **117**(5) (2002) 2264.
- [351] L. Schimka, J. Harl, A. Stroppa, A. Grneis, M. Marsman, F. Mittendorfer, and G. Kresse. Accurate surface and adsorption energies from many-body perturbation theory. *Nat. Mater.*, **9** (2010) 741–744.
- [352] S. Reich, C. Thomsen, and J. Maultzsch. *Carbon Nanotubes – Basic Concepts and Physical Properties*. Wiley-VCH, Weinheim, 2004.
- [353] M. S. Dresselhaus, G. Dresselhaus, and P. Avouris, Eds. *Carbon Nanotubes: Synthesis, Structure, Properties and Applications*. Springer Berlin Heidelberg, 2001.
- [354] Y.-S. Lee, M. B. Nardelli, and N. Marzari. Band Structure and Quantum Conductance of Nanostructures from Maximally Localized Wannier Functions: The Case of Functionalized Carbon Nanotubes. *Phys. Rev. Lett.*, **95** (2005) 076804.
- [355] A. A. Mostofi, J. R. Yates, Y.-S. Lee, I. Souza, D. Vanderbilt, and N. Marzari. wannier90: A tool for obtaining maximally-localised Wannier functions. *Comp. Phys. Comm.*, **178**(9) (2008) 685 – 699.
- [356] L. van Hove. The Occurrence of Singularities in the Elastic Frequency Distribution of a Crystal. *Phys. Rev.*, **89**(6) (1953) 1189–1193.
- [357] A. Hirsch. Functionalization of Single-Walled Carbon Nanotubes. *Angew. Chem. Int. Ed.*, **41**(11) (2002) 1853.
- [358] K. Balasubramanian, M. Burghard, K. Kern, M. Scolari, and A. Mews. Photocurrent Imaging of Charge Transport Barriers in Carbon Nanotube Devices. *Nano Lett.*, **5**(3) (2005) 507–510. PMID: 15755103.
- [359] F. Ernst, T. Heek, A. Setaro, R. Haag, and S. Reich. Energy Transfer in Nanotube-Perylene Complexes. *Adv. Funct. Mater.*, **22**(18) (2012) 3921–3926.
- [360] F. Ernst, T. Heek, A. Setaro, R. Haag, and S. Reich. Functional Surfactants for Carbon Nanotubes: Effects of Design. *J. Phys. Chem. C*, **117**(2) (2013) 1157–1162.
- [361] M. J. O’Connell. Band Gap Fluorescence from Individual Single-Walled Carbon Nanotubes. *Science*, **297**(5581) (2002) 593–596.

-
- [362] S. M. Bachilo. Structure-Assigned Optical Spectra of Single-Walled Carbon Nanotubes. *Science*, **298**(5602) (2002) 2361–2366.
- [363] E. Y. Li, N. Poilvert, and N. Marzari. Switchable Conductance in Functionalized Carbon Nanotubes via Reversible Sidewall Bond Cleavage. *ACS Nano*, **5**(6) (2011) 4455–4465.
- [364] Y.-S. Lee and N. Marzari. Cycloaddition Functionalizations to Preserve or Control the Conductance of Carbon Nanotubes. *Phys. Rev. Lett.*, **97** (2006) 116801.
- [365] A. Maiti. Multiscale modeling with carbon nanotubes. *Microelectron. J.*, **39**(2) (2008) 208–221.
- [366] A. Maiti. Electromechanical and Chemical Sensing at the Nanoscale: DFT and Transport Modeling. In M. A. Ryan, A. V. Shevade, C. J. Taylor, M. L. Homer, M. Blanco, and J. R. Stetter, Eds., *Computational Methods for Sensor Material Selection*, Integrated Analytical Systems, p. 47–69. Springer US, 2010.
- [367] J. Hutter, M. Iannuzzi, F. Schiffmann, and J. VandeVondele. CP2K: atomistic simulations of condensed matter systems. *WIREs Comput. Mol. Sci.*, (2013) 15–25.
- [368] Amsterdam Density Functional Program; Theoretical Chemistry, Vrije Universiteit: Amsterdam. <http://www.scm.com>.
- [369] G. te Velde, F. M. Bickelhaupt, Evert Jan Baerends, C. Fonseca Guerra, S. J. A. van Gisbergen, J. G. Snijders, and T. J. Ziegler. Chemistry with ADF. *J. Comput. Chem.*, **22** (2001) 931–967.
- [370] G. te Velde and E. J. Baerends. Precise density-functional method for periodic structures. *Phys. Rev. B*, **44** (1991) 7888–7903.
- [371] M. J. Frisch, G. W. Trucks, H. B. Schlegel, G. E. Scuseria, M. A. Robb, J. R. Cheeseman, G. Scalmani, V. Barone, B. Mennucci, G. A. Petersson, H. Nakatsuji, M. Caricato, X. Li, H. P. Hratchian, A. F. Izmaylov, J. Bloino, G. Zheng, J. L. Sonnenberg, M. Hada, M. Ehara, K. Toyota, R. Fukuda, J. Hasegawa, M. Ishida, T. Nakajima, Y. Honda, O. Kitao, H. Nakai, T. Vreven, J. A. Montgomery, Jr., J. E. Peralta, F. Ogliaro, M. Bearpark, J. J. Heyd, E. Brothers, K. N. Kudin, V. N. Staroverov, R. Kobayashi, J. Normand, K. Raghavachari, A. Rendell, J. C. Burant, S. S. Iyengar, J. Tomasi, M. Cossi, N. Rega, J. M. Millam, M. Klene, J. E. Knox, J. B. Cross, V. Bakken, C. Adamo, J. Jaramillo, R. Gomperts, R. E. Stratmann, O. Yazyev, A. J. Austin, R. Cammi, C. Pomelli, J. W. Ochterski, R. L. Martin, K. Morokuma, V. G. Zakrzewski, G. A. Voth, P. Salvador, J. J. Dannenberg, S. Dapprich, A. D.

- Daniels, O. Farkas, J. B. Foresman, J. V. Ortiz, J. Cioslowski, and D. J. Fox. Gaussian 09 Revision A.1. Gaussian Inc. Wallingford CT 2009.
- [372] R. Vincent, S. Klyatskaya, M. Ruben, W. Wernsdorfer, and F. Balestro. Electronic read-out of a single nuclear spin using a molecular spin transistor. *Nature*, **488**(7411) (2012) 357–360.
- [373] M. Ganzhorn, S. Klyatskaya, M. Ruben, and W. Wernsdorfer. Carbon Nanotube Nanoelectromechanical Systems as Magnetometers for Single-Molecule Magnets. *ACS Nano*, **7** (2013) 6225–6236. PMID: 23802618.
- [374] M. Schneiderbauer, M. Emmrich, A. J. Weymouth, and Franz J. Giessibl. CO Tip Functionalization Inverts Atomic Force Microscopy Contrast via Short-Range Electrostatic Forces. *Phys. Rev. Lett.*, **112** (2014) 166102.
- [375] N. M. Caffrey, K. Buchmann, N. Hauptmann, C. Lazo, P. Ferriani, S. Heinze, and R. Berndt. Competing Forces during Contact Formation between a Tip and a Single Molecule. *ACS Nano*, **15** (2015) 5156–5160.
- [376] P. C. Rusu and G. Brocks. Surface Dipoles and Work Functions of Alkylthiolates and Fluorinated Alkylthiolates on Au(111). *J. Phys. Chem. B*, **110**(45) (2006) 22628–22634.
- [377] M. Kotiuga, P. Darancet, C. R. Arroyo, L. Venkataraman, and J. B. Neaton. Adsorption-Induced Solvent-Based Electrostatic Gating of Charge Transport through Molecular Junctions. *Nano Lett.*, **15**(7) (2015) 4498–4503.
- [378] E. Malic, A. Setaro, P. Bluemmel, C. F. Sanz Navarro, P. Ordejón, S. Reich, and A. Knorr. Carbon nanotubes as substrates for molecular spiropyran-based switches. *J. Phys.: Condens. Matter*, **24** (2012) 394006.
- [379] P. Bluemmel, A. Setaro, C. Maity, S. Hecht, and S. Reich. Designing a spiropyran-based molecular switch for carbon nanotube functionalization: Influence of anchor groups and tube-switch separation. *physica status solidi (b)*, **249**(12) (2012) 2479–2482.
- [380] Y. Zhao, C. Huang, M. Kim, B. M. Wong, F. Léonard, P. Gopalan, and M. A. Eriksson. Functionalization of Single-Wall Carbon Nanotubes with Chromophores of Opposite Internal Dipole Orientation. *ACS Applied Materials & Interfaces*, **5**(19) (2013) 9355–9361.
- [381] F. Paul, J.-Y. Mevellec, and C. Lapinte. Electron-rich Fe(II) and Fe(III) organoiron σ -alkynyl complexes bearing a functional aryl group. Vibrational spectroscopic investigations of the substituent effect on the C–C triple bond. *J. Chem. Soc., Dalton Trans.*, **8** (2002) 1783–1790.
- [382] E. A. Ziemann, J. B. Mietner, M. Deffner, N. Van Steerteghem, K. Clays,

-
- C. Herrmann, and J. Heck. Extended Threefold-Symmetric Second-Harmonic-Generation Chromophores Based on 1,3,5-Trisubstituted Benzene Complexes. *Eur. J. Inorg. Chem.*, **2015**(25) (2015) 4244–4253.
- [383] A. V. Marenich, C. J. Cramer, and D. G. Truhlar. Reduced and quenched polarizabilities of interior atoms in molecules. *Chem. Sci.*, **4** (2013) 2349.
- [384] A. Krawczuk, D. Pérez, and P. Macchi. PolaBer: a program to calculate and visualize distributed atomic polarizabilities based on electron density partitioning. *J. Appl. Cryst.*, **47** (2014) 1452–1458.
- [385] A. Krawczuk-Pantula, D. Pérez, K. Stadnicka, and P. Macchi. Distributed atomic polarizabilities from electron density. 1. Motivations and Theory. *Trans. Am. Crystallogr. Assoc.*, (2011) 1–25.
- [386] R. S. Mulliken. Electronic Population Analysis on LCAO-MO Molecular Wave Functions I. *J. Chem. Phys.*, **23**(10) (1955) 1833–1840.
- [387] P.-O. Löwdin. On the Non-Orthogonality Problem Connected with the Use of Atomic Wave Functions in the Theory of Molecules and Crystals. *J. Chem. Phys.*, **18**(3) (1950) 365.
- [388] E. R. Davidson. Electronic Population Analysis of Molecular Wavefunctions. *J. Chem. Phys.*, **46**(9) (1967) 3320–3324.
- [389] K. R. Roby. Quantum theory of chemical valence concepts I. Definition of the charge on an atom in a molecule and of occupation numbers for electron density shared between atoms. *Mol. Phys.*, **27** (1974) 81–104.
- [390] J. Cioslowski. A New Population Analysis Based on Atomic Polar Tensors. *J. Am. Chem. Soc.*, **111**(22) (1988) 8333–8337.
- [391] A. E. Reed, R. B. Weinstock, and F. Weinhold. Natural population analysis. *J. Chem. Phys.*, **83**(2) (1984) 735–746.
- [392] A. E. Clark and E. R. Davidson. Population Analyses That Utilize Projection Operators. *Int. J. Quantum Chem.*, **93** (2003) 384–394.
- [393] J. G. Ángyán, G. Jansen, M. Loss, C. Hättig, and B. A. Heß. Distributed polarizabilities using the topological theory of atoms in molecules. *J. Chem. Phys. Lett.*, **219**(3-4) (1994) 267–273.
- [394] E. Ramos Cordoba, E. Matito, I. Mayer, and P. Salvador. Toward a Unique Definition of the Local Spin. *J. Chem. Theory Comput.*, **8** (2012) 1270–1279.
- [395] I. Mayer. Local spins: An alternative treatment for single determinant wave functions. *Chem. Phys. Lett.*, **440** (2007) 357–359.
- [396] C. Herrmann, J. Neugebauer, J. A. Gladysz, and M. Reiher. Theoretical Study

- on the Spin-State Energy Splittings and Local Spin in Cationic [Re]-C_n-[Re] Complexes. *Inorg. Chem.*, **44** (2005) 6174–6182.
- [397] M. Podewitz, C. Herrmann, A. Malassa, M. Westerhausen, and M. Reiher. Spin–Spin interactions in polynuclear transition-metal complexes. *Chem. Phys. Lett.*, **451** (2008) 301–308.
- [398] J. Meister and W. H. E. Schwarz. Principal Components of Ionicity. *J. Phys. Chem.*, **98** (1994) 8245–8252.
- [399] A. E. Clark and E. R. Davidson. Local spin,. *J. Chem. Phys.*, **115**(16) (2001) 7382–7392.
- [400] A. E. Clark and E. R. Davidson. Local spin III: Wave Function Analysis along a reaction Coordinate, H Atom Abstraction, and Addition Processes of Benzyne,. *J. Chem. Phys. A*, **106** (2002) 6890–6896.
- [401] E. R. Davidson and A. E. Clark. Local Spin II,. *Mol. Phys.*, **100**(3) (2002) 373–383.
- [402] T. A. O’Brien and E. R. Davidson. Semiempirical Local Spin: Theory and Implementation of the ZILSH Method for Predicting Heisenberg Exchange Constants of Polynuclear Transition Metal Complexes. *Int. J. Quantum Chem.*, **92** (2003) 294–325.
- [403] K. E. Laidig and R. F. W. Bader. Properties of atoms in molecules: Atomic polarizabilities. *J. Chem. Phys.*, **93**(10) (1990) 7213–7224.
- [404] R. Bader, T. Keith, K. Gough, and K. Laidig. Properties of atoms in molecules: additivity and transferability of group polarizabilities. *Mol. Phys.*, **75**(5) (1992) 1167–1189.
- [405] N. Marzari and D. Vanderbilt. Maximally localized generalized Wannier functions for composite energy bands. *Phys. Rev. B*, **56**(20) (1997) 12847–12865.
- [406] B. Kirchner and J. Hutter. Solvent effects on electronic properties from Wannier functions in a dimethyl sulfoxide/water mixture. *J. Chem. Phys.*, **121**(11) (2004) 5133–5142.
- [407] S. Lubner, M. Iannuzzi, and J. Hutter. Raman spectra from ab initio molecular dynamics and its application to liquid S-methyloxirane. *J. Chem. Phys.*, **141** (2014) 094503.
- [408] S. Lubner. Local electric dipole moments for periodic systems via density functional theory embedding. *J. Chem. Phys.*, **141** (2014) 234110.
- [409] C. R. Jacob and J. Neugebauer. Subsystem density-functional theory. *WIREs Comput. Mol. Sci.*, **4**(4) (2014) 325–362.

-
- [410] T. Dresselhaus and J. Neugebauer. Part and whole in wavefunction/DFT embedding. *Theor. Chem. Acc.*, **134** (2015) 97.
- [411] M. Thomas, M. Brehm, R. Fligg, P. Vohringer, and B. Kirchner. Computing vibrational spectra from ab initio molecular dynamics. *Phys. Chem. Chem. Phys.*, **15** (2013) 6608–6622.
- [412] M. Thomas, M. Brehm, and B. Kirchner. Voronoi dipole moments for the simulation of bulk phase vibrational spectra. *Phys. Chem. Chem. Phys.*, **17** (2015) 3207–3213.
- [413] R. F. W. Bader and C. F. Matta. Properties of atoms in crystals: Dielectric polarization. *Int. J. Quantum Chem.*, **85**(4-5) (2001) 592–607.
- [414] K. B. Wiberg and P. R. Rablen. Comparison of atomic charges derived via different procedures. *J. Comp. Chem.*, **14**(12) (1993) 1504–1518.
- [415] B. Gellatly and J. Finney. Calculation of protein volumes: An alternative to the Voronoi procedure. *J. Mol. Biol.*, **161**(2) (1982) 305–322.
- [416] R. F. W. Bader and P. M. Beddall. Virial Field Relationship for Molecular Charge Distributions and the Spatial Partitioning of Molecular Properties. *J. Chem. Phys.*, **56**(7) (1972) 3320–3329.
- [417] R. F. W. Bader, P. M. Beddall, and J. Peslak. Theoretical development of a virial relationship for spatially defined fragments of molecular systems. *J. Chem. Phys.*, **58**(2) (1973) 557–566.
- [418] R. F. W. Bader and R. R. Messer. Virial Partitioning of Charge Distributions and Properties of Diatomic Hydrides. *Can. J. Chem.*, **52**(12) (1974) 2268–2282.
- [419] R. F. W. Bader and P. M. Beddall. Virial partitioning of charge distributions and properties of diatomic hydrides. *J. Am. Chem. Soc.*, **95**(2) (1973) 305–315.
- [420] P. L. A. Popelier. *Atoms in Molecules: An Introduction*. Prentice Hall, London, 2000.
- [421] F. Hirshfeld. Bonded-atom fragments for describing molecular charge densities. *Theor. Chim. Acta*, **44**(2) (1977) 129–138.
- [422] F. De Proft, C. van Alsenoy, A. Peeters, W. Langenaeker, and P. Geerlings. Atomic Charges, Dipole Moments, and Fukui Functions Using the Hirshfeld Partitioning of the Electron Density. *J. Comp. Chem.*, **23**(12) (2002) 1198–1209.
- [423] E. N. Maslen and M. A. Spackman. Atomic charges and electron density

- partitioning. *Aust. J. Phys.*, **38** (1985) 273.
- [424] D. A. Egger, Z.-F. Liu, J. B. Neaton, and L. Kronik. Reliable Energy Level Alignment at Physisorbed Molecule-Metal Interfaces from Density Functional Theory. *Nano Letters*, **15**(4) (2015) 2448–2455.
- [425] T. A. Keith. *The Quantum Theory of Atoms in Molecules: From Solid State to DNA and Drug Design, Chapter 3*. WILEY-VCH Verlag GmbH & Co. KGaA, Weinheim, 2007.
- [426] R. F. W. Bader, A. Larouche, C. Gatti, M. T. Carroll, P. J. MacDougall, and K. B. Wiberg. Properties of atoms in molecules: Dipole moments and transferability of properties. *J. Chem. Phys.*, **87**(2) (1987) 1142–1152.
- [427] G. Henkelman, A. Arnaldsson, and H. Jónsson. A fast and robust algorithm for Bader decomposition of charge density. *Comp. Mater. Sci.*, **36**(3) (2006) 354–360.
- [428] S. Sanvito. Injecting and controlling spins in organic materials. *J. Mater. Chem.*, **17** (2007) 4455–4459.
- [429] W. Tang, E. Sanville, and G. Henkelman. A grid-based Bader analysis algorithm without lattice bias. *J. Phys.: Condens. Matter*, **21** (2009) 084204.
- [430] L. Groß and C. Herrmann. Local electric dipole moments: a generalized approach, under revision, 2016.
- [431] R. F. W. Bader. <http://www.chemistry.mcmaster.ca/aimpac/>.
- [432] F. W. Biegler-König, T. T. Nguyen-Dang, Y. Tal, R. F. W. Bader, and A. J. Duke. Calculation of the average properties of atoms in molecules. *J. Phys. B: At. Mol. Phys.*, **14** (1981) 2739.
- [433] F. W. Biegler-König, R. F. W. Bader, and T.-H. Tang. Calculation of the average properties of atoms in molecules. II. *J. Comp. Chem.*, **3**(3) (1982) 317.
- [434] P. L. A. Popelier. A fast algorithm to compute atomic charges based on the topology of the electron density. *Theor. Chem. Acc.*, **105**(4-5) (2001) 393–399.
- [435] W. Koch and M. C. Holthausen. *A Chemist’s Guide to Density Functional Theory*. Wiley VCH, Weinheim, 2nd ed., 2001.
- [436] R. Ahlrichs, M. Bär, M. Häser, H. Horn, and C. Kömel. Electronic Structure Calculation on Workstation Computers: The Program System Turbomole. *Chem. Phys. Lett.*, **162**(3) (1989) 165–169.
- [437] P. Giannozzi, S. Baroni, N. Bonini, M. Calandra, R. Car, C. Cavaz-

-
- zoni, D. Ceresoli, G. L. Chiarotti, M. Cococcioni, I. Dabo, A. Dal Corso, S. de Gironcoli, S. Fabris, G. Fratesi, R. Gebauer, U. Gerstmann, C. Gougousis, A. Kokalj, M. Lazzeri, L. Martin Samos, N. Marzari, F. Mauri, R. Mazzarello, S. Paolini, A. Pasquarello, L. Paulatto, C. Sbraccia, S. Scandolo, G. Sclauzero, A. P. Seitsonen, A. Smogunov, P. Umari, and R. M. Wentzcovitch. QUANTUM ESPRESSO: a modular and open-source software project for quantum simulations of materials. *J. Phys.:Condens. Matter*, **21** (2009) 395502. available from <http://www.quantum-espresso.org>.
- [438] T. A. Keith. AIMAll (Version 14.11.23), TK Gristmill Software, Overland Park KS, USA, 2014; available from aim.tkgristmill.com.
- [439] T. Lu. MULTIWFN — A multifunctional wavefunction analyzer, 2011. version 2.01.
- [440] A. Zahab, L. Spina, P. Poncharal, and C. Marlière. Water-vapor effect on the electrical conductivity of a single-walled carbon nanotube mat. *Phys. Rev. B*, **62** (2000) 10000–10003.
- [441] T. Someya, P. Kim, and C. Nuckolls. Conductance measurement of single-walled carbon nanotubes in aqueous environment. *App. Phys. Lett.*, **82**(14) (2003) 2338–2340.
- [442] P. S. Na, H. Kim, H.-M. So, K.-J. Kong, H. Chang, B. H. Ryu, Y. Choi, J.-O. Lee, B.-K. Kim, J.-J. Kim, and J. Kim. Investigation of the humidity effect on the electrical properties of single-walled carbon nanotube transistors. *App. Phys. Lett.*, **87**(9) (2005) 093101.
- [443] R. A. Bell, M. C. Payne, and A. A. Mostofi. Does water dope carbon nanotubes? *J. Chem. Phys.*, **141**(16) (2014) 164703.
- [444] J. Kong, N. R. Franklin, C. Zhou, M. G. Chapline, S. Peng, K. Cho, and H. Dai. Nanotube Molecular Wires as Chemical Sensors. *Science*, **287** (2000) 622–625.
- [445] C. P. Collier, G. Mattersteig, E. W. Wong, Y. Luo, K. Beverly, J. Sampaio, F. M. Raymo, J. F. Stoddart, and J. R. Heath. A [2]Catenane-Based Solid State Electronically Reconfigurable Switch. *Science*, **289**(5482) (2000) 1172–1175.
- [446] A. Goldoni, R. Larciprete, L. Petaccia, and S. Lizzit. Single-Wall Carbon Nanotube Interaction with Gases: Sample Contaminants and Environmental Monitoring. *J. Am. Chem. Soc.*, **125**(37) (2003) 11329–11333.
- [447] D. Goldfarb and D. Arieli. Spin density distribution and the location of protons in paramagnetic proteins. *Annu. Rev. Biophys. Biomol. Struct.*, **33**

- (2004) 441–468.
- [448] J. Zhang, A. Boyd, A. Tselev, M. Paranjape, and P. Barbara. Mechanism of NO₂ detection in carbon nanotube field effect transistor chemical sensors. *Appl. Phys. Lett.*, **88** (2006) 123112.
- [449] S. Santucci, S. Picozzi, F. Di Gregorio, L. Lozzi, C. Cantalini, L. Valentini, J. M. Kenny, and B. Delley. NO₂ and CO gas adsorption on carbon nanotubes: Experiment and theory. *J. Chem. Phys.*, **119**(20) (2003) 10904.
- [450] Y. W. Chang, J. S. Oh, S. H. Yoo, H. H. Choi, and K.-H. Yoo. Electrically refreshable carbon-nanotube-based gas sensors. *Nanotechnology*, **18**(43) (2007) 435504.
- [451] S. Peng and K. Cho. Chemical control of nanotube electronics. *Nanotechnology*, **11**(2) (2000) 57.
- [452] H. Chang, J. D. Lee, S. M. Lee, and Y. H. Lee. Adsorption of NH₃ and NO₂ molecules on carbon nanotubes. *Appl. Phys. Lett.*, **79**(23) (2001) 3863.
- [453] J. Zhao, A. Buldum, J. Han, and J. P. Lu. Gas molecule adsorption in carbon nanotubes and nanotube bundles. *Nanotechnology*, **13**(2) (2002) 195–200.
- [454] J. Zhao, J. P. Lu, J. Han, and C.-K. Yang. Noncovalent functionalization of carbon nanotubes by aromatic organic molecules. *Appl. Phys. Lett.*, **82**(21) (2003) 3746.
- [455] L. M. Woods, c. C. Bădescu, and T. L. Reinecke. Adsorption of simple benzene derivatives on carbon nanotubes. *Phys. Rev. B*, **75** (2007) 155415.
- [456] F. Tournus and J.-C. Charlier. Ab initio study of benzene adsorption on carbon nanotubes. *Phys. Rev. B*, **71** (2005) 165421.
- [457] A. Sadrzadeh, A. A. Farajian, and B. I. Yakobson. Electron transport of nanotube-based gas sensors: An ab initio study. *Appl. Phys. Lett.*, **92** (2008) 022103.
- [458] M. D. Ganji, M. Mohseni, and A. Bakhshandeh. Simple benzene derivatives adsorption on defective single-walled carbon nanotubes: a first-principles van der Waals density functional study. *J. Mol. Model.*, **19**(3) (2012) 1059–1067.
- [459] K. Azizi and M. Karimpanah. Computational study of Al- or P-doped single-walled carbon nanotubes as NH₃ and NO₂ sensors. *Appl. Surf. Sci.*, **285** (2013) 102–109.
- [460] J. Kong and H. Dai. Full and Modulated Chemical Gating of Individual Carbon Nanotubes by Organic Amine Compounds. *J. Phys. Chem. B*, **105** (2001) 2890–2893.

-
- [461] S. Peng, K. Cho, P. Qi, and H. Dai. Ab initio study of CNT-NO₂ gas sensor. *Chem. Phys. Lett.*, **387**(4-6) (2004) 271–276.
- [462] A. Maiti, J. Hoekstra, J. andzelm, N. Govind, A. Ricca, A. Svizhenko, H. Mehrez, and M. P. Anantram. Electronic transport through carbon nanotubes - effect of contacts, topological defects, dopants and chemisorbed impurities. *NSTI-Nanotech*, **3** (2005) 236–239.
- [463] K. Chikkadi, M. Muoth, C. Roman, M. Haluska, and C. Hierold. Advances in NO₂ sensing with individual single-walled carbon nanotube transistors. *Beilstein J. Nanotech.*, **5** (2014) 2179–2191.
- [464] R. Waser. *Nanoelectronics and Information Technology: Materials, Processes, Devices*. Wiley-VCH Verlag GmbH & Co. KGaA, 2. edition ed., 2005.
- [465] V. Derycke, R. Martel, J. Appenzeller, and P. Avouris. Controlling doping and carrier injection in carbon nanotube transistors. *Appl. Phys. Lett.*, **80**(15) (2002) 2773.
- [466] K. Bradley, J.-C. P. Gabriel, M. Briman, A. Star, and G. Grüner. Charge Transfer from Ammonia Physisorbed on Nanotubes. *Phys. Rev. Lett.*, **91** (2003) 218301.
- [467] N. Peng, Q. Zhang, C. L. Chow, O. K. Tan, and N. Marzari. Sensing Mechanisms for Carbon Nanotube Based NH₃ Gas Detection. *Nano Lett.*, **9**(4) (2009) 1626–1630.
- [468] J. Suehiro, H. Imakiire, S.-i. Hidaka, W. Ding, G. Zhou, K. Imasaka, and M. Hara. Schottky-type response of carbon nanotube NO₂ gas sensor fabricated onto aluminum electrodes by dielectrophoresis. *Sensors and Actuators B: Chemical*, **114**(2) (2006) 943–949.
- [469] A. Goldoni, L. Petaccia, S. Lizzit, and R. Larciprete. Sensing gases with carbon nanotubes: a review of the actual situation. *J. Phys.:Condens. Matter*, **22**(1) (2010) 013001.
- [470] J. Dai, P. Giannozzi, and J. Yuan. Adsorption of pairs of NO_x molecules on single-walled carbon nanotubes and formation of NO+NO₃ from NO₂. *Surf. Sci.*, **603**(21) (2009) 3234–3238.
- [471] D. Riccardi, P. Schaefer, Y. Yang, H. Yu, N. Ghosh, X. Prat Resina, P. König, G. Li, D. Xu, H. Guo, M. Elstner, and Q. Cui. Development of Effective Quantum Mechanical/Molecular Mechanical (QM/MM) Methods for Complex Biological Processes. *J. Phys. Chem. B*, **110** (2006) 6458–6469.
- [472] S. Peng and K. Cho. Ab Initio Study of Doped Carbon Nanotube Sensors. *Nano Lett.*, **3**(4) (2003) 513–517.

- [473] K. Imani, M. R. Abolhassani, and A. A. Sabouri Dodaran. Electronic transport calculation of adsorbate NO₂ and NO molecules on graphene using Maximally Localized Wannier functions. *Eur. Phys. J. B*, **74**(1) (2010) 135–138.
- [474] E. Akbari, Z. Buntat, M. Ahmad, A. Enzevaeae, R. Yousof, S. Iqbal, M. Ahmadi, M. Sidik, and H. Karimi. Analytical Calculation of Sensing Parameters on Carbon Nanotube Based Gas Sensors. *Sensors*, **14**(3) (2014) 5502–5515.
- [475] Y. Li, M. Hodak, W. Lu, and J. Bernholc. Mechanisms of NH₃ and NO₂ detection in carbon-nanotube-based sensors: An ab initio investigation. *Carbon*, **101** (2016) 177–183.
- [476] S. Grimme. Semiempirical GGA-type density functional constructed with a long-range dispersion correction. *J. Comp. Chem.*, **27** (2006) 1787–99.
- [477] G. Liu, M. Liu, S. Pu, C. Fan, and S. Cui. Synthesis and photochromic properties of novel pyridine-containing diarylethenes. *Dyes and Pigments*, **95**(3) (2012) 553–562.
- [478] J. Yin, G.-A. Yu, H. Tu, and S. H. Liu. Novel photoswitching dithienylethenes with ferrocene units. *Appl. Organomet. Chem.*, **20**(12) (2006) 869–873.
- [479] N. B. Zuckerman, X. Kang, S. Chen, and J. P. Konopelski. Synthesis of a ferrocene-functionalized unsymmetrical benzo[b]thienyl-thienylethene photo-switch with a cyclopentene core. *Tetrahedron Letters*, **54**(11) (2013) 1482–1485.
- [480] P. A. Liddell, G. Kodis, A. L. Moore, T. A. Moore, and D. Gust. Photonic Switching of Photoinduced Electron Transfer in a Dithienylethene–Porphyrin–Fullerene Triad Molecule. *J. Am. Chem. Soc.*, **124**(26) (2002) 7668–7669.
- [481] M. Milek, F. W. Heinemann, and M. M. Khusniyarov. Spin Crossover Meets Diarylethenes: Efficient Photoswitching of Magnetic Properties in Solution at Room Temperature. *Inorg. Chem.*, **52**(19) (2013) 11585–11592.
- [482] G. Szalóki and J.-L. Pozzo. Synthesis of Symmetrical and Nonsymmetrical Bisthienylcyclopentenenes. *Chemistry – A European Journal*, **19**(34) (2013) 11124–11132.
- [483] T. Steenbock, A. Escribano, J. Heck, and C. Herrmann. Photoswitching Behavior of a Cyclohexene-Bridged versus a Cyclopentene-Bridged Dithienylethene System. *Chem. Phys. Chem.*, **16**(7) (2015) 1491–1501.
- [484] C. Li, J. Ly, B. Lei, W. Fan, D. Zhang, J. Han, M. Meyyappan, M. Thompson, and C. Zhou. Data Storage Studies on Nanowire Transistors with Self-Assembled Porphyrin Molecules. *J. Phys. Chem. B*, **108** (2004) 9646–9649.
- [485] M. Zhuang, P. Rocheleau, and M. Ernzerhof. Approximate density functionals

-
- applied to molecular quantum dots. *J. Chem. Phys.*, **122** (2005) 154705.
- [486] A. C. Whalley, M. L. Steigerwald, X. Guo, and C. Nuckolls. Reversible Switching in Molecular Electronic Devices. *Journal of the American Chemical Society*, **129**(42) (2007) 12590–12591.
- [487] J. Huang, Q. Li, H. Su, and J. Yang. Transport properties through diarylethene derivatives between carbon nanotube electrodes: A theoretical study. *Chem. Phys. Lett.*, **479**(1-3) (2009) 120–124.
- [488] M. K. Ashraf, N. A. Bruque, J. L. Tan, G. J. O. Beran, and R. K. Lake. Conductance switching in diarylethenes bridging carbon nanotubes. *J. Chem. Phys.*, **134**(2) (2011).
- [489] K. Matsuda, M. Ikeda, and M. Irie. Photochromism of Diarylethene-capped Gold Nanoparticles. *Chem. Lett.*, **33** (2004) 456–457.
- [490] J. He, F. Chen, P. A. Liddell, J. Andréasson, S. D. Straight, G. D. T. A. Moore, A. L. Moore, J. Li, O. F. Sankey, and S. M. Lindsay. Switching of a photochromic molecule on gold electrodes: single-molecule measurements. *Nanotechnology*, **16**(6) (2005) 695.
- [491] T. Kudernac, S. J. van der Molen, B. J. van Wees, and B. L. Feringa. Uni- and bi-directional light-induced switching of diarylethenes on gold nanoparticles. *Chem. Commun.*, **408**(34) (2006) 3597–3599.
- [492] D. Sysoiev, A. Fedoseev, Y. Kim, T. E. Exner, J. Boneberg, T. Huhn, P. Leiderer, E. Scheer, U. Groth, and U. E. Steiner. Synthesis and Photoswitching Studies of Difurylperfluorocyclopentenes with Extended π -Systems. *Chem. Eur. J.*, **17**(24) (2011) 6663–6672.
- [493] P. T. C. Arramel, T. Kudernac, N. Katsonis, M. van der Maas, B. L. Feringa, and B. J. van Wees. Reversible light induced conductance switching of asymmetric diarylethenes on gold: surface and electronic studies. *Nanoscale*, **5** (2013) 9277–9282.
- [494] T. C. Pijper, O. Ivashenko, M. Walko, P. Rudolf, W. R. Browne, and B. L. Feringa. Position and Orientation Control of a Photo- and Electrochromic Dithienylethene Using a Tripodal Anchor on Gold Surfaces. *J. Phys. Chem. C*, **119**(7) (2015) 3648–3657.
- [495] S. J. van der Molen and P. Liljeroth. Charge transport through molecular switches. *J. Phys.: Condens. Matter*, **22**(13) (2010) 133001.
- [496] M. Ikeda, N. Tanifuji, H. Yamaguchi, M. Irie, and K. Matsuda. Photoswitching of conductance of diarylethene-Au nanoparticle network. *Chem. Commun.*, (2007) 1355–1357.

- [497] C. Sciascia, R. Castagna, M. Dekermenjian, R. Martel, A. R. Srimath Kandada, F. Di Fonzo, A. Bianco, C. Bertarelli, M. Meneghetti, and G. Lanzani. Light-Controlled Resistance Modulation in a Photochromic Diarylethene-Carbon Nanotube Blend. *J. Phys. Chem. C*, **116**(36) (2012) 19483–19489.
- [498] A. U. Wurl. Kohlenstoff-Nanoröhren-Transistoren und ihre Wechselwirkungen mit thiophenbasierten Molekülen. Dissertation, Universität Hamburg, 2012.
- [499] A. U. Wurl and C. Klinke. Unpublished data.
- [500] A. Star, T.-R. Han, J.-C. P. Gabriel, K. Bradley, and G. Grüner. Interaction of Aromatic Compounds with Carbon Nanotubes Correlation to the Hammett Parameter of the Substituent and Measured Carbon Nanotube FET Response. *Nano Lett.*, **3**(10) (2003) 1421–1423.
- [501] J. Oh, S. Roh, W. Yi, H. Lee, and J. Yoo. Conductivity change of carbon nanotube with strong electron-donating and withdrawing molecules. *Journal of Vacuum Science & Technology B*, **22**(3) (2004) 1416–1419.
- [502] K. E. Knowles, M. T. Frederick, D. B. Tice, A. J. Morris Cohen, and E. A. Weiss. Colloidal Quantum Dots: Think Outside the (Particle-in-a-)Box. *J. Phys. Chem. Lett.*, **3**(1) (2012) 18–26.
- [503] E. A. McArthur, A. J. Morris Cohen, K. E. Knowles, and E. A. Weiss. Charge Carrier Resolved Relaxation of the First Excitonic State in CdSe Quantum Dots Probed with Near-Infrared Transient Absorption Spectroscopy. *J. Phys. Chem. B*, **114**(45) (2010) 14514–14520.
- [504] M. T. Frederick and E. A. Weiss. Relaxation of Exciton Confinement in CdSe Quantum Dots by Modification with a Conjugated Dithiocarbamate Ligand. *ACS Nano*, **4**(6) (2010) 3195–3200.
- [505] D. Devault. Quantum mechanical tunnelling in biological systems. *Quarterly Reviews of Biophysics*, **13** (1980) 387–564.
- [506] R. A. Marcus. On the Theory of Oxidation-Reduction Reactions Involving Electron Transfer. I. *J. Chem. Phys.*, **24**(5) (1956) 966–978.
- [507] M. D. Newton. Quantum chemical probes of electron-transfer kinetics: the nature of donor-acceptor interactions. *Chem. Rev.*, **91**(5) (1991) 767–792.
- [508] E. Alguire and J. E. Subotnik. Diabatic couplings for charge recombination via Boys localization and spin-flip configuration interaction singles. *J. Chem. Phys.*, **135** (2011) 044114.
- [509] Q. Wu and T. Van Voorhis. Direct optimization method to study constrained systems within density-functional theory. *Phys. Rev. A*, **72** (2005) 024502.

-
- [510] C. Lian and M. D. Newton. Ab initio studies of electron transfer: pathway analysis of effective transfer integrals. *J. Chem. Phys.*, **96**(7) (1992) 2855–2866.
- [511] M. D. Newton. Comparison of electron-transfer matrix elements for transition-metal complexes: t_{2g} vs. e_g transfer and ammine vs. aqua ligands. *J. Phys. Chem.*, **90**(16) (1986) 3734–3739.
- [512] R. S. Mulliken. Molecular Compounds and their Spectra. III. The Interaction of Electron Donors and Acceptors. *J. Phys. Chem.*, **56**(7) (1952) 801–822.
- [513] N. S. Hush. Intervalence-transfer absorption. Part 2. Theoretical considerations and spectroscopic data. *Prog. Inorg. Chem.*, **8** (1967) 391.
- [514] S. F. Boys. Construction of molecular orbitals to be approximately invariant for changes from one molecule to another. *Rev. Mod. Phys.*, **32** (1960) 296.
- [515] J. E. Subotnik, S. Yeganeh, R. J. Cave, and M. A. Ratner. Constructing diabatic states from adiabatic states: Extending generalized Mulliken–Hush to multiple charge centers with Boys localization. *J. Chem. Phys.*, **129** (2008) 244101.
- [516] D. M. Adams, L. Brus, C. E. D. Chidsey, S. Creager, C. Creutz, C. R. Kagan, P. V. Kamat, M. Lieberman, S. Lindsay, R. A. Marcus, and et al. Charge Transfer on the Nanoscale: Current Status. *J. Phys. Chem. B*, **107**(28) (2003) 6668–6697.
- [517] D. L. Dexter. A Theory of Sensitized Luminescence in Solids. *J. Chem. Phys.*, **21**(5) (1953) 836–850.
- [518] V. May and O. Kühn. *Charge and Energy Transfer Dynamics in Molecular Systems*. International Series of Monographs on Chemistry. Wiley-VCH, Weinheim, 2004.
- [519] R. van Grondelle. Excitation energy transfer, trapping and annihilation in photosynthetic systems. *Biochimica et Biophysica Acta (BBA) - Reviews on Bioenergetics*, **811**(2) (1985) 147–195.
- [520] Maxima, a Computer Algebra System. Version 13.04.2, 2014.
- [521] F. Scholz, L. Dworak, V. V. Matylitsky, and J. Wachtveitl. Ultrafast Electron Transfer from Photoexcited CdSe Quantum Dots to Methylviologen. *Chem. Phys. Chem.*, **12** (2011) 2255–2259.
- [522] L. Dworak, V. V. Matylitsky, T. Ren, T. Basché, and J. Wachtveitl. Acceptor Concentration Dependence of Förster Resonance Energy Transfer Dynamics in Dye–Quantum Dot Complexes. *J. Phys. Chem. C*, **118**(8) (2014) 4396–4402.

- [523] A. Zabet Khosousi and A.-A. Dhirani. Charge Transport in Nanoparticle Assemblies. *Chem. Rev.*, **108**(10) (2008) 4072–4124.
- [524] P. Deák, T. Frauenheim, and M. R. Pederson, Eds. *Computer Simulation of Materials at Atomic Level*. Wiley-VCH Verlag GmbH & Co. KGaA, 2005.
- [525] W. Peter Wuelfing, Stephen J. Green, Jeremy J. Pietron, David E. Cliffl, and Royce W. Murray. Electronic Conductivity of Solid-State, Mixed-Valent, Monolayer-Protected Au Clusters. *J. Am. Chem. Soc.*, **122**(46) (2000) 11465–11472.
- [526] R. A. Marcus. Electron Transfer Reactions in Chemistry: Theory and Experiment (Nobel Lecture). *Angew. Chem. Int. Ed. Engl.*, **32**(8) (1993) 1111–1121.
- [527] J. Hafner. Ab-initio simulations of materials using VASP: Density-functional theory and beyond. *J. Comp. Chem.*, **29**(13) (2008) 2044–2078. <http://cms.mpi.univie.ac.at/vasp/>.
- [528] R. Ahlrichs, M. K. Armbruster, R. Bachorz, H.-P. B. M. Bär, R. Bauernschmitt, F. A. Bischoff, S. Böcker, A. M. Burow, N. Crawford, P. Deglmann, F. D. Sala, M. Diedenhofen, M. Ehrig, K. Eichkorn, S. Elliott, D. Friese, F. Furche, A. Glöß, N. Graf, Lu. Grajciar, F. Haase, M. Häser, C. Hättig, A. Hellweg, B. Helmich, S. Höfener, H. Horn, C. Huber, U. Huniar, M. Kattannek, W. Klopper, A. Köhn, C. Kölmel, M. Kollwitz, M. Kühn, K. May, P. Nava, C. Ochsenfeld, H. Öhm, M. Pabst, H. Patzelt, D. Rappoport, O. Rubner, A. Schäfer, G. Schmitz, U. Schneider, M. Sierka, D. P. Tew, O. Treutler, B. Unterreiner, M. von Arnim, F. Weigend, P. Weis, H. Weiss, and N. Winter. TURBOMOLE V6.6 2014, a development of University of Karlsruhe and Forschungszentrum Karlsruhe GmbH, 1989-2007, TURBOMOLE GmbH, since 2007; available from <http://www.turbomole.com>.
- [529] A. Schäfer, C. Huber, and R. Ahlrichs. Fully optimized contracted Gaussian basis sets of triple zeta valence quality for atoms Li to Kr. *J. Chem. Phys.*, **100**(8) (1994) 5829.
- [530] J. Perdew, K. Burke, and Y. Wang. Generalized gradient approximation for the exchange-correlation hole of a many-electron system. *Phys. Rev. B*, **54** (1996) 16533–16539.
- [531] A. D. Becke. Density-functional thermochemistry. III. The role of exact exchange. *J. Chem. Phys.*, **98**(7) (1993) 5648–5652.
- [532] B. I. Dunlap, J. W. D. Connolly, and J. R. Sabin. On some approximations in applications of X_α theory. *J. Chem. Phys.*, **71** (1979) 3396–3402.
- [533] E. J. Baerends, D. E. Ellis, and P. Ros. Self-consistent molecular Hartree–

-
- Fock–Slater calculations. I. The computational procedure. *Chem. Phys.*, **2** (1973) 41–53.
- [534] A. Schäfer, H. Horn, and R. Ahlrichs. Fully Optimized Contracted Gaussian Basis Sets for Atoms Li to Kr. *J. Chem. Phys.*, **97**(4) (1992) 2571–2577.
- [535] F. Weigend, M. Hr, H. Patzelt, and R. Ahlrichs. RI-MP2: optimized auxiliary basis sets and demonstration of efficiency. *Chem. Phys. Lett.*, **294**(1-3) (1998) 143–152.
- [536] S. Grimme, S. Ehrlich, and L. Goerigk. Effect of the damping function in dispersion corrected density functional theory. *J. Comp. Chem.*, **32**(7) (2011) 1456–1465.
- [537] D. Corso. Quantum Espresso Pseudopotentials – PSLibrary 0.3.1.; SISSA, Italy; available from <http://theosrv1.epfl.ch/Main/Pseudopotentials>.
- [538] J. T. H. Dunning. Gaussian basis sets for use in correlated molecular calculations. I. The atoms boron through neon and hydrogen. *J. Chem. Phys.*, **90** (1989) 1007–1023.
- [539] P. J. Hay and W. R. Wadt. Ab initio effective core potentials for molecular calculations. Potentials for the transition metal atoms Sc to Hg. *J. Phys. Chem.*, **82** (1985) 270–283.
- [540] P. J. Hay and W. R. Wadt. Ab initio effective core potentials for molecular calculations. Potentials for main group elements Na to Bi. *J. Phys. Chem.*, **82** (1985) 284–298.
- [541] P. J. Hay and W. R. Wadt. Ab initio effective core potentials for molecular calculations. Potentials for K to Au including the outermost core orbitals. *J. Phys. Chem.*, **82** (1985) 299–310.
- [542] C. Herrmann, G. C. Solomon, and M. A. Ratner. Organic radicals as spin filters. *J. Am. Chem. Soc.*, **132** (2010) 3682–3684.
- [543] M. D. Hanwell, D. E. Curtis, D. C. Lonie, T. Vandermeersch, E. Zurek, and G. R. Hutchison. Avogadro: an advanced semantic chemical editor, visualization, and analysis platform. *J. Cheminf.*, **4**(1) (2012) 17.
- [544] W. L. Delano. The PyMOL Molecular Graphics System, 2002. DeLano Scientific, Palo Alto, CA, USA (<http://www.pymol.org>).
- [545] E. Sanville, S. D. Kenny, R. Smith, and G. Henkelman. Improved grid-based algorithm for Bader charge allocation. *J. Comp. Chem.*, **28**(5) (2007) 899–908.
- [546] T. Weymuth, M. P. Haag, K. Kiewisch, S. Luber, S. Schenk, Ch. R. Jacob,

- C. Herrmann, J. Neugebauer, and M. Reiher. Vibrational spectroscopy with a robust meta-program for massively parallel standard and inverse calculations. *J. Comput. Chem.*, **33** (2012) 2186–2198.
- [547] Jmol: an open-source Java viewer for chemical structures in 3D. <http://www.jmol.org/>.
- [548] W. Humphrey, A. Dalke, and K. Schulten. VMD – Visual Molecular Dynamics. *J. Mol. Graph.*, **14** (1996) 33–38.
- [549] T. Williams and C. Kelley. Gnuplot 4.4: an interactive plotting program. <http://gnuplot.sourceforge.net/>, March 2010. organized by: Lars Hecking.
- [550] B. Harrington. Inkscape. <http://www.inkscape.org/>.
- [551] F. Biegler-König, J. Schönbohm, and D. Bayles. AIM2000 – A Program to Analyze and Visualize Atoms in Molecules. *J. Comp. Chem.*, **22**(5) (2001) 545–559. available from <http://www.aim2000.de/>.
- [552] F. Biegler-König and J. Schönbohm. Update of the AIM2000-Program for atoms in molecules. *J. Comp. Chem.*, **23**(15) (2002) 1489–1494.
- [553] J. C. O. Alba. *Xaim—A graphical user interface to programs that can perform the Bader analysis*, 2015.
- [554] M. Kohout. DGrid 4.6 – A program for the generation of property values on an equidistant grid and the analysis of those gridded fields, inclusive the basin search. <http://www.cpfs.mpg.de/kohout/dgrid.html>, 2014.
- [555] A. Volkov, P. Macchi, L. J. Farrugia, C. Gatti, P. Mallinson, T. Richter, and T. Koritsanszky. XD2006 - a computer program for multipole refinement, topological analysis of charge densities and evaluation of intermolecular energies from experimental or theoretical structure factors, 2006; available from <http://xd.chem.buffalo.edu/>.
- [556] T. Verstraelen, S. Vandenbrande, M. Chan, F. H. Zadeh, C. González, P. A. Limacher, and A. Malek. Horton 1.2.1, 2013. (<http://theochem.github.io/horton/>).
- [557] M. Barzaghi. PAMoC: Properties of Atoms and Molecules in Molecular Crystals from theoretical and experimental electron densities, 2014. <https://sites.google.com/site/pamocproject/>.
- [558] D. Kozłowski and J. Pilmé. New Insights in Quantum Chemical Topology Studies Using Numerical Grid-based Analyses. *J. Comput. Chem.*, **32**(15) (2011) 3207–3217. available from <http://www.lct.jussieu.fr/pagesperso/pilme/topchempage.html>.

-
- [559] B. Silvi. TopMod. Laboratoire de Chimie Théorique Université Pierre et Marie Curie; available from <http://www.lct.jussieu.fr/pagesperso/silvi/topmod.html>, 2010.
- [560] J. M. Solano-Altamirano and J. M. Hernández-Pérez. DensToolKit: A comprehensive open-source package for analyzing the electron density and its derivative scalar and vector fields. *Comp. Phys. Comm.*, **196** (2015) 362–371.
- [561] P. L. A. Popelier. MORPHY, a program for an automated atoms in molecules analysis. *Comp. Phys. Comm.*, **93**(2-3) (1996) 212–240.
- [562] P. L. A. Popelier. A method to integrate an atom in a molecule without explicit representation of the interatomic surface. *Comp. Phys. Comm.*, **108**(2-3) (1998) 180–190.

Declaration on oath

I hereby declare, on oath, that I have written the present dissertation by my own and have not used other than the acknowledged resources and aids.

Eidesstattliche Versicherung

Hiermit erkläre ich an Eides statt, dass ich die vorliegende Dissertationsschrift selbst verfasst und keine anderen als die angegebenen Quellen und Hilfsmittel benutzt habe.